Hard X-ray quantum optics in thin-film nanostructures

Dissertation zur Erlangung des Doktorgrades
an der Fakultät für Mathematik, Informatik und
Naturwissenschaften
Fachbereich Physik
der Universität Hamburg

vorgelegt von Johann Friedrich Albert Haber

aus Bonn

Hamburg, 2016

Gutachter der Dissertation:	Prof. Dr. Ralf Röhlsberger
	Prof. Dr. Andreas Hemmerich
Mitglieder der Prüfungskommission:	Prof. Dr. Daniela Pfannkuche
	Prof. Dr. Ralf Röhlsberger
	Prof. Dr. Andreas Hemmerich
	Prof. Dr. Christian Schröer
	Prof. Dr. Wilfried Wurth
Datum der Disputation:	31. März 2017
Vorsitzende des Prüfungsausschusses:	Prof. Dr. Daniela Pfannkuche
Leiter des Fachbereichs Physik:	Prof. Dr. Jan Louis
Vorsitzender des Fach-Promotionsausschusses:	Prof. Dr. Wolfgang Hansen
Dekan der MIN-Fakultät:	Prof. Dr. Heinrich Graener

Zusammenfassung. Diese Arbeit beschreibt quantenoptische Experimente mit Röntgenstrahlung, die das Ziel haben, den Bereich der starken Kopplung von Licht und Materie zu erreichen. Dabei wird die besondere Wechselwirkung ausgenutzt, die resonante Materie mit Röntgenstrahlung in speziellen Dünnschichtsystemen erfährt, die ihrerseits als Resonatoren ausgelegt sind. Die resonante Materie besteht hier aus Tantal-Atomen und dem Eisenisotop ^{57}Fe. Diese begrenzen die Zahl der Lichtmoden, mit denen die resonante Materie wechselwirkt, und verstärkt die Wechselwirkung mit den Röntgenstrahlen. Es ist uns gelungen, mit Röntgenstrahlung so eine Reihe von Phänomenen nachzuweisen, die der Quantenoptik schon länger bekannt sind, und als zentrale Bestandteile möglicher und bestehender Anwendungen der Quantenoptik etwa in der Messtechnik gelten. Dazu zählen die Beobachtung von starker Wechselwirkung zwischen Licht und Materie, und der damit einhergehende wiederholte Austausch einzelner virtueller Photonen zwischen zwei verschiedenen System, die sogenannten Rabi-Oszillationen. Ferner haben wir einen in der Röntgenoptik bisher nicht verwendeten Weg, Resonatoren für Licht herzustellen, erstmals getestet. Zu guter Letzt entwickeln wir ein neuartiges Verfahren zur Mössbauer-Spektroskopie an Synchrotron-Beschleunigern. Es basiert auf der ursprünglich mikroskopischen Technik der Ptychographie, und eröffnet die Möglichkeit, nicht nur hochaufgelöste Mössbauer-Spektren zu messen, sondern auch die Phase des gestreuten Lichts zu rekonstruieren. Die Ergebnisse ermöglichen neuartige Ansätze in der Quantenoptik mit Röntgenstrahlung, insbesondere mit Blick auf die baldige Verfügbarkeit von hochbrillianter Strahlung aus freien Elektronenlasern.

Abstract. This thesis describes quantum optical experiments with x-rays with the aim of reaching the strong-coupling regime of light and matter. We make use of the interaction which arises between resonant matter and x-rays in specially designed thin-film nanostructures which form x-ray cavities. Here, the resonant matter are Tantalum atoms and the Iron isotope ^{57}Fe. Both limit the number of modes available to the resonant atoms for interaction, and enhances the interaction strength. Thus we have managed to observe a number of phenomena well-known in quantum optics, which are the building blocks for sophisticated applications in e.g. metrology. Among these are the strong coupling of light and matter and the concurrent exchange of virtual photons, often called Rabi oscillations. Furthermore we have designed and tested a type of cavity hitherto unused in x-ray optics. Finally, we develop a new method for synchrotron Mössbauer spectroscopy, which not only promises to yield high-resolution spectra, but also enables the retrieval of the phase of the scattered light. The results open new avenues for quantum optical experiments with x-rays, particularly with regards to the ongoing development of high-brilliance x-ray free-electron lasers.

Publications within the scope of this thesis:

Johann Haber, Kai S. Schulze, Kai Schlage, Robert Loetzsch, Lars Bocklage, Tatiana Gurieva, Hendrik Bernhardt, Hans-Christian Wille, Rudolf Rüffer, Ingo Uschmann, Gerhard G. Paulus & Ralf Röhlsberger
Collective Strong Coupling in a nuclear optical lattice, Nature Photonics **10**, 445449 (2016)

Publications outside the scope of this thesis:

T. Salditt, S. Hoffmann, M. Vassholz, **J. Haber**, M. Osterhoff, and J. Hilhorst *X-Ray Optics on a Chip: Guiding X Rays in Curved Channels*, Phys. Rev. Lett. **115**, 203902 (2015)

M. Bartels, M. Krenkel, **J. Haber**, R.N. Wilke, and T. Salditt *X-Ray Holographic Imaging of Hydrated Biological Cells in Solution*, Phys. Rev. Lett. **114**, 048103 (2015)

H. Neubauer, S. Hoffmann, M. Kanbach, **J. Haber**, S. Kalbfleisch, S. P. Krüger and T. Salditt *High aspect ratio x-ray waveguide channels fabricated by e-beam lithography and wafer bonding*, Journal of Applied Physics. **115**, 214305 (2014);

Y. Friedman, E. Yudkin, I. Nowik, I. Felner, H.-C. Wille, R. Röhlsberger, **J. Haber**, G. Wortmann, S. Arogeti, M. Friedman, Z. Brand, N. Levi, I. Shafir, O. Efrati, T. Frumson, A. Finkelstein, A. I. Chumakov, I. Kantor and R. Rüffer *Synchrotron radiation Mössbauer spectra of a rotating absorber with implications for testing velocity and acceleration time dilation*, Journal of Synchrotron Radiation. **22**, 723-728 (2015);

Contents

Chapter I

Introduction

Since the discovery of x-rays by Wilhelm Conrad Röntgen in 1898 [1], they have become one of the most indispensable tools of research, both basic and applied. X-rays are the yardsticks by which we measure distances between atoms and molecules [2] and permit us to find out the structure of the molecules that make up the organic world [3]; x-rays allow us to determine the structure of proteins, measure the gravitational redshift [4], obtain medical images of tissue [5], estimate the properties of matter under pressures close to those in the center of Jupiter [6], and x-rays resolve the interactions and correlations which give complex solid-state systems the properties we hope to harvest for future technological progress [7]. Over a hundred years the brilliance of x-ray sources has grown by over fifteen orders of magnitude, and the advent of hard x-ray free electron lasers [8] indicates that their importance will not wane any time soon.

The field of quantum optics is a success story of similar importance and magnitude, albeit rather younger. Stimulated by the invention of the laser, it began in the 1960s with the study of the quantum properties and description of radiation [9, 10]. It received a boost in the 1980s, when the first tentative successes in controlling the interaction of light and matter by mirror cavities surfaced [11]. This sub-field, dubbed cavity quantum electrodynamics, turned out to be the driving force behind the ascent of quantum optics to one of the dominant fields of physics in the 21st century, culminating with the award of the Nobel prize to David Wineland and Serge Haroche in 2012. The triumphs it racked up along the way included successful tests of the fundamental principles of quantum mechanics [12, 13, 14]; the advancement of metrology by a refinement in the precision of atomic clocks [15, 16]; the production of non-classical states of light [17] and implementations of quantum computing methods [18]. Over the years, many physical systems and frequency bands have been used to perform quantum optical experiments. From

the beginnings with microwaves and Rydberg atoms [19], the development ranges over infrared radiation and excitonic quantum wells [20], until recently quantized electric circuits operated with radiofrequencies [21], as well as visible light and ions or Bose-Einstein condensates [22] have moved into focus.

In light of the two developments sketched above, an obvious question arises. Is it possible to unite the fields of quantum optics and x-ray physics? Can the techniques of quantum optics be extended to x-ray physics in order to refine our control over its properties and enhance the range of accessible experiments? The motivation for these questions is clear. The particular properties of x-ray radiation, especially the short wavelength and the high absorption length give it a near-monopoly on the resolution of certain questions; for example the microscopic properties of correlated materials in the bulk. If our control over x-rays were as advanced as it is over visible light or microwaves, we might not only gain new insights into a great many materials, but also new 'tuning knobs', i.e. our control over the materials' properties and behaviour could be extended as well.

Unfortunately there are plenty of reasons why our control over x-rays is far from perfect. The range of optical elements available is severely limited to essentially perfect crystals [23, 24], and thin films in grazing incidence. Recently, compound refractive lenses [25, 26] and efficient zone plates [27] have become available as well for hard x-rays, but these are used for focusing, and are not an option for cavity design. Even then, the reflectivities are sub-par when compared to those achievable for visible light. As a consequence, the wide range of efficient and commercially available tools such as polarizing beam splitters etc. are not an option in this field, or have to be replaced by complicated custom solutions.

Nevertheless, in the last six years, the field of hard x-ray quantum optics has emerged. First forays into the subject were performed in the 1970s by Eisenberger et al [28, 29] and early 2000s by researchers around Adams [30, 31], who observed the first instances of non-linear x-ray optics at laboratory and synchrotron sources respectively. In a sense, Mössbauer quantum optical experiments with nuclear resonances have been performed much earlier, with Hamermesh and others [32] measuring and classically calculating the transmission of single Mössbauer photons through an absorber foil, and Harris [33, 34] supplying the quantum mechanical explanation for the observed phenomena. Some of these authors also predicted [35] an Autler-Townes-like [36] line splitting in the Mössbauer resonance due to strong coupling of the low-lying hyperfine levels with a strong electromagnetic field of microwave frequency. This was later observed in permalloy films [37]. More recently, free-electron lasers have given the field a new impetus. Both second-harmonic generation [38] and x-ray-optical wave-mixing [39] results were published; first

lasing in the x-ray range was observed [40, 41], and new, nonlinear regimes of Compton scattering were explored [42].
Outside of these results, which rely on new sources, classical Mössbauer spectroscopy has also contributed by opening new avenues for the control of single-pulse waveforms [43, 44, 45].
Additionally, a great number of theoretical proposals have surfaced, which for years to come promise exciting work for experimentalists [46, 47, 48, 49, 50, 51].
This thesis, however, rests on another strand of that rapidly developing field. For some years now, x-ray quantum optics has profited from the methodologies of cavity quantum electrodynamics being applied to it via the use of thin film nanostructures. This approach has yielded a great number of spectacular results. It was used to measure the collective Lamb shift of an ensemble of ^{57}Fe- nuclei [52], and to observe electromagnetically induced transparency in a similar system [53]. After theoretical proposals by Heeg and Evers [54], slow light [55], spontaneously generated inter-level coherences [56] and Fano resonances [57] could also be substantiated. On the other hand, the important milestone of collective strong coupling between a cavity mode and a nuclear ensemble has not been reached yet.
This is the aim of this thesis. Our approach is threefold:

- We attempt to reach the strong coupling limit by using an electronic resonance instead of ^{57}Fe nuclei. This also extends the reach of x-ray cavity quantum electrodynamics to other systems.

- instead of using the cavity design of the thin-film multilayer that was customary in all previous experiments we intend to capitalize on the possibility of using periodic multilayers, which display an enhanced light-matter interaction strength close to and at their band gaps

- Extending a previous experiment [53] and relying on theoretical proposals by Evers [58] and Pálffy [59, 60] we plan to achieve strong coupling not between a nuclear ensemble and a cavity, but between two nuclear ensembles by coupling them via a cavity in the dispersive limit.

The structure of the thesis is as follows. In Chapter 2, we introduce the scientific basis of this thesis, which includes a short, general purpose description of the effects we rely on, fundamental x-ray optics, the Mössbauer effect, nuclear resonant forward scattering, and a brief description of the origins of synchrotron radiation.
In Chapter 3, we will get somewhat more technical; we describe the experimental challenges of synchrotron-radiation based nuclear resonant forward scattering, and how to solve them. We also

include a description of our sample fabrication and characterization scheme, and a brief classical discussion of the workings of our multilayers.

The next Chapter is devoted to a discussion of the theoretical tools we use. We present a discussion of a transfer matrix algorithm for the quantitative analysis of our data. We introduce basic quantum optics and add theoretical models pioneered by Heeg and Evers to deal with our specific sample system, and add others we have found useful. The final Chapters are dedicated to the experiments themselves; their technical specifics, the resulting data, and its analysis. It may also include some theoretical discussion that has not found a place in the previous Chapter.

Chapter II

Physical Fundamentals

II.1. Introduction

This thesis is concerned with many-body x-ray quantum optics of Mössbauer nuclei in structured reservoirs. This means that we use layered nanostructures forming both cavities and periodic multilayers, or one-dimensional photonic crystals and optical lattices in order to (a) enhance the x-ray interaction with the nuclei and (b) restrict the number of electromagnetic field modes available for interaction with the nuclei. The thesis will mostly use the standard formalisms of quantum optics, i.e. the Schrödinger equation both in its standard and more refined versions, such as the Master equation including dissipation, the Lindblad formalism [61]. However, since the physical system at hand is different from the usual subjects of quantum optics such as cold atoms or excitonic nanostructures, we begin by giving a brief introduction to some aspects of it which might be unfamiliar to readers which are more acquainted with the aforementioned fields. This background will help those readers understand some technical and experimental subtleties appearing in this thesis, and point out the peculiarities of this subject.

II.2. X-ray Optics

This section deals with fundamental aspects of non-resonant electronic x-ray scattering, i.e. x-ray optics in stratified media. A good general-purpose resource on this and many other topics in x-ray physics is found in ref. [3]. The means we use to tailor the light-nuclei interaction are, as we said, nanostructures, specifically sputtered thin films. Under certain circumstances, these can be used as mirrors which enclose the resonant material, forming a cavity. We will follow several approaches, which will be outlined in Chapter IV. For the moment, we will elucidate the

basic physical mechanisms and effects that allow the use of thin films as mirrors. We begin by discussing the simplest case: non-resonant matter.

X-rays that illuminate a slab of non-resonant matter interact with it. They do so by several processes. The most important of these is non-resonant elastic Thompson scattering, which is the one we will be dealing with exclusively when we speak of non-resonant scattering or interaction. A simple classical description goes thus: a free, or quasi-free electron is accelerated by the electromagnetic field; since accelerated charges emit electromagnetic radiation, the accelerated electron emits light of the same frequency as the impinging light. For future calculations, we will use a slightly different description, based on scattering theory [62]. A wave that is scattered by a particle can be described as follows:

$$\Psi_s = e^{ikz} + f(\omega)\frac{e^{i\vec{k}\vec{r}}}{\vec{r}} \tag{1}$$

where the first term describes the incoming plane wave and $\vec{r} = (x, y, z)$ is a spatial coordinate. ω is the frequency of the electromagnetic field, f is the so-called scattering amplitude, which describes the strength with which the wave is scattered. For an atom, is given by [63]

$$f(\omega) = \frac{2\pi}{k_0}(-Zr_0 + i\frac{k_0}{4\pi}\sigma_t(\omega)) \tag{2}$$

where k_0 is the wave vector of the impinging electromagnetic field, Z is the atomic number, and σ_t is the total absorption cross-section. Obviously, the scattering amplitude depends on the number of electrons of the atom, as one would expect. For a stratified medium, the scattering amplitude can be expressed by multiplying it with the atomic number density ρ [62]. In order to use this in semiclassical calculations, we rephrase this quantity as the index of refraction n:

$$n = 1 + \frac{2\pi\rho}{k_0.^2}(-Zr_0 + i\frac{k_0}{4\pi}\sigma_t(\omega)) \tag{3}$$

which is usually expressed more concisely as

$$n = 1 - \delta + i\beta \tag{4}$$

δ and β are the so called *decrements* of the x-ray index of refraction. For all practical purposes they are looked up in a suitable database, i.e. CXRO [64]. Depending on the frequency, their order of magnitude varies between 10^{-4} and 10^{-6} for hard x-rays between, say, 10 and 30 keV. In this form, the most unusual features of the x-ray index of refraction is clearly revealed. First of all, it is very close to unity, the index of refraction of the vacuum. As one would expect, that makes it very hard to use stratified, amorphous media as mirrors for x-rays (crystal optics is another matter outside the scope of this thesis). But there is a loophole. The index of refraction is smaller than

unity. Therefore, the phase velocity of light within the medium is superluminal, and the angle of refraction (measuring parallel to the vacuum-matter interface) is actually smaller than the angle of incidence. As one decreases the angle of incidence, the angle of refraction decreases more, until it goes to zero at some particular angle. This angle, different for all materials and energies is called the critical angle, and if a medium is illuminated below it, it effectively functions as a high-quality mirror. This is essentially total external reflection: recall that the vacuum is the optically dense medium. A good approximation for the value of the critical angle is

$$\phi_c = \sqrt{2\delta} \tag{5}$$

The principle is illustrated in Fig. 1. If the surface is illuminated above the critical angle, almost all radiation propagates into the sample, and is not reflected. Inside the stratified medium, it is absorbed. To characterize the strength of absorption the concept of penetration depth has proved useful. It is the distance after which the intensity of the incoming beam has been attenuated by a factor e^{-1}. For x-rays of the energy range we are interested in, this is typically on the order of a few to a few dozen microns, depending on the material.

Of course, even in the case of total external reflection, the x-ray radiation partially penetrates the material it is reflected on, before it is reflected. The depth of this penetration is only a few nanometers; the closer the reflection is to the critical angle, the larger it is. This introduces some absorption into the equation. Indeed, the reflectivity close to the critical angle is different from 1, closer to 0.95 due to this absorption.

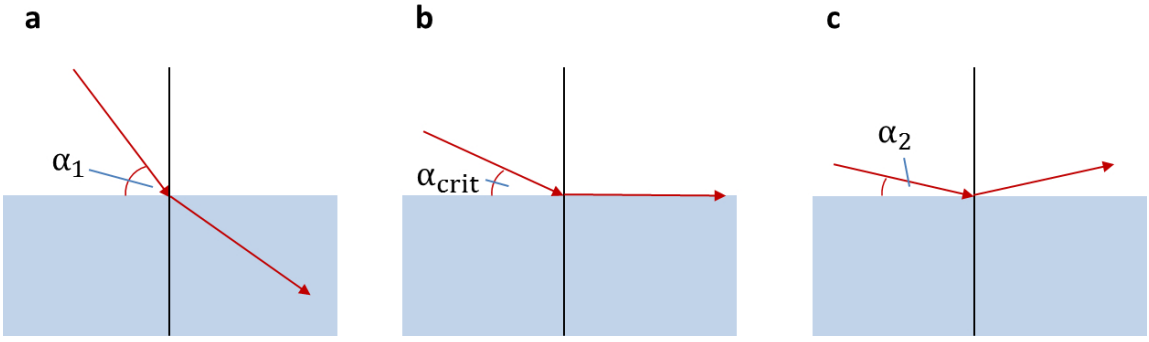

Figure 1: *The principle of total external reflection of hard x-rays and the critical angle. (a) the beam illuminates the sample above the critical angle, and is diffracted away from the normal. (b) the beam illuminates the sample above the critical angle, and is diffracted parallel to the normal. (c) the beam illuminates the sample below the critical angle and is fully reflected.*

II.3. The Mössbauer Effect

Discovered in 1958 by Rudolf Mössbauer in the course of experiments on the ^{191}Ir isotope [65, 66] and building on theoretical work by Lamb [67] and Dicke [68] the Mössbauer effect is the result of a complicated interplay between the electromagnetic degrees of freedom of the nuclear shell, and the collective kinetic degrees of freedom of an ensemble of atoms. Prior to the discovery of the Mössbauer effect, most absorption and fluorescence experiments with hard x-rays had been performed with gases [69]. At these energies, the following problem arises. Resonant absorption or emission of radiation with frequency ω of the resonant transition by a single nucleus results in a strong recoil due to momentum conversion, endowing the nucleus with a velocity v, where

$$-v = \frac{\hbar\omega}{Mc} \tag{6}$$

and M is the mass of the nucleus, and c the velocity of light, and ω the frequency. A rough estimate for ^{57}Fe then gives a velocity of $76\frac{m}{s}$ that the iron atom will take. The Doppler shift Δ of a moving nucleus is given by $\Delta \approx \frac{v}{c}\omega$, where c is the velocity of light. The Doppler shift is then orders of magnitude larger than the natural linewidth which corresponds to a Doppler velocity of $0.1\frac{mm}{s}$ for ^{57}Fe. Absorbed and emitted light are drastically detuned from each other, making spectroscopic investigations virtually impossible. A way out of this dilemma is offered by the Mössbauer effect.

The Mössbauer effect takes place in solid state systems comprising a number of nuclei. In such systems, the movements of nuclei are coupled, and therefore the momentum is exchanged between the x-rays and a phonon, a collective excitation of the nuclear lattice. Roughly speaking, the immense mass of the lattice will absorb the momentum instead of just a single nucleus. If the recoil energy of the free atom is much smaller than the average phonon energy, most of the emission or absorption process will take place without involving phonon excitation, so that effectively, the whole crystal acts as a rigid recoil partner. Consequently the velocity the lattice takes will be zero. A more diligent quantum mechanical calculation is possible [70], but outside the scope of this thesis. The nuclear resonant system which this thesis focuses on is the Mössbauer iron isotope ^{57}Fe. It has a nuclear magnetic dipole resonance at 14.41 keV with a natural linewidth of 4.66 neV, corresponding to a natural lifetime of 141 ns. The scattering cross section is 2464 kbarn, a value unrivaled among Mössbauer isotopes. Furthermore, its Lamb-Mössbauer factor, which determines how much of the incoming radiation is scattered without recoil, is 0.8 at room temperature. Many other Mössbauer isotopes require cooling to reach similar values. If an external magnetic field is applied, the hyperfine interaction leads to a Zeeman splitting of the levels. The basic features of

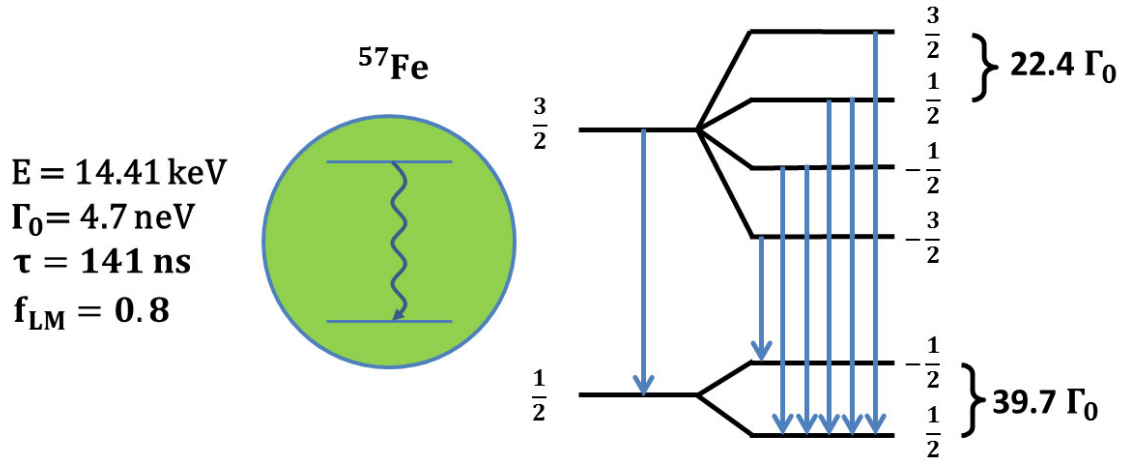

Figure 2: *The properties of the Mössbauer isotope ^{57}Fe-transition. E is the energy, Γ_0 the linewidth, f_{LM} the Lamb-Mössbauer factor and τ the life time. On the right we show the Zeeman splitting for a hyperfine magnetic field of* 33.6T*, the most common case.*

^{57}Fe are given in Fig. 2. The convenient physical properties and the importance of Fe in magnetic systems combine to make ^{57}Fe the workhorse isotope for Mössbauer spectroscopy, with over 95000 published papers.

II.4. Nuclear Resonant Scattering

Conventional Mössbauer spectroscopy is an extremely important experimental technique, but there are some experimental challenges. For one, the number of emitted photons is relatively low and they are emitted to 4π. To produce a small, collimated beam with high intensity, as necessary for the bulk of experiments in this thesis, is virtually impossible. The solution to this conundrum is to use for nuclear resonance excitation synchrotron radiation. In storage rings, a group of electrons (a so-called 'bunch') is accelerated in a ring particle accelerator to relativistic energies of a few GeV. They emit a wide spectrum of photon energies, depending on the electron energy. In special insertion devices located at the electron orbit along the circumference, so-called undulators, arrays of magnets with alternating polar orientation serve to accelerate the electrons such that they emit radiation of high intensity in a preferred particular energy band. Most 3rd generation synchrotron sources offer a bunch mode in which there are spacings of up to 800 ns between the bunches. Obviously, this is ideal for the observation of the temporal decay patterns of excited ^{57}Fe. In the following, we discuss theoretical aspects of nuclear forward scattering, which is essentially Mössbauer spectroscopy in the temporal domain. We will follow the lines of the

discussion of electronic scattering in the first section, with the focus now on the nuclear scattering contributions. The treatment is taken from [63], but the theory itself has its roots in the works of Hannon and Trammell, [71, 72, 73], Smirnov [74] and Afanas'ev, Kagan and Kohn [75]. The nuclear scattering length of a Mössbauer transition is expressed as

$$\vec{N}_{\mu\nu} = \frac{4\pi f_{LM}}{k_0} \sum_{M=-L}^{L} [\vec{\epsilon}_\nu \cdot \vec{Y}_{LM}(\vec{k}_0)][\vec{Y}_{LM}(\vec{k}_0) \cdot \vec{\epsilon}_\mu] F_{LM} \tag{7}$$

where

$$F_{LM}(\omega) = \sum_{\alpha,\eta} \frac{p_\alpha p_\alpha(\eta) \Gamma_x(\alpha M \eta L)}{(E(\eta) - E(\alpha) - \hbar\omega) - i\Gamma(\eta)/2} \tag{8}$$

and α and η mark the initially occupied and unoccupied states, with p_α and $p_\alpha(\eta)$ designating the probabilities that the states are occupied or unoccupied; Γ is the linewidth of the respective transition; L is the multipolarity of the transition (for a dipole: $L = 1$); M is the change of quantum number between the levels; $\vec{\epsilon}$ is the polarization vector, and $\vec{Y}_{LM}$ are the vector spherical harmonics, f_{LM} is the Lamb-Mössbauer factor (note that LM here is just an abbreviation of the names, and not connected to the multipolarity. In Eq. (7), the terms in the brackets describe the anisotropy of photon emission and absorption i.e. the fact that photons of one polarization can be scattered into another by the absorption-emission process, depending on the experimental setup.

As often in the following pages, we will restrict ourselves to the case of just one nuclear transition, equivalent to an absence of nuclear hyperfine interactions due to magnetic fields or electric field gradients. In that case the nuclear scattering length reduces to

$$\vec{N}_{\mu\nu} = (\epsilon_\nu \cdot \epsilon_\nu) \frac{k_0 \sigma_0 f_L M}{\hbar(\omega - \omega_0) + i\Gamma/2} \tag{9}$$

where

$$\sigma_0 = \frac{2\pi}{k_0^2} \frac{2I_e + 1}{2I_g + 1} \frac{1}{1 + \alpha} \tag{10}$$

and I_g and I_e are the nuclear spins of the ground and excited states, α is the coefficient of internal conversion. All this is valid for single atoms as well. To treat the interaction with an ensemble of atoms, we generalize the approach taken for non-resonant x-ray optics taken in a previous section Again, we calculate the scattering matrix first. The scattering matrix is calculated by summing the scattering length $\vec{N}$ over all atoms in the sample. In the case of very many nuclei and a high density, this can be replaced by multiplying $\vec{N}$ with the number density of the relevant material.

$$\vec{F} = \frac{2\pi}{k_0} \sum_i \rho_i \vec{N} \tag{11}$$

where ρ_i is again the density of the i-th atom species. The propagation of a wave field of amplitude $\vec{A}$ in a slab of material can be described by the equation

$$\frac{d\vec{A}}{dz} = i\vec{F}\vec{A} \tag{12}$$

or

$$\vec{A}(z) = e^{i\vec{F}z}\vec{A}(0) \tag{13}$$

in the case of a homogeneous material. In case $\vec{F}$ is not diagonal (i.e. if the sample is magnetized or subject to an electric field gradient), it has to be diagonalized, giving the eigenpolarizations. After diagonalization of $\vec{F}$, the exponential is easily calculated. After that, the forward propagation matrix is transformed back into the basis of linear polarizations. As there is an intrinsic dependence of $\vec{F}$ on the energy ω, this value gives the transmission through a slab of thickness z for any particular energy. Fourier transforming the result for a range of energies gives the temporal decay pattern for a slab of resonant matter.

A somewhat more intuitive derivation of this pattern can be given in a semiclassical approximation, as in [74, 76, 77]. For this, we return to the index of refraction. Its original derivation can be extended to contain resonant contributions by adding the nuclear resonant scattering length to the electronic scattering length, and then proceeding as before. For simplicity, we here replace the electronic part by the nuclear one.

We set

$$\vec{P} = \chi\epsilon_0\vec{E} \tag{14}$$

where χ is the susceptibility $\chi = \frac{\lambda^2}{\pi}\vec{N}$, $\vec{E}$ is the electrical field, and $\vec{P}$ is the polarization. By standard manipulations of the Maxwell equations and the above equation we arrive at the wave equation

$$(\frac{k^2}{K^2} - 1)\vec{E} = \chi\vec{E} \tag{15}$$

with $K = \frac{\omega}{c}$. Inside the material, the new wave vector k is

$$k = K + \delta K \tag{16}$$

Inserting Eq. (16) into Eq. (15), ignoring higher order terms and resolving for δ gives $\delta = \frac{\chi}{2}$. Of course, the refractive index $n = 1 - \delta$, hence we have derived the relation between the refractive index and the scattering amplitude. We set the boundary condition $E = E_0$ where E_0 is the incident wave, and obtain an expression for the transmitted wave

$$E_{tr} = E_0 e^{i\omega t - iK(1+\chi/2)z} \tag{17}$$

Performing the Fourier transform of this yields

$$E_{tr} = \epsilon_{\omega_0} e^{-\frac{\mu_e z}{2}}\delta(t) - \frac{1}{2t_0}\mu_z e^{i\omega_0 t - qt/2t_0}\frac{J_1(\sqrt{\mu_z t/t_0}}{\sqrt{\mu_z t/t_0}} \tag{18}$$

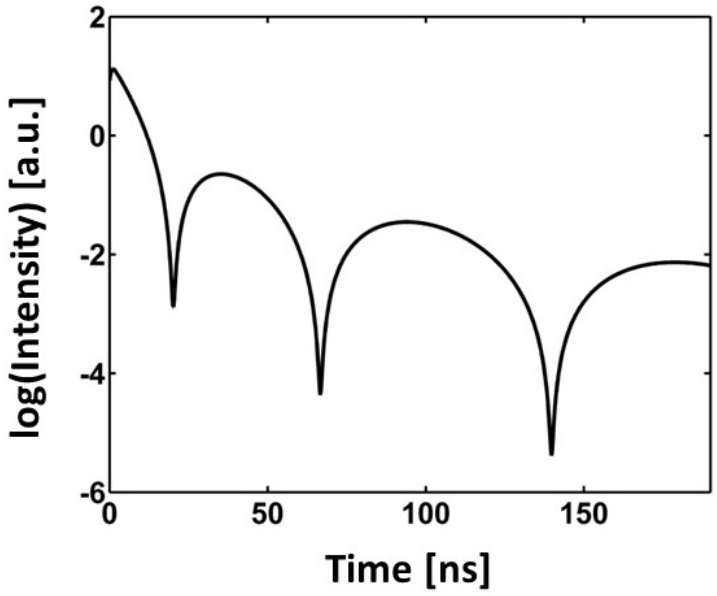

Figure 3: *The decay caused by multiple nuclear resonant scattering in the forward direction in an extended sample. The decay has the shape of a Bessel-function, with beats whose period increases with time. The larger the sample, and the higher the density of nuclei in it, the more beats are visible in a fixed timespan.*

Our treatment has implied that E_0 has a high energetic bandwidth, corresponding to an extremely short pulse. This is a very good approximation for synchrotron-based experiments. The term containing the δ-function models the instantaneous transmission of the non-interacting part of the pulse. The second term containing the Bessel-function gives the part of the pulse that results from the system response. A typical Bessel-function is shown in Fig. 3.

II.5. X-ray absorption spectroscopy

Mössbauer nuclei have a wealth of properties to recommend them for x-ray quantum optical experiments. The small spectral width also means that even tiny changes of the physical surroundings manifest themselves in measurable shifts. Besides the obvious materials science applications, this has led to spectacular results such as the first measurement of the gravitational redshift, and there are current proposals to use Mössbauer physics in much the same vein [78]. However, as so often in physics, the properties that appear to be advantages from one vantage point seem like distinct drawbacks from another. Even state-of-the-art third generation synchrotron sources do not possess the brilliance necessary to produce more than one resonant photon per pulse

in the standard operation modes. Free-electron laser facilities may provide bunches with up to 50 photons resonant with the 14.41 keV line of ^{57}Fe, but here the extremely high brilliance leads to a host of technical and experimental problems; of course the radiation pulses, which are monochromatized to a standard 0.5 eV bandwidth, do also carry an extremely high number of non-resonant photons, which are detected by the APD as well. This results in too large a current flowing through the APD with all the problems that this entails: excess noise, non-linearities and material damage.
Electronic resonances on the other hand, are spectrally very broad. Therefore they offer in principle the opportunity to perform multi-photon quantum optics experiments with nanostructured multilayers and hard x-rays at conventional synchrotron sources. This is beyond the scope of this thesis, but nonetheless, the question is interesting in its own right: is it possible to repeat the successes of nuclear quantum optics with electronic resonances? As it turns out it is. We sketch the physical foundations in the following.

II.5.1. X-ray absorption spectroscopy and the white line

The interaction of the electronic excitations of matter and x-rays has been one of the most long-standing subjects of x-ray physics, present from nearly the very beginning. The field has been dominated by x-ray absorption spectroscopy, a rich and multi-faceted technique which uses the interaction to extract information on the electronic states involved in the resonant transitions. We here give a very brief survey of the results of the field that will be of interest to us.
X-ray absorption spectroscopy is almost exclusively performed on solid-state samples [79]. This means that the interactions are by necessity interactions between light and collective states of matter [80]; this is no different than in Mössbauer-based quantum optics. However, when dealing with electronic resonances, additional phenomena which complicate the picture can come into play. First and foremost, the only interaction between individual nuclei is mediated by their common interaction with the vacuum or a light beam illuminating it. Atoms, however, are far larger than nuclei. In a crystal, they are so close to each other that they interact via the Coulomb interaction. This means that not only the electrons of different atoms repel each other, but also that electrons are attracted to the positive nuclei of several different atoms. For even moderately-sized atoms this results in an enormously complicated interaction resulting in the formation of electronic bands [70]. Calculations then have to deal not with a discrete set of states which can be excited and decay, but with bands and density of state calculations [80, 81]. We now deal with continua, rather than discrete states, or discrete states placed near or in continua. Adding to the strains this

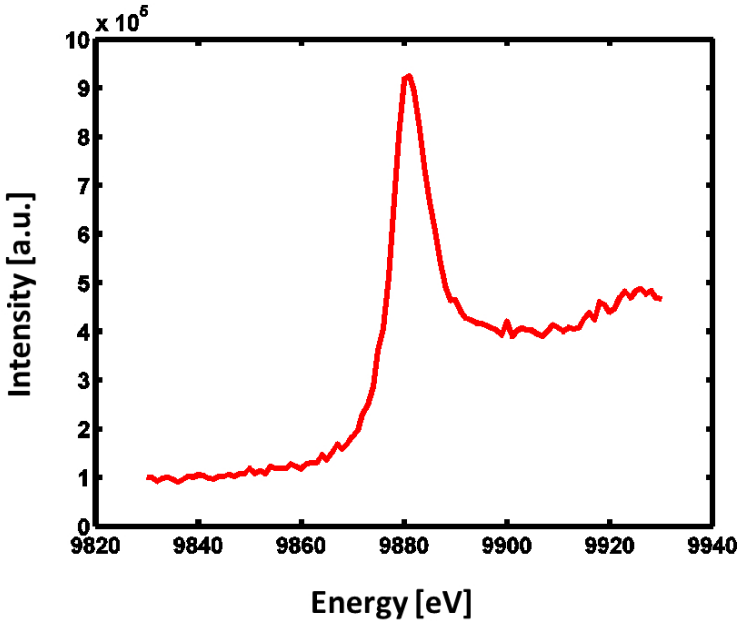

Figure 4: *The spectral signature of the white line at the Tantalum L_{III} edge. The spectrum was taken from a Ta-layer embedded in a multilayer cavity with the layout Pt* 20 *Å/ C* 110 *Å/ Ta* 25 *Å/ C* 123 *Å/Pt* 152*, more details in Tab. V.1. The cavity was strongly angularly detuned to minimize the effect of the vacuum interaction. The x-ray monochromator was scanned in constant-q mode (where the wave vector component perpendicular to the sample is kept constant) over a range of* 100 *eV around the resonance. By placing a fluorescence detector above the sample, we measured the photons scattered in* 4π *at every energy to measure the spectrum. Counting time was 1s. The Lorentzian peak in the center is the white line corresponding to the electric dipole transition, while the background on the right is the continuum of states corresponding to the lowest unoccupied band. It can roughly be modeled by a Heaviside function. The linewidth is approximately 5 eV.*

places on a simple theoretical explanation, it also means an enhanced background in experiments. Furthermore, once an electron is excited to a higher band, there are new possibilities of non-radiative decay, and intermediate states. For instance, another electron may decay into the state left vacant by the excited electron, which then in turn may decay to the state freed by the previous photon, a process called Auger decay [82]. Similar processes may take place with electrons hailing from different atoms. The quantum mechanical waves corresponding to these processes may interfere, leading to interference fringes in the spectra [83]. All these phenomena are fruitfully used to analyze the properties of solids, such as for instance the average distance of atoms from each other in disordered materials and cluster, information on next-neighbor interactions etc. For x-ray quantum optical experiments, they pose a huge problem since the effects we intend

to observe may become hidden under the spectroscopic signals of these strong and dominant interactions. Luckily, there is a remedy in the form of some resonant effects which have very similar properties to nuclear excitons. In x-ray absorption parlance, they are often referred to as 'white lines' [79]. These are strongly absorbing resonances which used to leave the detection film unexposed hence the name. Usually, when a core electron is excited, it leaves behind an unoccupied state, commonly called a 'hole' [84]. Much as in semiconductor physics [70], this hole can be treated as a fictitious positive charge attracting the negatively charged electronic states in higher bands. A distinction between x-ray physics and semiconductor physics (which deals with energies on the order of meV) is that in the latter, electrons from higher shells of bands are excited into even higher bands. In x-ray physics, electrons close to the core lower shells are excited [85, 86]. The many electrons in between will often shield the higher-band electrons from the attraction, a process called 'Coulomb-shielding' [80, 85]. This is not present in semiconductor physics. And in some cases this Coulomb shielding is also weak enough for higher energies to permit attractive interactions between the excited electron and the core hole, which leads to the formation of a strongly localized Frenkel exciton [87]. Localization in this context means that the excited electron and the core hole are localized on the same atom, although the collective nature of the excitation still means that every single atom in the ensemble can be excited with equal probability. Within the realm of white lines, there are some subdivisions. The selection rules are still obeyed, so the white lines of some transitions are electric dipoles, while others are quadrupolar transitions [79]. The latter for example appear often among the K-shell transitions of semiconductors such as *Se* or *Ge*. Usually, quadrupolar transitions are not observed or very weak [88]. But this only holds for transitions whose interaction Hamiltonian fulfills the electric dipole approximation, which hold that the electric dipole contribution to the interaction Hamiltonian is dominant when the wavelength of the energy of the transition is longer than the dimensions of the atomic system. For hard x-rays of about 10keV this approximation tends to break down, and therefore quadrupolar transitions may be observed easily, either in the form of white lines or so-called 'pre-edge peaks'. We would like to point out that this may very well be a unique feature of x-ray cavity QED and certainly deserves further attention. In the following however, we will not treat these systems, but confine ourselves to the simple and well-explored case of an electric dipole transition. These correspond to L_I-L_{III} edges. Not all of them display white lines, but they are especially prevalent in the 3d and 5d transition metals and their oxides [79, 88]. The latter are in the 10 keV energy range for which thin-film multilayer cavities work rather well, and therefore we will focus on Tantalum, which displays a strong white line. In Fig. 4 we show the white line of the Tantalum L_{III}-edge. The most drastic difference to Mössbauer lines is immediately obvious. The spectral

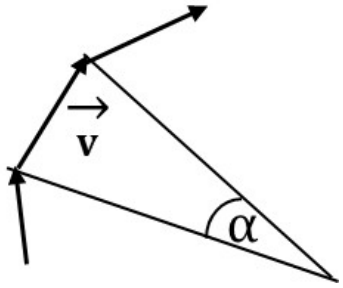

Figure 5: *An electron moves along a circular segment. The segment is decomposed into a series of linear segment, along which the electron moves with a velocity $\vec{v}$. The angle enclosed by the segment is α.*

linewidth is about 5eV. This is indeed the order of magnitude of the linewidth for most white lines - a good 10 orders of magnitude larger than that of ^{57}Fe.

II.6. Synchrotron Radiation

Modern experiments in Mössbauer spectroscopy, and consequently in nuclear quantum optics are based on the technique of nuclear resonant forward scattering, whose theoretical background was briefly described in Chapter II.6. The method requires pulses that are both extremely short on the temporal scale (picosecond range) and relatively narrowband ($\approx$ 1meV). Ideally, the pulses should be spaced by more than the decay time of the nuclear isotope, and have a high intensity in the relevant energy range, as well as spatial coherence. There is only one source of x-rays which can fulfill this host of preconditions, which is synchrotron radiation. In this chapter, we will give a brief introduction, explaining its origins and properties.

In storage rings used for producing synchrotron radiation electrons circulate at velocities very close to the speed of light. Beginning as a tool of experimental high energy and elementary particle physics, from the 1970s onwards they have increasingly been used as a source for soft and hard x-rays. On the following pages we will briefly describe the fundamentals of synchrotron radiation, discuss some particulars pertaining to our experiments, and sketch the standard setup of nuclear resonant forward scattering experiments. A classical, pedagogical treatment goes like this:

Suppose an electron moves straight on a series of infinitesimally small chords of a circular arc with a velocity of v as shown in Fig. 5 In uniform motion, a charge does not radiate, but at every bend marking the transition from one chord to another it changes its direction, and therefore undergoes acceleration in a particular direction. Accelerated charges emit radiation. Let the time that passes between two such accelerating bursts be $\Delta t'$. While the electron moves on the straight chord, the radiation it has emitted at the previous bend moves faster. By the time the electron has

reached the second bend Δ_t' the light has traveled a distance of $c\Delta_t'$ towards the observer, which we suppose to be in a location downstream of the propagation of light and electrons, at a position on the extension of the chord. In the laboratory frame, the light wave's distance from the electron is $(c-v)\Delta_t'$. The light wave being emitted at the second bend arrives with a delay $\Delta_t = (c-v)\frac{\Delta_t'}{c}$. Following an identical argument with other bends, we arrive at an almost identical equation, which merely introduces the effect of angular dispersion:

$$\Delta_t = (v - c\cos\alpha)\frac{\Delta_t'}{c} \tag{19}$$

where α is the angle between the chords of the circular arc. Both $\frac{v}{c} = \beta$ and $\cos\alpha$ are very close to unity, therefore we perform an expansion

$$\delta_t \approx 1 - (1 - \frac{1}{2\gamma^2})(1 - \frac{\alpha^2}{2}) \approx (\frac{1 + (\alpha\gamma)^2}{2\gamma^2}) \tag{20}$$

where $\gamma = \frac{1}{\sqrt{1-\beta^2}}$. With α close to zero, and γ very large, we can see that Δ_t is minuscule. In the laboratory frame, the time between the arrival of the first and the second pulses is compressed so much as to be barely perceptible. The compression is of course maximal whe $\alpha = 0$, and suppressed by a factor of two if $\alpha = \frac{1}{\gamma}$. From this argument we can deduce that the opening angle of synchrotron radiation is $\frac{1}{\gamma}$. The shorter the delay is, the brighter the radiation seems to the observer. We have not discussed the energy of the observed radiation yet. To access that, we make use of a simple model. Suppose the magnetic field responsible for accelerating the electron is given by $\vec{B}$. Equating the Lorentz force $e\vec{v}\vec{B}$ with the centripetal force $\frac{v^2}{\rho}$ where ρ is the radius of the electron trajectory, and inserting $\vec{p} = m\vec{v}$ appropriately we get $\gamma mc = \rho eB$. This gives the radius

$$\rho = 3.3\frac{E_e[GeV]}{B[T]} \tag{21}$$

where E_e is the electron energy, which for modern sources is some GeV. From this we can derive some rules of thumb. In order to get a high electron energy, which is needed for low divergence and high intensity, strong magnets as well as large ring circumferences are required. To the observer, an electron moving on a series of arcs roughly parallel to the optical axis seems like an electron that undergoes a half-oscillation perpendicular to the optical axis. This is because of the curvature of the ring. The velocity of that half-oscillation depends on the angular frequency with which the electron traverses the ring. A segment a is passed in $\frac{T}{2\pi\gamma} = \frac{1}{\gamma\omega_0}$, but to the observer, as we have seen, this appears to be shorter by a factor of $\frac{1}{\gamma_0}$. This is the length of the oscillation of the electron that the observer sees; consequently, this is the temporal shape of the pulse of dipole radiation that the observer sees. Fourier-transforming the length of the pulse gives the energy spectrum.

The above considerations give a good qualitative picture of the basics of synchrotron radiation, and explain why electrons traversing a bending magnet at relativistic speeds radiate x-rays. But modern, 3rd generation synchrotron sources have better, more efficient ways of producing x-rays. These are grouped under the name 'insertion devices', a term which comprises both so-called undulators and wigglers.

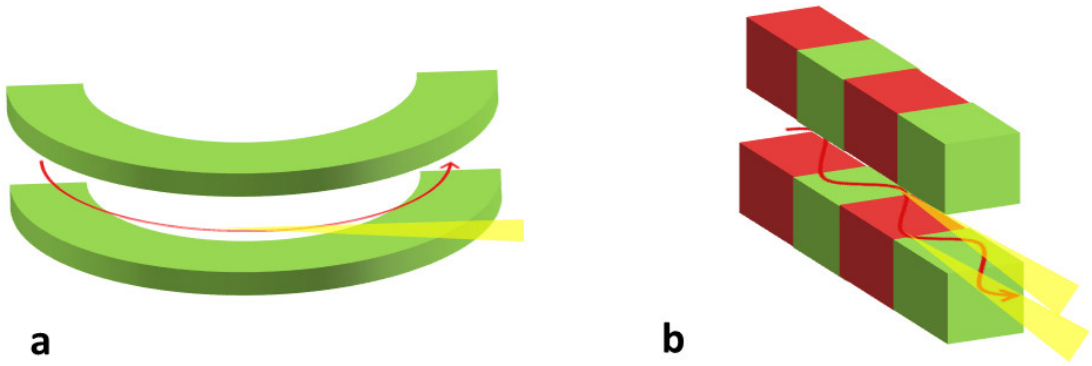

Figure 6: *Sketch of two different schemes for accelerating electrons. (a) in a bending magnet, the electron is forced on a circular path. The constant acceleration to the center of the circle forces it to emit radiation. (b) in a wiggler or undulator opposite alternating magnets force the electron to change its direction every period, leading to multiple acceleration periods. The light emitted from each cycle interferes constructively.*

II.7. Insertion devices

A wiggler consists of two arrays of alternating opposite strong magnets. The space between them is kept in vacuum conditions, so electrons can traverse it with minimal losses and scattering. The electron beam is introduced between the arrays. Due to the alternating poles, the magnetic field changes direction several times during the propagation of the electron, leading to the electron's being accelerated in different directions. On the whole, it is a sinusoidal trajectory through the wiggler. In the previous section, we have argued that the time interval difference between the electron and the light emitted by the electron leads to a compression of the wavefronts. The same thing happens during the transmission of an electron through a wiggler, but it repeats several times, with the light being emitted in the same direction. The path difference can be calculated from simple geometric arguments. The electron path length is

$$l_e = \lambda_u(1 + \frac{K^2}{4\gamma^2}) \tag{22}$$

where λ_u is the wiggler period, $K = \frac{2\pi\gamma A}{\lambda_u}$ is the so-called undulator parameter, and A is the amplitude of the sinusoidal trajectory. K determines the opening angle of the beam; it is therefore important to keep it low. With the Lorentz force and some geometrical approximation we can express it as

$$K = \frac{eB}{mck_u} \tag{23}$$

where k_u is the wave vector of the modulation, i.e. the inverse of λ_u. Examining K further, we note that to decrease K, a smaller magnetic field strength or wiggler period is necessary.

If K is small enough (≈ 1), the light emitted from a particular wiggler period can coherently interfere with the light emitted from the electrons in other wiggler periods. If this condition is fulfilled, we speak of an undulator. The undulator emits radiation of a particular wavelength ('fundamental wavelength') and its higher harmonics.

Chapter III

Experimental Methods

III.1. Introduction

This section is concerned with issues faced by the experimentalist in nuclear resonant scattering in general, and how to resolve them. Furthermore, we introduce the basic experimental setup and introduce a classical treatment of the reflectivity from stratified media.

III.2. Experimental Issues

The root of all experimental problems in nuclear resonant forward scattering of synchrotron radiation is the sheer mass of non-resonant photons. While we have claimed in the previous section that undulator radiation is quasi-monochromatic, the bandwidth is many orders of magnitude larger than the linewidth of a typical Mössbauer isotope. In a way, this is the inescapable drawback of having short pulses. With a standard monochromator available at most synchrotron beamlines, which have bandwidths of about $1 - 2$ eV, this means that the bandwidth of the beam is about 8 orders of magnitude larger than the nuclear linewidth. This creates several problems. How can we distinguish the (few) resonant photons from the (many) non-resonant ones? Does the multitude of non-resonant photons impede our ability to measure resonant photons? Very early on in nuclear resonant scattering, it became clear that the answer to this puzzle was to measure the nuclear response signal in the temporal domain, instead of in the energy domain, as in Mössbauer spectroscopy. The first experiments exploiting that effect were performed by the group of Erich Gerdau in Hamburg in the 1980s. They employed Fe-containing crystals like Yttrium iron garnet (YIG) or Iron borate ($FeBO_3$) enriched with ^{57}Fe to enhance the signal and chose crystal reflections that strongly suppressed purely electronic scattering [89, 90, 91, 92]. As we have indicated in the

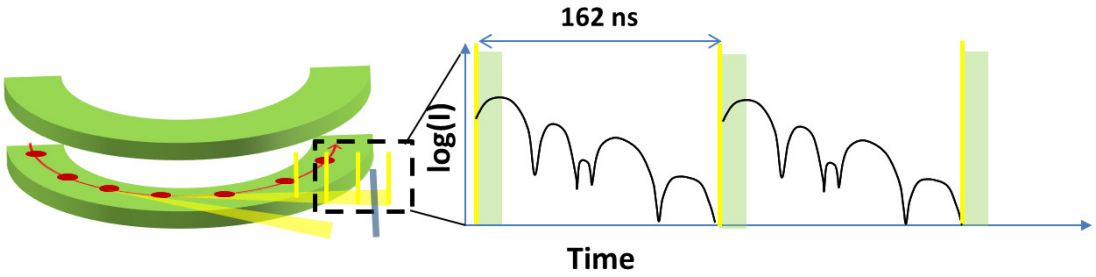

Figure 7: *The principle of time-resolved nuclear forward scattering. The electrons accelerated in the synchrotron move in bunches, marked by the red dots. They are usually spaced a fixed distance apart, the distance determining the mode. The 16-bunch mode of the ESRF for instance, has 176 ns-spaced bunches. The bunches send out pulsed synchrotron radiation (prompts), which is scattered by a sample; the scattered signal (black solid line) is delayed with respect to the prompt (yellow peak). The APD does not measure the prompt and the immediate aftermath, as indicated by the transparent green window.*

theoretical treatment, the signal of a pulse traversing a nuclear resonant sample consists of two parts: first the δ-like unchanged incident pulse, which consists largely of non-resonant photons and resonant photons which have failed to interact with the sample, and then a signal that is delayed by a time on the order of the decay time of the sample nucleus. This is the signal due to the complicated many-body quantum optical interaction of nuclei with light, and this is what we are looking for. We will call the unchanged pulse 'prompt' and the delayed signal the 'nuclear signal' for clarity. Simply by ignoring the first few nanoseconds of the decay signal we sort out all non-resonant photons; from the remaining temporal signal, information about the properties of the sample and the nature of its interaction with x-rays can be inferred. From a more technical perspective, it is also imperative that the first few nanoseconds of response time are to be ignored; the detector, usually an avalanche photodiode (APD) is incapable of performing single photon counting at high intensities; and the prompt, containing even after monochromatization 10^6ph/s, has a high intensity. Therefore a so-called time gate is introduced by standard nuclear instruments module (NIM) electronics. Its width is usually on the order of 5-20 ns. A second requirement is that some time passes between individual pulses exciting the sample, which is at least as long as the decay time of the nuclear isotope that is being examined. Otherwise new prompt pulses would interfere with signals from old ones, and make the measurements not just unreliable, but impossible.To this end, the synchrotron is operated in bunch mode. A bunch that passes a

bending magnet, or is partially funneled into an undulator emits the desired pulse. The scheme is indicated in Fig. 7. The temporal spacing between the bunches is dependent on the mode the ring is operated in. For example, the 16-bunch mode of the European Synchrotron Radiation Facility (ESRF) has a spacing of 176 ns; the 40-bunch mode of PETRA III has a spacing of 192 ns. Both these spacings are larger than the decay time of ^{57}Fe; hence both modes are suitable for nuclear forward scattering experiments on that isotope. In the following we will discuss in some more detail the individual components of a typical NRS experiment, all of which are employed (in varying combinations) in our setup.

III.3. High-resolution monochromator

Instead of standard synchrotron radiation monochromators, which monochromatize the incoming beam to a bandwidth of about $1 - 2$ eV, NRS employs specialized and optimized monochromators, which currently can reach a bandwidth of about 1 meV . These monochromators have between one and four channel-cut crystals; typically they use asymmetric Bragg reflections to match the angular acceptance to the divergence of the incoming beam. Specifics can be gleaned from [63, 23]

III.4. The detection setup

The centerpiece of the detection setup is the avalanche photodiode. The active region is a doped layer of silicon of several dozen μm length. The region is reverse biased. Charge carriers that are mobilized due to the absorption of an x-ray photon form secondary electron-hole pairs in collisions. These are accelerated equally by the voltage applied and create more electron-hole pairs. This is the avalanche that occurs, which amounts to the amplification of the electric signal by about 1-3 orders of magnitude. The signal from the APD is amplified again, and then fed into a complex NIM network. A constant fraction discriminator pre-selects the signal (if it is too low, it is discarded) and transmits a standardized short pulse. This is the start signal for a time to amplitude converter. The stop signal is provided by the bunchclock.

III.5. Time-gated detection

The setup we have discussed so far allows measuring the temporal decay pattern of a sample. In forward scattering geometry, this is really all we require. The measured spectrum can be fitted with the program package CONUSS [93, 94] (COherent NUclear Scattering by Single crystals) to retrieve the parameters of the hyperfine field. In the case of our reflectivity spectra however, there

are many non-nuclear parameters massively influencing the field, so the parameter space is really much larger. In order to study the spectral properties of the scattered radiation, we would like to measure energy spectra, similar to conventional Mössbauer spectra. The synchrotron beam remains many orders of bandwidths larger than the actual resonances. This means we cannot simply scan the beam energy to probe the sample's energetic response. Therefore, we use an absorption setup. In this case, we mount a tempered stainless steel foil enriched with ^{57}Fe on a Mössbauer drive normally used for the radioactive source of classical ^{57}Fe Mössbauer spectroscopy, and insert it into the beam *after* the sample. Upon moving, the Doppler shift slightly detunes the energy of the stainless steel foil according the the equation

$$\Delta = \omega \frac{v}{c} \tag{24}$$

where Δ is the energy detuning, v the velocity of the drive, c the velocity of light and ω the frequency of the resonance - in this case obviously 14.4 keV, or 2.19×10^{19}Hz. At the energetic position of the resonance of the stainless steel (SS) foil, it will absorb more than off the resonance. If we sum up the counts for one particular velocity, and do so for all velocities we will get a Mössbauer spectrum. It will be inverted from the original one. A problem is that the more the SS foil absorbs, the broader its line because of dynamical scattering effects; i.e. for a measurement with a high contrast between the baseline and the features of the spectra, there are trade-offs in energy resolution and vice versa. A final caveat is that the prompt still has to be gated away in this scheme; the SS foil does not absorb the non-resonant radiation sufficiently to solve this problem. This amounts to taking a time spectrum of the combined sample-SS-foil system for a particular velocity of the foil, and summing up the photon counts outside the gating range. This procedure is referred to as time-gating detection [95, 96, 97]. A final disadvantage is that the time gating introduces a background modulation into the spectra so obtained; the larger the time gating window, the smaller the oscillation periods of that modulation. A method to circumvent this will be presented in the next section.

III.6. Polarizer-Analyzer setup

A second way to distinguish prompt and delayed signal has recently been developed and can be applied to a particular set of experiments [98, 99]. We have already pointed out that in ^{57}Fe there are six different allowed transition lines, see Fig. 2. Those that involve a transition in which the spin quantum number difference is ± 1 result in a rotation by 90° of the polarization of the scattered light as opposed to the incoming. If the incoming light is σ-polarized, the outgoing is π-polarized [100]. Photons which have not interacted with the sample do not undergo this

polarization rotation. It figures that by employing a polarizer-analyzer setup, we can distinguish scattered light, the pure nuclear signal, from unscattered light, the prompt. Note that this is only possible for particular combinations of magnetic field direction, direction of the incoming light, and polarizer-analyzer configurations [63].
The setup we use, developed by Marx *et al*. in some of these experiments consists of two single-channel cut silicon crystals in a crossed setting. Each crystal supports six 45° reflections on the Si (800) reflex [101]. The polarizer is used to improve the polarization purity of the synchrotron beam; the light passes through it, being scattered on the sample; light scattered into a different polarization is deflected onto the suitably positioned APD by the analyzer. The setup reaches a purity on the order of 10^{-10} [102], quite enough in order to suppress even very strong prompt signals. Note that any crystal reflecting only light polarized in a particular direction is a polarizing beam splitter (PBS), since all other light is transmitted. A PBS is a ubiquitous tool in quantum optics schemes both basic and advanced. The advent of this technology in x-ray quantum optics could help engender similar control schemes in this energy range.
The great advantage of the polarizer-analyzer setup is that it permits taking conventional Mössbauer spectra, but since no time-gating is necessary, the artifacts, i.e. time-window effects mentioned in the previous section do not appear.

III.7. The Synchrotron Mössbauer Source

Another pathway to probing Mössbauer isotopes at synchrotrons, recently developed at the ESRF, is the synchrotron Mössbauer source. The basic setup is shown in Fig. 8.

It combines the advantages of synchrotron radiation and conventional spectroscopy in that it is essentially a monochromator able to reduce the bandwidth of the incoming light to the natural linewidth of ^{57}Fe. The source consists of a $^{57}FeBO_3$ crystal which is inserted into the beam such that the (333) crystal reflex is illuminated, a setup originally proposed by Smirnov [76]. This is an electronically forbidden reflection. But due to the presence of resonant nuclei, light that is scattered from these nuclei undergoes an additional phase shift. Resonant light can therefore be reflected. The reflection consequently has the same bandwidth as an unperturbed ^{57}Fe nucleus. A problem complicating the issue is the presence of a crystal order-induced hyperfine field and the ensuing hyperfine splitting. But by heating up the crystal to 348.5 K the crystal undergoes a Néel phase transition, at which the hyperfine field breaks down. The quadrupole splitting remains, but a residual interaction with the magnetic hyperfine interaction suppresses one line of the remaining doublet [104, 105]. The reflection is then a single line. By mounting the crystal on a

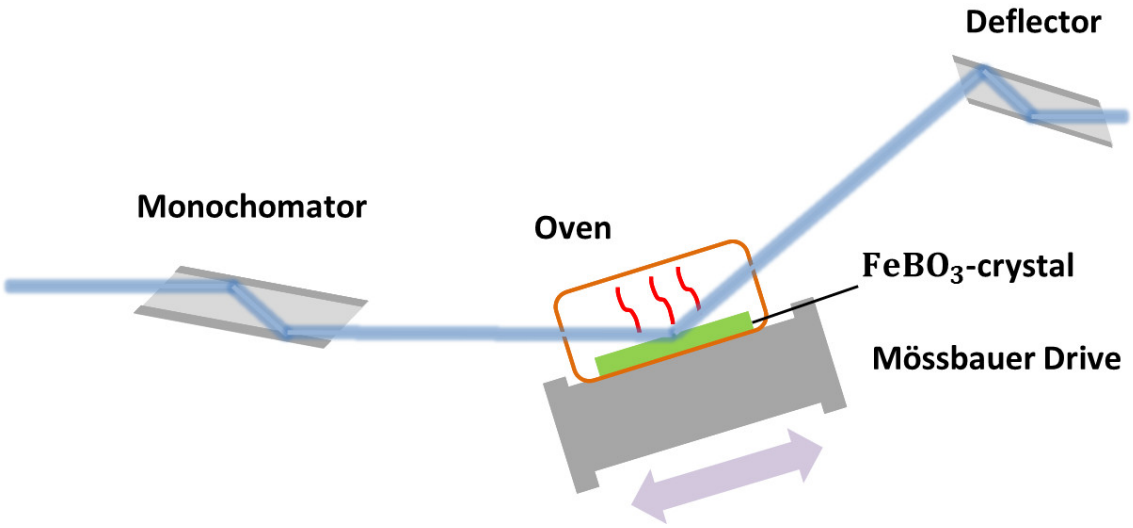

Figure 8: *Setup of the synchrotron Mössbauer source at the European Synchrotron Radiation Facility [103]. From the monochromator, the beam is guided to the $FeBO_3$ crystal. The latter is placed on a Mössbauer drive, whose movement shifts the energy of the resonance via the Doppler effect; an oven regulates the temperature to near the Neel point. A deflector levels the reflected beam and guides it towards the sample. Monochromator and deflector are schematically depicted; both consist of multiple crystals.*

Mössbauer drive, the energy can be tuned, and Mössbauer spectroscopy can be performed [106]. After some development, such a scheme is now available for user operation at the ID18 beamline of the ESRF [103].

III.8. Sample Fabrication

The vehicle we will use in this thesis to manipulate and enhance the interaction of x-rays and matter are thin-film nanostructures. There is a wealth of modern techniques to fabricate these sorts of samples. The choice of the technique depends strongly on the desired properties of the thin-films. For purely monocrystalline thin films, for example, molecular beam epitaxy or pulsed laser deposition are the most advantageous [107]. For x-ray reflectivity experiments in grazing incidence, however, other features are more important and meaningful, chief among them a low roughness of the thin films [108, 109, 110]. The necessary quality can be achieved by the most important workhorse technique for thin film deposition: sputter deposition [107, 111]. Used widely in industrial applications, sputtering employs accelerated ions to vaporize single atoms of a desired species from the target and steers them onto the sample material. The process is sketched in Fig. 9.

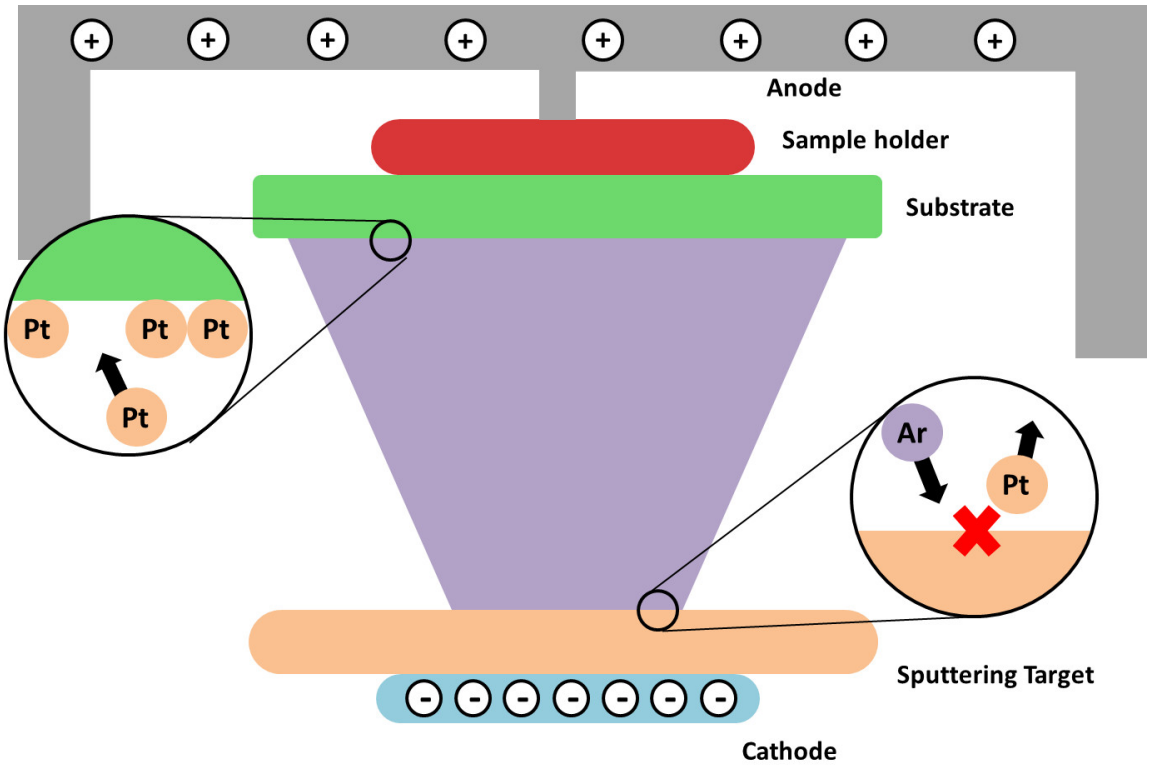

Figure 9: *A sketch demonstrating the operation principle of a sputtering setup. The sputtering target containing the material to be deposited and the substrate on which the thin film is to be deposited are placed above a cathode and anode respectively. A voltage is applied between them. The whole setup is placed in a low-pressure Argon atmosphere. Argon atoms are ionized by cosmic radiation, and accelerated by the applied field. After some acceleration, they impact on the sputtering target. The ensuing momentum transfer between the ions and the atoms of the target material leads to the latter being ejected and traveling to the substrate.*

The process can be well-controlled, which means it can be used to fabricate films as thin as a single monolayer of a given material.

III.8.1. DC sputtering

In this case, the voltage between the cathode and the anode is constant. Free electrons coming from arbitrary external sources such as cosmic radiation are accelerated towards the anode. On their way there they collide with Argon atoms and ionize them, forming an Argon plasma. The ions in turn are accelerated towards the cathode. Upon collision, secondary electrons are excited and move towards the anode, to repeat this process. In this way, the plasma is stabilized. Some of the ions will extract atoms or clusters from the target. These atoms now have a strong momentum

directed towards the substrate which is placed over the anode. There, they assemble and form first clusters, and later thin films. DC sputtering requires the sputtering target to be conducting, otherwise the current keeping the plasma stable would break down.

III.8.2. RF sputtering

This technique uses the same setup, but the DC voltage is replaced by an AC voltage with oscillates with a radiofrequency (RF), typically some MHz. The high frequency is mandatory, because under a certain treshold of about 50 kHz, both electrodes would alternate as sputtering targets. Above the treshold, free electrons start to oscillate and ionize the sputtering gas by impact ionization. There is no current flow by gas discharge between the electrodes, but there are still argon ions which can sputter the material off the target onto the substrate. Since there is no current, RF radiofrequency sputtering permits sputtering with non-conducting materials.
hold, free electrons start to oscillate and ionize the sputtering gas by impact ionization. There is no current flow by gas discharge between the electrodes, but there are still argon ions which can sputter the material off the target onto the substrate. Since there is no current, RF radiofrequency sputtering permits sputtering with non-conducting materials.
Beyond these founding principles, HF sputtering requires some refinements. The electrode on which the sputtering target is mounted is wired in series with a capacitor. This is necessary because at typical frequencies of the AC voltage the argon ions are almost stationary, while the electrons are highly mobile. The capacitor leads to a higher net negative charge of the electrode it is wired in series with, a process known as self-biasing. Averaged over time, this self-bias functions as an effective negative voltage ensuring that the sputtering takes place on the target.

III.8.3. Magnetron sputtering

A further refinement valid for both AC and DC sputtering techniques is magnetron sputtering. A permanent magnet is mounted under the cathode. The resulting Lorentz force acting on the secondary electrons originating from the source drives them in a spiral trajectory around the axis connecting the electrodes. This leads to a greater number of collisions and ionised atoms than a straight trajectory would.
Magnetron sputtering is performed on round targets. The spiral trajectory of the secondary electrons induces the risk that the sides and back of the target holder instead of the actual target disk are sputtered off. Naturally, this gives rise to a strong degradation in thin film quality. The solution to this problem is to include a so-called dark-field screen which has to be placed extremely

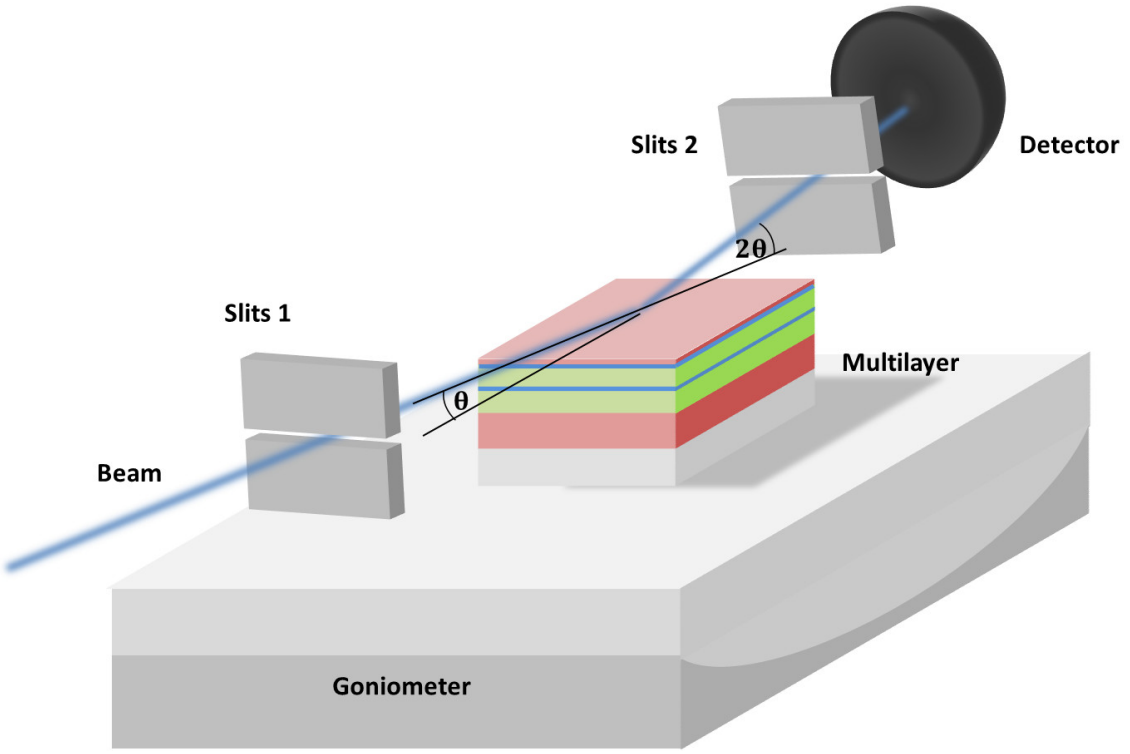

Figure 10: *Setup for the reflectivity measurements. The sample is mounted on a* $\Theta - 2\Theta$*-goniometer, and the angle is varied with respect to the incoming beam. At the same time, the detector angle with respect to the beam is changed by double the amount. Slits are used to minimize the beamsize, which results in a better quality and less divergence of the beam, but also enhance the times necessary to get high quality reflectivity curves.*

close to and around the sample holder. It has to be close enough to keep the gas ions from being accelerated against the side of the target holder, which would sputter off the latter and result in a degradation of the sample quality. When a gas ion collides with the substrate, the energy transfer usually, that is in 75% of cases, results in heating of the substrate. The target has to be cooled well during the sputtering process, otherwise the ensuing heat can reduce the permanent magnetic field of the magnetron gun, which would deteriorate the sputtering rates dramatically. Only 1% of the deposited energy is transfered to a target atom or cluster being detached.

III.9. Reflectivity measurements

The basic setup for reflectivity measurements is shown in Fig. 10. The incoming x-ray beam is fixed; for every angular step that the sample is moved with respect to it, the detector is moved

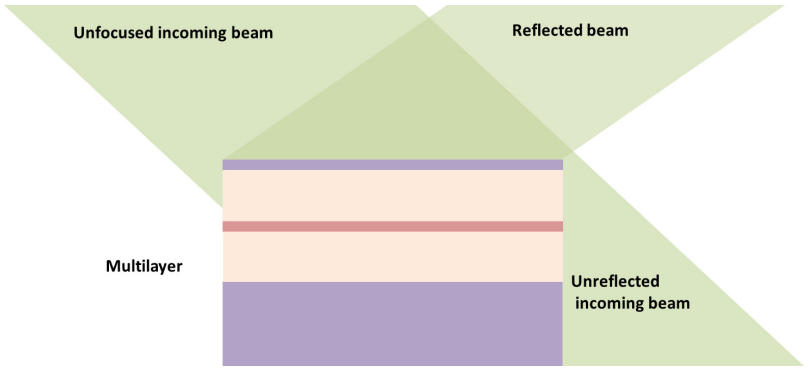

Figure 11: *Sketch of a collimated beam impinging on a sample at an angle. The beam is shown in green. Due to the angle, the beam's cross section is larger than the sample itself, and parts of the beam are not reflected, or even scattered from the sample. The portion of the beam that is actually impinging and not bypassing the sample is called the footprint.*

by double the amount, such that it is always positioned in the reflected beam. It measures the reflected intensity for a range of angles. The result is called a reflectivity curve. Below the critical angle, most radiation is reflected; significantly above that angle, the radiation penetrates into the material and the reflectivity decreases following a q^{-4} law, with q being the momentum transfer. Therefore a logarithmic depiction is often necessary. But however little radiation has been reflected, it has been reflected from the sample below surface; the reflectivity curve at these higher angles contains information on the structure of the thin-film sample, which can be extracted by a fit [110]. In the following, we discuss some basic experimental issues. The incoming beam is guided through a slit, which decreases the beam size and total intensity, but also decreases the divergence, which serves to enhance the resolution of the setup, particularly at the small angles which interest us. A smaller, collimated beam also reduces the footprint of the beam on the sample; only part of the sample is illuminated by the beam, while for a large beam, the entire sample is illuminated as shown in Fig. 11.

If the sample is inhomogeneous, as is sketched in Fig. 12, a large beam may be detrimental to the rocking curve quality, because the detector receives a signal from different parts of the sample, which have different thicknesses. This can be avoided if the incoming beam's cross section is made very small. This can be achieved by focusing it via a Kirkpatrick-Baez mirror [112] or compound refractive lenses [113], both standard equipment at nuclear resonant scattering beamlines. They suffer from a strong drawback, however, which is the presence of beam divergence.

This is shown schematically in Fig. 13. If the sample is fixed with a certain angle with respect to the center of the beam, the actual illumination includes different angles, which are equally

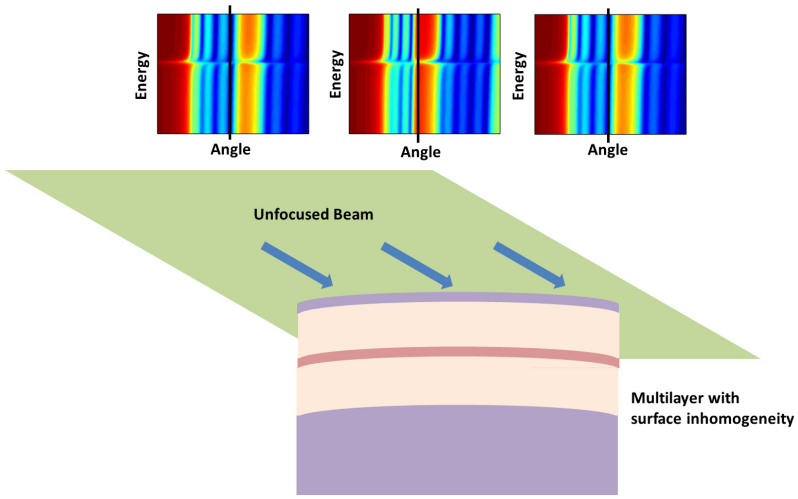

Figure 12: *Sketch of a collimated beam impinging on an inhomogeneous sample. The three insets show the reflectivity of three slightly different multilayers, with the angle on the x-axis, the energy detuning on the y-axis, and the reflectivity encoded in the color map. When the sample is inhomogeneous, the effect is the same as measuring the reflectivity from several different samples at the same angle, as indicated in the figure. As the angle is increased, the footprint decreases, until it is so small that the sample is not homogeneous anymore across the footprint. The reflectivity then includes differing information at different angles, complicating the analysis.*

reflected and sent to the detector. This can be ameliorated if the slits in front of the detector are spaced closely apart, but this has the price of decreased intensity, and longer data acquisition time.

For practical purposes, one often uses a combination of small slit widths and moderate focusing to deal with the problems at hand. To facilitate the experimental analysis, we need some procedures to incorporate these experimental shortcomings into our description of the reflectivity; otherwise we risk importing errors into the results we receive from simulations and fits. They will be given in Chapter IV.1.

III.10. Thin-film cavities

Multilayer-based thin film cavities for x-rays were first pioneered from the 1970s on [114]. Their breakthrough came in the 1990s [115, 116] and they quickly found use in providing beam compression of x-ray synchrotron beams for imaging studies [117, 118, 119, 120, 121]. A first success in using them for manipulating the light-matter interaction followed soon [122]. Interestingly, even in one of the first papers on the matter [116] the authors remark upon spectroscopic shifts.

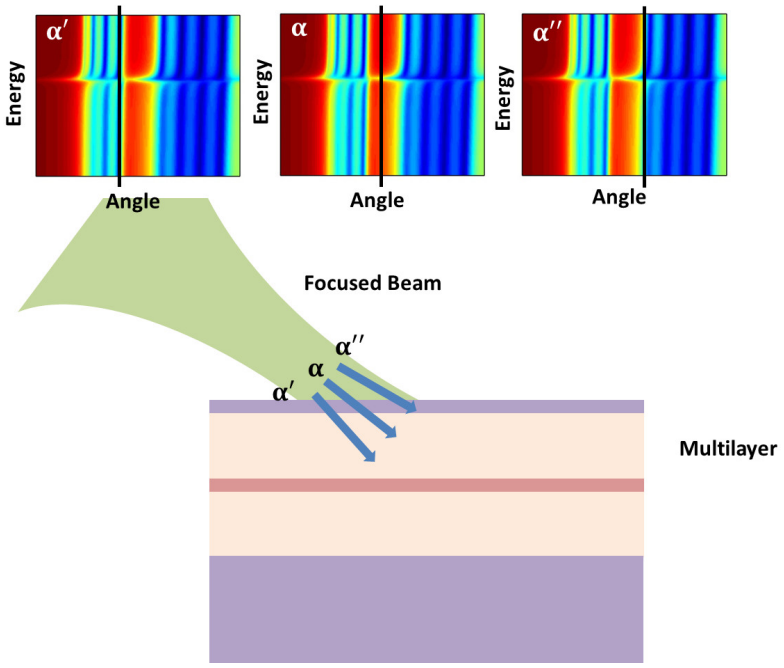

Figure 13: *Sketch of a focused beam illuminating a sample. The three insets above show the resonant reflectivity of the sample, with the angle on the x-axis, the energy detuning on the y-axis, and the reflectivity encoded in the color bar. The black lines mark slightly different angles, whose reflectivities differ strongly from each other. The footprint is relatively small, even at small angles, so inhomogeneity plays less of a role. The distinct drawback is that the divergence is greatly increased. This corresponds to the sample being illuminated from different angles at the same time, as indicated in the figure.*

Measuring the fluorescence intensity of a zinc layer centered in a thin film waveguide by varying the x-ray energy, they comment that "the resonance peak position in energy is extremely sensitive to the incidence angle". The authors do not follow up on that remark, but it is likely that they saw something akin to the collective Lamb shift, which we will elucidate on later.

The fundamental principle of x-ray waveguides are explained easily enough. In the introduction to the physical fundamentals of this thesis, we have already mentioned the critical angle, below which any material functions as a mirror for hard x-rays. If we now have a combination of materials, two of which have a high critical angle (this is true for high-Z materials) sandwiching a low-Z material with a low critical angle, there is an angular range where the impinging light cannot propagate in the outer materials (the mirrors of the cavity, called cladding) but can propagate in the material between them (called core). The light can, however, tunnel through the mirrors, and is then confined in the core for some time. As illustrated in Fig. 14, we can picture the cavity as a finite quantum well, where the confining walls are formed by the regions whose real δ decrement

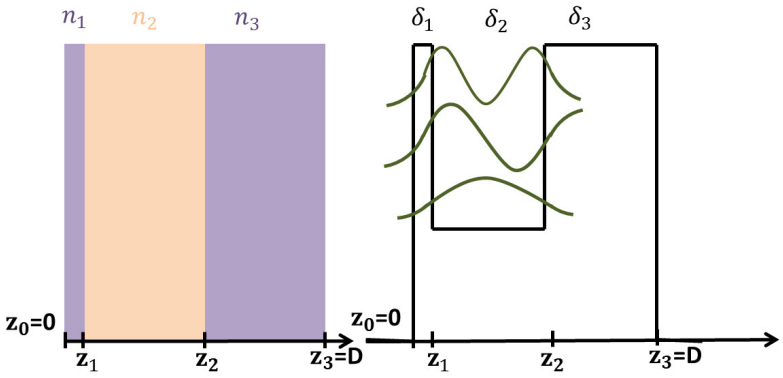

Figure 14: *On the left, a sketch of a typical thin film cavity, consisting of three layers. Typically, the outer (cladding) layers are the same material. Their electron density should be far higher than that of the inner (core) layer. This makes the three layer a quantum well for light, where the number of states is given by the well depth, as indicated on the right.*

of the refractive index is large. This quantum well then holds several different modes, depending on the depth. We do not give a detailed calculation here, but remark that the Helmholtz equation can be used to describe the problem. The Helmholtz equation being mathematically similar to the Schrödinger equation [123], it can be solved in a very similar way, by choosing the appropriate boundary conditions [124].

We conclude this brief overview by noting that some literature on the optimization of these x-ray resonances has already appeared [123, 125]; however this was geared to optimizing the field strength inside the cavity, without taking into account resonant layers, which is related, but not identical to optimizing the coupling strength. These methods can be used but should not be relied on uncritically when designing cavities.

Chapter IV

Theoretical Tools

IV.1. The transfer matrix algorithm

In the course of this thesis we will introduce several quantum optical models which describe the interaction of light with thin film nanostructures. However useful these models are for understanding the formers' fundamental physics, they also have shortcomings. Not all of them deal realistically with dissipation; they cannot deal with experimental imperfections of the sample and the setup; and therefore we here introduce a simple model to address these shortcomings. It is the so-called transfer matrix method, which is ubiquitous in many areas of physics dealing with the propagation of light through matter composed of many atoms [126, 127, 128], and has great success in the quantitatively correct description of such processes. Originally a purely classical description of the interaction of light with a layer having the refractive index n, it has been extended to a semiclassical description to describe the sample's characteristics when it consists of or includes atoms resonant with the frequency of impinging light. In the case of nuclear resonant scattering, a fully quantum electrodynamical description for weak fields has been found [109]. In the following, we will describe it in semiclassical terms, but note that the scattering amplitudes and refractive indices we use were derived in a fully quantum electrodynamical way [129].

We assume that the propagation of light through a stratified medium can be described by a transfer matrix:

$$\begin{pmatrix} A_+(z) \\ A_-(z) \end{pmatrix} = \mathbf{M}(\omega) \begin{pmatrix} A_+(0) \\ A_-(0) \end{pmatrix} \tag{25}$$

where $\mathbf{M}$ is the transfer matrix, which is energy-dependent in general, and A_+ and A_- are the forward and backward propagating wave amplitudes at depths z in the sample, with $z = 0$ being

the position of the top surface, see Fig. 14. Supposing that the sample is not homogeneous, but consists of different layers, we can decompose the transfer matrix:

$$\begin{pmatrix} A_+(z) \\ A_-(z) \end{pmatrix} = M_1 M_2 ... M_n \begin{pmatrix} A_+(0) \\ A_-(0) \end{pmatrix} \tag{26}$$

where each layer has a separate transfer matrix denoted by the index, and we have omitted the energy dependence. The number of layers is N. For the procedure determining the transfer matrix for nuclear resonant layers from first principles, we refer the reader to [63]. We give the results here, remarking that the only difference to other methods is the calculation of the index of refraction. The transfer matrix for a single layer is

$$M_1 = \begin{pmatrix} 1 & r_{01} \\ r_{01} & 1 \end{pmatrix} \begin{pmatrix} e^{ik_z z} & 0 \\ 0 & e^{-ik_z z} \end{pmatrix} \begin{pmatrix} 1 & r_{10} \\ r_{10} & 1 \end{pmatrix} \frac{1}{t_{01} t_{10}} \tag{27}$$

where $r_{01}(r_{10})$ are the reflection coefficients from the vacuum to the first layer and vice versa, $t_{01}(t_{10})$ are the respective transmission coefficients, k_{1z} are the wave vector components in the direction of growth (i.e. the direction where the layer changes) and z is the location. $k_{1z} = k_{0z}\beta$ where

$$\beta = \sqrt{1 + \frac{2(n-1)}{k_{0z}}} \tag{28}$$

and

$$r_{ij} = \frac{\beta_i - \beta_j}{\beta_i + \beta_j} \tag{29}$$

$$t_{ij} = \frac{2\beta_i}{\beta_i + \beta_j} \tag{30}$$

and n is the index of refraction of the layer in question. All these quantities have to be calculated for each individual layer; the transfer matrix for a stack of layers can be calculated by appending the matrices for all layers. We will call the total transfer matrix M_{tot}, and D is the position where the layer stack ends, see Fig. 14.

$$\begin{pmatrix} A_+(D) \\ A_-(D) \end{pmatrix} = M_{tot} \begin{pmatrix} A_+(0) \\ A_-(0) \end{pmatrix} \tag{31}$$

where

$$M_{tot} = \begin{pmatrix} M_{++} & M_{+-} \\ M_{-+} & M_{--} \end{pmatrix} \tag{32}$$

Now, assuming that the incident wave is incoming from the positive direction, and that there is no field incident from the negative direction, we can set $A_+(0) = A_0$ and $A_-(D) = 0$ where A_0 is the amplitude of the incoming wave. We then get two equations

$$\begin{aligned} A_-(0) &= -(\tfrac{M_{-+}(D)}{M_{--}}(D))A_0 = RA_0 \\ A_+(D) &= (M_{++}(D) - \tfrac{M_{+-}(D)M_{-+}(D)}{M_{--}(D)})A_0 = TA_0 \end{aligned} \tag{33}$$

where R and T are the reflectivity coefficients.

For periodic layer structures, we adopt the same formalism. We again decompose the electromagnetic field illuminating the sample into a forward- and backward propagating component called A_+ and A_-. The amplitudes of both components at the upper and lower boundaries of a given layer are connected to each other via a transfer matrix

$$\begin{pmatrix} A_+(m+1) \\ A_-(m+1) \end{pmatrix} = \mathbf{M}(\omega) \begin{pmatrix} A_+(m) \\ A_-(m) \end{pmatrix} \tag{34}$$

Here, m is the number of the period of the periodic multilayer. The above can be expressed in vector notation as

$$\vec{A} = \boldsymbol{M}(\omega)\vec{A}_0. \tag{35}$$

$\mathbf{M}$ can be more precisely expressed as $e^{i\vec{F}z}$, where $\vec{F}$ the scattering matrix of the medium, and z is the propagation distance, i.e. the thickness of the film. Supposing that our multilayer is infinite, we can use an alternative description for the field propagation across one period in the ML structure:

$$\begin{pmatrix} A_+(m+1) \\ A_-(m+1) \end{pmatrix} = \begin{pmatrix} e^{ik_{0z}a} & 0 \\ 0 & e^{-ik_{0z}a} \end{pmatrix} \begin{pmatrix} A_+(m) \\ A_-(m) \end{pmatrix} \tag{36}$$

where k_{0z} is the z-component of the wave vector of the incident light and a is the thickness of the period. (z is the so-called surface normal, i.e. the direction in which the multilayer is periodic, see Fig. 14.) The above equation is the Bloch theorem for a two-beam case, which states that in a periodic system, a wave can be described as the superposition of the wave function within a period and a plane wave with a wave vector whose length corresponds to the period length of the system. Upon inserting Eq. (36) into Eq. (34) we can see that $e^{ik_{0z}a}$ are the eigenvalues of $\mathbf{M}$. Simple algebraic manipulations give

$$cos(k_{0z}a) = \frac{Tr(\boldsymbol{M}(\omega))}{2}. \tag{37}$$

This is the dispersion relation of the light in the multilayer system. Conventionally, a dispersion relation is resolved for ω; this can only be performed in special cases for periodic systems. It can, however, be calculated numerically. To go in this direction, we have to calculate $\mathbf{M}$. We have already pointed out its relation to the scattering matrix and elaborate on that now. In a nuclear resonant layer which is very thin, $\mathbf{M}$ can be given as

$$\boldsymbol{M} = \mathbf{1} + i\boldsymbol{F_n}d_1 \tag{38}$$

where d_1 is the layer thickness, F_n the nuclear scattering matrix and **1** the unity matrix. F_n is

$$\boldsymbol{F}_n = \begin{pmatrix} f_n + k_{0z} & f_n \\ -f_n & -f_n - k_{0z} \end{pmatrix} \tag{39}$$

where $f_n = f_n(\omega)$ is the frequency-dependent nuclear scattering amplitude. We will assume that the non-resonant parts, that is the electronic scattering amplitude of the layer is included in the nuclear one. This comes down to adding a constant term, since the electronic scattering is basically constant over the energy range of the nuclear scattering amplitude in almost all Mössbauer systems. In an isotopic multilayer, which consists of alternating layers of non-resonant ^{56}Fe and resonant ^{57}Fe, the reflection and transmission coefficients at the interfaces are merely due to resonant scattering, which allows us to ignore electronic contributions in the following. For the non-resonant layer then, only changes incurred in the propagation through the layer appear; the corresponding transfer matrix is

$$\boldsymbol{M}_{nr} = \begin{pmatrix} e^{ik_{0z}nd_2} & 0 \\ 0 & e^{-ik_{0z}nd_2} \end{pmatrix} \tag{40}$$

where d_2 is the thickness of the non-resonant layer. Multiplying Eqs. (38) and (40) and inserting the product into Eq. (37), we get

$$\frac{cos(k_{0z}a)}{2} = cos(k_{0z}nd_2) + i(f_n + k_{0z})d_1 sin(k_{0z}nd_2) \tag{41}$$

This is the dispersion relation for an infinite ML; it can be calculated numerically. Calculating the dispersion relation for a finite ML is not possible analytically, but we can calculate the transfer matrix for one with N layers:

$$\boldsymbol{M}_N(\omega) = \frac{\sin(Nk_{0z}d)}{\sin(k_{0z}d)}\boldsymbol{M}(\omega) - \frac{\sin((N-1)k_{0z}d)}{\sin(k_{0z}d)}\mathbf{1} \tag{42}$$

From this, we can calculate the reflectivity, transmittivity, and absorption as a function of ω for this structure

$$R = \frac{M_{N(1,2)}(\omega)}{M_{N(2,2)}(\omega)}$$

$$T = \frac{M_{N(2,1)}(\omega)}{M_{N(2,2)}(\omega)} \tag{43}$$

$$A = 1 - R - T.$$

This method yields quantitative predictions against which experimental results can be tested. However, the theoretical predictions refer to the case of an ideal experiment. This includes a

sample/multilayer of infinite lateral length (or an infinitely small beam), a beam without any divergence and other assumptions that are not warranted in reality, but often fulfilled to a good approximation. We now introduce the methods required to calculate the reflectivity correctly even in imperfect experimental conditions.

For the divergence, the procedure is straightforward [110]. The reflectivity curve is simply convoluted with a Gaussian whose FWHM corresponds to the divergence:

$$R_{corr}(\Theta) = \frac{\int R(\Theta - \phi) D(\phi) d\phi}{\int D(\phi) d\phi} \tag{44}$$

where $D(\phi)$ is the Gaussian describing the divergence, R is the reflectivity, and R_{corr} is the reflectivity taking into account the beam divergence. The next issue is the problem of beam width and sample length. At zero degrees incidence angle (as mentioned we define the incidence angle as the angle between the surface and the beam), half the beam passes the sample and is transmitted into the detector. As the angle of the sample is changed, some of the radiation that was transmitted before is reflected now, and is detected at double the incidence angle. Only part of the beam actually is reflected; the size of this part is referred to as the footprint. As the angle is increased further and further, larger parts of the beam are reflected. This has the curious effect of increasing the reflected intensity of radiation until the tilted sample blocks the whole beam, even though the actual reflectivity decreases as the angle is increased. This effect can be incorporated into the transfer matrix method (TMM) used to calculate the reflectivity by multiplying the reflectivity with an angle-dependent prefactor. The functional form of the prefactor depends on the beam shape; the relevant cases are a square and a Gaussian beam shape. For both, the prefactors can be derived by simple geometrical considerations, given in [130]. We give the results here for the square beam:

$$f = \frac{d}{l \sin \alpha} \tag{45}$$

where d is the diameter of the square beam, l is the sample length in the direction of propagation, and α is the angle of incidence. Naturally, this prefactor has to be applied only for those angles for which the footprint is larger than the sample length, that is from $\alpha = 0$ to $\alpha = \arcsin \frac{d}{l}$.

For a Gaussian beam, the formula is more complicated:

$$f_g = \frac{\int^{Lsin(\Theta)/2} g(t) dt}{\int_0^{t_m} g(t) dt} \tag{46}$$

where g is the Gaussian describing the beam, t is the variable describing the distance from its center, t_m is the position at which we assume the Gaussian to be zero (we have chosen six FWHMs for this), L is the size of the sample, and Θ the angle of incidence.

IV.2. Basic Quantum Optics

In this section we will discuss some of the basic problems of quantum optics in order to fix the terminology and lay out the motivation for our experiments. This section deals with the most fundamental description of the interaction of light with matter. We introduce the terminology and results which form the basic building blocks of the more complicated theories which we will introduce later on to describe our experiments. We will first discuss the interaction of an atom with light in free space. These results are invaluable in understanding why the interaction of light and matter is fundamentally changed when the atoms are inserted into a cavity. Later on, we will give a brief description of the phenomena which can be observed when light and atoms interact in a cavity, and hint at why the control thus gained is so desirable. Finally, we introduce the theoretical description of light with a large ensemble of atoms. Not only is this a fascinating and beautifully simple result of many-body physics in its own right, it is also vital for the understanding of our experiments, since we will always deal with a large number of resonant atoms or nuclei by default.

IV.2.1. Spontaneous emission and the Wigner-Weisskopf theory

Wigner and Weisskopf [131] were the first to deal with the problem of spontaneous emission of a photon by an atom. Suppose an atom is in an excited state, while the electromagnetic field is in the vacuum state. We denote this initial state as $\Psi_i = |e, 0\rangle$. In this model, the atom interacts with all the modes in the electromagnetic vacuum, meaning the final state is $\Psi_f = |g, 1_{\vec{k}}\rangle$. The time-dependent state of the system is then

$$|\Psi(t)\rangle = a(t)\,|e, 0\rangle + \sum_{\vec{k}} b_{\vec{k}}(t)\,|g, 1_{\vec{k}}\rangle \tag{47}$$

where the sum goes over all modes $\vec{k}$ in the electromagnetic field, and a and b are the probability amplitudes that the system is in the respective state. We are ignoring polarization effects. The rotating wave approximation [132] has been performed. The appropriate Hamiltonian reads

$$H = \hbar\omega\sigma_z + \sum_{\vec{k}} \hbar\omega_{\vec{k}} a^\dagger_{\vec{k}} a_{\vec{k}} + \sum_{\vec{k}} g\sigma_+ a_{\vec{k}} + g^* a^\dagger_{\vec{k}} \sigma_- \tag{48}$$

where the first term denotes the energy of the atom/nucleus, the second term the energy of all modes of the electromagnetic field, and the third the interaction energy between atom and field modes. The interaction term can be related to the energy of a dipole in the electromagnetic field

$$H_{int} = -\vec{d} \cdot \vec{E}. \tag{49}$$

However, this stems from the dipole approximation, which implies that the resonance is an electric dipole and that the wavelength of the light is far larger than the size of the resonant atom. The first assumption is not a given when dealing with nuclear resonances, which are often magnetic dipoles or electric quadrupoles; the second one is not necessarily applicable when dealing with electronic resonances and x-rays, since the latters' wavelength is usually smaller than an atom. The main conclusion, important for further discussions is the following, that the interaction strength depends mostly on (a) the matrix element of the respective transition and (b) the electromagnetic density of states. This is valid for both electronic and nuclear resonances. In fact, it is a general principle known as Fermi's golden rule [133].

Our choice of quantum state involves truncating the Hamiltonian after the one-excitation subspace. Inserting Hamiltonian and state ansatz into the time-dependent Schrödinger equation we get the coupled equations of motion

$$\begin{aligned} \dot{a} &= i \sum_{\vec{k}} g e^{-i(\omega_k - \omega_0)} b_{\vec{k}}(t) \\ \dot{b}_{\vec{k}} &= i g^* e^{i(\omega_k - \omega_0)} a(t) \end{aligned} \tag{50}$$

Formally integrating the second equation and re-inserting it into the first yields

$$\dot{a}(t) = -\sum_{\vec{k}} |g|^2 \int_0^t dt' e^{-i(\omega_k - \omega_0)(t-t')} a(t') \tag{51}$$

Here, we perform the Markov approximation [133], i.e. we assume that the behaviour of $a(t)$ varies with a rate that is much slower than the rotation of the exponential term. In that case, $a(t')$ does not vary much while the rest of the integrand is non zero; we can approximate it as depending only on t itself.

$$\dot{a}(t) = -\sum_{\vec{k}} |g|^2 a(t) \int_0^t e^{-i(\omega_k - \omega_0)(t-t')} dt' \tag{52}$$

This is the so-called Markov approximation. It means that the systems behaviour depends only on the current time, and not on its behaviour in the past. In other words, the system has no memory. This has far-reaching implications, for example that the decay is non-reversible [133]. A rather complicated complex integration yields the result

$$\int_0^t e^{-i(\omega_k - \omega_0)(t-t')} dt' = \pi \delta(\omega - \omega_k) + i \mathcal{P} \frac{1}{\omega_k - \omega_0} \tag{53}$$

where $\mathcal{P}$ is the Cauchy principal value. This part is usually neglected in non-relativistic calculations because it leads to a divergence; a renormalization treatment yields the Lamb shift. Inserting the remainder of the result into Eq. (51) results in

$$a(t) = a(0) e^{-\Gamma t} \tag{54}$$

where Γ is the natural lifetime, and can be expressed as

$$\Gamma = \pi\omega_0^3 \sum_{\vec{k}} |g|^2. \tag{55}$$

Thus an excited atom decays exponentially and irreversibly. Obviously, this means that this physical situation is useless for any advanced schemes of the coherent control of light, and therefore for any practical uses of quantum optics. To alleviate this, another scheme is needed.

IV.2.2. The Jaynes-Cummings model

In the Wigner-Weisskopf approach, the atom interferes with a continuum of modes. Roughly speaking, the atom cannot reabsorb a photon because the probability amplitudes from all modes interfere destructively. When the atom interacts with only one mode, this is not the case. This is the so-called Jaynes-Cummings model [132]. The Hamiltonian is identical to that in Eq. (48), but the sum over all modes is dropped, as the atom interacts with only one mode. Proceeding as in the last section, we get for the temporal dynamics

$$|\Psi(t)\rangle = -i\frac{g^2}{g^2+\Delta^2}\sin(\sqrt{g^2+\Delta^2}t)\,|e,0\rangle + \left[\cos(\sqrt{g^2+\Delta^2}t) - i\frac{\Delta}{\sqrt{g^2+\Delta^2}}\sin(\sqrt{g^2+\Delta^2}t)\right]|g,1\rangle \tag{56}$$

where g is the coupling strength and Δ the detuning between the frequency of the atom and the mode. We have assumed that the atom is initially in the ground state. It follows from the above that the mode and the atom periodically exchange populations with a frequency given by the interaction strength and the energetic detuning. This was observed for the first time with fine structure transitions in the microwave range by Rabi *et al* [134]. If the detuning is zero, the equation simplifies to

$$|\Psi(t)\rangle = \sin(gt)\,|e,0\rangle + \cos(gt))\,|g,1\rangle \tag{57}$$

In this context, g is often referred to as Ω, the Rabi frequency. For reasons that will become clear, we will call $g = \Omega_c$ and $\sqrt{g^2+\Delta^2} = \Omega_R$. With the above equations, we can calculate the probabilities of finding the atom in the excited or ground state. Clearly, this probability varies sinusoidally with the time, with the frequency being Ω_c or Ω_R. A cursory inspection reveals that the frequency becomes larger if the field and the atomic level energy are detuned, but also that the probability of finding the atom in the excited state becomes much smaller. This phenomenon can also be described in energy instead of temporal space. The Hamiltonian in matrix formulation for the one-excitation subspace is [135]

$$H = \begin{pmatrix} \omega_a & g \\ g^* & \omega_m \end{pmatrix} \tag{58}$$

Diagonalizing this, we get the eigenstate energies dispersion relation

$$\omega_{1,2} = \frac{\omega_m + \omega_a}{2} \pm \sqrt{(\frac{\omega_m - \omega_a}{2})^2 + |g|^2} \tag{59}$$

where clearly $\omega_m - \omega_a = \Delta$. Evidently, the splitting between the branches corresponds to twice the Rabi frequency. If the detuning is large, clearly one branch of this dispersion relation will have an energy that is close to the atomic energy; we refer to it as 'matter-like'. The other one will have an energy almost identical to the mode of the electromagnetic field, and will be called 'light-like'. The corresponding eigenstates at zero detuning are

$$|+\rangle = \frac{1}{2}(|g,1\rangle + |e,0\rangle) \tag{60}$$

$$|-\rangle = \frac{1}{2}(|g,1\rangle - |e,0\rangle) \tag{61}$$

$$\tag{62}$$

Extending this beyond the one-excitation subspace is simple. In the rotating wave approximation, only states with the same number of total excitations are coupled, e.g. $|g, n+1\rangle$ and $|e, n\rangle$. This is the so-called Jaynes-Cummings ladder [136]. The only additional change that has to performed in the above formulas is to replace every instance of g by $g\sqrt{n+1}$.

Any practical implementation of the Jaynes-Cummings model will be in one of the many varieties of cavity quantum electrodynamics that have sprung up in the last 30 years. The archetypical system is a microwave cavity with spherical mirrors that permits only one mode in a reasonable energetic range around an atom inside the cavity [19]. The atom is usually introduced into the cavity by means of an atomic beam; the velocity of that beam determines the time the atom stays in the cavity and is the prime way of manipulating the quantum states of the combined cavity-atom system and of producing entanglement [13]. Naturally, all these systems share a set of flaws: dissipativity and decoherence, though in each system one of them is dominant. In all cases, no matter how good the cavity, it will have losses to the continuum of modes outside the cavity; equally the atomic system will spontaneously emit photons into modes outside of the cavity, instead of into the cavity mode. This can be quickly and largely correctly modeled by introducing imaginary terms into the diagonal elements of the matrix representing the Hamiltonian. The imaginary terms indicate the width (in Hz) of the cavity or atomic line.

At this point, problems appear. When g is not larger than both κ (the cavity linewidth) and γ (the atomic linewidth), the Rabi splitting does not take place, since the width of the splitting between the lines is proportional to $2g$. At least one line is wider than the splitting, therefore the splitting is not observed [137, 138]. At first this might sound like a spectroscopic resolution criterion, which in principle it is. But a large linewidth of the cavity or the atom means that effectively

the atom interacts with many modes of the electromagnetic field. Then, there is no coherent exchange of energy between the atom and the mode, but the system as a whole undergoes a Wigner-Weisskopf-like irreversible decay, which may only be slightly modified by the cavity - the so-called Purcell effect [139, 140]. If, however, the splitting can be resolved, atom and cavity mode exchange an excitation periodically. The decay is not irreversible, at least in the short term, and offers opportunities for quantum optical manipulations. This regime is called the strong coupling regime [141], and in the majority of most modern cavity QED experiments and schemes, it is a precondition.

IV.2.3. Many body quantum optics and the Dicke model

The experimental situation where one photon interacts with one atom is hard to produce. While even at modern synchrotron sources the occurrence of more than one photon in the bandwidth of the ^{57}Fe 14.4 keV resonance at a time is extremely rare, we will always see it interact with a huge ensemble of atoms. The one-excitation subspace will therefore describe phenomena described in the remainder of this thesis very well. More important for our purposes is the question of what happens when the number of atoms or nuclei is larger than one. To deal with this question we turn to the Dicke model [142, 143]. Dicke was the first to notice that a number of N atoms interacting with a single mode can be described by a set of pseudo-angular momentum operators. For a single atom i

$$\sigma_+^i = |e_i\rangle \langle g_i| \tag{63}$$

$$\sigma_-^i = |g_i\rangle \langle e_i| \tag{64}$$

$$\sigma_z^i = |e_i\rangle \langle e_i| - |g_i\rangle \langle g_i| \tag{65}$$

are the raising, lowering and population inversion measurement operators respectively. For N atoms we define the new set of operators

$$S_+ = \sum_i^N \sigma_+^i \tag{66}$$

$$S_- = \sum_i^N \sigma_-^i \tag{67}$$

$$S_z = \sum_i^N \sigma_z^i \tag{68}$$

The standard angular momentum commutation relations are fulfilled for the new operators. Using these new operators requires that the Hamiltonian be transformed into the new Dicke basis of collective states. This can be compared to a spin system. Consequently, the ground state is

$S = -\frac{N}{2}$. Other states available are $-\frac{N}{2} \leq n \leq \frac{N}{2}$. However, this accounts for only $N+1$ states. However, in the single-atom basis, the number of different combinations of excited and ground state atoms should be 2^N. Of course, several combinations of excited and ground states can have an identical total spin. It turns out a new quantum number has to be introduced to describe this accurately. In going with Dicke, we will call it r. It is constrained by $|n| \leq r \leq \frac{N}{2}$ and explains the degeneracy. Degenerate levels have in common that they have the same number of total excitations, but shared among the constituting atoms in different linear combinations of varying symmetry. n and r correspond to the magnetic and azimuthal quantum numbers of angular momentum algebra respectively. The eigenstates of the new system are described by superpositions of the states of the previous basis.

As we shall describe later on, the truncation of our system to the one-excitation subspace (where only one quantum of energy is involved) permits us to examine the interaction of the electromagnetic field only with the Dicke states which have a quantum number of $S = -\frac{N}{2} + 1$ and $S = -\frac{N}{2}$. We can also assume that the field excites only the maximally symmetric Dicke states, which for the chosen subspace has a quantum number of $r = -\frac{N}{2} + 1$, and the form

$$\Psi_{Dicke} = \frac{1}{\sqrt{N}} \sum_i |gg...e_i...g\rangle \tag{69}$$

which means that it is an equally weighted sum over all states where one atom (or nucleus) is excited, and all others are not. Recently, a particular type of Dicke state has excited a lot of interest in quantum optics, which is usually referred to as a 'timed' Dicke state [144, 145, 146, 147]. The difference between a timed Dicke state and a regular one is that the timed Dicke state displays a different phase factor for every atom included in the Dicke state. The physical situation this corresponds to is that of a set of atoms spatially dispersed over an area much larger than the wavelength of the resonant radiation illuminating the ensemble. As pointed out by several authors [146], the interaction of a timed Dicke state and the electromagnetic vacuum has a very useful aspect to it. The interaction always comes with a factor

$$\frac{1}{\sqrt{N}} \sum_i^N e^{i(\vec{k}-\vec{k}')r_i} \rightarrow \int e^{i(\vec{k}-\vec{k}')r_i} \rightarrow \delta(\vec{k}-\vec{k}') \tag{70}$$

which is valid in the limit of a large, disordered, low-density sample. This means that the timed collective Dicke state effectively interacts with only one mode, the one from which it got excited in the first place. We see that the nuclear exciton, which is the excitation shared by an ensemble of nuclei is one example. Similar mathematics and reasoning was also used by Hopfield in his derivation of the polariton [148]. So it turns out that the presence of a lot of spatially spread nuclei in the cavity mode is really a boon for enhancing the light-matter interaction. Not only does an

extra term $\sqrt{N}$ enhance the collective interaction [149], but the very fact that the excitation is phased ultimately enforces that the ensemble's collective states only interact with the mode which fits the phasing pattern - which is of course the mode the state was excited from. So the nuclear ensemble interacts always with one mode only, and it is always the one we choose by illuminating it. This does not mean that the cavity itself cannot be detuned from that mode.
In light of the fact that we are using a cavity anyway, this may not mean a great deal. But our cavity does not quite meet the definition and requirements that are commonplace in other areas of optics. The electric field is only quantized in one direction, the direction of growth. In the other two dimensions, a single atom would be perfectly free to interact with a continuum of modes. There is a huge number of publications debating whether Rabi oscillations and energy splitting might still be observed under certain circumstances for a single atom or a non-phased ensemble, see for example [150, 151, 152, 153].

IV.3. Quantum Optical Models

We will recap a slightly simplified version of a quantum optical model of the QED/Cavity interaction devised by Heeg and Evers [54, 58], where the main difference will be that we restrict ourselves to one level. We begin by modeling the cavity and the drive. The cavity is schematically shown in Fig. 15

IV.3.1. Cavity

The Hamiltonian of the cavity in the Schrödinger picture is

$$H_C = \omega_C a^\dagger a + i\sqrt{2\kappa_r}(a_{in}e^{-i\omega t}a^\dagger - a_{in}^* e^{i\omega t}a). \tag{71}$$

Here, ω_C is the cavity mode frequency and $a(a^\dagger)$ is the photon annihilation (creation) operator for the cavity mode. Synchrotron radiation consists of a coherent electromagnetic field. Furthermore, within the bandwidth required to excite a nucleus, the intensity of the synchrotron x-ray beam is usually very low (on the order of 10^3 photons/sec), with a repetition rate of 5×10^6 Hz. When taking into account the low brilliance of the beam, it is therefore justified to model the driving beam as a weak classical field, whose strength is given by a_{in}, because the number of resonant photons is very low. κ_r is associated with the output noise of the cavity. To facilitate calculations, we transform this Hamiltonian into the interaction Hamiltonian by performing the unitary transformation

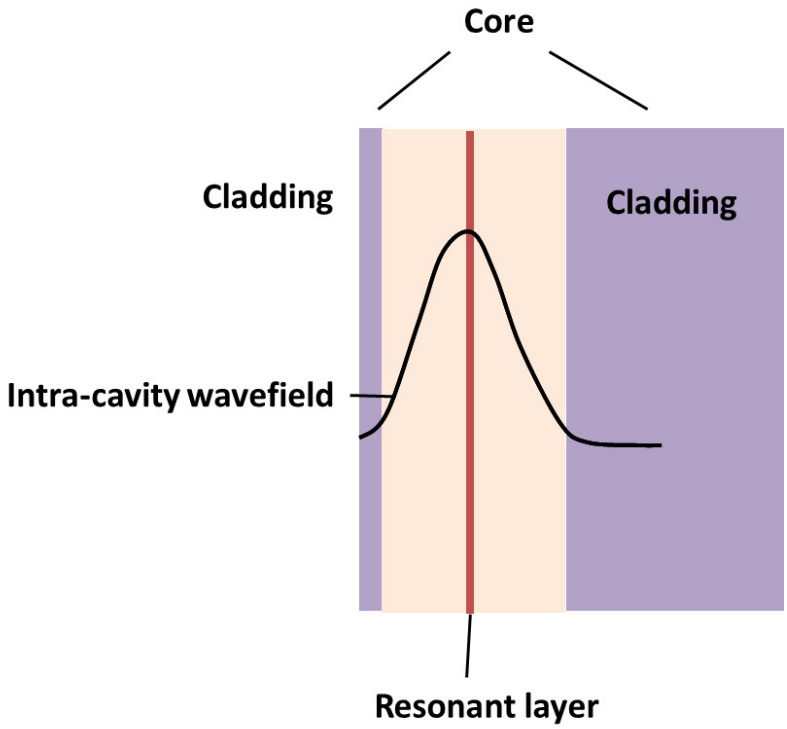

Figure 15: *The basic design of the cavity. A low-Z core is sandwiched by a high-Z cladding; in the center, where the guided electromagnetic field is strongest, a resonant layer is placed.*

$$H_C^I = UH_C^S U^\dagger - H_T \tag{72}$$

where $H_T = \omega a^\dagger a$ and $U = e^{iH_T t}$. This yields

$$H_C^{(I)} = \Delta_C a^\dagger a + i\sqrt{2\kappa_r}(a_{in}a^\dagger - a_{in}^* a). \tag{73}$$

Δ_C is the detuning between drive and cavity. For practical purposes, the detuning will take place both by illuminating the cavity with slightly different energies and by changing the angle of incidence. The angular detuning can be transformed to energetic detuning by the formula

$$\Delta_C(\alpha) = \omega_0(\frac{\sin(\alpha_0)}{\sin(\alpha)} - 1) \tag{74}$$

where α_0 is the angle at which the cavity is driven exactly at mode frequency, and α is the incidence angle. Experimentally, we probe the system by performing reflectivity measurements. The cavity is one-sided, the electromagnetic input and output fields couple to the cavity via the same port, namely the upper mirror. The standard input-output formalism of quantum optics is tailor-made

for a situation of this kind. We give its main result here, which is

$$a_{out} = -a_{in} + \sqrt{2\kappa_r}a \tag{75}$$

The reflection coefficient itself is

$$R = \frac{\langle a_{out} \rangle}{a_{in}} \tag{76}$$

Or with Eq. (75)

$$R = -1 + \frac{\sqrt{2\kappa_r}\langle a \rangle}{a_{in}} \tag{77}$$

Obviously, the reflectivity can be found by calculating the steady-state value of a, i.e. setting $\dot{a} = 0$.

IV.3.2. Nuclear ensemble

Beginning again in the Schrödinger picture, the Hamiltonian of a single nucleus is

$$H_N^{(S)} = \omega_g \left|g\right\rangle \left\langle g\right| + \omega_e \left|e\right\rangle \left\langle e\right| + g\sigma_+ a + g^* \sigma_- a \tag{78}$$

where ω_g and ω_e are the ground and excited state energies respectively, g is the coupling constant and $\sigma_\pm$ are the raising/lowering operators for the nucleus. In order to convert this Hamiltonian to the interaction picture, we proceed as in the previous section, but replace the H_T by

$$H_T = \omega a^\dagger a + \omega_g \left|g\right\rangle \left\langle g\right| + (\omega_e + \omega) \left|e\right\rangle \left\langle e\right| \tag{79}$$

Note that this new transformation can be applied to both the cavity and nuclear Hamiltonian. The nuclear Hamiltonian in the interaction picture is

$$H_N^{(I)} = -\Delta \left|e\right\rangle \left\langle e\right| + G\sigma_+ a + G^* \sigma_- a \tag{80}$$

where Δ is simply the detuning between the nucleus and the drive frequency. For N nuclei, the above can simply be summed up. Since the coupling strength g is the same everywhere, but is phased, we write $G = ge^{i\vec{k}\vec{r}_n} = g^{(n)}$. Since the Hamiltonian for the entire ensemble is obviously $\sum_i^N H_N^{(I)}$ we can replace the individual ladder operators by the collective operators.

$$H_N = -\sum_i^N \Delta \left|e\right\rangle_i \left\langle e\right|_i + gS_+ a + gS_- a. \tag{81}$$

Note that this is only valid if the coupling is identical for all nuclei involved in the collective state that is raised or lowered by the operator

IV.3.3. Dissipation and losses

Both cavity and nuclei are subject to energy dissipation. In the case of the nuclei, this takes the form of spontaneous emission into non-cavity modes of the electromagnetic field or non-radiative decay. For the cavity, standard absorption in cladding and core, as well as scattering and emission outside the cavity make up the dissipation. For simplicity, we will ignore non-radiative loss channels and subsume them into the radiative channels. This allows us to treat the problem with the standard Lindblad operator [138] derived from a Master equation approach [154]. A Lindblad operator is defined as

$$\mathcal{L}(\rho, O^+, O^-) = O^+O^-\rho + \rho O^+O^- - 2O^-\rho O^+ \tag{82}$$

where O is any operator. The Lindblad operator generally describes the irreversible emission of a single system interacting with a bath, in our case the continuum of modes outside the cavity. The specific decay terms for cavity and a single nucleus are

$$\begin{aligned} \mathcal{L}_C &= -\kappa\mathcal{L}(\rho, a^\dagger, a), \\ \mathcal{L}_N &= -\tfrac{\gamma}{2}\mathcal{L}(\rho, \sigma^+, \sigma^-) \end{aligned} \tag{83}$$

and they are added to the Hamiltonian for a full description of the system.

IV.3.4. Solutions

Broadly, there are two pathways for obtaining the reflectivity. Heeg and Evers have opted to adiabatically eliminate the cavity mode on account of the fact that in a typical set up its linewidth is larger than the nuclear linewidth by some 10 orders of magnitude. A photon entering the cavity is therefore unlikely to be absorbed and emitted multiple times by the nuclear ensemble within the cavity - the system is far outside the strong-coupling regime. This approach delivers accurate results and is extremely convenient when dealing with Zeeman splitting of the lines. In that case, Heeg and Evers have shown that both cavity mode-induced self-interactions of individual nuclei resonances, as well as interactions between resonances of individual nuclei and interactions between different resonances of different nuclei take place. In this way, they could explain a range of observed effects, all due to interactions induced by the cavity vacuum. These were the collective Lamb shift of the ensemble [52], and spontaneously generated coherences [56] between the collective states of different sublevels, leading to the suppression of spontaneous emission at certain positions in the energy spectrum. However, in the context of a single-line system, it is straightforward to solve the system by solving the Heisenberg-Langevin equations in the steady

state. We will first reproduce Heeg's and Evers' derivation involving the adiabatic elimination, then take the second approach involving only the steady-state solution. Finally, we introduce Heeg's and Evers' generalized version of their first result, involving multiple cavity modes and layers.

The Heisenberg-Langevin equations for our model are

$$\begin{aligned} \dot{a} &= i[H, a] - \kappa a \\ \dot{\sigma^-} &= i[H, \sigma^-] - \gamma \sigma^- \end{aligned} \tag{84}$$

To perform the adiabatic elimination of the cavity mode, we calculate the Heisenberg-Langevin equation of the cavity mode, and set the derivative to zero. Resolving for a, we get

$$a = \frac{\sqrt{2\kappa_r} a_{in} - i \sum_n g^{(n)^*} \sigma_-^{(n)}}{\kappa + i\Delta_C} \tag{85}$$

Eq. (85) can be introduced into the Master equation

$$\dot{\rho} = i[H, \rho] - \mathcal{L}[\rho] \tag{86}$$

yielding the effective Hamiltonian which describes the system and its dynamics purely in terms of the nuclear raising and lowering operators. The effective Hamiltonian and effective Lindblad operators are:

$$\begin{aligned} H_\Omega &= \sum_{n=1}^N \Omega g^n \sigma_+^{(n)} + h.c. \\ H_{LS} &= \sum_{n,m=1}^N \delta_{LS} g^{(n)} g^{(m)^*} \sigma_+^{(n)} \sigma_-^{(m)} \\ \mathcal{L}_{cav}^{eff} &= -\xi \sum_{n,m}^N g^{(n)} g^{(m)^*} \mathcal{L}[\rho, \sigma_+^{(n)}, \sigma_-^{(m)}] \end{aligned} \tag{87}$$

where $\Omega = \frac{\sqrt{2\kappa_r} a_{in}}{\kappa + i\Delta_C}$ and $\delta_{LS} = -\frac{\Delta_C}{\kappa^2 + \Delta_C^2}$ and $\xi = \frac{\kappa}{\kappa^2 + \Delta_C^2}$. The first Hamiltonian includes the effective driving of the ensemble of nuclei by the drive after elimination of the cavity. The second one includes the self interaction of nuclei due to the cavity vacuum (for $m = n$), and the interaction of different nuclei due to re-emission and re-absorption for $m \neq n$. The former term results in an enhanced Lamb shift of a single nucleus due to the cavity vacuum; the second one results in a collective Lamb shift.

The expression for a arising from adiabatic elimination can also be introduced into Eq. (77) for the reflection coefficient:

$$R = -1 + \frac{2\kappa_r}{\kappa + i\Delta_C} - \frac{i\sqrt{2\kappa_r}}{a_{in}(\kappa + i\Delta_C)} \sum_n^N g^{(n)^*} \langle \sigma_-^{(n)} \rangle \tag{88}$$

Recall that $\langle A \rangle = Tr(\rho A)$, where A is any operator.

To proceed, we perform a change of basis. This is largely analogous to the Dicke model basis transformation, but since our sample exceeds the Dicke-limit in one dimension, we have to add

another phase factor. Moreover, in all calculations, we will use only one excited state, namely $(-\frac{N}{2}+1, \frac{N}{2})$, which is the maximally symmetric Dicke state in the one-excitation subspace of Dicke states. The ground state will be denoted by $|G\rangle$.
In the old basis, the singly excited state of nucleus n is

$$|E^{(n)}\rangle = \sigma_+^{(n)} |G\rangle \tag{89}$$

In the new basis, the excited state is a coherent superposition of all singly excited states, with an additional phase factor to account for spatial distribution. Again, this is the so-called 'timed Dicke state'.

$$|E^+\rangle = \frac{1}{\sqrt{N}} \sum_n^N e^{i\vec{k}\vec{r}_n} |E^{(n)}\rangle \tag{90}$$

where $\vec{k}$ is the wave vector of the radiation exciting the timed Dicke state, and $\vec{r}_n$ is the position of the n-th nucleus. This change of basis allows us to simplify the effective Hamiltonian and Lindblad terms:

$$H_\Omega^{eff} = \Omega g \sqrt{N} |E^+\rangle \langle G| + h.c. \tag{91}$$

$$H_{LS}^{eff} = \delta_{LS} |g|^2 N |E^+\rangle \langle E^+| \tag{92}$$

$$\mathcal{L}[\rho] = -\xi_s |g|^2 N \mathcal{L}[\rho, |E^+\rangle \langle G|, |G\rangle \langle E^+|] \tag{93}$$

Note that $|E^+\rangle \langle G|$ is essentially a coherent phased superposition of raising operators $\sum_n^N e^{-i\vec{k}\vec{r}_n} \sigma_+^{(n)}$. It can be interpreted as a new operator, which adds an excitation inside the symmetric subspaces of the many body system. An equivalent argument is valid for the lowering operator. If we restrict ourselves to the symmetric state of the one-excitation subspace, a single layer of ^{57}Fe can be regarded as a two-level system with an $\sqrt{N}$-fold enhanced interaction with the environment. It is not entirely clear how large N is; in principle it should account for all nuclei in a cavity. However, planar cavities, such as ours have a transverse quantum-correlation length [155], sometimes referred to as effective area [156], which limits this number. Briefly, it can be interpreted as the length over which resonant atoms in the cavity interact collectively with the mode. This is not necessarily the cavity length. We therefore always give the collective coupling strength, and do not calculate the strength for an individual nucleus or atom. We can insert the lowering operator into the term Eq.(88). Performing the trace, we get

$$R = -1 + \frac{2\kappa_r}{\kappa + i\Delta_C} - \frac{i\sqrt{2\kappa_r}}{a_{in}(\kappa + i\Delta_C)} \sum_n^N g^{(n)^*} \langle E^+| \rho |G\rangle . \tag{94}$$

It follows that we will have to solve the Master equation

$$\dot{\rho} = i[H^{eff}, \rho] - \mathcal{L}^{eff}[\rho] \tag{95}$$

to calculate the matrix element appearing in Eq. (94). Once more, we solve the system of equations in the steady state. We also assume that $\langle G|\,\rho\,|G\rangle = 1$ and $\langle E^+|\,\rho\,|E^+\rangle = 0$, neglecting the possibility of population redistributions. We end up with

$$\langle E^+|\,\rho\,|G\rangle = \frac{iN\Omega g}{\Delta + i\frac{\gamma}{2} + N|g|^2(i\xi_s - \delta_{LS})} \tag{96}$$

which can be inserted into Eq. (94) to calculate the reflectivity. A cursory inspection reveals that the reflectivity spectrum around resonance is given by a modified Lorentzian, which is shifted in energy by $N|g|^2\delta_{LS}$ linewidths and has an additional decay term given by $N|g|^2\xi_s$. These changes, Lamb shift and superradiant decay enhancement, are the result of the enhancement of the light-matter interaction due to the cavity. Keep in mind that their magnitude depends not only on the cavity mode characteristics, but also of the detuning both angular and energetic of the incoming beam from the resonance. Introducing additional resonances into this model results in additional coherences between the levels induced by the cavity mode interaction.

IV.3.5. Reflectivity without adiabatic elimination

In this section we present a derivation of the reflectivity without employing the adiabatic elimination, which is the same as that used in [157, 140] It has the drawback of not allowing for as simple an interpretation of the many-body interactions within the layer, and not permitting an easy treatment of the spontaneously generated coherences, but offers a more intuitive picture of the interaction of the cavity mode with an ensemble of nuclei.

From the last section, we recall the collective states $|E^+\rangle$. Projecting these onto the ground state $\langle G|$, we get essentially a new operator S_+. We recall from the Dicke model that we can in a similar manner construct a great many energy eigenstates of the ensemble of nuclei, all of which are superpositions of excited and ground states of single nuclei. The operators obey an angular momentum algebra. We may think of the ensemble of nuclei as a large pseudospin with the operators S_z, S_+, and S_- which give the projection onto the z-axis (the m quantum number) or raise and lower it respectively. The cavity mode is coupled to this pseudospin; if a photon in the cavity is absorbed by the nuclear ensemble, the spin quantum number m is raised; in the opposite case it is lowered. Without taking into account the losses for now, the Hamiltonian is given by

$$H = \Delta_c a^\dagger a + \Delta S_z + (g a S_+ + g^* a^\dagger S_-) + a_{in}\sqrt{2\kappa_R}(a + a^\dagger) \tag{97}$$

where the first term is the energy of the cavity mode, the second that of the nuclear ensemble/pseudospin, the third term gives the interaction between both, and the fourth term takes account of the driving of the cavity mode by an outside classical field, whose interaction strength

with the cavity is given by $\sqrt{\kappa_R}$. We have already, as in the last section, transformed the Hamiltonian into the interaction picture, hence the energies are given by the detunings from the driving field δ_C and δ of the mode and the nuclear ensemble respectively. We now calculate the Heisenberg equations of motion:

$$\dot{a} = i[H, a] - \kappa a \tag{98}$$

$$\dot{S_-} = i[H, S_-] - \gamma S_- \tag{99}$$

The decay constants κ and γ have been added phenomenologically; they can also be more rigorously introduced by forming the Master equation and assuming that the number of quanta in the system is low (one-excitation subspace), as laid out in the last sections. A noise operator is not necessary at the energies we envision. Calculating the equations of motion yields

$$\dot{a} = -i\Delta_c a - ig^* S_- - \kappa a - a_{in}\sqrt{2\kappa_R} \tag{100}$$

$$\dot{S_-} = -i\Delta S_- - igaS_z - \gamma S_- \tag{101}$$

Setting the left-hand side derivatives to zero to obtain the solution in the steady-state limit, and resolving for a yields

$$a = \frac{\sqrt{2\kappa_R}a_{in}(\kappa + i\Delta_c)}{(\kappa + i\Delta_c)(\gamma + i\Delta) + |g|^2} \tag{102}$$

which can be inserted into the result for the input-output formalism Eq. (77) and leads to

$$R = -1 + \frac{2\kappa_R(\kappa + i\Delta_c)}{(\kappa + i\Delta_c)(\gamma + i\Delta) + |g|^2} \tag{103}$$

Before we resume to show the reflectivity, let us briefly discuss the quantum mechanics behind this system. A sketch is given in Fig. 16

In the one-excitation subspace, i.e. with just one energy quantum (one photon, or one nuclear excitation) in the system, we have three possible states which interact. The first one is the state $|g0\rangle$ where neither the cavity nor the nuclear ensemble is excited. In that case, the photon is located in the beam with which we pump the cavity. The second state, which we pump from the ground state, is $|g1\rangle$ where the photon is in the cavity, but the nuclear ensemble is in the ground state. This state couples via the cavity vacuum to the third state $|e0\rangle$ in which there is no cavity photon, but the nuclear ensemble shares one excitation. The cavity has a very high decay constant κ, the nuclear ensemble a very low decay constant γ; the coupling g between the two upper states is typically much larger then γ, but much lower than κ. This is almost exactly the set-up of electromagnetically induced transparency, and the physical features of the reflectivity can be explained as follows. We have a weak probe field, which is the classical field we use to

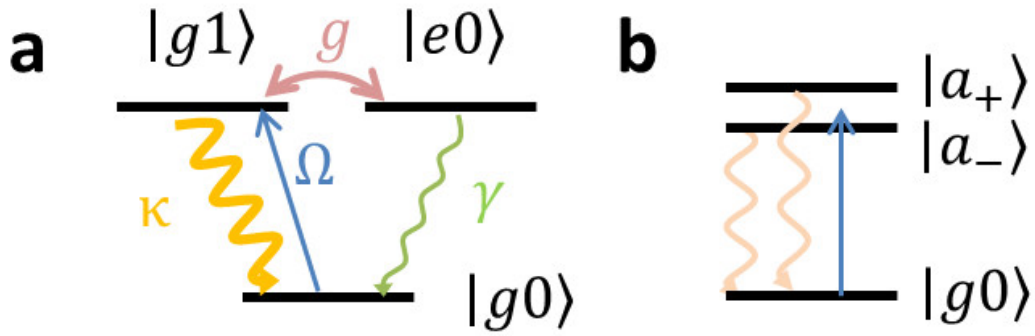

Figure 16: *Undressed and dressed level systems of the composite nuclear ensemble-cavity system. (a) from the ground state, the excited cavity state is driven (blue line). It interacts with the nuclear exciton (red double-arrowed line) and strongly decays incoherently to the ground state (thick wavy orange arrow). The nuclear exciton decays weakly (thin green wavy arrow) to the ground state. Diagonalizing the appropriate Hamiltonian gives the dressed state picture, shown in (b): both dressed upper states decay at the same rate. Their spectral width is larger than the energetic splitting between them. If we try to excite any of them by driving them, they will destructively interfere with each other, resulting in none of them getting excited.*

illuminate the cavity. Describing the classical field as a coherent state $|\alpha\rangle$, typically $\alpha \ll 1$, i.e. there is on average far less than one resonant photon per bunch in the synchrotron beam, supporting this assumption. We have a relatively strong coupling field coupling the two upper levels, which in our case is given by the cavity vacuum. In this situation, describing the system in terms of its eigenstates yields a very particular solution. Two of the eigenstates are coherent superpositions of all three undressed states; the third one, which has exactly the energy of the nuclear ensemble and is dispersionless, is a superposition of the type $a\,|g0\rangle + b\,|e0\rangle$, where $a \gg b$. In other words, the eigenstate is basically identical to the ground state with the photon in the field outside the cavity. The cavity is not excited at all; it cannot accept a photon, and therefore, all light illuminating the cavity is reflected when it has the energy of that particular state. A slightly modified view of the situation is shown in Fig. 16(b) for the particular case where $\Delta_c = \Delta$. The upper eigenstates are shifted symmetrically towards opposite energies around the undressed state energies; they have the same decay width, which is larger than the energetic splitting between the states. If we try to excite one of the states, they both destructively interfere with the probe field, and none of them can be excited. The photon remains in the ground state of the system, which means it remains outside the cavity. This means that the system reflects all radiation that is incoming, and none is absorbed.

IV.3.6. Multiple layers and multiple modes.

The treatment of multiple layers and multiple modes interacting together is a straightforward extension of that in the last section [58]. The derivation largely follows the same lines. The Hamiltonian, the Lindblad operator, and the input-output relation are taken over a sum of j modes. The Hamiltonian is also a sum taken over n nuclei, which will decomposed later over the layers. Each mode is eliminated adiabatically. The new effective Hamiltonian terms are

$$H_\Omega = \sum_n \sum_j \Omega^{[j]} j g_{n,j}^{[j]} \sigma_+^{(n)} + h.c. \tag{104}$$

$$H_{LS} = \sum_{n,m} \sum_j (\delta_{LS}^{[j]} g_{n,j}^{[j]} g_{m,j}^{[j]*}) \sigma_+^{(n)} \sigma_-^{(m)} \tag{105}$$

$$\mathcal{L}_{cav}[\rho] = \sum_{n,m} \sum_j (-\xi^{[j]} g_n^{[j]} g_m^{[j]*}) \mathcal{L}[\rho, \sigma_+^{(n)} \sigma_-^{(m)}] \tag{106}$$

where $\delta_{LS}^{[j]}, \xi^{[j]}$ and $\Omega^{[j]}$ have the same form as in the previous section, but take mode-specific values for the detuning and spectral mode width. Suppose we have two layers and one mode. A term like $\sum_n \Omega g_n \sigma_+^{(n)} + h.c.$ can then be split into $\sum_{n1} \Omega g_{n1} \sigma_+^{(n1)} + \sum_{n2} \Omega g_{n2} \sigma_+^{(n2)}$ where n_1 and n_2 count the nuclei in the first and second layer respectively. It follows that if $|g_{n1}|$ and $|g_{n2}|$ are not identical, we have to introduce two new collective operators in the manner of the previous section, namely $S_+^{(1)} = |E_+^{(1)}\rangle \langle G| = \frac{1}{\sqrt{N}} \sum_{n1} e^{i\vec{k}\vec{r}_n} \sigma_+^{(n)}$ and $S_+^{(2)} = |E_+^{(2)}\rangle \langle G| = \frac{1}{\sqrt{N}} \sum_{n2} e^{i\vec{k}\vec{r}_n} \sigma_+^{(n)}$ and equivalent destruction operators. Using operators which define a nuclear exciton over the two layers is only permissible if these two layers are coupled to the field with identical strength, and the layers are indistinguishable in any other way. If this is violated, the angular momentum algebra used by Dicke does not close anymore, and the state is not a Dicke state (although it can still be used for calculations) [158].

Suppose that we set the position of one layer in the axis of cavity quantization equal to zero, $z = 0$. Also, $\vec{k}\vec{r} = k_x x + k_z z$ Since the electromagnetic field strength, and hence g does not greatly vary in z-direction across one layer $k_z z$ is identical for each and every nucleus in that layer, while it is zero in the other layer. Therefore, the excitation and deexcitation operators in the former layer have an additional phase factor $e^{ik_z z}$ in front of them, which we ignore in the following. The Hamiltonian can now be written

$$\begin{aligned} H = (\Omega_1 S_+^{(1)} + h.c.) + (\Omega_2 S_+^{(2)} + h.c.) + (\delta_1 - \Delta) S_+^{(1)} S_-^{(1)} + (\delta_2 - \Delta) S_+^{(2)} S_-^{(2)} + \\ \delta_{1,2} S_+^{(1)} S_-^{(2)} + h.c. \end{aligned} \tag{107}$$

where

$$\Omega_l = \sum_j \Omega^{[j]} g_l^{[j]} \sqrt{N_l} \tag{108}$$

$$\delta_l = \sum_j \delta_{LS}^{[j]} g_l^{2[j]} N_l \tag{109}$$

$$\delta_{1,2} = \sum_j \delta_{LS}^{[j]} g_1^{[j]} g_2^{[j]*} \sqrt{N_1 N_2} \tag{110}$$

where the l mark the different layers; they have potentially a different coupling strength, which is why we assign to each a single exciton operator set. For the Lindblad operator we write equally

$$\begin{aligned} \mathcal{L} = &-(\frac{\gamma}{2} + \gamma_1)\mathcal{L}[\rho, |E_+^{(1)}\rangle \langle G|, |G\rangle \langle E_+^{(1)}|] \\ &-(\frac{\gamma}{2} + \gamma_2)\mathcal{L}[\rho, |E_+^{(2)}\rangle \langle G|, |G\rangle \langle E_+^{(2)}|] \\ &(\frac{\gamma}{2} - \gamma_{1,2})\mathcal{L}[\rho, |E_+^{(1)}\rangle \langle G|, |G\rangle \langle E_+^{(2)}|] \\ &(\frac{\gamma}{2} - \gamma_{1,2})\mathcal{L}[\rho, |E_+^{(2)}\rangle \langle G|, |G\rangle \langle E_+^{(1)}|] \end{aligned} \tag{111}$$

where

$$\gamma_l = \sum_j \xi g_l^{[2j]} N_l \tag{112}$$

$$\gamma_{1,2} = \sum_j \xi g_1^{[j]} g_2^{[j]*} \sqrt{N_1 N_2}. \tag{113}$$

To calculate the reflectivity, the equations of motion ρ_{1G} and ρ_{2G} for the coherences are derived from the Master equation, with the result

$$\frac{d}{dt}\rho_{1G} = i[(\Delta - \delta_1) - \gamma_1 - \gamma/2]\rho_{1G} - i\Omega_1 - (i\delta_{(1,2)} + \gamma_{(1,2)})\rho_{2G} \tag{114}$$

$$\frac{d}{dt}\rho_{2G} = i[(\Delta - \delta_2) - \gamma_2 - \gamma/2]\rho_{2G} - i\Omega_2 - (i\delta^*_{(1,2)} + \gamma^*_{(1,2)})\rho_{1G} \tag{115}$$

Setting the derivatives on the left-hand side to zero for the steady-state solution, we obtain

$$\rho_{1G} = \frac{\Delta_2\Omega_1 - (-\delta_{(1,2)} + i\gamma_{(1,2)})\Omega_2}{\Delta_1\Delta_2 - \Omega_C^2} \tag{116}$$

$$\rho_{2G} = \frac{\Delta_1\Omega_2 - (-\delta^*_{(1,2)} + i\gamma^*_{(1,2)})\Omega_1}{\Delta_1\Delta_2 - \Omega_C^2} \tag{117}$$

$$\tag{118}$$

where we have set

$$\Delta_l = \Delta - \delta_l + i(\frac{\gamma}{2} + \gamma_l) \tag{119}$$

$$\Omega_C^2 = (\delta_{1,2} - i\gamma_{1,2})(\delta^*_{1,2} - i\gamma^*_{1,2}) \tag{120}$$

We observe that the above equations (118) have the form of the refractive index of an electromagnetically induced transparency medium, with Ω_C taking on the role of the coupling field strength. The reflectivity of the system, much as for the one-layer case has the form

$$R = -1 + \frac{2\kappa_R}{\kappa + i\Delta_C} - \frac{i}{a_{in}} \frac{\sqrt{2\kappa_R}}{\kappa + i\Delta_C} g_1^* \sqrt{N}\rho_{1G} + -\frac{i}{a_{in}} \frac{\sqrt{2\kappa_R}}{\kappa + i\Delta_C} g_2^* \sqrt{N}\rho_{2G}. \tag{121}$$

Naturally, the layers couple to all allowed modes of the cavity, albeit with different strengths. The parameters of the effective Hamiltonian need to be adjusted of course; but this amounts to taking, for the parameters of each layer, the sum over all the modes contributing to each parameter. The collective Lamb shift of each ensemble is then the sum of the collective Lamb shifts induced by each mode; the superradiant decay time is the sum of the superradiant decay times induced by each individual mode etc. Let us briefly discuss this. Naturally ξ_S and δ_{LS} have same functional dependency for every cavity mode, but are angularly or energetically displaced from each other, since their maxima are situated at zero detuning of the effective mode. Close to or at the cavity mode zero detuning position, the effective interaction is strongest, because ξ_S and δ_{LS} are at or close to their respective maximum. This is a good reason to make the assumption that we can confine ourselves to one cavity mode only, namely the one which we are investigating by our reflectivity experiment. The contributions of all other cavities to the Lamb shift and to the superradiance should be negligible, on account of them being far detuned. But this would be a mistake. While these physical effects functionally depend on ξ_S and δ_{LS} their actual magnitude, as can be seen from Eq. (**??**) is also dependent of the collective coupling strength $g\sqrt{N}$. The coupling strength itself is a function of the electromagnetic field strength at the position of the resonant layer. This can give rise to a situation that is sketched in Fig. 17.

Two layers are coupled to two modes each. But the first layer is strongly coupled to the first mode, and extremely weakly coupled to the second one, while the second layer is strongly coupled to the second mode and weakly to the first one. (We use 'strongly coupled' here in the sense that the coupling constant is relatively high, not in the usual sense described in previous sections). If we drive the first mode by the exterior classical electromagnetic field and monitor its reflectivity, we will observe the spectral signatures of the two layers. The first one will display a collective Lamb shift and a superradiance that is due to its interaction with the first mode. The second layer however does not couple to first mode in any meaningful way. But it couples with a high coupling constant to the second mode. It may happen that this coupling is so strong that its effects dominate over the coupling to the first, driven mode, even though the second mode is detuned by a large amount. In that case both layers will show spectral signatures of vacuum coupling, although only one of them is coupled significantly to the interrogated cavity. More importantly,

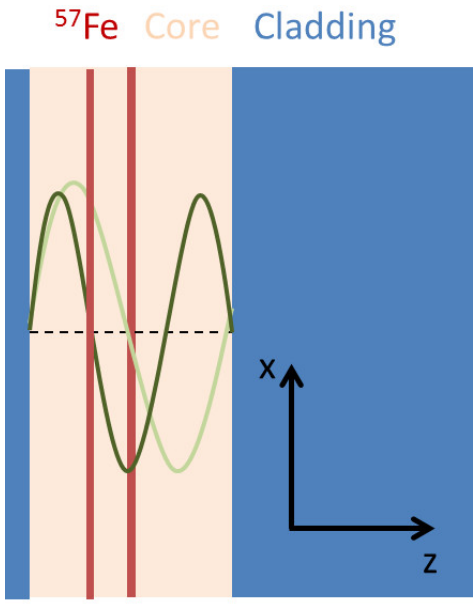

Figure 17: *Sketch of two layers inside of a cavity interacting with two modes. Shown are the second and third modes of a thin-film cavity; in reality, the first and possibly further higher-order modes also contribute. The second mode (light green) is coupled to the first layer near one of its antinodes, the field strength is high and the coupling therefore significant. The second layer is located in its node, with a field strength of almost zero, and consequently almost no coupling. For the third mode (dark green) the situation is reversed. Depending on the mode that is driven by the external field, one layer interacts chiefly with the pumped mode, while the other interacts mostly with a far-detuned mode.*

the terms $\delta^{[1,2]}$ and $\xi^{[1,2]}$ become somewhat larger, i.e. the cross-coupling between the layers is enhanced, since it takes place over multiple modes. Even more importantly the product of them in Eq. (120) is now the product of two sums

$$\Omega_C^2 = N(\sum_j \frac{g_1^{[j]} g_2^{[j]*}}{\Delta_C^{[j]} - i\kappa^{[j]}})(\sum_j \frac{g_1^{[j]*} g_2^{[j]}}{\Delta_C^{[j]} - i\kappa^{[j]}}) \tag{122}$$

In the extreme case where the coupling of the first layer to the second mode would be zero and vice versa, Eq. (122) ensures that Ω_C^2 remains non-zero, which is equivalent to an effective strong coupling field being applied between the two layers, i.e. a situation where the EIT-condition is fulfilled. If there were only one mode to which both layers would couple, and the coupling of one of the layers were very small, Ω_C would also vanish. This however is not the main reason why the model without multiple modes would fail to predict the EIT signature in a multi-resonant layer cavity. The main reason is that in this case, one of the normal modes that form is a dark state, which cannot be excited by the driving field, as shown in several works dealing with similar

or equivalent systems [159, 158]. The presence of an additional mode modifying the system results in the breakdown of that dark state, which suddenly can be excited by the external field; hence the presence of the dip in the spectrum. Another way to look at it is this: the second layer couples strongly to a higher-order mode. At the angle which resonantly drives the first mode, the higher-order mode is also driven, albeit far-detuned. We then deal with an eigenstate of the coupled system which is far detuned from the anti-crossing with the higher-order cavity mode. This means that it is matter-like, spectrally narrow and close to the nuclear resonance, which fits with the behaviour of the EIT-dip.

IV.3.7. Strong coupling and Rabi oscillations in the effective Hamiltonian of a two-layer system

The following section is slightly amended from [60]. When dealing with small excitation numbers it is permissible to ignore the third terms of the individual Lindblad operators in Eq. (93). It is well known that the remainder can be absorbed into a Hamiltonian such that the equations of motion are given by $d\rho/dt = \mathcal{H}\rho - \rho\mathcal{H}^\dagger$ [160]. This effective Hamiltonian can be diagonalized to find the eigenvalues of the system [138]. We give it here:

$$\mathcal{H} = \begin{pmatrix} 0 & \Omega_1 & \Omega_2 \\ \Omega_1^* & \Delta - \delta_1 - i(\frac{\gamma}{2} + \gamma_1) & \delta_{(1,2)} - i\gamma_{(1,2)} \\ \Omega_2^* & \delta^*_{(1,2)} - i\gamma^*_{(1,2)} & \Delta - \delta_2 - i(\frac{\gamma}{2} + \gamma_2) \end{pmatrix} \tag{123}$$

One can take this Hamiltonian to describe as system where two atoms with different decay times and slightly different energy levels interact with each other via a dipole-dipole-like interaction, and are each simultaneously driven by a classical field. This system is relatively simple in principle. However, the interactions are highly untrivial, and strongly vary depending on the detuning from the cavity, i.e. the angle, as given in Eq. (**??**). In Fig. 18 we plot the basic dependences of the Lamb shift and superradiant enhancement terms. It can be seen that the former decay far slower than the latter. This will turn out to be convenient later.

We point out a couple of interesting facts concerning the effective Hamiltonian. First of all, it is not Hermitian. Secondly, the detuning changes more than just the magnitudes of the matrix elements. For example, at zero detuning all off-resonant matrix elements are overwhelmingly imaginary, as can be immediately seen by inserting $\Delta_C^{[j]} = 0$ into Ω_i and $\delta^{[1,2]}$; Only tiny contributions from the far detuned modes contribute significantly to the driving and interaction terms. But most interesting is the situation when all modes are far detuned from the nuclear resonances, i.e. when we drive the cavity far detuned from all its modes. In that case, $\Delta_C \gg \kappa$ and the Ω

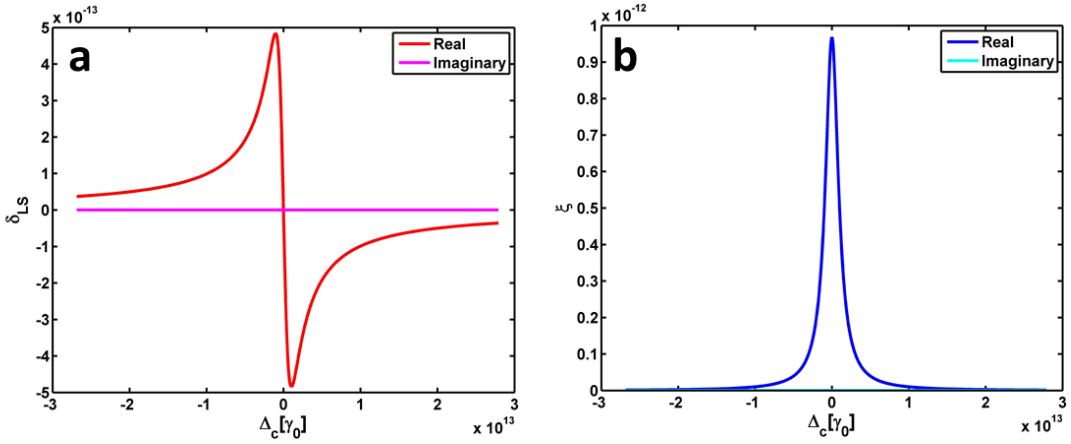

Figure 18: *The real and imaginary parts of (a) δ_{LS} and (b) ξ obtained from the quantum optical model of two layers coupled to multiple cavity modes. The coupling strengths are rather arbitrary; the main thing to look out for are the different functional behaviours when the cavity is detuned from the resonances - the real part decays much slower than the imaginary part. Both values depend only on the detuning from the cavity mode and the (constant) spectral cavity width κ. In this case, $\kappa = 1.45 \times 10^{12}\gamma_0$, where γ_0 is the spectral width of ^{57}Fe. Interestingly, the dispersion is clearly similar to that of resonant matter. The units are given in Hz. Multiplied with the coupling strenghts, they yield Lamb shifts and superradiant decay linewidths.*

driving terms become overwhelmingly real. Similarly, δ_{LS}, which decays with $\frac{1}{\Delta_C^{[j]}}$ will turn out to be far larger than ξ_S which decays with $\frac{1}{\Delta_C^{[j]2}}$. This means that $\delta^{[1,2]}$ will be far larger than $\xi^{[1,2]}$, meaning that the latter, which are imaginary in the dipole-dipole like coupling transfer matrix element between the two ensembles can be assumed to be zero. In that case, the Hamiltonian reverts to being (to first approximation) a Hermitian Hamiltonian describing two coupled states probed from a third level. Similar systems have been explored in a number of theoretical and experimental papers on quantum optics, for instance [159]; it is often referred to as the dispersive cavity limit and is used to manipulate the interaction between two or more resonant two-level systems via virtual interactions. In our particular case it offers a particularly tantalizing option, namely to realize strong coupling between the two layers. To see this, refer again to Fig. 18. It only shows what we have described before: ξ decays far faster than δ_{LS} when the cavity is detuned. Since ξ determines the speed of decay of the excitation of the corresponding layer, and δ_{LS} the interaction between the layers and their collective Lamb shift, this offers the opportunity for the interaction strength to outpace the decay strength of both levels, in other words, to realize $g \gg \gamma_1 \gg \gamma_2$, or to couple the two ensembles strongly. Some care is needed here in order to not confuse strong coupling and the collective Lamb shift. For the moment, we ignore the driving

terms in the effective Hamiltonian, and merely diagonalize the interaction between the two layers. In that case the eigenenergies will be (assuming that the detunings of the cavity mode from the resonance are far larger than the collective Lamb shifts)

$$E_{\pm} = \Delta_c \pm \sqrt{(\delta^{[1]} - \delta^{[2]})^2 + (\Omega_c)^2} \tag{124}$$

From comparing this with the eigenenergies for strong coupling, it is immediately clear that the splitting is given by the term $2\sqrt{(\delta^{[1]} - \delta^{[2]})^2 + (\Omega_C)^2}$, so the term can be interpreted as twice the Rabi frequency. We will refer to it by $2\Omega_R$. It can be seen that it depends both on the direct interaction and on the detuning by the collective Lamb shifts. If the latter term dominates, the Rabi oscillations will not result in the full population of the excitation of one ensemble of atoms being exchanged with the other. We will refer to $\delta^{[1]} - \delta^{[2]}$ as Δ. Now the analogy to the simple Jaynes-Cummings model can be clearly seen; the cavity vacuum induced interaction Ω_c plays the role of the interaction strength of field and atom; the difference of the collective Lamb shifts Δ plays the role of the detuning of the electromagnetic mode from the atomic transition frequency. The two ensembles exchange a photon analogously to the Rabi oscillations.

Chapter V

X-ray quantum optics in thin-film cavities

V.1. Introduction

In this chapter, we will describe some experiments we have performed with the interaction of x-rays with resonant ensembles in thin-film cavities. Before we begin, we briefly comment on the difference between electronic and nuclear resonances. In the previous sections, we have largely used the terms atoms and nuclei interchangeably. And indeed, when we restrict ourselves to the use of one level, the theoretical descriptions of the x-ray - matter interaction is wholly identical. There is no reason to think of nuclear and electronic transitions as completely different phenomena; both of them are simply two-level systems with an energy in the x-ray range. It is one of the aims of this thesis to prove this point, and therefore we start with an experiment on electronic resonances. This has the added benefit that its setup corresponds to the most simple theoretical description, that of one ensemble interacting with one field mode.

Of course, there are massive practical differences between electronic and nuclear resonances from an experimental perspective, all stemming from the fact that they have natural lifetimes that differ by $9-10$ orders of magnitude. This means that the decay of nuclear excitations can be observed in the temporal domain, but not that of electronic resonances. On the other hand, the latter do not require complicated monochromatization schemes; a simple high-heat load monochromator suffices to reduce the bandwidth of the incoming beam. Furthermore, nuclear resonances are not necessarily of the same type. Electric and magnetic dipoles and electric quadrupoles all react differently to the application of external electric and magnetic fields; this offers ways to manipulate

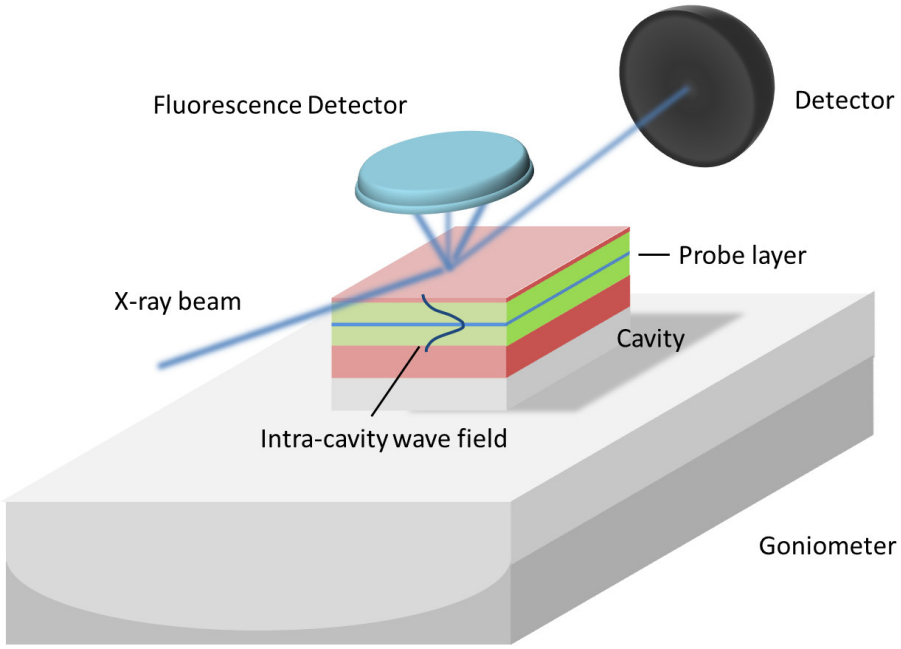

Figure 19: *Experimental setup for measuring the spectroscopic features of a resonant electronic layer embedded in a thin film multilayer cavity. The cavity is illuminated at grazing incidence. Both angle and energy of the incoming beam is varied. The reflectivity is recorded. Additionally, a detector is positioned above the sample to measure the fluorescence in a solid angle above the cavity.*

the light-matter interaction for instance in magnetic dipoles [56] that is not available for electric dipoles.

In later sections we will observe the coherent exchange of virtual photons between multiple layers in several different setups, and introduce a kind of cavity setup hitherto not used in the x-ray regime.

V.2. Cavity QED with electronic resonances

In this section, the electronic resonance which we will excite is the L_{III}-edge white line of Tantalum. It has an energy of 9881 eV, with a linewidth of approximately 5 eV. A more thorough description of the background is given in Chapter II.5, see also Fig. 4

V.2.1. Experiment

The experiment was performed at the P09 endstation of PETRA III in Hamburg. The experimental setup is shown in Fig. 19. The multilayer cavity is positioned in a typical reflection geometry. The angle is varied by steps, and for every angle the monochromator is scanned to take a reflectivity spectrum. Furthermore, we have installed a fluorescence detector above the cavity, which measures all fluorescence photons detected in a solid angle. It also has the capability to perform a (very rough) energy binning. Naturally, the photons also include photons from other processes than the resonant excitation and decay in the probe layer, so we have fluorescent photons across a whole range of energies. In order to distinguish the resonant processes that interest us from others, we have taken two energy spectra, one at the resonant energy of Tantalum, and one significantly below it. In a certain energy range of the fluorescence detector, corresponding to the resonant energy, this resulted in a marked drop of intensity between the two spectra. This region was marked as the region of interest; the photons within this region were summed up for every monochromator and angular position to yield resonant fluorescence spectra. This is the equivalent to time-gating the diode for the prompt and measuring only the delayed signal for nuclei, which is of course not an option here due to the extremely short decay time of the electronic exciton. The aim of this experiment was to test whether quantum optics with electronic resonances is a viable path at all. To protect the APD from damage we included several absorbers in the beam. Typically, absorbers placed into the beam before it illuminated the sample were chosen such that they decreased the intensity by about two orders of magnitude. We placed another layer of absorbers (700 μm) of Aluminum between sample and APD. The aim of this was to protect the APD but also to ensure that the beam intensity was high enough to produce a significant fluorescence signal. The beam was also slightly focused by 20 Beryllium lenses so that most photons actually illuminated the sample, rather than passing by it due to the small angles of coincidence. This also increased the total intensity on the sample, helping to achieve briefer measurement times and a satisfying fluorescence signal. This came at the price of a slight increase of divergence; however we have taken reflectivity curves both with and without the lenses in the beam. There is a difference in intensity of the signal, but no serious change in the shape of the reflectivity curve.

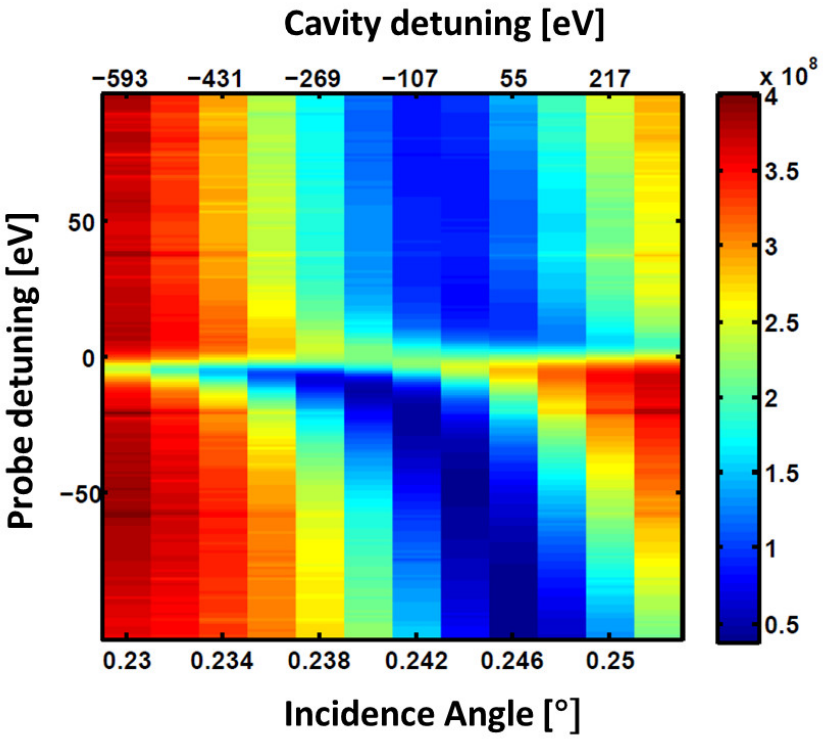

Figure 20: *Resonant reflected intensity of the cavity across a range of angles. An anticrossing-like behaviour is observable, but the preconditions for genuine strong coupling are not met. The lower x-axis gives the angle of the incident beam; on the upper x-axis we have indicated the corresponding energetic detuning from the cavity center in electron Volts. The reflected intensity is given in photons counted per second. The zero point of the y-axis is located at* 9881 *eV, the literature value for the Ta* L_{III} *white line. Individual spectra are shown along with quantum optical fits in Fig. 24*

V.2.2. Results

Tantalum

In Fig. 20 we present the reflectivity data for a cavity containing a resonant Tantalum layer, which displays a L_{III} electric dipole resonance at 9881 eV with a linewidth of about 5 eV.

The spectra were taken at different angles around the first guided mode. We fixed the angle and scanned the energy via the monochromator of beamline P09 from 9800 to 10000 eV. The dimensions of the cavity were Pt 20 Å/ C 110 Å/ Ta 25 Å/ C 123 Å/Pt 152 as extracted from the fit in Fig. 21 fabricated on a polished silicon substrate of $15 \times 20 \times 0.5$ mm. The formation of two branches is visible in the reflectivity; obviously some sort of normal-mode splitting takes

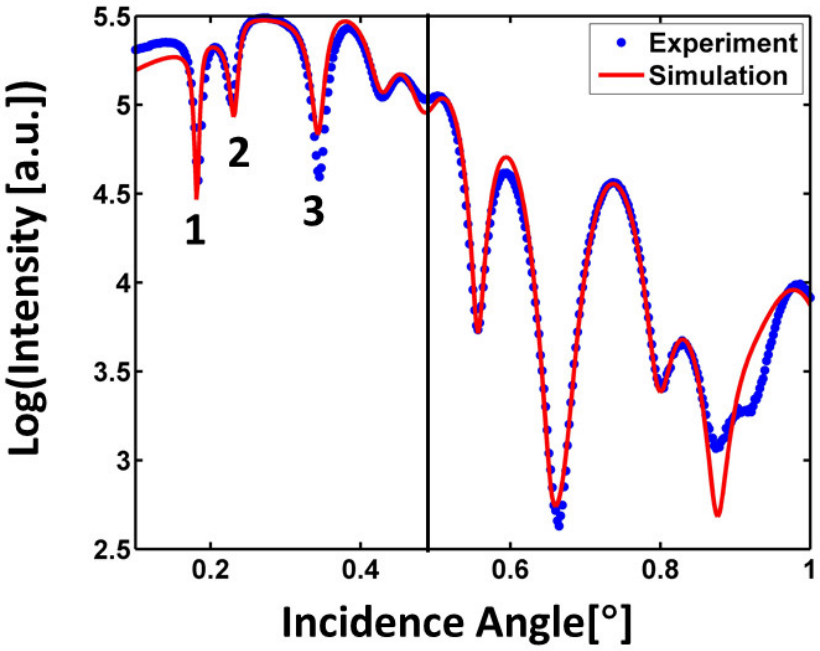

Figure 21: *Reflectivity curve of a thin film multilayer cavity and fit (red solid line) via the Parratt algorithm. The cavity dimensions according to the fit are Pt 14.5 Å/ C 243 Å/ Ta 19 Å/ C 240 Å/Pt 112 Å. The first few modes are indicated by numbers. The solid black line indicates the critical angle. Small deviations of the fit from the data at low angles are due to the divergence of the incoming focused beam, which is not treated in the Parratt algorithm.*

place. To judge whether this corresponds to genuine strong coupling or is merely an interference effect, we will turn to the theoretical description of the physics behind the observations. For completeness, we begin with the reflectivity curve as calculated by the Parratt algorithm fitting program GenX [110], shown in Fig. 21.

Cavity dimensions, layer material densities and roughnesses as well as the beam width were fitted. The cavity dimensions and properties obtained by the fit are listed in Tab. V.1 Most of the values obtained by the fit seem credible enough. The layer thicknesses are very close to the design parameters, and the material densities close to the literature values, with the exception of Tantalum, which is a littler higher, but not disturbingly so. The roughness values are getting higher as we move from bottom to topmost layer - this is expected and physically intuitive, since small imperfections of a surface on which a layer is sputter deposited amplify the roughness of that layer. It is slightly worrying that the roughness of the top layer ends up to be so high, but it turns out that this is not particularly significant; small changes of the roughness do not

	Platinum	Carbon	Tantalum	Carbon	Platinum
Thickness [nm]	2.0	11.0	2.5	12.3	15.4
Density [g/cm^3]	22	2.33	17.98	2.25	21.61
Roughness rms [nm]	1.4	1.1	0.8	0.8	0.04

Table V.1: *Properties of the Tantalum thin film cavity extracted from the Parratt algorithm fit. Any errors would not be reliable, since the simulations delivers good results in a range of values around the given ones; however, we estimate that any deviations are not above* 0.5 *nm; The densities and the roughness have similar ranges relative to the given value.*

worsen the fit quality noticeably. To calculate the resonant reflecivity, the numerical values of the non-resonant index of refraction were taken from the X-Ray database of the center for x-ray optics CXRO [64] taking into account the results for the material densities obtained from the fit. To model the resonant refractive index contribution of the Tantalum white line we added real and imaginary parts of a Lorentzian centered at 9881 eV with a level width of 5 eV to the CXRO data. The strength of the Lorentzian was roughly adjusted such that the relation between the height of the white line and the background index step function corresponded approximately to measured data. As can be seen in Fig. 22, this procedure produces satisfying but not completely perfect results.

The position of the center of the cavity and the dispersion is adequately retrieved, but the relative intensities are not predicted perfectly by this method. Often, this results from beam divergence, which leads to a beam illuminating the sample at several incident angles at the same time. But we have already ascertained that this cannot be the case in this experiment, as the reflectivity was found to not change appreciably around the electronic resonance. A possible reason explaining this phenomenon is the inhomogeneity of the sample. Due to imperfections in the sputtering process, the edges of the sample have measurably diminished thin film thicknesses compared with the center. Since the thicknesses are among the dominant factors in determining the angular positions of the modes, this means that the cavity has different modes at its center and its edges. This effectively mimics the properties of divergence. Photons of a particular energy that would couple into the cavity at the center are reflected when they impinge on the cavity edges and vice versa. The result is a reflectivity curve different from the pure theory. Another likely issue is the modeling of the resonance. The CXRO database does not include the effects of white lines, so these had to be included heuristically. At the exact L_{III}-edge, there is a complicated interplay between the properties due to the onset of the continuum and the white line, which

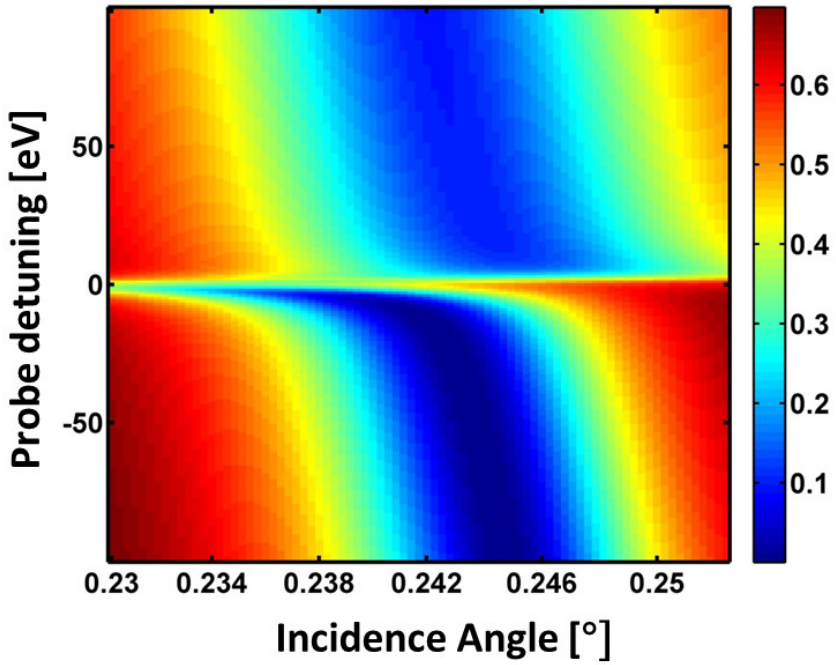

Figure 22: *Simulation of the resonant reflectivity of a Pt 20 Å/ C 110 Å/ Ta 25 Å/ C 123 Å/Pt 152 Åsample by the Parratt transfer matrix algorithm. The graph shows a good qualitative agreement with the measured data in Fig. 20. Any discrepancies, such as the slight differences in dispersion and reflectivity are probably due to sample inhomogeneity and an insufficiently accurate modeling of the index of refraction close to the white line.*

we have only treated cursorily. Nevertheless, the basic features of the reflectivity are observable in the simulation in Fig. 22, which demonstrates that the Parratt algorithm is a good device to theoretically examine and select other resonant systems for future use in hard x-ray cavity QED. We now examine the experimental results by means of the quantum optical model. The phyiscal situation permits treatment of the system by much the same means as those used for modeling cavities containing Mössbauer cavities. Accordingly, we employ Eq. (94) to simulate the reflectivity. This approach permits identification of the intermediate coupling regime, but it suffers from a few drawbacks:

(a) it models the system as a collective interaction between a cavity and an ensemble with one resonant level. The more complicated physical situation, which includes the background index of refraction step indicating the continuum of free electrons is, avoided. This does not really change the interaction of the white line and the cavity resonance, but it adds additional absorption and

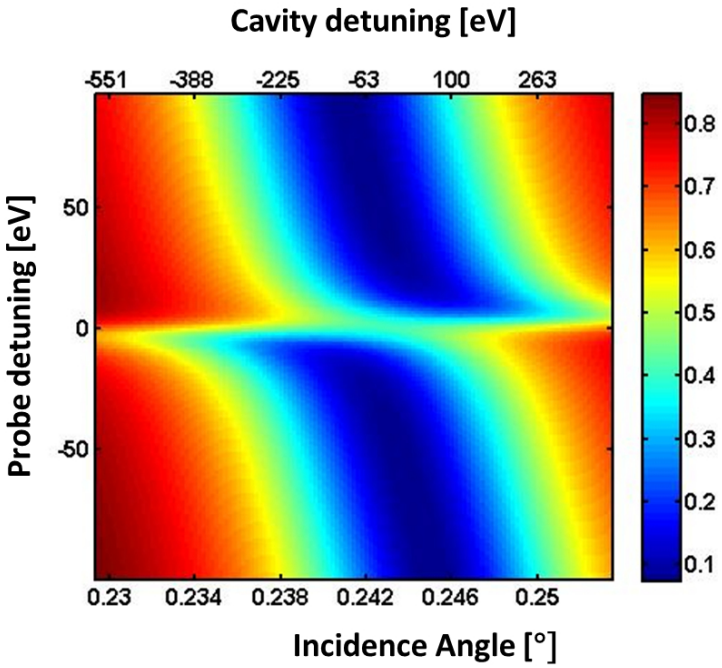

Figure 23: *Reflectivity of the cavity according to the quantum optical model. The features of the measured data are distinctly recognizable, with a few exceptions. One is the fact that both dips are equally deep in this simulation, reflecting the fact that the influence of the continuum of states is unaccounted for.*

refraction to light traversing the thin film cavity, which changes the cavity properties. Effectively, the cavity is perturbed by the Tantalum layer. Of course, this approach will not be able to identify and explain differences between the higher-energy and lower-energy branches dispersion relation that were observed in the experimental data.

(b) The reflectivity slightly diminishes at higher angles even when they are below the critical angle. This could be circumvented by multiplying the reflectivity with an envelope function that consists of the reflectivity of a slab of the top cladding material. However this heuristic change does not really add any physical understanding, so we will omit it and accept that the model will not be able to give a quantitative fit to the data.

(c) Of course, as for the Parratt algorithm, the inhomogeneity of the sample is not taken into account. This means that there is a distribution of detunings and cavity interactions, as the cavity has different widths at different positions. A fit would give a kind of median value across the whole cavity.

With this in mind, it is clear that the resulting parameters for the cavity decay, coupling strength etc. are merely educated guesses, but cannot make any claim to great precision. We therefore

	κ	κ_r	γ	$\sqrt{N}$g
Strength [eV]	297	103	5	37

Table V.2: *Parameters of the simulation of the quantum optical model. κ is the cavity linewidth, γ the Tantalum resonance linewidth, $\sqrt{N}g$ the collective coupling strength and κ_r the driving strength.*

omit to make a complete fit, and focus on a rough simulation; the superfically enhanced precision such a procedure might yield would not carry the validity necessary to merit the effort. Luckily, deviations between theory and experiment are mostly of quantitative nature; the fundamental physics is still described very well by our simple models, as will be shown in the corresponding figures. The reflectivity according to the quantum optical simulation is shown in Fig. 23. At first glance, this looks like a highly satisfying simulation. We give the cavity and matter parameters we have used to obtain it in Tab. V.2. We point out that the coupling strength is much larger than the linewidth of the Tantalum L_{III} white line, and less than an order of magnitude smaller than the linewidth of the cavity. This means that the intermediate coupling regime is definitely reached; the strong coupling regime has been missed by a wide margin, but it is not inconceivable that in future experiments it can be surpassed, especially with some improvements which we will discuss in the conclusion to this section.

Here, we resume with a more detailed discussion of the experimental results. It is clear that in the intermediate coupling regime the Fano resonances and the dispersion that were observed in [57] for the case of resonant ^{57}Fe-nuclei in a cavity has been replicated for the case of an electronic resonance in the hard x-ray energy range. To further support this point, we show some individual spectra in Fig. 24, which clearly give a very good qualitative description of the data. A serious quantitative description would, as mentioned, involve treatment of the continuum background, which is beyond the scope of this thesis. Finally, let us discuss the results of the fluorescence collective Lamb shift measurements. As shown in Fig. 25, we have observed a fluorescent line which follows the characteristic CLS dispersion around the cavity mode.

But here, too, the continuum disturbs the image, since it emits a lot of fluorescence itself, which partially obscures the Lorentzian. Nevertheless, we use the parameters of the quantum optical model to calculate the Lamb shift, as prescribed in [54] by Eq. (96). The result is displayed in Fig. 26.

It clearly reproduces the result in Fig. 25, bar the continuum fluorescence. We show additional details in Fig. 27, where we have fitted the spectra at two angles with a simple Lorentzian each, obtaining Lamb shifts of up to 3eV, with a superradiantly enhanced spectral width of $\approx$ 10 eV.

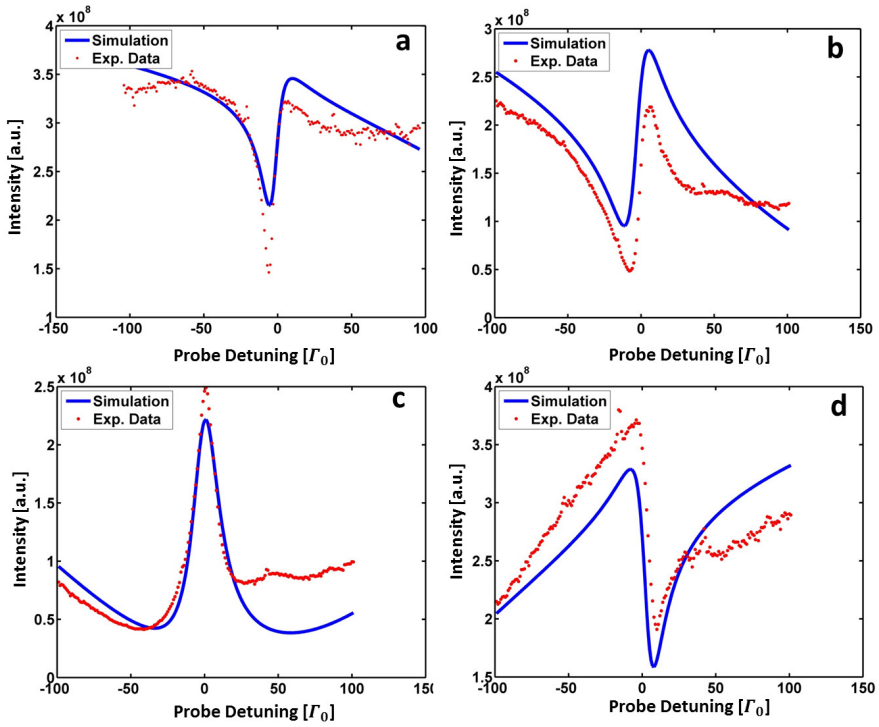

Figure 24: *Comparison of the reflectivity as simulated by the quantum optical model and the experimental data. All theoretical curves were calculated by using the same set of parameters and multiplying it by the same prefactor in order to normalize them. There is no quantitative, but qualitative agreement. The main discrepancies are at higher energies, where we have omitted to include the electronic continuum which spoils the cavity. The shown data and simulations are line cuts from Figs. 22 and 23.*

V.2.3. Discussion

We have performed what is to the best of our knowledge the first experiments in hard x-ray cavity quantum electrodynamics with electronic resonances. Some of the results are very promising. By using an ensemble of Tantalum atoms that collectively interacts with a cavity mode via its L_{III} white line excitonic resonance, we have unambiguously shown via a quantum optical model that the collective intermediate coupling regime has been reached. This extends the range of available systems for hard x-ray quantum optics, and suggests new avenues for experimentalists in the field. The experiment also shows that transfer matrix algorithms based on classical optical models are a valid way to test and preselect excitonic resonances in the hard x-ray regime for their suitability in cavity QED. On the other hand, in a second experiment involving the 11215 eV resonance of Iridium, we have shown that not necessarily all white lines are appropriate for this purpose. This

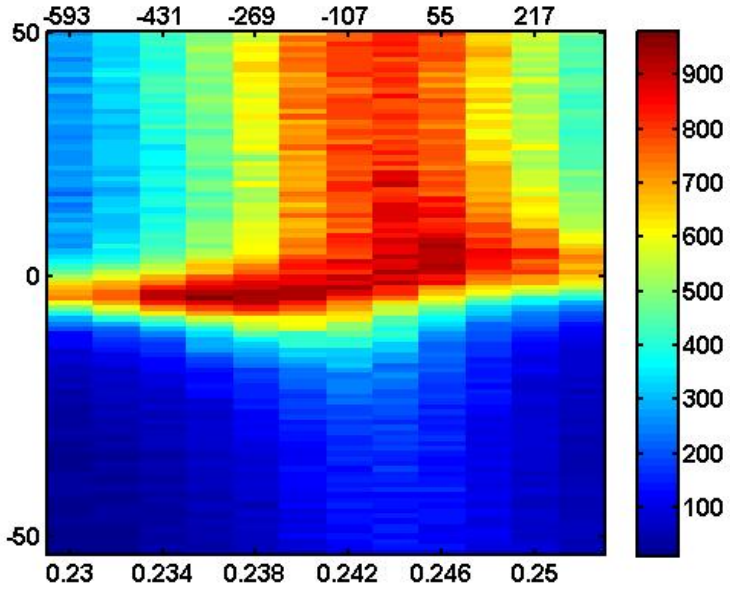

Figure 25: *Measured Ta fluorescence of a cavity containing a Ta layer. The y-axis shows the energy of the incident radiation, the lower x-axis shows the angle of the incident radiation, and the upper x-axis shows the energetic detuning of the cavity from the white line. The fluorescence is composed of two parts: a Lorentzian-like with a slight dispersion around 9881 eV that depends on the detuning, and a more or less flat one above 9881 eV which more or less follows the cavity dispersion. The latter is from the recombination of electrons that got excited into the electronic continuum, the former is the due to the interaction of the x-rays with the two-level system that corresponds to the white line.*

is shown in Appendix B. The white line needs to be high relative to the background absorption for the coupling to be well-resolved. It is also not entirely clear whether some of the white lines exist only in bulk or whether interface effects may perturb them strongly.

We will highlight several promising possibilities in differing detail, and discuss the challenges that they pose. To begin with, the salient limitation of x-ray cavity QED with Mössbauer resonances is the extremely low spectral density of the synchrotron sources these experiments are performed with. This ensures that at most one resonant photon is present in a single synchrotron pulse, since the resonance has a linewidth of 4.7 neV. Electronic resonances, however, have linewidths of several eV, allowing the possibility of multiple photons of that energy per pulse. If the cavity-ensemble interaction can be manipulated suitably, this might open the door to the observation of nonlinear hard x-ray optics in thin film nanostructures.

The second argument goes along similar lines. In previous work [55], the slow propagation of

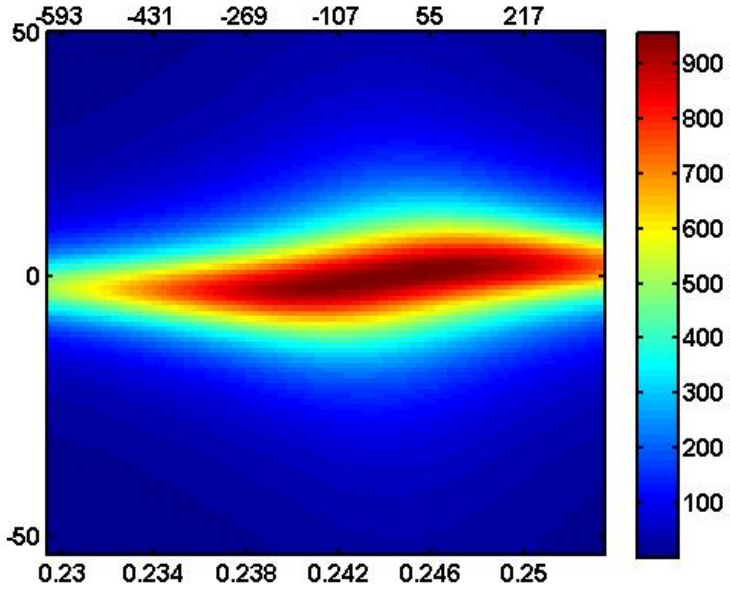

Figure 26: *Simulation of the fluorescence of a cavity containing a tantalum layer. Around the position of zero detuning of the cavity, the fluorescence shows the characteristic properties of the Lamb shift, i.e. a dispersion which depends on the detuning from the cavity and vanishes at exact cavity resonance. The y-axis shows the energetic detuning of the monochromator, the lower x-axis the angle of incidence of the incoming radiation and the upper x-axis shows the corresponding detuning of the cavity resonance from the Tantalum white line energy. It is obvious that the dispersion is very similar to the measured data, save for the absence of the scattering due to the electronic continuum. The parameters $\sqrt{N}g$,γ and κ are the same as for the simulation of the reflectivity.*

x-rays in thin-film nanostructures with ^{57}Fe-nuclei has been observed. Due to the differing spectral widths of the pulse (1 meV) and the resonant nuclei (4.7 neV) only a small part of the incident light was delayed, which could be observed in the time domain. While the coupling regime in our case is identical, the relevant energy widths are different. Our incident pulse has a wider bandwidth (1 eV), but so has the resonant system (5 eV). It follows that the entire incident pulse can be delayed upon reflection. However, the delays are tiny (on the order of 10^{-16} s), which is beyond any current means of detection. It is still interesting however, that such minimal delays could be engineered by performing relatively rough changes in the experimental setup like changing the angle or tuning the energy.

Other thin-film structure designs could also be adapted for electronic x-ray quantum optics, such as the resonant distributed Bragg reflectors (DBR) discussed in Chapter VI.3; equally DBR defect

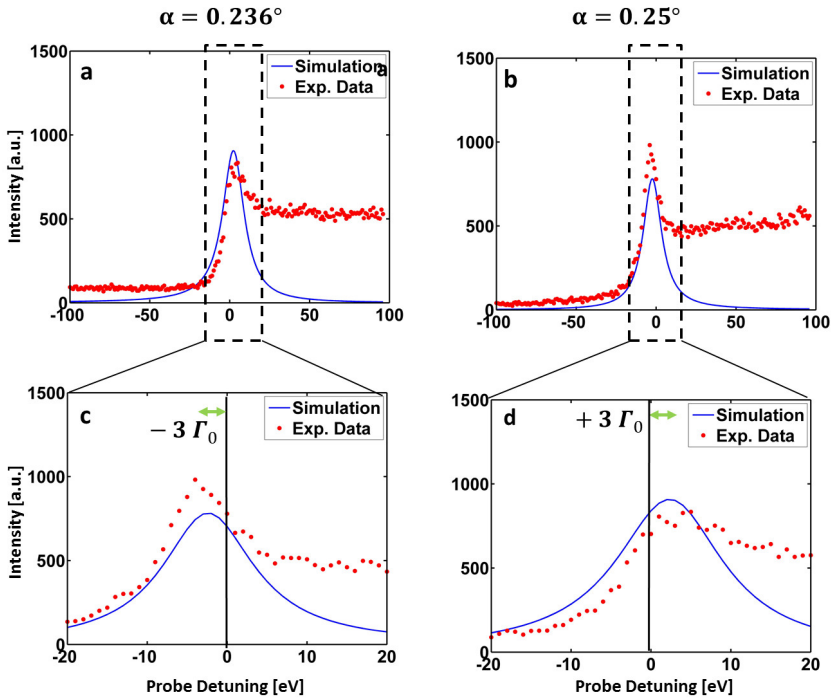

Figure 27: *The collective Lamb shift of Tantalum embedded in a thin-film cavity. In (a) and (b), the fluorescence spectra of the system at two different angles are shown. The angles correspond to equidistant positive and negative detunings from the cavity mode. Red shows the experimental data, blue shows a simulation consisting of a Lorentzian. The electronic continuum which manifests itself in the step function is not taken into account. The spectra clearly show that the Tantalum resonance is shifted in opposite directions by about 3 eV, which is particularly obvious in (c) and (d) which show enhanced details of (a) and (b).*

cavity modes could be used. The latter have the distinct advantage that their modes can have an angular acceptance that is above the incident angle; in this range it may be possible to have a comparatively large angular acceptance but a low corresponding spectral linewidth of the cavity. It should also be possible to introduce several layers of resonant material into the cavity mode, or thicker layers, in order to enhance the collective coupling strength.

Finally, a different choice of resonant materials might advance the field. The *K*-edges of several more complex materials, such as the chromates [161], ferrates and some manganates and titanates [88] show extremely sharp pre-edge peaks which are well resolved from the continuum absorption.

V.3. Rabi Oscillations by strong coupling of two nuclear resonant layers

V.3.1. Introduction

The experiment discussed in this section is in many ways a variation of a previous experiment by Röhlsberger *et al*, which was theoretically described in Chapter IV.3.6. In that experiment, electromagnetically induced transparency was observed in a cavity containing two resonant ^{57}Fe-layers, one of which was positioned in an antinode, the other of which was positioned in the node of the 3rd mode. The experiment has since been repeated and discussed in several different systems [162, 163, 164]. One important observation could not be explained, however. Simulations showed that the appearance of the EIT effect depended on the relative positioning of the two layers with respect to each other. If the layer in the antinode (strongly coupled to the cavity mode) was uppermost, simulations indicated that EIT could not be observed. On the contrary, if the weakly coupled layer, positioned in the mode node was the upper layer, a sharp dip indicative of EIT was predicted by reflectivity simulations and observed experimentally. Heeg and Evers managed to explain [58] the phenomenon by incorporating multiple cavity modes in the theoretical description of the experiment. In that interpretation, one mode is driven at zero detuning. This mode is not coupled to one of the layers. However, several other modes are driven, albeit at extremely large detunings. The cavity modes are widely detuned from the nuclear resonance energy. However, they still form eigenmodes with the layers, and may form eigenmodes with the weakly coupled layer as well. At large detunings, these are almost dispersionless, and 'matter-like' i.e. they have the spectral width of the matter resonance and their eigenstates consist mostly of contributions from the excited atoms. To examine these predictions, we endeavoured to measure the dispersion of the cavity mode. That is, by taking the reflectivity over a range of angles around the main, resonant mode, we wanted to verify whether the central mode was indeed dispersionless and spectrally narrow enough to agree with the prediction of Heeg and Evers. Kong and Pálffy [60] noticed that, when the nuclear resonance and the incoming beam are far detuned from all cavity modes, the so-called dispersive regime, an effective interaction arises between the two layers. This is essentially the Fano-Agarwal coupling of two states coupled to each other indirectly via a state they are both coupled to. Here, the common state is the cavity mode, and the physical situation allows its adiabatic elimination giving rise to an effective interaction. Under certain circumstances, the strength of this interaction is larger than the spectral bandwidth of the excitations. In this case, we observe strong coupling, and can additionally observe Rabi oscillations. The theoretical details

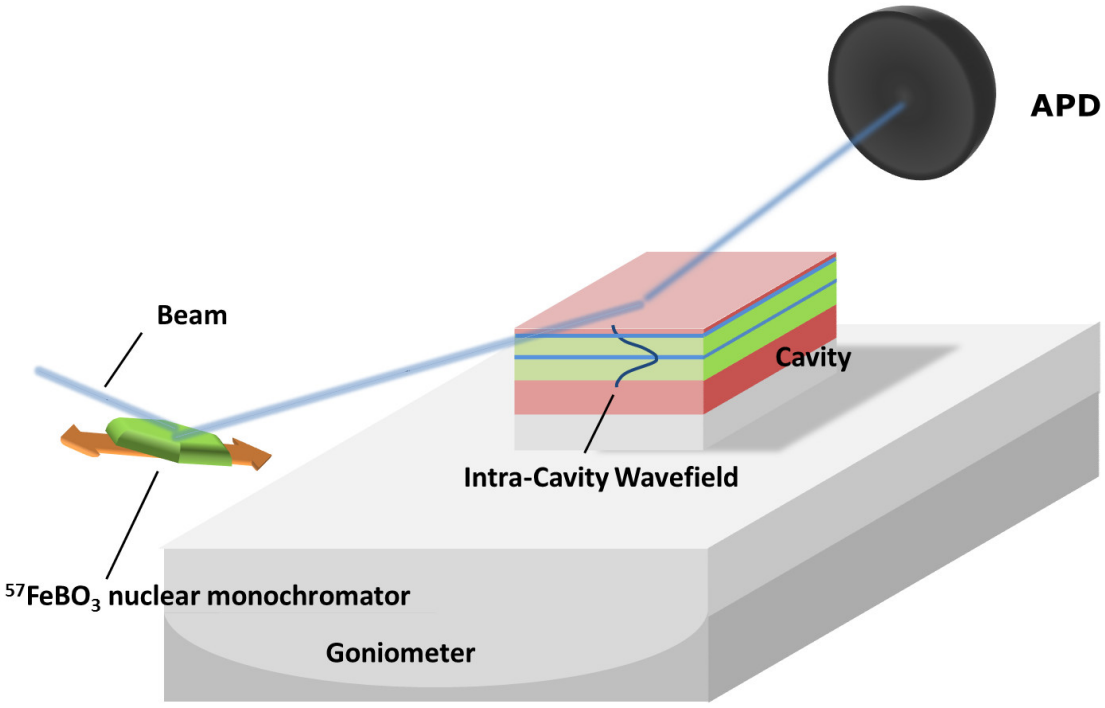

Figure 28: *Setup of the experiment. From the high-heat load monochromator, the radiation is monochromatized to a bandwidth of* $1\Gamma_0$*, by the SMS, which is moved to provide the energy detuning by Doppler shift. After that, it is focused by an KB mirror onto the sample. The reflected radiation is detected by an APD.*

have been given in Chapter IV.3.7.

V.3.2. Experiment

The experiment was performed at beamline ID18 of the European Synchrotron Radiation Facility. In order to achieve the necessary monochromatization of the synchrotron beam we employed the synchrotron Mössbauer source (SMS) described in a previous section. To enhance the count rate and improve the statistical quality of the measurements we focused the beam with a Kirckpatrick-Baez mirror. Theoretically, this should make for a very smooth experiment, since no time-gating or polarimetry was necessary. Count rates were good as well. However, the experiment was beset by difficulties, not all of which can be completely explained. For starters, a $^{57}FeBO_3$ crystal of the SMS of inferior quality led to a strong decline of the resolution of the spectra, but we were able to replace it in time for the experiment to finish

More importantly, there was a significant and persistent drift and/or jumps of the angular position of the sample with respect to the beam. Since the beam impinges on the surface of the iron borate

at an angle oblique with respect to the laboratory ground plane, and the reflected beam is in that plane, minor deviations and misalignments of the pre-borate crystal optics may actually minimally change the angle of incidence of the incoming beam. This might not be a problem were it the foil whose angle was changed, but for reflectivity measurements, this is of course highly unfavourable. We observed this behaviour by taking spectra at a particular position, and then taking a second spectrum - without moving the motor in the meantime. This essentially makes the angle of the reflectivity measurement an unknown quantity for the purposes of data analysis.

A second grave problem that appeared is the appearance of an uneven, sinusoidal background in the spectra. This background vanished and reappeared in the course of the experiment without any trace of systematic behaviour. A raw spectrum is shown in the Appendix A. Upon inspecting these spectra, the following will be noted. During the deacceleration-acceleration round-trip of the Mössbauer drive that the SMS is mounted on, the Mössbauer drive passes each velocity twice, once upon accelerating from zero velocity, and once upon deaccelerating from the maximum velocity. Each spectral point is hence twice measured, each spectrum effectively taken twice, but mirrored. At least, that is how it is intended to work. Not only is there an issue with the sinusoidal signal background, which may take different strengths in different spectra, but the very spectra themselves differ! This points to a particular explanation. Since the incoming radiation is reflected from the synchrotron Mössbauer source $FeBO_3$ crystal, which is mounted on the Mössbauer drive, instabilities there should be the reason. For example, a slight vibration of the crystal, or some inhomogeneity in the drive movement might cause the beam to be reflected in slightly different directions. In a transmission experiment, which is the usual modus operandi of the SMS, this will be barely noticeable. But in a reflection experiment which depends extremely sensitively on the angle such as ours, this will result in a world of difference. While we do not have conclusive proof that this is the cause of our troubles, we strongly believe that this is the case, at least where the different spectra are concerned. The sinusoidal background appears in the raw data of transmission spectra as well; discussions with the responsible beamline scientists indicate that during the MB drive movement, the crystal may temporarily move slightly out of the center of the beam resulting in a reduced intensity of the radiation reflected from the crystal. However, a temporary slight misalignment of the angle would show similar symptoms.

This suggests a different problem that is not immediately obvious from a glance at the raw data: What if the angle of incidence on the sample changes continuously while the energy is varied? Then, every point in the reflectivity energy spectrum would be taken at a slightly different angle. Due to the multitude of problems with the raw data, we summarize them briefly, before we discuss the steps we have taken in the data post-processing and analysis to ensure a correct interpretation

of the experiment.

- It is not clear at which angles the spectra were taken, or at least, the information is not reliable, since spectra taken at ostensibly the same angle are wildly different
- The occasional dissimilarity of two spectra in one set of raw data indicate that they were taken at different angles, even if that angle was not varied *at all* by the experimentalists
- There is a sinusoidal background that is most likely due to differences in the intensity reflected from the SMS.

To remove these sources of error and insecurity, we have devised a scheme given in appendix A. While the spectra thus gained look credible enough, other problems remain unsolved, notably the question of the angle under which a spectrum has been taken; and even more importantly, whether the spectra are usable in general. We address them by first performing a fit by GenX [110] of the reflectivity curve of the cavity. Having determined the cavity parameters from this fit, we calculate the resonant reflectivity spectra with the transfer matrix method under a range of angles. Into these simulations we also introduce some more general parameters. The resonant layers of our cavity consist of 95% stainless steel which is untempered. While stainless steel is essentially a single-line resonant material because of the absence of strong hyperfine interactions, in untempered sputtered stainless steel a small hyperfine field distribution is present, leading to an effectively broadened line. This is because sputtered thin films are disordered, leading to electric field gradients at the position of the nuclei and a corresponding distribution of nuclear quadrupole interactions and isomer shifts. By annealing them for some 20 minutes at $400 - 550^{\circ}$C, the disordered thin films can in principle be induced to take the austenitic and/or martensitic phases, which do not give rise to magnetic hyperfine interactions. This does not take place when the thin film is sandwiched by carbon layers however; the interdiffusion with the carbon may hamper the process [165]. We simulate this by convoluting the Lorentzian scattering amplitude with a Gaussian with an FWHM of $2\Gamma_0$. This leads to an effective linewidth of about $4.5\Gamma_0$ of the scattering amplitude. We should point out here that conventional Mössbauer studies of a 200 nm thick layer of enriched ^{57}Fe stainless steel indicate an effective linewidth of approximately $10\Gamma_0$ [166]; however a direct comparison is not possible, since the stainless steel layers of the cavity are surrounded by a carbon matrix; this is bound to influence the hyperfine field distribution. We cannot assume that it is the same as for the relatively thick stainless steel layer tested in the Mössbauer experiment, where interface and boundary effects vanish compared to a 1-2 nm thick layer in a carbon matrix. We also introduce a shift to account for the isomer shift of stainless steel

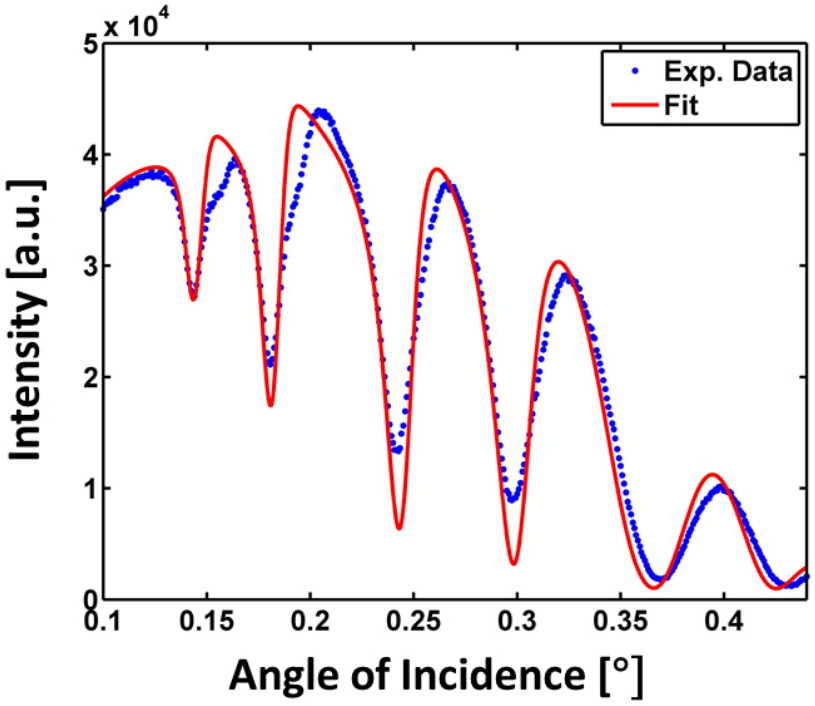

Figure 29: *Reflectivity of a cavity with an EIT arrangement of the layers, as shown in Fig. 30*

with respect to $FeBO_3$; the shift is $3.5\Gamma_0$ which amounts roughly to the literature value [106]. We then proceed to assign the measured spectra to the resonant simulations calculated in the way described above; spectra that do not fit satisfactorily are assumed corrupted and discarded.

In Fig. 29 we show the measured non-resonant reflectivity curve of the EIT-cavity along with the fit obtained by GenX. The parameters of the cavity extracted from the fit are listed in Tab. V.4 Additionally, the fit has yielded that the incident beam was Gaussian with a vertical cross section (half width) of 32μm, with a divergence of 7.8×10^{-5} rad. The fitted reflectivity was multiplied with a prefactor 5.1×10^4 to account for the measured intensity.

In Fig. 30 we show a sketch of the cavity with the most relevant parameters. The plot of the fit and data show that in particular the first mode is well described by the fit. The parameters extracted are consequently valuable for identifying and assigning the angles of the spectra from the data. The results of this procedure are shown in Figs. 31 and 32.

Fig. 31 (b) shows the reflectivity calculated by the TMM across a range of angles and energies around the first mode encoded in the color map. Fig. 31 (c) shows the corresponding spectra ordered according to their agreement with the results of the TMM. It is obvious that there is

	Platinum	Stainless Steel	Carbon	Stainless Steel	Carbon	Platinum
Thickness [nm]	2.7	1.8	13.6	1.8	13.6	15.5
Density [g/cm^3]	21.45	7.7	2.1	7.7	2.1	21.45
RMS [nm]	0.7	1.1	0.8	0.6	1.5	0.8

Table V.3: *Cavity parameters of the EIT cavity according to the fit performed by GenX. Additional parameters important to the fit are given in the main text.*

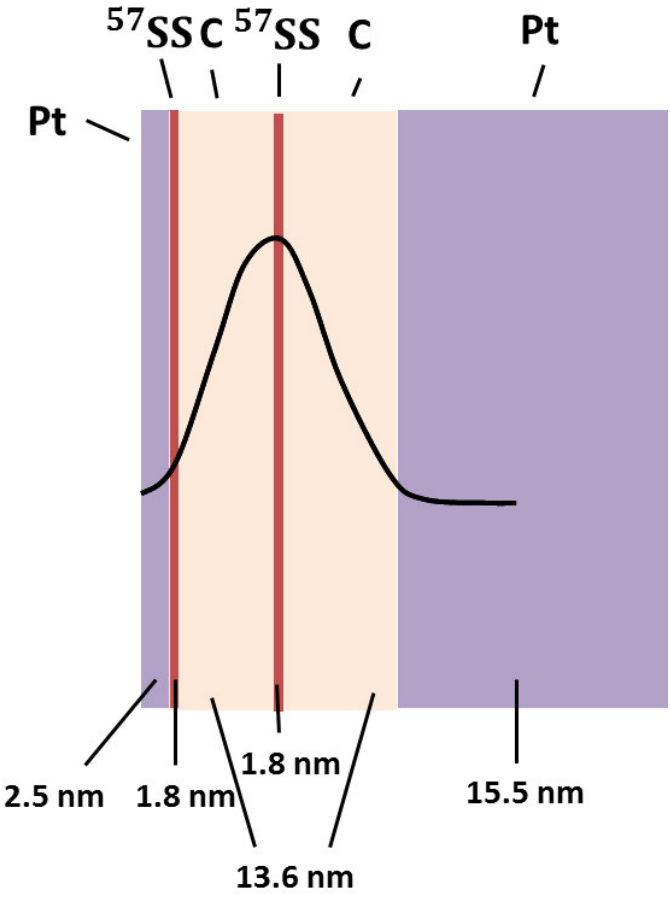

Figure 30: *Sketch of the cavity used in the experiment; widths are not to scale, but indicated to the right of the sketch. SS means stainless steel enriched with ^{57}Fe.*

broad agreement between the two datasets, which justifies our treatment of the data, and permits applying the quantum optical model for further analysis. Before we proceed to that, we show, in Fig. 32 the individual spectra along with the TMM reflectivities. While the theory and the data are

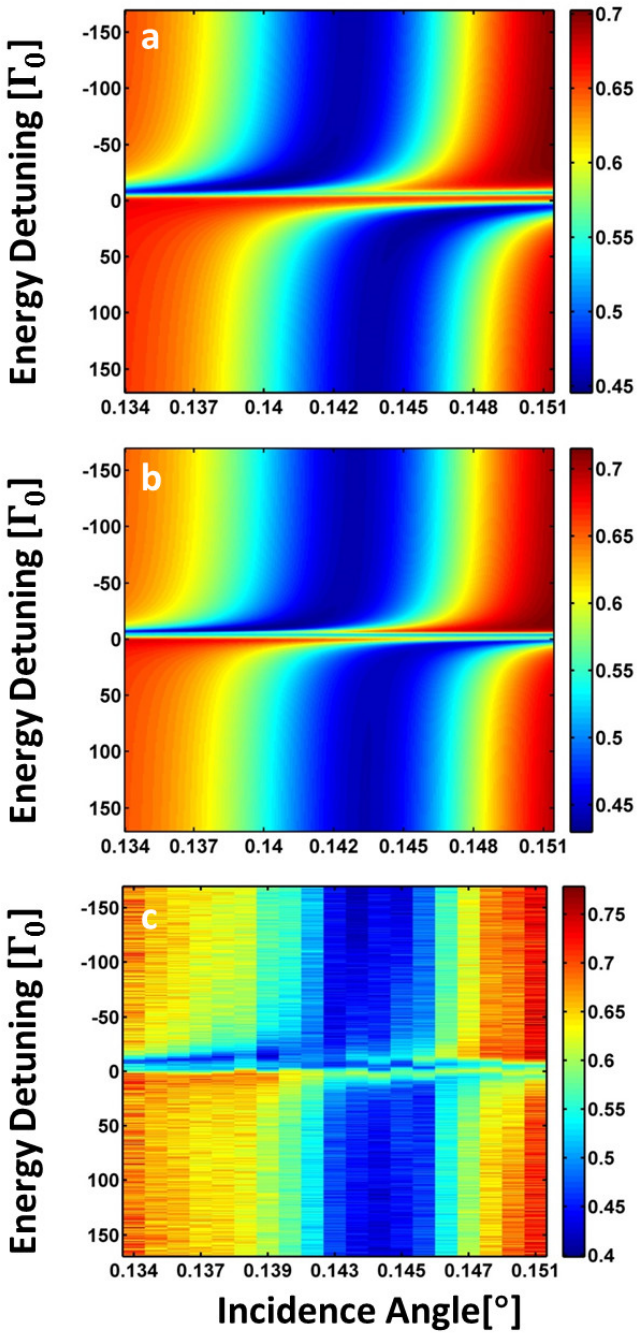

Figure 31: *Overview of the spectra. (a) shows the reflectivity according to the quantum optical model, (b) the results of the transfer matrix algorithm and (c) the actual experimental data. The intensity is encoded in the color map.*

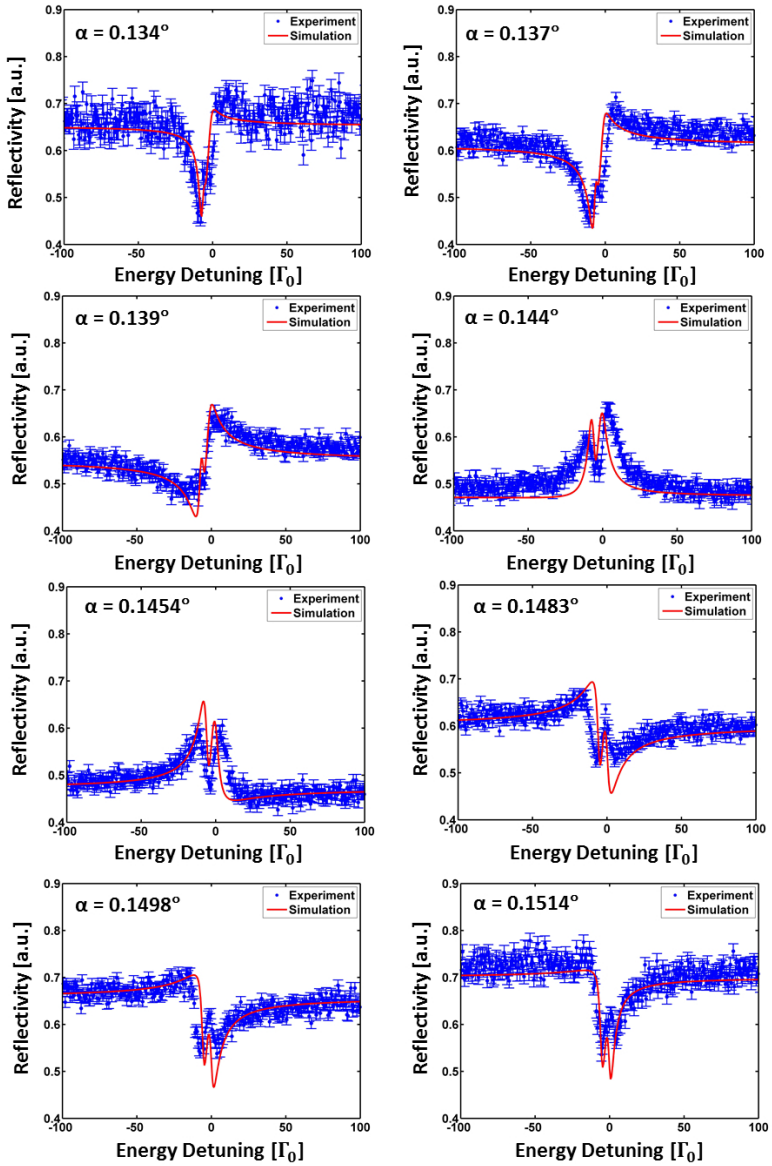

Figure 32: *Measured spectra (blue dots) and TMM simulations (red lines) of the EIT cavity for a range of angles, indicated in the figures. The measured spectra have been multiplied with varying prefactors to concur with the simulations. The error bars of the spectra are Poissonian. The agreement between simulation and spectra is very good.*

not always perfectly aligned there is, on the whole, strong qualitative and quantitative agreement between the data and the simulation.

This is an encouraging development, and we proceed to the next step, which is the comparison with the quantum optical theory. The theory has been described in a previous section, so we jump

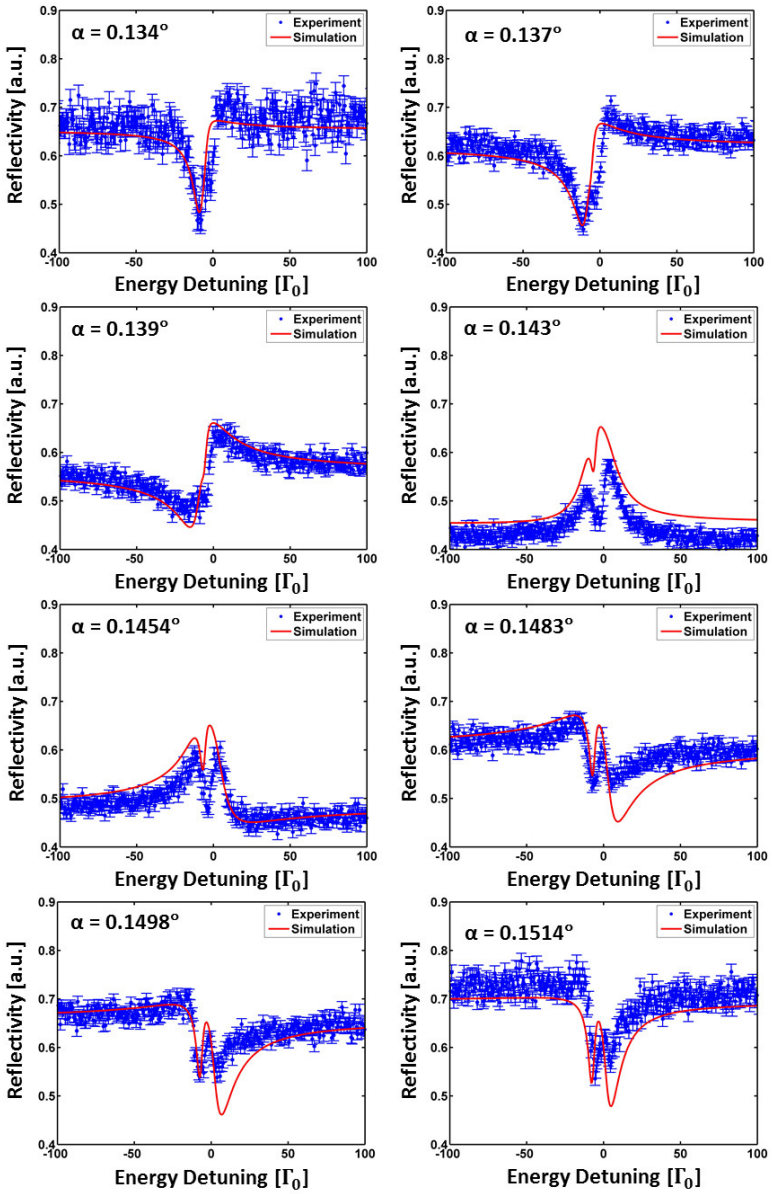

Figure 33: *Measured spectra (blue dots) and QO simulations (red lines) of the EIT cavity for a range of angles, indicated in the figures. The error bars of the spectra are Poissonian. The agreement between simulation is qualitatively excellent and quantitatively satisfying, which demonstrates that reliable parameters can be extracted from the model.*

straight to the results of the QO simulation, which are shown in Fig. 31 (a) and Fig. 33.

We point out that we have included some of the treatment of the TMM theory into this quantum optical theory; i.e. we have convoluted the quantum mechanically calculated reflectivity with

Cavity mode #	1	2	3	4	5
Mode spectral width κ [Γ_0]	3×10^{10}	4.1×10^{10}	7×10^{10}	7.1×10^{10}	5.7×10^{10}
Mode driving strength κ_R[Γ_0]	9.5×10^{9}	1.7×10^{10}	2.8×10^{10}	3.9×10^{10}	2.56×10^{10}
Coupling Layer A g_A [$2 \times 10^5 \Gamma_0$]	$0.94 + 0.54i$	$3.4 + 7.06i$	$1.5 + 2.8i$	$0.53 + 1.5i$	$0.4 + 3.4i$
Coupling Layer B g_B [$2 \times 10^5 \Gamma_0$]	$3.91 + 3.65i$	$-0.26 + 0.3i$	$-2.1 - 2.4i$	$0.29 - 0.15i$	$1 + 0.65i$

Table V.4: *Parameters of the quantum optical simulation which yield the data shown in Figs. 33 and 31.*

the same Gaussian as the TMM reflectivity, and also included the geometrical factor describing the footprint of the beam on the sample, in order to ensure that the data and the theory fit quantitatively. Omitting this step would have caused a different fit results; the change in the parameters would have been due to experimental details not related to the cavity and its properties. The same general agreement between theory and data is evident as in the previous treatment; a slight difference is that towards higher angles, our quantum optical simulation seems to slightly over-estimate the coupling strength and consequently the splitting between the normal modes, but not in any drastic manner. We also have some difficulty in getting the quantitative agreement just right, but by and large the simulation describes the data excellently. Since, for example in Fig. 33 at 0.1514° we can make out a splitting and describe it accurately using the quantum optical theory, we conclude that we have strong evidence for the presence of normal mode splitting between two nuclear ensembles in the dispersive regime of a cavity.

Conclusive proof of this claim, however, requires the observation of Rabi oscillations in the temporal domain. The periodicity of the oscillations is given by the Rabi frequency Ω_R, which should be half of the frequency splitting between the normal modes. Note that this is the Rabi frequency including the detuning. The detuning here is, as shown in the quantum optical model in the last section, not the detuning between the incoming radiation and the upper level, but the detuning between the two nuclear ensembles, which is caused by the individual collective Lamb shifts they experience. To observe this unambiguously is of paramount importance. We have decided to perform another experiment to ameliorate the shortcomings present in this one. The two most fundamental changes were that it was performed in the 40-bunch mode of the ESRF and without the synchrotron Mössbauer source and KB focusing. This allowed for an almost divergence-less beam, and permitted us to take time spectra to observe the Rabi oscillations. The drawback of this setup was that we had to use time-gating (6 ns) to evade overload of the APD by the prompt pulse, and introduce a thin enriched stainless-steel foil ($1\mu m$) mounted on a Mössbauer drive to perform the energy discrimination. This was of course not required to observe the Rabi

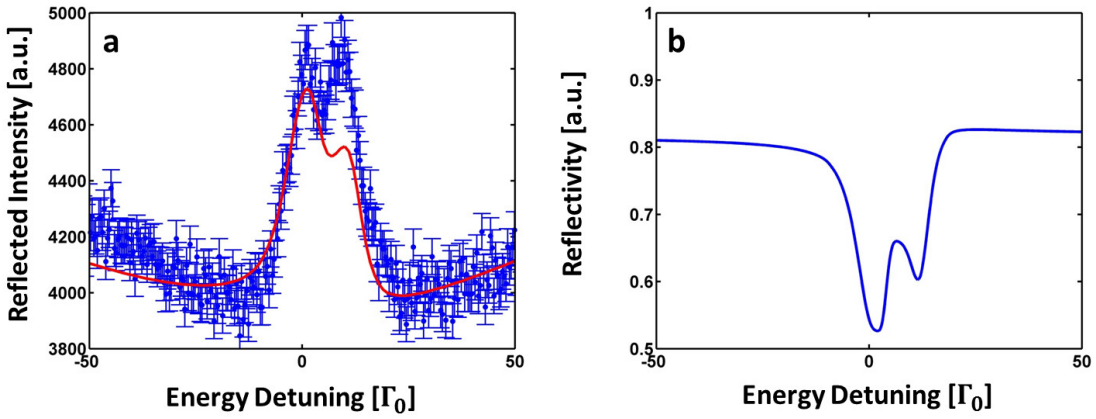

Figure 34: *Measured and simulated reflectivity of the cavity at* 0.162°*. In (a) we show the measured reflectivity and a simulation taking into account the time gating and the propagation through an* ^{57}*Fe absorber foil; hence the background modulation and inversion of the dips, which is not present in direct reflectivity measurements by the SMS, as shown in Fig. 33 In (b) the spectrum as it would appear without these measurement-induced effects is shown. It consists of two Lorentzians each with a width of about* $4\Gamma_0$ *spaced apart by about* $10\Gamma_0$*, which corresponds to the Rabi oscillation predicted by the QO model.*

oscillations, but we took an additional energy spectrum to compare the measured splitting with the Rabi frequency extracted from the Rabi oscillations. As described in a previous section, this introduces oscillations into the spectra; but this can be accounted for in the data analysis. The results are shown in Fig. 34.

The spectrum was measured at 0.162° and is shown in (a). The splitting is well-resolved and consistent with the simulation, although the magnitudes are not perfectly reproduced. The background modulation is reproduced as well; however, this was achieved by assuming a timegating of 5 ns instead of 6 ns. This is well possible; in the time spectra we observed little spikes which indicate a slight APD overload and reflections; this is equivalent to a slightly larger fraction of the prompt being measured by the APD. In (b), the corresponding energy spectrum simulation without the changes accounting for the time gating is shown. Again the splitting is well resolved; it corresponds to about $10\Gamma_0$. Is this consistent with the quantum optical model? We employ the parameters we obtained in the previous experiment, and plot some key values around 0.156° to check. In Fig. 35 (a) we show twice the Rabi frequency Ω_R calculated by the model compared to the ξ_{L1} and ξ_{L2} which describe the superradiant enhancements, i.e. the enhanced bandwidths in units of natural linewidths, by which the resonances of the layers decay faster than without the cavity. We find, as predicted before, that Ω_R decays much slower when the cavity is

detuned, and that ξ_{L1} and ξ_{L2} are below one linewidth at 0.162°. Furthermore $2\Omega_R$ has a value of about $10\Gamma_0$ which is confirmed by the spectrum we have measured, see Fig. 34. In (b), we show $2\Omega_R$ compared to $2\Omega_c$. Ω_R is extracted from the fit by the quantum optical model; so were the collective Lamb shifts of the two ensembles. We calculated Ω_c by resolving $\Omega_R = \sqrt{\Omega_c^2 + \Delta^2}$ for Ω_c; $\Delta = \delta^{[1]} - \delta^{[2]}$. It turns out that Ω_R is mostly induced by the detunings, as shown in Fig. 35. While this will not change the frequency of the Rabi oscillations, it means that the layers will only exchange a tiny fraction of the population, i.e. only a fraction of the probability that the photon is in layer A will be transfered to layer B in the course of a Rabi oscillation. Fig. 35 (c) confirms this by showing the collective Lamb shifts in the same angular range. According to the model $\Omega_R \approx 5\Gamma_0$, and $\Omega_c \approx 0.5\Gamma_0$.

Finally, we show the measured time spectra in Fig. 36. We have added the time spectra according the CONUSS model we have used to calculate the energy spectra, and a simple decay which mimics the features of the Rabi oscillations which is

$$c(t) = e^{-\Gamma t} cos(\Omega_R t). \tag{125}$$

where Γ is chosen to be $3.5\Gamma_0$ to take account of the line broadening.

There are some deviations between the measured data and the simulations, and the simulations itself; They concern mostly the visibility of the fringes. Their source is most likely an incorrect implementation of the line broadening due to the hyperfine field in the simulations. Recall that stainless steel has a line broadening due to a distributed hyperfine magnetic field on its own, and the presence of a carbon matrix around the thin layers is likely to add a distribution of isomer shifts and the hyperfine magnetic field itself as well, and could introduce a hyperfine electric field gradient as well, as it does for α-Fe layers in a carbon matrix [52]. As described above, in the quantum optical model we have implemented this by assuming a linewidth of $3.5\Gamma_0$ instead of $1\Gamma_0$; in the CONUSS simulations we have taken a slightly more sophisticated approach by assuming a hyperfine field of 1 T which has a Gaussian distribution of. This explains why the latter model gives a better fit to the data than the quantum optical one. There is some deviation at the end of the spectrum as well; but this is just an effect of insufficient statistics; a beating could not be resolved yet, since the signal-to-noise level is not high enough from about 120 ns on. All in all, both models reproduce the most important features of the data, which are the decay time and the beating period, and our assumptions are therefore confirmed. The only drawback is the fact that we have not achieved full Rabi oscillations, where the population is fully coherently exchanged several times during the lifetime. This is the focus of the next section.

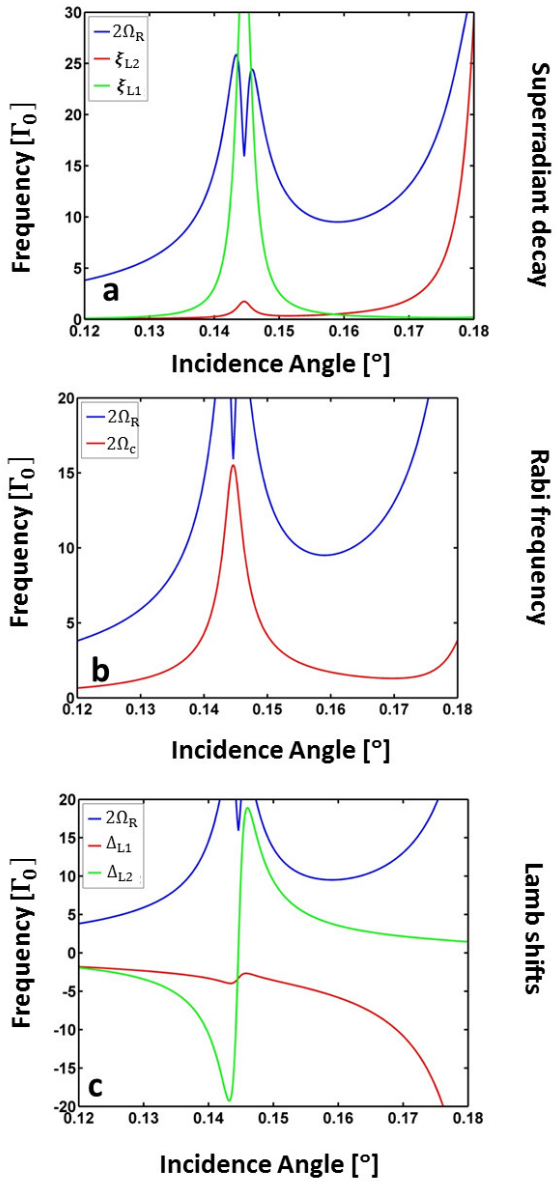

Figure 35: *The effective coupling parameters, collective Lamb shifts and superradiant decay enhancement factors obtained by fitting the measured spectra to the QO model. In (a) we show the Rabi frequency times 2 (corresponding to the splitting) compared to the superradiant decay enhancement factors of the two layers; the latter are below* $1\Gamma_0$*, while the former is about* $10\Gamma_0$*, corresponding to a Rabi frequency of* $5\Gamma_0$*. In (b) we compare the portion of the Rabi frequency that is due to the interaction between the two layers with the total Rabi frequency, which includes the effective detuning, which we extracted from the QO model as well. The bulk of the Rabi frequency is due to the effective detuning, as confirmed by (c) where we demonstrate that there are significant Lamb shifts at the relevant angle, which is indicated by the black line in all three panels. The rise of the curves to the right is due to the interaction of the first layer with the second mode, which is relatively strong.*

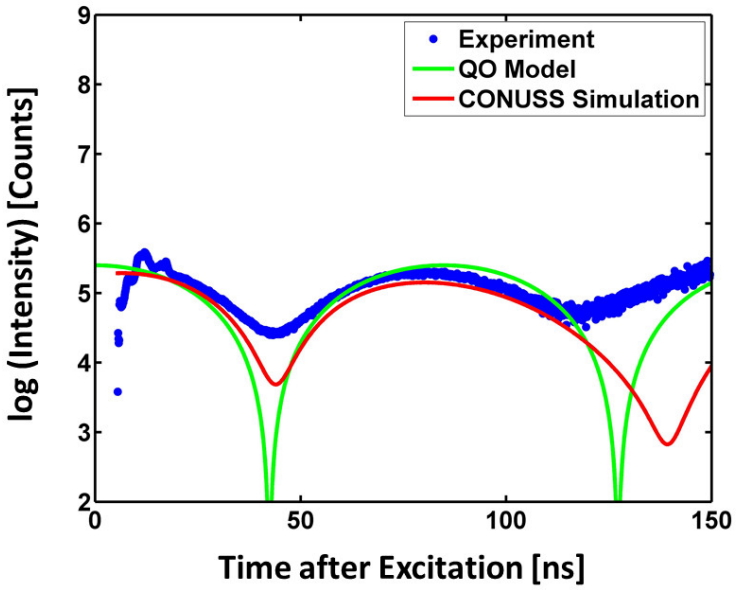

Figure 36: *Measured Rabi oscillations at* 0.162° *along with quantum optical and CONUSS simulations. The quantum optical simulations consist of a simple exponentially decaying cosine with the frequency and lifetime obtained from the QO energy spectra simulations,* $\Omega_R \approx 5\Gamma_0$ *and* $\Gamma = 3.5\Gamma_0$*. Data and simulations have been divided by the exponential decay to ensure better visibility of the low-count part of the spectrum. The CONUSS spectra have been obtained by Fourier transforming the energy spectra obtained by CONUSS; the resonance has been assumed to be broadened by a magnetic hyperfine field with a Gaussian distribution around 1T. Any discrepancy between models and data is most likely a result of an insufficient theoretical description of the line broadening. For details refer to the main text.*

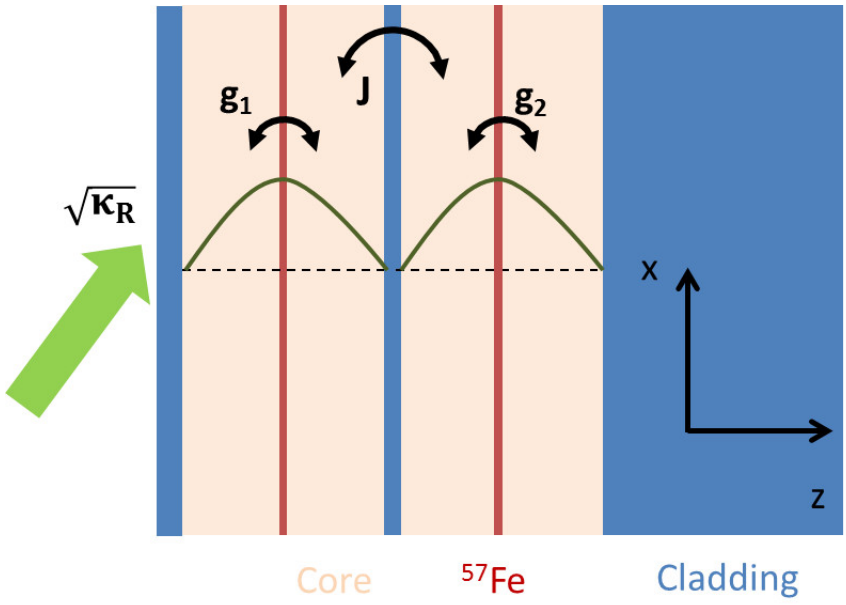

Figure 37: *Sketch of a coupled cavity setup. The cavities are at the same time divided and coupled via a very thin cladding layer. The thickness of the layer needs to be carefully chosen; a thin layer means both cavities have a high bandwidth but couple with a high J; a thick layer means the opposite. Each cavity is coupled with a thin resonant ^{57}Fe-layer such that the resonant layers are in the antinode of the first mode of each cavity, ensuring that the coupling constants g_1 and g_2 are roughly equal. The first cavity is illuminated by a classical external field.*

V.4. Rabi Oscillations in a double cavity system

In this section, we introduce an improved scheme, which will allow us to observe Rabi oscillations which are due to the interaction, not the Lamb-shift induced detuning of the layers. Our line of thought is thus: the Lamb shift is red- or blue shifted depending on whether the mode which induces it is red- or blue shifted from the resonance. We want to design a cavity where at a particular angle, the Lamb shift contributions from two modes cancel each other. Since the interaction between the layers depends on the magnitude squared of the Lamb shift only, it remains and is solely responsible for the interaction and hence the Rabi oscillations. The thin-film cavity setup we have developed is sketched in Fig. 37. It consists of two cavities, with the first being on top of the second, and the second placed on a silicon substrate.

The cavities are divided by a thin cladding layer, through which they couple with each other. Each cavity contains a layer of resonant ^{57}Fe atoms, or more precisely a stainless steel layer containing resonant ^{57}Fe atoms. This ensures that due to the lack of magnetic ordering in stainless

steel the nuclei are not subject to a magnetic hyperfine field; therefore the ^{57}Fe sublevels are degenerate and the layer functions as an effective single level layer. The Hamiltonian of the setup is

$$\begin{aligned} H_M &= \Delta_C a_1^\dagger a_1 + \Delta_C a_2^\dagger a_2 + J(a_1 a_2^\dagger + a_1^\dagger a_2) \\ +i\sqrt{2\kappa_{r1}}(a_{in}a_1^\dagger - a_{in}^* a_1) &+ \sum_l (S_{1l+}a_1 + S_{1-}a_1^\dagger) + \sum_l (S_{2l+}a_2 + S_{2l-}a_2^\dagger) \end{aligned} \tag{126}$$

where we have already performed the transformation to the interaction picture. $a_1(a_1^\dagger)$ are the destruction (creation) operators for the first mode of the upper cavity; $a_2(a_2^\dagger)$ likewise for the lower. We omit higher order modes for both cavities; while they would lead to valuable corrections of Lamb shifts and interaction strengths, they are not absolutely necessary to explain the phenomena we would like to observe here. a_{in} characterizes the driving strength with which an external field drives the upper (and only the upper) cavity mode. The final terms describe the interaction of the ^{57}Fe layers with their respective cavity modes. Finally, the third term describes the interaction between the two cavity modes by tunneling. The Hamiltonian is limited to the one-excitation subspace. To solve it, we take a look at its matrix form:

$$H = \begin{pmatrix} \Delta_c & J & g_1 & 0 \\ J^* & \Delta_c & 0 & g_2 \\ g_1^* & 0 & \Delta_e & 0 \\ 0 & g_2^* & 0 & \Delta_e \end{pmatrix}. \tag{127}$$

where we have assumed that both cavities have the same frequencies of the first mode. Prediagonalizing the mode-mode interaction we get

$$H = \begin{pmatrix} \Delta_c + \frac{J}{2} & 0 & \frac{g_1}{2} & \frac{g_2}{2} \\ 0 & \Delta_c - \frac{J}{2} & \frac{g_1}{2} & -\frac{g_2}{2} \\ \frac{g_1^*}{2} & \frac{g_1^*}{2} & \Delta_e & 0 \\ \frac{g_2^*}{2} & \frac{g_2*}{2} & 0 & \Delta_e \end{pmatrix}. \tag{128}$$

We can see that we now have two supermodes [167] coupled to both layers each, which is the same as in the previous section. Our theoretical treatment continues as laid out there, we proceed to adiabatically eliminate the cavity modes. The scheme is sketched in Fig. 38 The fundamental difference is physical. The two supermodes come into existence because of the coupling of the bare modes. Their angular distance from each other can be tuned. Indeed, they can be spaced apart very closely; far enough that the superradiant decay enhancement has already decayed to zero, but still so close that the coherent interaction between the layers is enhanced much more than it would be in a conventional cavity. What's more, in the last section we noticed that the Rabi

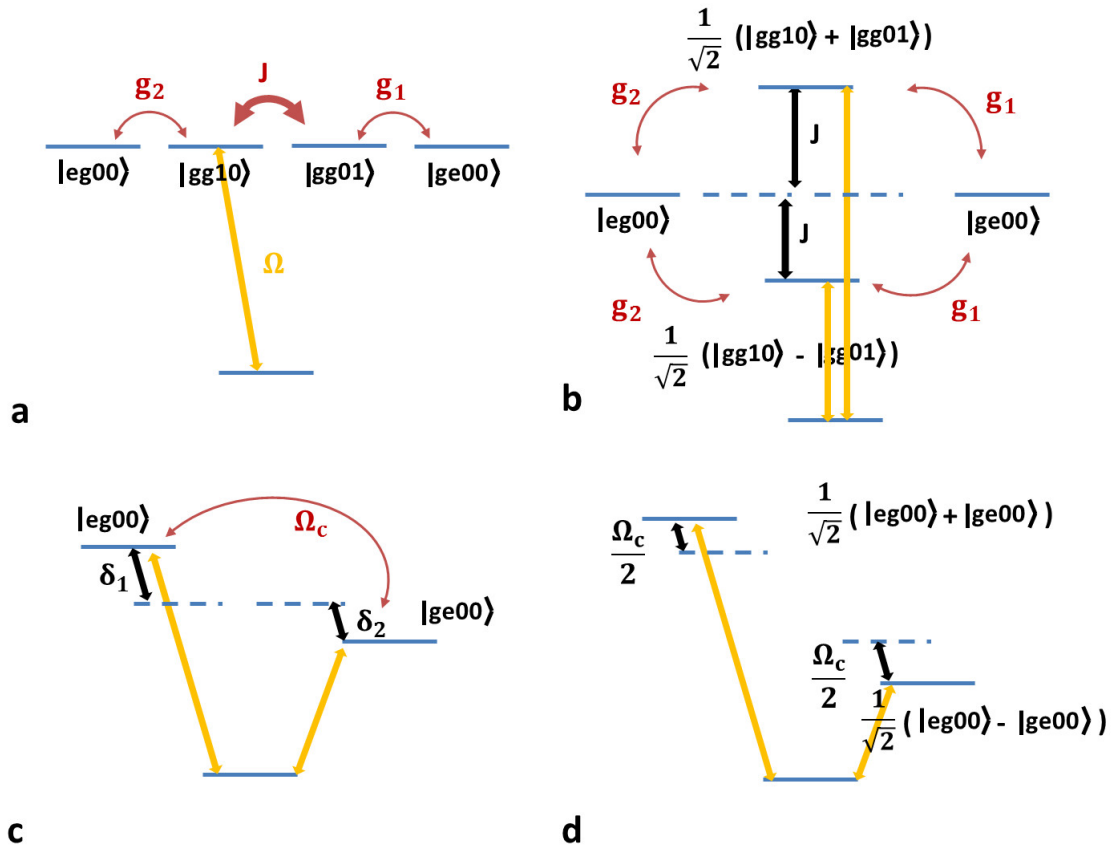

Figure 38: *Sketch of the theoretical treatment of the double cavity. Interactions are given in red, driving terms in orange, states and energy detunings in black. We have omitted dissipative terms for clarity. (a) the system, with the cavities tuned to the nuclear energies, includes four states: photon in mode 1 (i.e. the upper cavity) ($|gg10\rangle$), no ensemble excited; photon in mode 2, no ensemble excited ($|gg01\rangle$); ensemble 1 excited ($|eg00\rangle$), ensemble 2 excited ($|ge00\rangle$), and finally the ground state with no excitations in the system at all ($|gg00\rangle$). (b) after prediagonalization, we have two supermodes, which are energetically detuned by J the interaction strength, from the nuclear energies. (c) after the adiabatic elimination, we have further detunings due to the collective Lamb shifts δ, and an interaction term Ω_c. (d) After diagonalizing the remaining Hamiltonian, we have an additional splitting due to the interaction. If the cavity is properly designed, there will be no contributions due to the CLS in (c).*

oscillations were mostly due to the collective Lamb shifts of the layers. In the symmetric situation we have now, the collective Lamb shifts for each layer cancel at the position between the cavity modes, because the red- and blue-detuned cavities lead to a red- and blue-detuned Lamb shift of equal magnitude; i.e. the total Lamb shift is zero. The coherent coupling strength depends on the magnitude of the CLS, and not on whether it is positive or negative; hence the coupling strength

	Mode 1	Mode 2
κ [Γ_0]	8×10^9	4×10^9
κ_R [Γ_0]	9×10^8	1.5×10^9

Table V.5: *Paramters of the cavity supermodes. κ are the cavity linewidths, κ_R the driving strengths.*

remains, but the Lamb shifts vanish.

V.4.1. Experiment

The experimental setup is identical to the one for the measurements of the Rabi oscillations in the last section. We have neglected to focus the beam in order to minimize divergence. The sample was irradiated by 14.4 keV radiation from the ID18 beamline of the ESRF in the 16-bunch mode, which leaves 176 ns between the bunches. The prompt was eliminated by using a 7 ns time gating window. A stainless steel analyzer foil enriched with ^{57}Fe was moved at velocities of $\pm 10 \frac{mm}{s}$. This corresponds to an energy detuning of $\pm 103\Gamma_0$. The slits in front of the detector had a width of 1 mm.

V.4.2. Results and Analysis

The resonant layer in the cavity consisted of ^{57}Fe enriched steel; the cladding was made out of Palladium, and the core of Carbon. The design parameters intended for the cavity to be perfectly symmetric, i.e. both cavities were supposed to have the same core sizes. But we have not managed to find a fit to the reflectivity measurements that confirms this. Therefore we analyze the data purely with the quantum mechanical model developed in ref. [58]. In Fig. 39 we show the reflectivity curve of the multilayer around the region of interest along with a quantum optical fit of the cavity parameters, which are given in Tab. V.5. The angular range over which we analyze the data is very small, and we will analyze only one spectrum, so we ignore modifications of the reflected intensity by beam size effects and the envelope of the reflectivity. To include the effects of the hyperfine magnetic field distribution and the possibility of isomer shift distributions etc., we have assumed that the nuclear resonance has a width of $4\Gamma_0$. In Fig. 40 we show the energy spectrum measured at 0.176°, along with a fit taking into account the time-gating detection. The figure also shows the calculated reflectivity, without taking into account the detection process. The splitting is obvious, and has a width of about $24\Gamma_0$. The parameters used for the fit are given in Tab. V.6 . In Fig. 41 we show the measured temporal decay pattern of the cavity. The beating indicative of Rabi oscillations is clearly visible. We compare the result to the Fourier

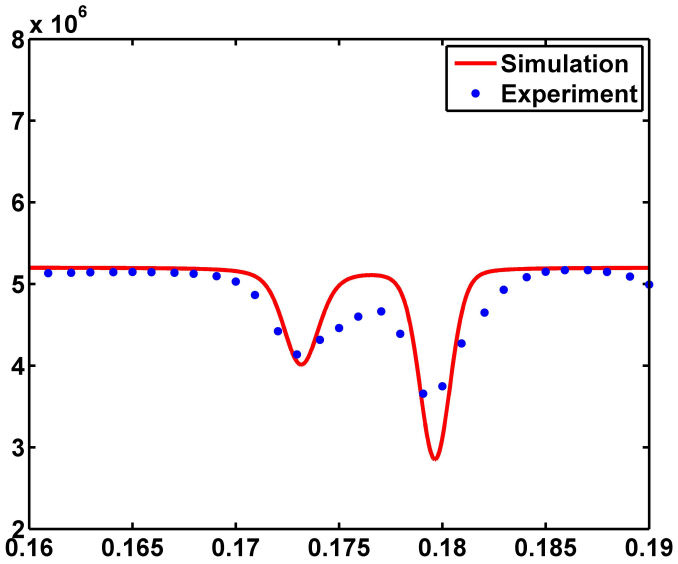

Figure 39: *Reflectivity of the double cavity around the first two supermodes along with a quantum optical simulation. We have assumed a very slight divergence of* 8×10^{-6}*. The second supermode seems to overestimate the quality of the cavity, but this is possible; note that the resolution of the curve is not too good. Using these parameters in the fits of the spectra to come yields good results.*

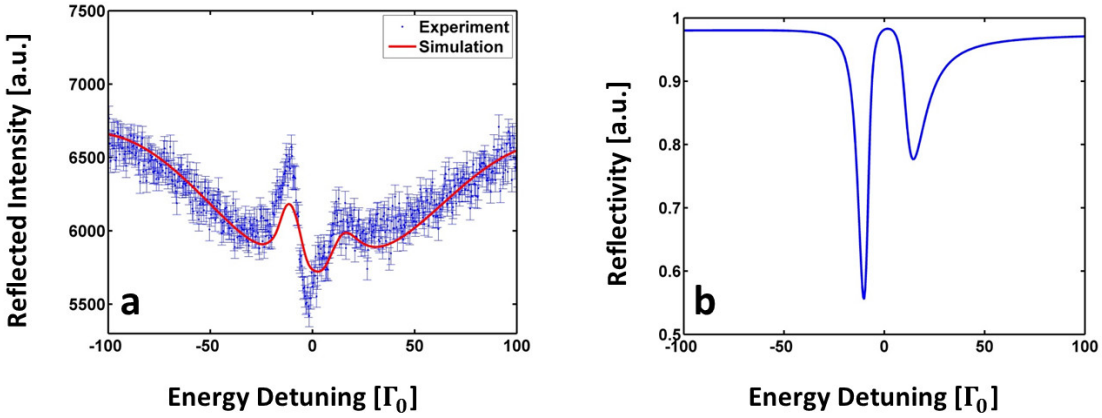

Figure 40: *(a) Spectrum of the reflectivity at* 0.176°*, along with a simulation taking into account the 7 ns time gating window. The agreement is good. (b) simulation of the bare spectrum without any time gating. The splitting is about* $24\Gamma_0$*, meaning* $\Omega_R \approx 12\Gamma_0$*.*

transformation of the bare spectrum in Fig. 40 and a standard exponentially damped cosine with the frequency Ω_R. Both models adequately predict the periodicity of the beating, although there are some shortcomings in the description of the intensities. In the case of the damped cosine, it

	Mode 1	Mode 2
g_1 $[10^5\Gamma_0]$	5.508	5.508
g_2 $[10^5\Gamma_0]$	6.05	6.05

Table V.6: *Coupling strength parameters for the supermodes.*

clearly does not take into account the additional dephasing that stems from the hyperfine magnetic field distributions, therefore the calculated interference fringes are much more visible. The full quantum optical model mimics these distribution effects via the interactions strength parameters, and therefore does a much better job of predicting the intensities from about 20 ns after the excitation on; but it fails to predict the intensity at the beginning of the spectrum. Part of that might be just due to the leakage associated with the Fourier transform; but it is also conceivable that this is a systematic error that results from discrepancies between the energy spectrum and the simulation. Note that in Fig. 40 the dip in the spectrum at zero detuning is not accurately reproduced. In the bare spectrum, this manifests itself as a peak, which should be higher. This could be interpreted as a kind of superradiance that comes from interference between the two normal modes; the superradiant part at the beginning of the temporal decay pattern would be larger if this peak were larger.

We now examine whether the splitting and the decay oscillations we have observed is due to the collective Lamb shifts or the interaction, and whether the strong coupling condition is met (i.e. whether the splitting is larger than the superradiant decay enhancement of the eigenmodes). In Fig. 42 we plot the superradiant decay enhancements, Lamb shifts, and interaction strengths. The results are clear. At the angular position where we have measured the spectrum (indicated by the black line), the Rabi frequency is almost exclusively a result of the interaction strength between the layers, since the Lamb shifts are both almost zero there. Hence, the splitting is a genuine splitting due to the strong coupling of two ensembles mediated by several cavity modes and $\Omega_R = \Omega_c = 12\Gamma_0$. Furthermore, as can be seen in Fig. 42, this is larger than the superradiant decay widths. We therefore expect a strong signal showing Rabi oscillations, which are due to the exchange of the excitation populations between the two layers. We conclude that we have achieved strong coupling between two nuclear ensembles, and observed the coherent exchange of population between them in the form of Rabi oscillations. The splitting has a magnitude of $24\Gamma_0 \approx 160$ MHz. It is interesting that this is almost in the range where microwave cavities become available commercially. This offers the tantalizing opportunity to further manipulate this system with microwave photons, and perform quantum optics by interfacing x-rays and microwaves via

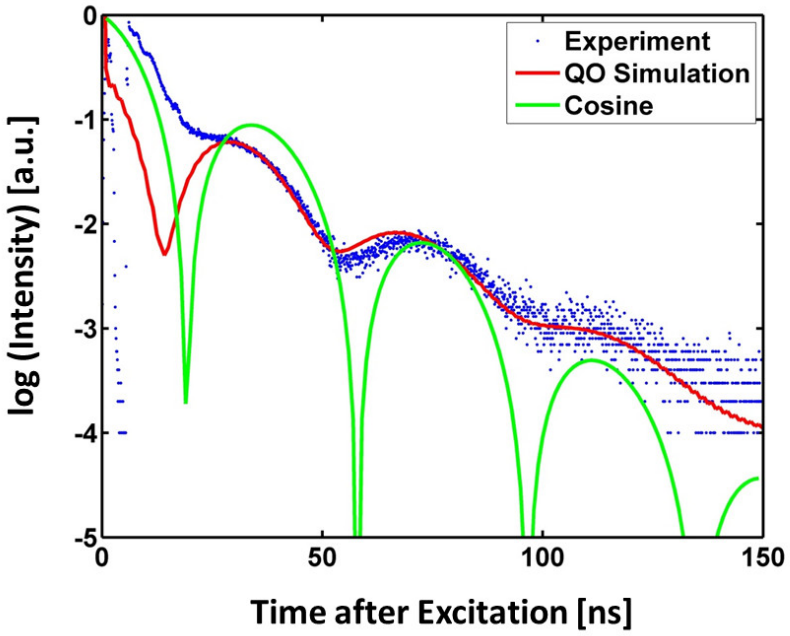

Figure 41: *Rabi oscillations in the double cavity system.* $\Omega_R = \Omega_c = 12\Gamma_0$. *The cosine is from the calculation of the Rabi oscillations; The quantum optical simulation is a Fourier transform of the energy spectrum calculated from the quantum optical model. Deviations are probably due to the hyperfine fields of the layers not being properly implemented.*

nuclear ensembles.

A more immediately accessible benefit is that this system offers the opportunity of designing and tuning three-level systems in the hard x-ray range. Suppose, for instance, that one ensemble was coupled to the cavity more strongly then the other. This can be achieved almost effortlessly through layer placement, or by making one layer thinner, reducing the collective coupling strength. Upon tuning the angle, one layer then experiences a greater Lamb shift then the other, and also a greater superradiant decay enhancement. Right at the center between two cavity minima, the Lamb shifts would cancel each other anyway, in what would appear as an anti - crossing, because of the interaction strength. Closer to the cavity minima, one branch would appear very far detuned and superradiant, with the other barely detuned and with a normal decay time, the interaction between them remaining. The whole setup would effectively turn into an artificial three-level Λ - atom with tunable level energies, decay times and interactions between the upper levels. And of course there remains the opportunity to add more degrees of freedom by using the multiple hyperfine levels available in $\alpha - {}^{57}Fe$ and adding more cavities. This brings closer to creating the

foundations for some of the more complicated proposals advanced by theorists in recent years for the coherent control of x-rays. Naturally, the principle can be extended to the electronic resonances we have discussed in Chapter V.2, see for reference Fig. 43.

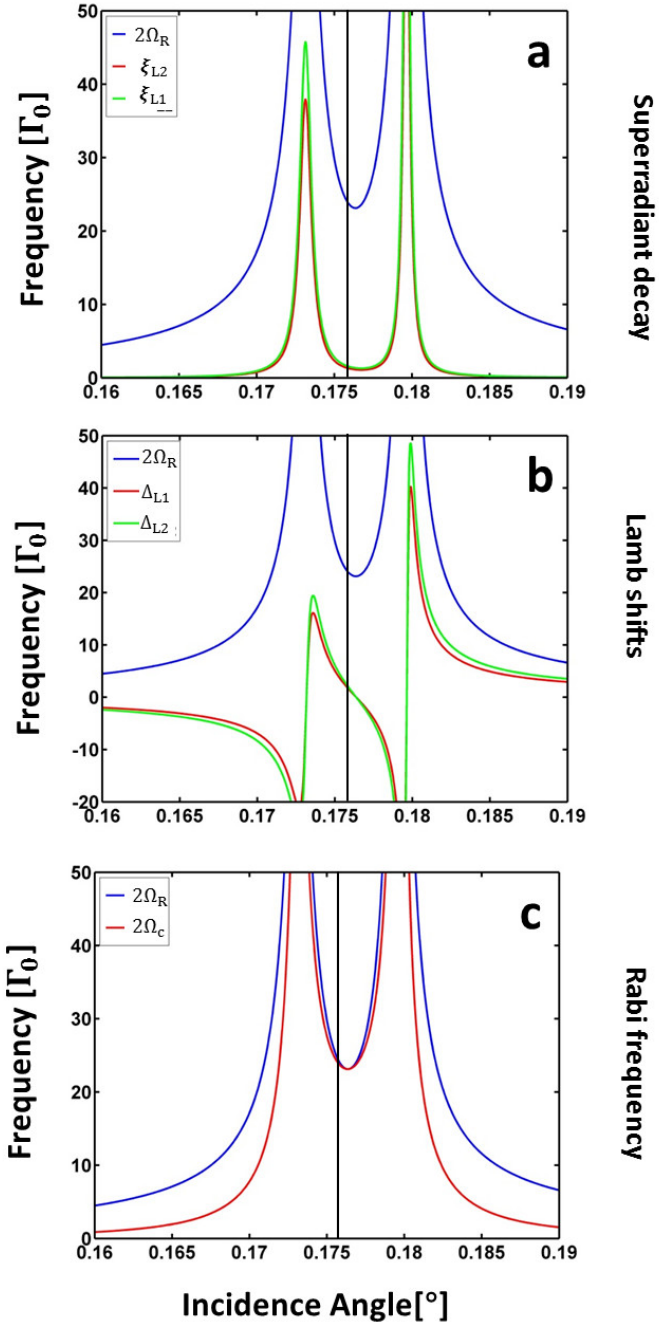

Figure 42: *(a) Interaction strengths between the layers vs. superradiant decay enhancements. The vertical black line marks the position at which the data were taken. The interaction between the nuclear ensembles has a frequency of about* $24\Gamma_0$*, obviously much stronger than the decay at the position where the reflectivity spectrum was taken. In (b) it is obvious that the collective Lamb shifts are minuscule at that angle as well, as laid out in the theory section. In (c) finally we compare the Rabi frequency that is due to the interaction strength to that due to the detunings. Obviously the interaction strength contributes the lion's share to the Rabi frequency.*

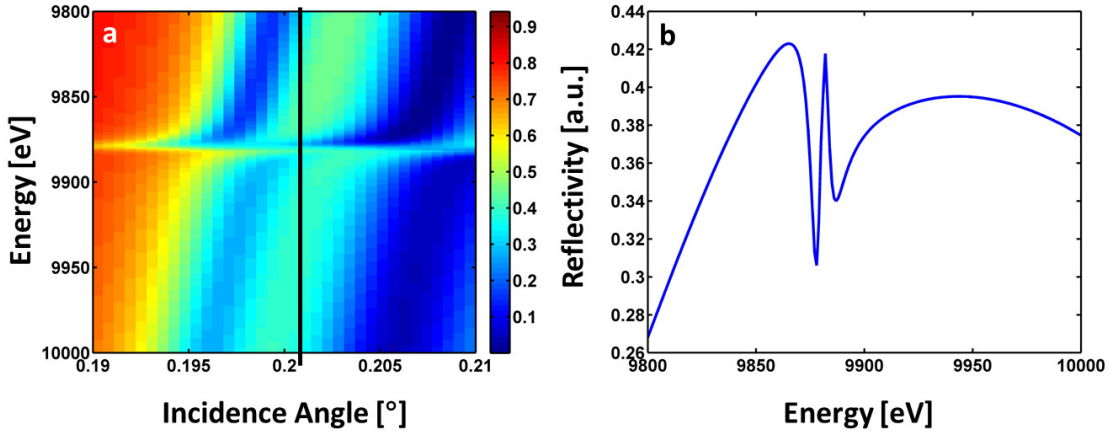

Figure 43: *(a) Parratt-simulated reflectivity of a double cavity with the dimensions 2 nm Pt/20 nm C/1 nm Ta/20 nm C/1 nm Pt/20 nm C/1 nm Ta/20 nm C/20 nm Pt. In the center between the two supermodes, marked by the black line, the matter-like parts of the excitation spectra are split by the effective interaction. The detailed spectrum is shown in (b).*

V.5. A distributed Bragg reflector defect cavity for hard x-rays

V.5.1. Introduction

All cavities previously treated in this thesis were based on the strong total external reflection of x-rays by high-Z materials under grazing-incidence illumination. Under these circumstances, the materials form mirrors. The drawback is obvious, but not huge at first glance: the reflectivities are restricted to small angles.

Upon further investigating the matter however, we find several reasons for wanting cavities that can be operated at slightly higher angles than possible under total external reflection. The most important one is that the equation relating the angular mismatch of mode and beam to the detuning is $\Delta = (\frac{\sin(\alpha_0)}{\sin(\alpha_1)} - 1)\omega_0$. It is clear that for the same angular mismatch $\alpha_0 - \alpha_1$, the above equation will yield vastly different values of the detunings depending on whether, say $\alpha_1 = 0.2^\circ$ and $\alpha_0 = 0.1^\circ$ or $\alpha_1 = 0.9^\circ$ and $\alpha_0 = 0.8^\circ$. In other words, a mode centered at 0.9° and one centered at 0.2° which have the same angular acceptances have completely different lifetimes or bandwidths, with the bandwidths for the mode centered at the higher angle being narrower. This has many advantages, chief among them that it might bring us closer to collective strong coupling in a conventional setup of one layer in a cavity mode. Particularly in the case of electronic resonances, where the coupling strengths and mode linewidths are often a mere order of magnitude apart, this could help tremendously. Whatever the advantages, the problem remains that at angles higher than the critical angle, the reflectivity of any material is equally low, effectively zero. And the range of energies that are of particular interest to us, say from 10-30 keV no available material has a critical angle above 0.5°.

The road we take to circumvent this problem is the use of a distributed Bragg reflector defect cavity. A sketch of one is shown in Fig. 44. Thin-film Bragg reflectors have been a established tool of x-ray optics for a considerable amount of time now [168, 169], and it has been shown that they can reach reflectivities comparable to those of grazing incidence total external reflection far above the critical angle and at multi-keV energies [170]. This enables us to extend a concept used with great success in semiconductor quantum optics at the interface between visible light and the near-infrared into the domain of hard x-rays. This concept is the DBR defect cavity [171, 172, 173, 174]. Its principle is fairly easy: Between two DBRs a defect is introduced. This defect takes the shape of a layer longer than the unit cell length. Depending on the length, index of refraction etc. of the periods and the defect, a defect mode appears within the band gap of the DBR mirrors. Much as for the modes in a conventional x-ray cavity, this defect mode coincides with a highly localized wave field

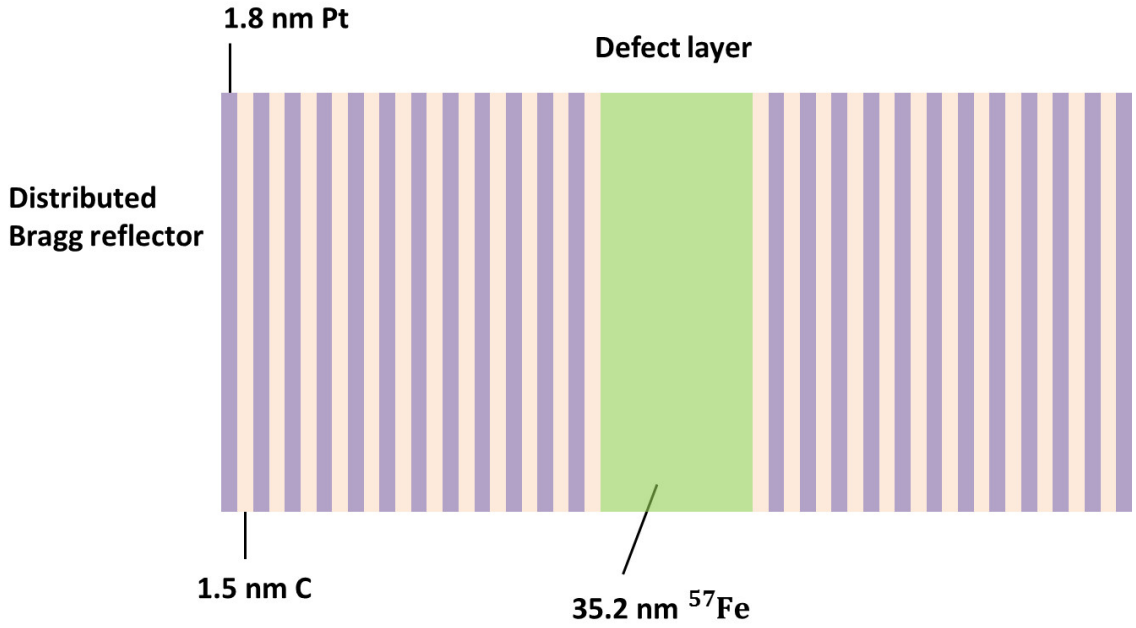

Figure 44: *A distributed Bragg reflector defect cavity. Two Bragg mirrors, stacks of double layers with alternating indices of refraction, sandwich a defect layer, in which a wave will be localized. In our case, we use a defect layer entirely of resonant matter; it is also possible to introduce a thin resonant layer into a low-Z defect layer, similar as for the total external reflection cavities.*

at the defect with an enhanced field strength. This is really all we require for quantum optical experiments.

In the following, we present a brief proof-of-principle experiment. We do not observe new quantum optical effects or manipulate the interaction in a fresh and interesting way. We merely prove the viability of DBR defect cavities for applications in x-ray CQED. To our knowledge, this is the first time such cavities have been examined in the x-ray range.

V.5.2. Experiment and Results

The experiment was performed at the ID18 endstation of the ESRF. To distinguish prompt pulse electronic radiation and the delayed nuclear resonant scattered radiation we used the polarizer analyzer setup. Consequently, of course, the cavity was placed in a constant external magnetic field with the magnetization parallel to the beam (Faraday geometry) to allow only the coupling between ± 1 transitions and the incoming light. To measure electronic reflectivity curves, the

analyzer was slightly detuned. For measuring only the resonant signal, we optimized it for maximum suppression of the prompt pulse. To perform the energy analysis, we used a $1\mu m$ thick stainless steel analyzer foil enriched with ^{57}Fe which was moved at velocities between $\pm 10\frac{mm}{s}$, permitting the detection of radiation between $\pm 103\Gamma_0$. The sample itself consisted of two stacks of DBR mirrors with respectively 12 and 13 periods of 1.8 nm Pt and 1.55 nm C (average sizes) between which a layer of solid ^{57}Fe with a length of 35.2 nm was positioned. The ^{57}Fe was magnetically ordered which leads to strong hyperfine interactions and an attendant splitting. Due to the Faraday geometry, we only coupled to ± 1 transitions. The reflectivity curve is given in Fig. 45, along with a simulation performed by GenX [110] confirming the above values. The dip indicating the defect mode is hardly visible, both in simulation and signal; this is partly a result of the roughness, partly due to the high absorbance of Pt; repeating this experiment with Pd for instance would yield far better results.

The most important graph of that figure is the bottom one however. This signal results purely from nuclear resonant scattering. It turns out that the signal is the highest at the position of the defect cavity mode, marked by 1 in the figure. This confirms our assumption that the cavity mode enhances the interaction of the nuclear ensemble with the light.

In the figure, we have not only marked the defect mode, but also several other modes by black lines. These modes are essentially standing waves within the DBRs, not within the defects. Since they have some evanescent tails, they also couple to the nuclear ensemble in the defect. At any angle, the nuclear resonant signal is probably a result of the interaction with several different modes, as evidenced by the fact that the nuclear signal does not split into peaks which occur at the same angular positions as the electronic dips.

To examine the cavity-mode interaction further, we have taken an energy spectrum of the reflectivity by means of the SS absorption foil. It is displayed in Fig. 46, along with a simulation. Clearly there are some discrepancies between the spectrum and the corresponding simulation. To account for them, recall that the simulation in Fig. 45 overestimates the quality of the cavity; the dips are far deeper in the simulation. We have calculated the energy spectrum simulation by extracting the cavity parameters from the GenX fit, and calculating the reflectivity spectrum via CONUSS, accounting for the detection mechanism. Since the contrast of the electronic reflectivity is worse than the fit can explain, it is obvious that the same must happen in the nuclear reflectivity, and indeed, that is exactly what can be observed. The functional shape of the spectra are identical, but the contrast between background and dips are higher in the simulation. The physical reason behind this is probably a long-range roughness which is enhanced with every added period and cannot be modeled straightforwardly by the fit.

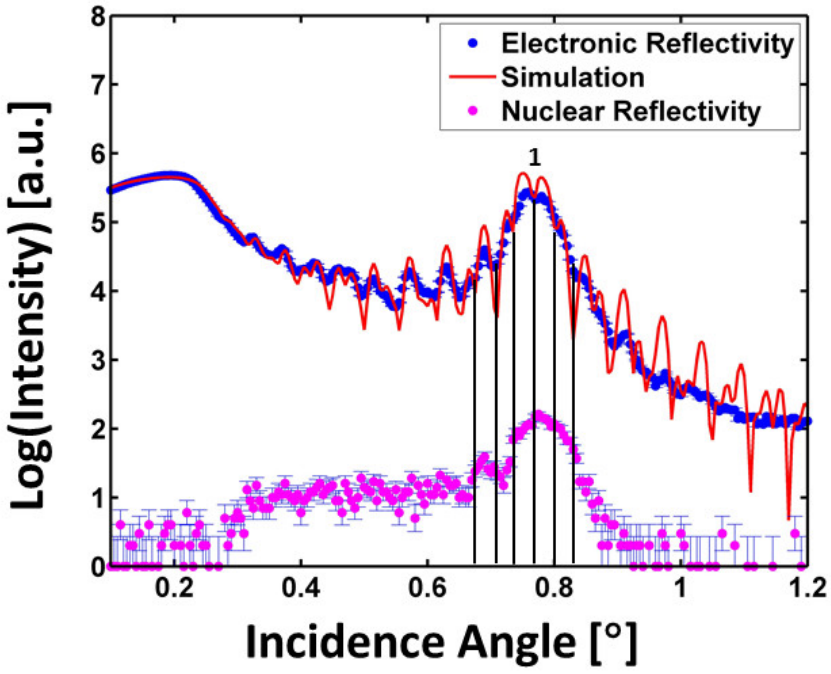

Figure 45: *Reflectivity of the DBR defect cavity. The electronic reflectivity is fitted by GenX, giving an overall good fit, although the contrast of the oscillations is not properly retrieved. This is probably a result of the roughness increasing with increasing number of layers, which cannot be fitted by GenX. The nuclear reflectivity shows that the interaction is strongest around the defect mode, which is marked by 1 in the figure. Several other modes, standing waves of the Bragg mirrors and marked by black lines, also interact with the resonant layer, even when angularly detuned from the incident beam, hence the modes cannot be resolved in the nuclear reflectivity. This could probably be changed by making the defect layer not solid ^{57}Fe, but introducing a thin resonant layer into a thick non-resonant defect layer. The evanescent tails of the gap edge modes of the mirrors will couple weakly to that layer.*

In Fig. 46 (b) we have plotted the spectrum without taking into account the detection mechanism. Here, one the splitting between the peaks than can be seen in (a) is even more pronounced. The splitting is effectively a multi-mode based effect. To prove this, we show the energy spectra plotted for a wide range of angles in two particular situations. In Fig. 47 (a) the reflectivity of the sample without an external magnetic field is shown. This corresponds to a single line sample. It is obvious that the non-defect modes at the corners of the image, although far detuned, have the matter-like parts of their dispersion relation close to the nuclear resonance in the angular range of the defect mode. In Fig. 47 (b) we show how this changes with a magnetic field and a polarizer-analyzer

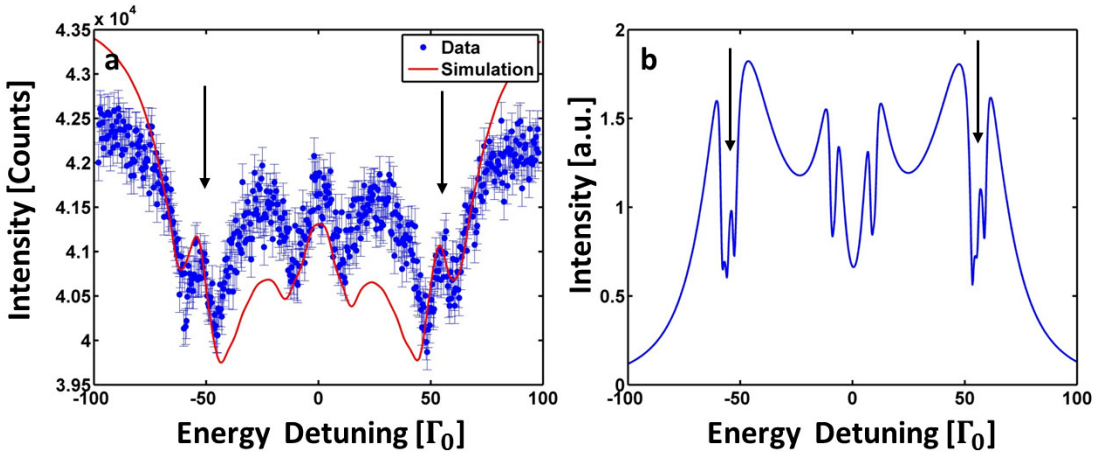

Figure 46: *(a) The energy spectrum of the reflectivity at* 0.76°*, the position of the defect mode. Evidence of quantum mechanical interactions are obvious, but overstated by the CONUSS simulation, which takes as input parameters for the cavity those extracted from the GenX fit. The simulation takes into account the detection scheme involving a stainless steel* ^{57}*Fe-enriched foil of* 1μm *thickness. (b) shows the energy spectrum without the absorber foil. Deep dips are clearly visible, explained in the main text and in Fig. 47. The arrows mark the ssplitting.*

setup. The dips remain dispersionless and visible across the range, even if the the rest of the dispersion relation vanishes. Although four peaks are visible in this scenario, each one interacts with the field as a single one would; there are no spontaneously generated coherences.

In conclusion, we have performed what is to the best of our knowledge the first experiment using a DBR defect cavity for quantum optics in the hard x-ray range. The results are very promising; the interaction is similarly strong as for total external reflection cavities. A significant difference is that the spectral distance of individual modes is less than for conventional cavities. This can be a curse or a blessing, depending on whether the influence of multiple cavity modes is desirable or not. An unambiguous advantage is the fact that the mode bandwidth is smaller even when the angular acceptance remains identical. This offers a possible path towards strong coupling with electronic resonances.

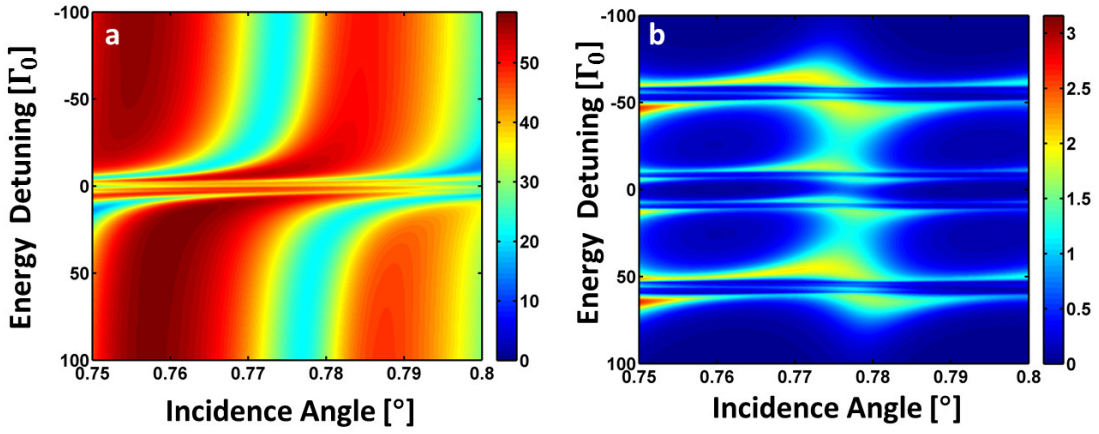

Figure 47: *Energy spectrum of a DBR defect cavity across a range of angles. In (a) we show that of a single-line ^{57}Fe defect layer; the Fano-like anti-crossing is clearly visible. It is also clear that the dips derive from the off-resonant band gap edge modes of the Bragg mirror. These modes play a similar role here as in the experiment with two layers in the cavity. In (b) we show the reflectivity including a hyperfine field of 33.6 T, as in the real experiment. The dips can be identified with those in (a). The intensity is encoded in the color map.*

Chapter VI

X-ray quantum optics in periodic nanostructures

VI.1. Introduction

The aim of quantum optics is to control and tailor the interaction of light and resonant systems. To this end, two important parameters must be controlled. One is the strength of the light-matter interaction; the other is the number of modes of the electromagnetic field that the resonant system interacts with. Too great a number leads to irreversible losses of excitation; the continuum of modes acts as a heat bath for the resonant system.

The prime system for exerting this control, and the one which we have been concerned with in the previous sections is a resonant cavity. It allows multiple modes; but for high-Q cavities, all but one of them are so far detuned from a judiciously chosen matter resonance that they can be ignored. However, our cavities are not single mode cavities even in that sense; them being essentially Fabry-Perot filters, the electromagnetic fields in them are quantized in the direction orthogonal to the surface, but continua in the two other dimensions. A scrupulous treatment of such a interaction reveals that while it is not technically impossible to reach the strong-coupling limit or observe other coherent effects, it is very hard and can only be done in very particular circumstances. However, we observe such effects, because our resonant system is a collective excitation spread in space, at least compared to the wavelength of the exciting radiation. As we have described previously, this enforces a coupling with one particular mode of the electromagnetic field, namely the one the nuclear exciton has been excited from. The cavity's role is merely to enhance the interaction strength by amplifying the electromagnetic field strength at the position of the resonant

layer.

This points the way to another method of coherent control. Since our nuclear exciton interacts with only one mode anyway, we can focus on enlarging the interaction without making use of a cavity, but by enlarging the number of nuclei that partake in the nuclear exciton, as the collective interaction strength depends on that number.

In the following, we will focus our attention in periodic multilayers or periodic resonant systems. These, often referred to in quantum optics as resonant photonic crystals or resonant optical lattices also restrict the number of modes the resonant matter interacts with. We will begin with a simple quantum optical toy model describing the fundamental physical features of the propagation of light through such systems.

VI.2. A nuclear optical lattice

The theory in this section is taken from [175]. The Hamiltonian of a system of N two-level atoms interacting with the electromagnetic field is

$$H = \sum_i^N \omega \sigma_i^\dagger \sigma_i + \sum_{\vec{k}} \omega_{\vec{k}} a_{\vec{k}}^\dagger a_{\vec{k}} - \sum_i^N \sum_{\vec{k}} g \sigma_i^\dagger a_{\vec{k}} e^{i\vec{k}\vec{r}_i} + g^* \sigma_i a_{\vec{k}}^\dagger e^{-i\vec{k}\vec{r}_i} \tag{129}$$

where $\sigma_i^\dagger(\sigma_i)$ are the creation (destruction) operators of a single nuclear excitation at position $\vec{r}_i$; g is the coupling constant; $\vec{k}$ is the wave vector of any electromagnetic field mode, and ω and $\omega_{\vec{k}}$ are the energies of the nuclear excitation and any field mode. The Hamiltonian is in the Coulomb gauge; the rotating wave approximation has been performed. We suppose that the nuclei are localized in an ordered array. Such a system of ordered resonant or near-resonant systems is implemented in an optical lattice. While our system is not quite the same as that it bears many similarities, and many of its features can be understood in terms of optical lattice phenomenology. We will therefore refer to our system in the following as an optical lattice. A sketch is given in Fig. 48.

We then perform the by now familiar transformation of defining an operator that acts upon a state in the Dicke state space; this is basically a Fourier transform of the operator:

$$b_{\vec{q}} = \frac{1}{\sqrt{N}} \sum_i b_i e^{-i\vec{q}\vec{r}_i} \tag{130}$$

$$b_{\vec{q}}^\dagger = \frac{1}{\sqrt{N}} \sum_i b_i^\dagger e^{i\vec{q}\vec{r}_i}. \tag{131}$$

$\vec{q}$ is the reciprocal space wave vector. The sum is limited to $\vec{q}$ in the first Brillouin zone; anything beyond that would imply that there were excitations in between the atoms. We also restrict ourselves to one excitation, which means that we can 'bosonize' the excitation [176]; the transformed

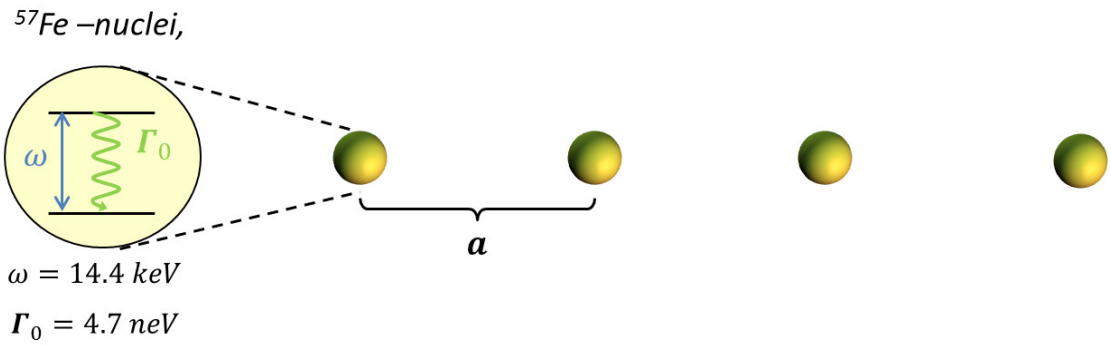

Figure 48: *Sketch of a nuclear optical lattice. It consists of periodically arrayed ^{57}Fe-nuclei with a distance of a. Strictly speaking, optical lattices are experimental implementations of such an array of resonant systems; we will use the term colloquially for the structure in general, which is a toy model describing the features of the propagation of light through our multilayers.*

operators are subject to a bosonic commutation relation $[b_{\vec{q}}, b^\dagger_{\vec{q}'}] \approx \delta_{\vec{q}\vec{q}'}$. For simplicity, we also assume that the array of atoms is one-dimensional, and drop the vector signs. We also set G as the reciprocal lattice vector, which will take the role of the impulse transfer vector. Substituting the above into Eq. (129) we get

$$H = \sum_k \omega b^\dagger_q b_q + \sum_G (\omega_{q+G} a^\dagger_{q+G} a_{q+G} - \sum_G ig\sqrt{N} b^\dagger_q a_{q+G} - ig^*\sqrt{N} a^\dagger_{q+G} b_q) \tag{132}$$

where the sums over G involve all reciprocal lattice vectors. However, here we are merely interested in the first one. The Hamiltonian then involves modes whose annihilation operators are a_q and a_{q+G}, which all couple to the same collective nuclear excitation. We should expect that the modes and the nuclear excitation mix then. The mixing is strongest when the energy of the participating photons and nuclear excitations are equal. The mode energies are equal in two cases (a) when G is zero and (b) when G is the first Brillouin zone vector. We can therefore restrict the sum over G in Eq. (132) to these two photon modes. The Hamiltonian is easily diagonalized, and yields the dressed state energy dispersion relations

$$\begin{aligned} E_0 &= \omega_q \\ E_\pm &= \tfrac{\omega+\omega_q}{2} \pm \sqrt{(\tfrac{\omega-\omega_q}{2})^2 + |g|^2} \end{aligned} \tag{133}$$

where $\omega_q = cq$. The requirement that only the above two modes are involved in the Hamiltonian is, of course, nothing but a restatement of the Bragg condition. If it is not quite fulfilled, the modes will have slightly different energies, and consequently mix differently. Other modes are physically involved, but their contributions are minimal. Of course, the Bragg condition is usually stated for

non-resonant scatterers or atoms; therefore, we will briefly discuss the differences that arise in the above dispersion relations. At first glance, we notice that $E_\pm$ corresponds exactly to the standard polaritonic dispersion relation of light-matter coupling. Of course, with the system being periodic, the branches of the polariton dispersion relation for which $k_z > \frac{\pi}{a}$ have to be folded back into the first Brillouin zone. The dispersion relation is shown in Fig. 49. The second remarkable instance is that the dispersionless E_0 branch of the dispersion relation is essentially a purely photonic superposition of the two modes - a 'photonic' polariton [175]. The similarity of the Hamiltonian to the EIT Hamiltonian indeed suggests that it bears some similarities to the dark state of that system. It is a photonic state that does not couple to the nuclei. In a true optical lattice, this is the standing wave that forms the optical lattice. All other electromagnetic waves interact with the nuclei, and are therefore expelled from the array. Now, what happens when the array is periodic in only one dimension, and light illuminates it at an angle? The wave vector of the light impinging on the structure changes only in the direction of periodicity. Expressing the wave vector component in that direction z in terms of the angle and the index of refraction, we can rewrite the dispersion relation of uncoupled light:

$$\omega_{q_z} = \frac{c q_{0z}}{\sqrt{n^2 - sin^2(\alpha)}} \tag{134}$$

where α is the angle of incidence measured from the parallel to the surface. q_{0z} is the free-space component of q in z-direction, and n is the (non-resonant) index of refraction of the medium. Strictly speaking it is not necessary in this case, because we assume that all scattering contributions stem from the resonance. In that case it can be set to one. This term can now be inserted into Eqns. (133). Instead of changing k, the wave vector of the incoming radiation in order to probe the system, we can change the angle of the incoming radiation and scan its energy for an angular position to do so. For all practical purposes in our experiments, the tuning capabilities afforded by this parameter are way too coarse, and we also have to perform some energy analysis via Mössbauer spectroscopy-like techniques. When the system is angularly slightly detuned from the Bragg condition, then $\omega_q \neq \omega_{q+G}$, and the diagonalization does not yield the simple form of Eq. (133). It is more convenient to diagonalize it numerically. An example is shown in Fig. 49 (b). Now, the central band corresponding to the dark state has a slight dispersion. One can show that it can be approximated by a harmonic oscillator potential around the Bragg peak. Just as with excitonic systems in semiconductors, the quasiparticle associated with the band then has an effective mass, which can be positive or negative depending on the detuning. Similar observations in excitonic microcavities have led to interesting results [177].

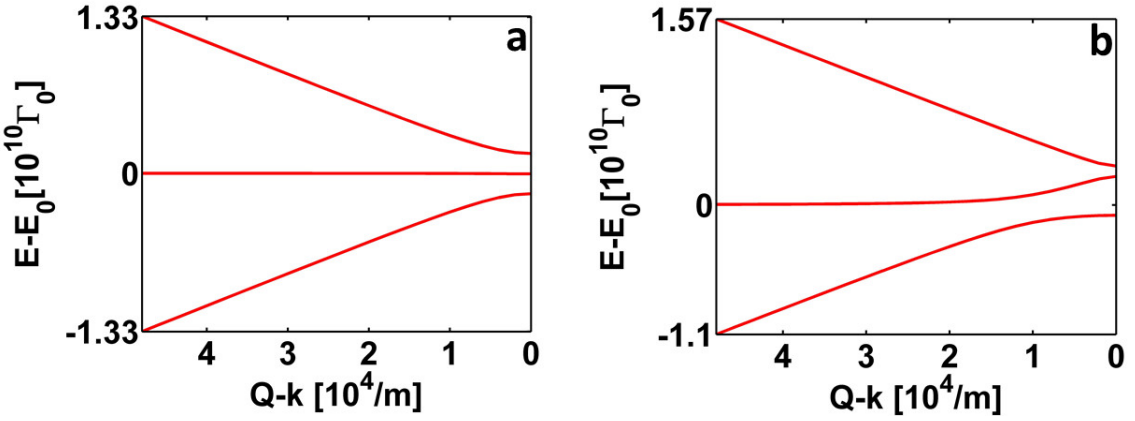

Figure 49: *The dispersion relation of an optical lattice at two different angles. The lattice parameter a is* 2.8*nm. Q is the wave vector for which* $k_z = \frac{\pi}{d}$*. (a) Dispersion relation at the Bragg angle, 0.0158 rad. The dispersionless contribution in the center of the band gap is clearly visible. This is the dark photonic state. (b) Dispersion relation detuned by* -11 *mrad. The center allowed band is slightly deformed; we have one (upper) photonic band gap and one (lower) polaritonic one. If the detuning were opposite, the band gaps would change their character as well.*

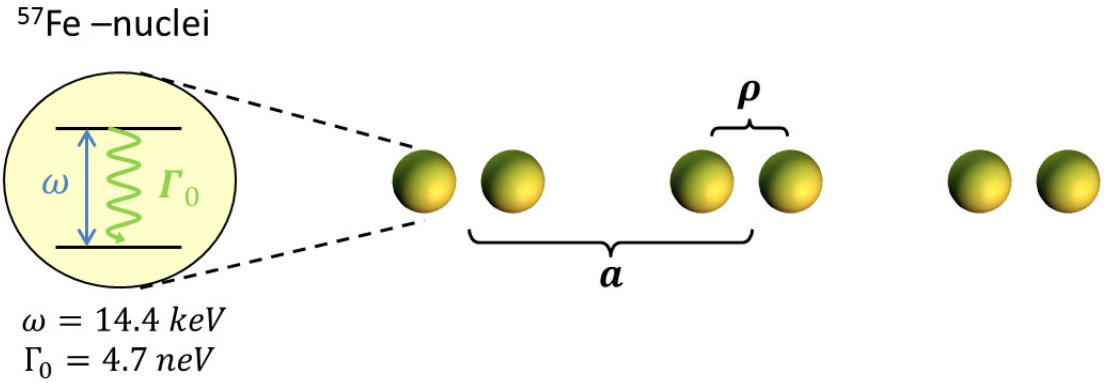

Figure 50: *A bichromatic optical lattice. It consists of an optical lattice with two atoms per unit cell. The unit cell length is a, the distance of the atoms within the cell is* ρ*.*

VI.2.1. A bichromatic nuclear optical lattice

The theory of Chong et al. was extended to the case of a bichromatic optical lattice in [178]. We give a condensed account of that work here.

We have already pointed out that the experimental system we employ to perform quantum optical experiments consists of one-dimensional multilayers, either non-periodic ones for cavity

QED or periodic MLs to simulate nuclear optical lattices or nuclear resonant photonic crystals. The model discussed in the previous section is a good toy model for understanding the most simple features of such systems. However, in experimental setups, we will usually employ ^{57}Fe layers which are several monolayers thick. To model this, we discuss a periodic system of resonant nuclei which contains two nuclei per unit cell. Such a system is often referred to as a bichromatic optical lattice; this is on account of the fact that to produce such a system with cold atoms, two laser beams with slightly detuned frequencies, i.e. different colors are required. An example of such a system is sketched in Fig. 50. The length of a unit cell is a; it contains two atoms, with a mutual distance of ρ. Only minor additions to the model of the previous section are necessary, but they yield significant differences in the photonic band structure and hence, reflection spectrum. The obvious requirement is the introduction of a second nuclear exciton or, in more general terms, collective excitation in momentum space. To distinguish it from the previous one, we denote its raising (lowering) operators by $d(d^\dagger)$:

$$d_q = \frac{1}{\sqrt{N}} e^{i\rho} \sum_i d_i e^{iqr_i}. \tag{135}$$

The reader will notice that we have appended a global phase factor of $e^{i\rho}$ to the sum, in order to account for the distance of the atoms in the gap. It is then intuitively clear that this nuclear exciton is a collective excitation shared by all the second atoms of each unit cell in the crystal; b_q is, as before shared by the other ones. Again, we assume that the excitons have a low excitation number, allowing us to bosonize them and to use bosonic commutation relations. Then, by a similar line of thought as in the previous section, we derive the Hamiltonian

$$H = \sum_k \omega b_q^\dagger b_q + \sum_G \omega_{q+G} a_{q+G}^\dagger a_{q+G} - \sum_G \left[ig\sqrt{N}(b_q^\dagger + e^{i\rho} d^\dagger) a_{q+G} - ig^* \sqrt{N} a_{q+G}^\dagger (b_q + e^{-i\rho} d_q) \right]. \tag{136}$$

Here, two nuclear excitons couple to two modes each, meaning that there is not only an effective coupling between the modes, but also between the nuclear excitons. We have assumed that the nuclear excitons have the same energy as well as the same coupling strength to the electromagnetic field. If we curtail our interest to the region around the Bragg angle, this is well satisfied, since in this region the z-component of the wavevector is approximately as long as the inverse period, meaning that all nuclei of a particular nuclear exciton are coupled to the modes in phase.

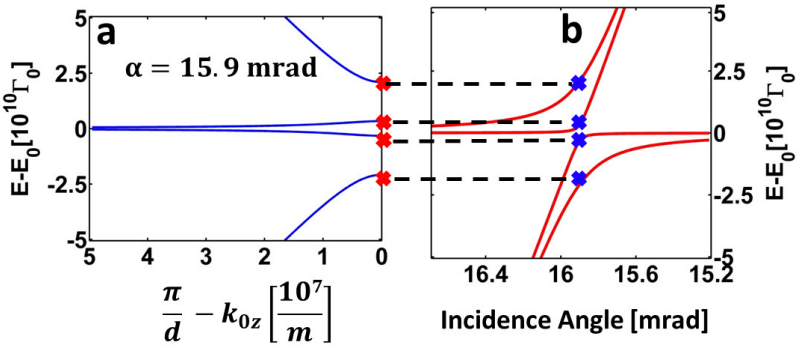

Figure 51: *The dispersion relation of an infinite bichromatic optical lattice. In (a) we show the dispersion relation in k-space for the angle of 15.9 mrad, which corresponds to the perfect Bragg position for the given parameters. The points marked by the red crosses in the figure represent the band gap edges. Between them, there are no allowed polaritonic states of any kind; that is why any light with a frequency in this region gets reflected. By detuning the angle, we change the dispersion relation and the energy of the band gap edges, so that there is a band gap dispersion, which is plotted in (b). In angular space, the band gap dispersion has a strong similarity to the avoided crossing of polaritonic light-matter systems or single atom-cavity strong coupling setups. We have strongly exaggerated the coupling strength in this figure so as to make the effects visible clearly.*

VI.2.2. Experiment

In Fig. 52 we show the setup we have used in this experiment, which was performed at the ID18 endstation of the ESRF in the $7/8+1$ bunch mode.

We have used the polarizer-analyzer setup we have described in the experimental methods section. The high purity that setup provides has permitted us to dismiss using the high-resolution monochromator and rely entirely on the high-heat load monochromator of ID18, which provided us with 14.4 keV radiation with a bandwidth of about 0.3 eV. The sample itself was magnetized by a magnetic field applied in the direction of the beam, a setup often referred to as the Faraday geometry [56, 63]. In this geometry, the ^{57}Fe line is split into six different transitions, only four of which can be excited, namely the ones which involve a $m = \pm 1$ change of the magnetic quantum number. This means that every photon that is scattered by a nucleus undergoes an orthogonal change in polarization (the system is optically active), which allows the user to distinguish between resonantly scattered photons and the prompt. The incoming radiation was σ-polarized, with the polarizer refining the purity. The analyzer only transmitted π-polarized radiation onto the APD. The quality of the setup was such that even despite the absence of the

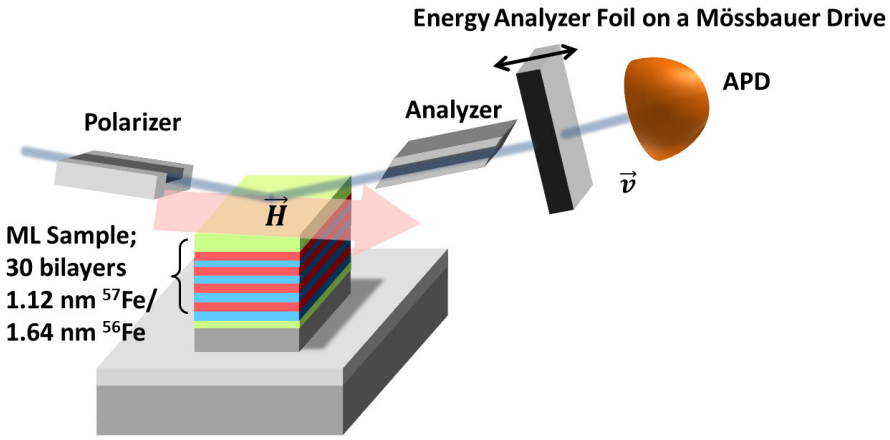

Figure 52: *Setup for measuring the reflectivity of a nuclear optical lattice.* 14.4 *keV radiation is guided through a polarizer to ensure pure σ polarization. It impinges in grazing incidence on the sample, where it undergoes strong $\sigma \to \pi$ orthogonal scattering. An analyzer transmits al π-polarized radiation, the energy of which is analyzed by a Mössbauer stainless steel absorption foil enriched with ^{57}Fe to* 95%. *The foil is mounted on a Mössbauer drive. The suppression of non-resonant radiation by the polarizer/analyzer setup makes both the high-resolution monochromator and time-gating of the APD superfluous.*

high-resolution monochromator, we were able to eschew the use of time gating. The energy analysis was performed by mounting a 6μm thick stainless steel foil, 95% enriched with ^{57}Fe on a Mössbauer drive. The velocity of the drive was $\approx \pm 10 \frac{mm}{s}$, yielding a width of the spectrum of $\pm 103\Gamma_0$.

The sample consisted of 30 periods of 1.12 nm^{57}Fe/ 1.64^{56}Fe, sandwiched by 2 4-nm Ta-layers. The bottom layer was deposited to ensure adhesion of the multilayer to the substrate; the top-layer was added to avoid oxidation. Since the electronic reflectivity cannot distinguish between resonant and non-resonant iron, the numbers above were extracted from the measured resonant energy spectra. They should be interpreted as average thicknesses; it is not possible to sputter layers with such precision. Even minimal changes in these thicknesses change the theoretical results drastically however. The first experimental step was to take reflectivity measurements, both resonant and non-resonant. To take the latter, the polarizer was slightly detuned from the position of maximal extinction, whereupon the electronic signal could be measured as well. The result is shown in Fig. 53. The peak visible in the resonant signal has no equivalent in the electronic one.

We therefore can conclude that it is of purely nuclear origin.

The second step involved tuning the sample at angles around the Bragg peak and measuring spectra by introducing the stainless steel foil on the Mössbauer drive into the beam. We present

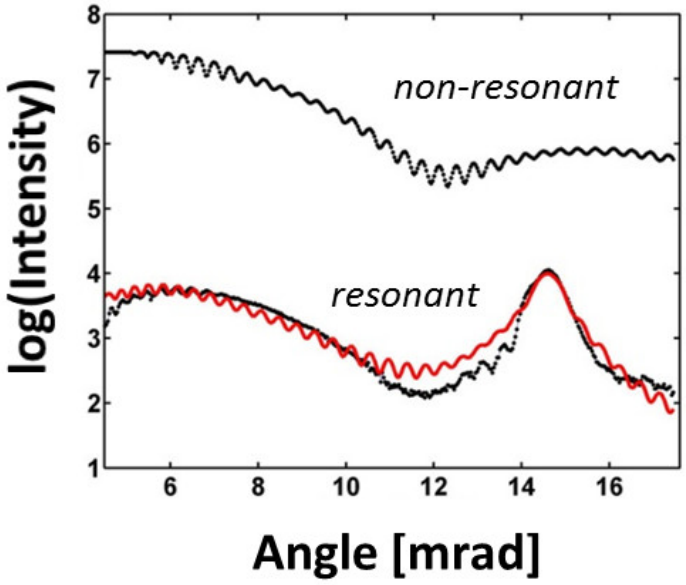

Figure 53: *The non-resonant and energy-integrated resonant reflectivity of the sample. The red line is a simulation of the non-resonant reflectivity yielding average period dimensions of* $1.12nm^{57}Fe/1.64nm^{56}Fe$*. The Bragg peak is purely nuclear, i.e. it has no equivalent in the electronic reflection.*

the results in Fig. 54

We begin our discussion of the results with the TMM simulations. In Fig. 55 we have plotted real and imaginary parts of the dispersion relation of an infinite layer with a period given by 1.12 nm ^{57}Fe/1.64 nm ^{56}Fe. The ^{57}Fe layers are 95% enriched. The color encodes the value of the wave-vector of the polaritons, corresponding to the energy of the light (y-axis) illuminating the sample at an angle (x-axis). Deep red corresponds to a wavevector of π/a, i.e. light that fulfills the Bragg condition. The band gaps can be seen to undergo an anticrossing that is qualitatively remarkably close to the band gap dispersion calculated by the quantum optical toy model for a bichromatic optical lattice. An added feature is a spectrally thin, almost dispersion-less band gap close to the nuclear resonance, shown in Fig. 56 (a). Since the nuclear resonant layer contains about 4-5 monolayers of ^{57}Fe, it is likely that weakly coupled extra atoms are the cause of this feature.

The imaginary part in Fig. 55 warrants some discussion, as it cannot be interpreted straightforwardly. It consists of three distinct contributions: (1) the nuclear resonant absorption, (2) the electronic absorption, and (3), the extinction coefficient. Clearly, the resonant absorption channel is dominant at and around zero detuning. At its peak, it is the strongest contribution to the

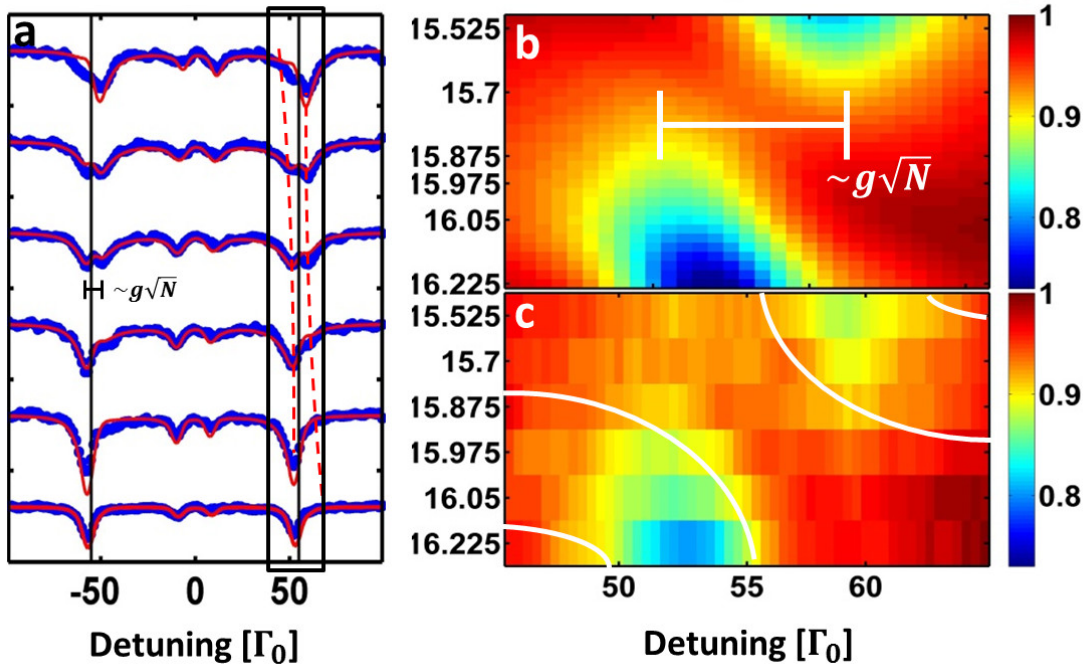

Figure 54: *Energy- and angle resolved reflectivity measurements and simulations. (a) overview of the measurements, simulations are in red, measurements in blue. The agreement is excellent. The dashed red line is a guide to the eye for the anticrossing. The section of the spectrum in the black box is reproduced in (b) for the simulation and (c) for the data, where the x-axis shows the energy detuning, the y-axis shows the angle, and the intensity is encoded in the color map.*

imaginary part of the dispersion relation, but it follows a Lorentzian line shape, and off-resonance quickly becomes negligible. There is no dependence on the angle of illumination. The electronic absorption is constant over all angles and energies (at least, in this limited energy range); compared to the nuclear absorption at zero detuning it is very weak, but far off-resonance, it dominates over the negligible nuclear absorption. The final contribution is the extinction coefficient, which is the most important one for the purposes of this discussion. The extinction coefficient determines how well the sample expels and reflects incoming light. If the extinction coefficient is high, very few periods suffice to reflect the light almost completely; if it is low a great many periods are needed to achieve the same. The extinction coefficient depends exclusively on the difference of the real parts of the indices of refraction of the two materials forming the multilayer. If, as in the present case, the difference depends on a resonant, energy-dependent index of refraction, then the extinction coefficient does too. Close to the resonance it is strong; far off, it gets progressively

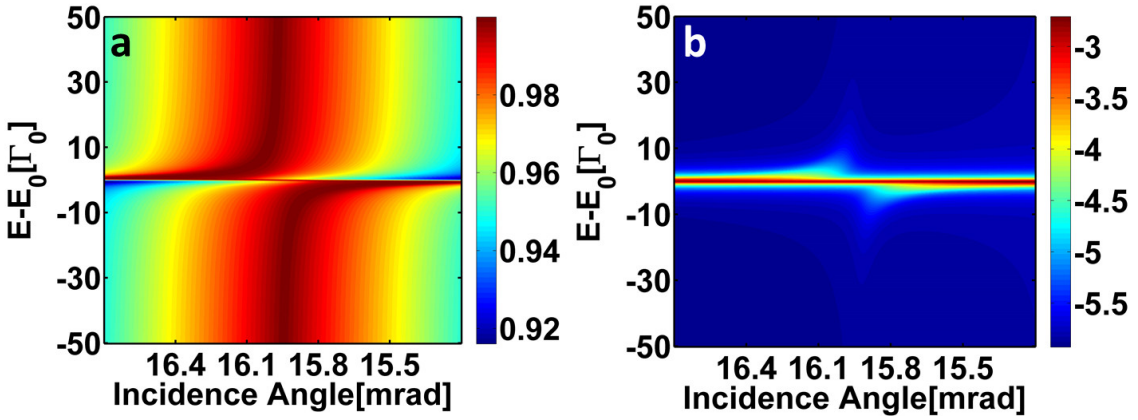

Figure 55: *Simulations of the real and imaginary parts of the dispersion of an infinite multilayer calculated with the transfer matrix method. We have chosen an ML with a* 1.12 *nm* ^{57}Fe/1.64 *nm* ^{56}Fe *period, and a single, unsplit line. The magnitudes of the real and imaginary parts of the dispersion relation are encoded in the color bar, and displayed for a range of angular and illuminating light energy detunings. (a) shows the real part; Re(k_{0z}) is given in units of π/d, i.e. the closer the value is to one, the closer the values of the corresponding wave vector are to the Brillouin zone border. The range in which they are approximately one constitutes a band gap, and is displayed in a dark red hue. An anticrossing between two bands is clearly visible, as well as a spectrally narrow, dispersion-less contribution close to the nuclear resonance. In (b), the imaginary contributions are presented. They are large around the resonance, and smaller off it, but the off-resonance anti-crossing behaviour is still visible. Note that the magnitude is encoded logarithmically in order to view off-resonant contributions in greater detail. For further discussion, see the text.*

weaker. This makes for a rather complicated interplay between the extinction coefficient and the absorption coefficients. At the resonance, i.e. at an energy detuning of zero or close to it, the extinction coefficient is strong; but the nuclear absorption is stronger. Far detuned from the resonance, the nuclear absorption is negligible, the extinction coefficient is stronger than the nuclear absorption, but weaker than the electronic one. In between these two extremes is a region where the extinction coefficient dominates both the electronic and nuclear absorptive channels; it is here that we expect strong reflection even with relatively few layers. Luckily, this region is close to the point where Bragg position and resonance coincide, i.e. around the anticrossing visible in Fig. 56 (b). In Fig. 57 we show the reflectivities for the above structure for different numbers of layers. For larger numbers, the splitting slightly increases, which can be interpreted in terms of the quantum optical model: a greater number of nuclei leads to a larger collective coupling strength $g\sqrt{N}$. Also, off-resonance the reflectivity increases with increasing period number; this can be explained in terms of the fact that for a larger number of layers, the system gets closer to

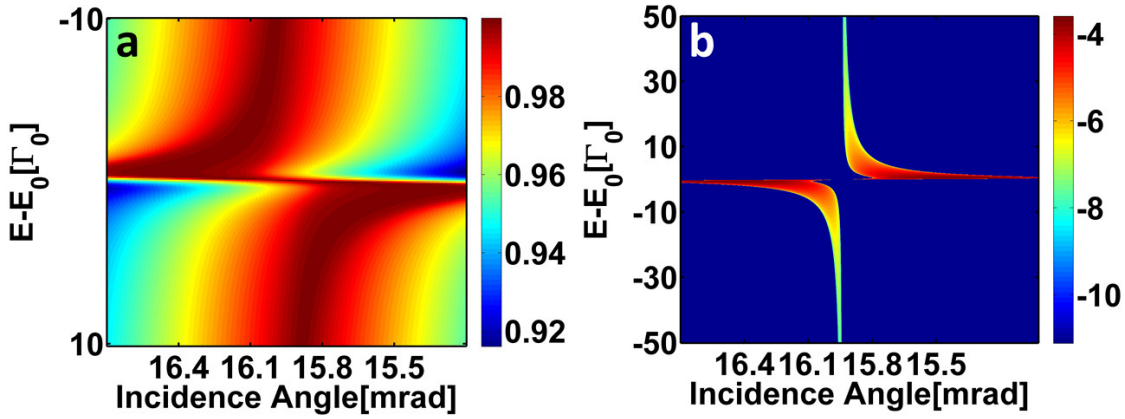

Figure 56: *Details of simulations of the real and imaginary parts of the dispersion of an infinite multilayer calculated with the transfer matrix method. The structure is the same as in Fig. 55. In (a), we show an enlarged detail of Fig. 55 (a), so the low-dispersion band can be observed. In (b), we show the extinction coefficient contribution to the imaginary part of the dispersion relation. The magnitude of the extinction coefficient determines how strongly impinging light is reflected. It depends on the real part index of refraction difference of two materials constituting a periodic multilayer. (b) was plotted by 'turning off' all electronic and nuclear absorptive parts in the TMM. The anticrossing of the band gaps is clearly visible. Note that the color map is logarithmically encoded.*

the ideal infinite periodic system we have based the quantum optical model on.

As final evidence that the quantum optical model of the previous section and the TMM deliver are in agreement, let us point to Fig. 58 where we have plotted the reflectivity of our system in (a). This is equivalent to Fig. 54 (b) but without the inversion due to the stainless steel foil absorption. Here, we have calculated the behaviour for only one resonance line; but this is not an issue since the four resonances of the experiment behave identically and independently from each other. In Fig. 58 we show the reflectivity of a sample with the same period, but a number of 100 periods; and finally in (c) the dispersion of the band gaps according to the quantum optical model. It is clear that (b) and (c) have virtually the same qualitative behaviour. We conclude that the quantum optical model is ideally suited to describing the quantum mechanical behaviour of resonant periodic multilayers without a background refractive index contrast, such as ours.

But what explains the differences between the model and our measurement? The most important answer to this is obvious; we have a finite number of layers, 30 periods precisely, and this is not enough to justify the assumption that our system is infinite - a key component of the derivation of the QO model. But as the simulation of the reflectivity of a 100-period multilayer in Fig. 58 shows, even for a longer layer, the band gaps are not fully formed. More layers would enhance

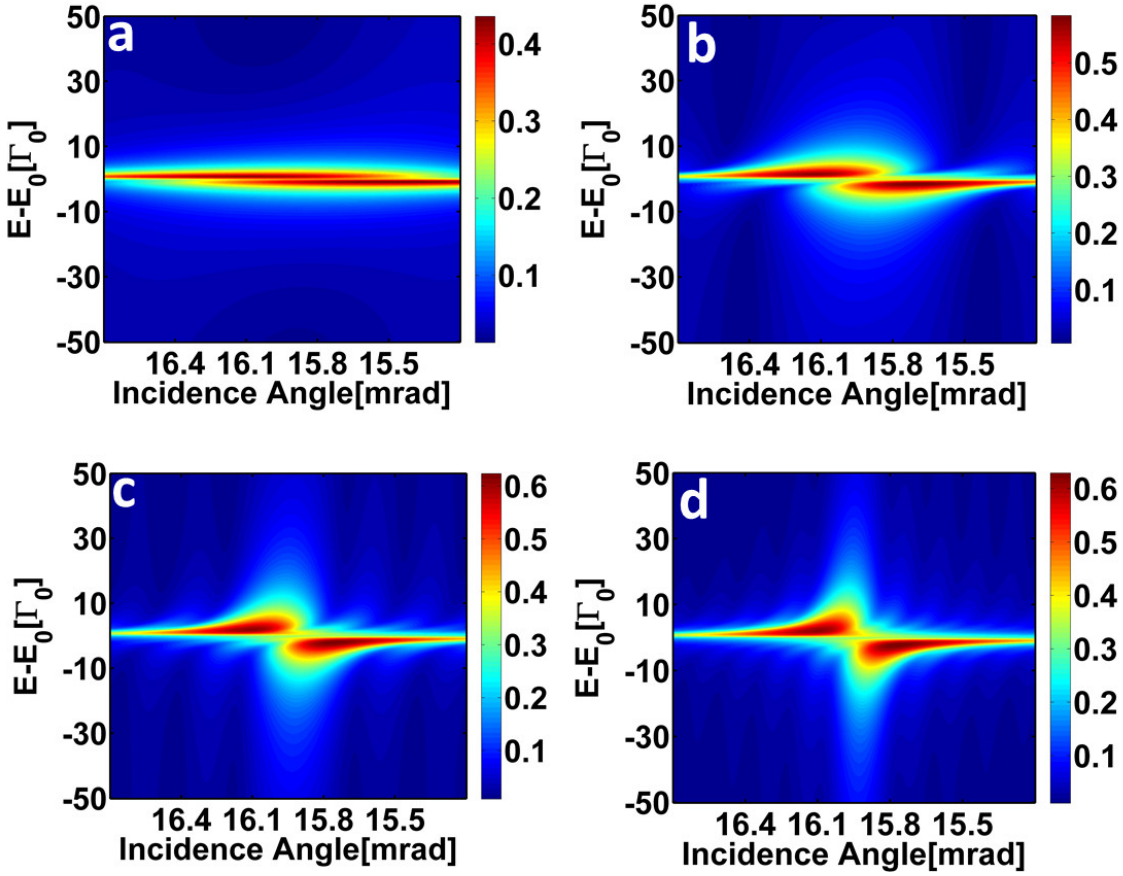

Figure 57: *Reflectivities of a finite ML with* 1.12 *nm* ^{57}*Fe/*1.64 *nm* ^{56}*Fe periods. (a) 10 periods, (b) 30 periods, (c) 60 periods, (d) 100 periods. The initially small splitting grows broader; with increasing number of periods, the off-resonance reflectivity of the band gaps is enhanced.*

the reflectivity. Here, our previous discussion of the interplay of the extinction coefficient and the electronic absorption plays a role. Far off the resonance, the extinction length is smaller than the electronic absorption length - the light gets absorbed, and is only partially reflected. Returning to the QO model, this means that we ought to include dissipativity and absorption to arrive at a more precise quantitative agreement with the experiment. However, to do so is somewhat pointless. It bears repeating that the number of nuclei per unit cell (resonant layer) in the multilayer is about $4-5$; a scrupulous treatment of such a complicated system would be unfeasible, especially since we would have to discard the assumption of infinity of the atomic chain.

Still, the model has served its purpose: we can pinpoint the reason for the splitting we observed in the data to a quantum mechanical reason, which is the strong coupling of two modes of radiation with a collective of nuclei. In this sense, we have reached the strong coupling limit in the x-ray

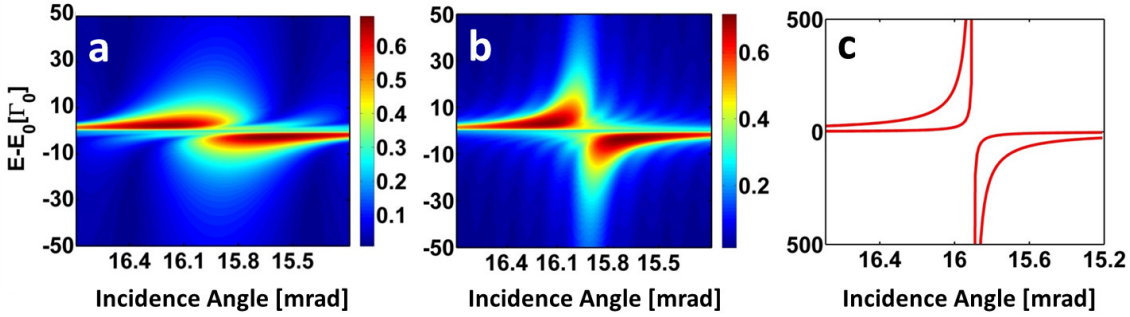

Figure 58: *The reflectivity of a* 1.12 *nm* ^{57}Fe/1.64 *nm* ^{56}Fe *ML with (a) 30 periods (b) 100 periods, and (c) the band dispersion of a nuclear optical lattice. As the number of layers goes closer to infinity, the predictions of the TMM and the quantum optical model tend to agree.*

range with our experiment. But can we use the model to extract the coupling parameter from the data? In a sense, yes. Observe from Fig. 56 (b) that the extinction coefficient is consistently the highest where the band gap edge is closest to the nuclear resonance. That means that the reflectivity will always be highest where the band gap edge closer to the resonance is located; these then, are the positions marked by the peaks in our sample. They can be calculated analytically in the case of the zero detuning from the Bragg peak, see Fig. 51 (b). The edge positions in that case are:

$$\omega_{j,\pm}(q) = \frac{\omega_{k_{0z}} + \omega}{2} \pm \sqrt{(\frac{\omega_{k_{0z}} - \omega}{2})^2 + N2g^2\left[1 - (-1)^j \cos(q\rho)\right]} \tag{137}$$

The edges then have the frequencies $\pm\sqrt{2Ng^2(1-(-1)^j cos(q\rho))}$, and the splitting is $4g\sqrt{N}f_j(q\rho)$ where $f_1(q\rho) = cos(\frac{q\rho}{2})$ and $f_2(q\rho) = sin(\frac{q\rho}{2})$ The difference arises from ρ: If it is smaller(larger) than $0.25a$ the bands marked by $j = 1(j = 2)$ form the inner edges. ρ generally plays a crucial role in this setup; when it is for instance $\rho = 0.5a$, we do not have bichromatic lattice anymore, but a monochromatic one with a period of half the length of the original one. The two central bands then become degenerate. Even in other situations, it can greatly enhance or reduce the interaction strength. Since we have no way of knowing ρ, we have to include it in the parameter we can give. Assuming, without loss of generality that ρ is smaller than a, we can assign

$$4g\sqrt{N}cos(\frac{q\rho}{2}) \approx 8\Gamma_0 \approx 57.3MHz. \tag{138}$$

This is the collective coupling strength of our system.

We finish this section with a brief overview over previous work in similar systems. To the best of our knowledge, two physical systems have yielded phenomena and observations similar to

ours: genuine optical lattices [127, 179, 180] and gratings of excitonic quantum wells. In excitonic quantum wells, a semiconductor is doped periodically; that way, the background refractive index is identical throughout, but there are periodically spaced regions where quantum well excitations are possible [181]. This medium is particular interesting, since it suffers from a similar drawback as ours: too few layers result in an unclear or incomplete formation of band gaps. Since the early 1990s, the results obtained from excitonic quantum wells have been described in a different framework. Instead of assuming an infinite structure, researchers calculated the eigenmodes of these systems for a small ≈ 10 number of layers [182, 183]. In that case, the eigenmodes are one superradiant Bragg mode, which reflects the radiation in a band much wider than the exciton resonance, and a number of dark modes. In a sense, this is the incipient Bragg band gap. However, experiments [184, 185] showed that with an increasing number of layers, dips in the superradiant mode and a saturation of its width appeared; researchers explained this later in terms of band gaps and standing waves within the band gaps [186, 187], much as the quantum optical model of this chapter. Something resembling a bichromatic array of quantum wells was examined in [188]; although the paper has a different focus, the observed phenomena resemble those in this section.

VI.3. A nuclear resonant photonic crystal

In the previous section we have introduced a nuclear resonant optical lattice, i.e. a periodic system where the background index of refraction is constant, but there is a periodic resonant modulation of the refractive index due to the nuclear resonance of ^{57}Fe. In this section, we will extend this work by discussing a nuclear resonant photonic crystal. This is a periodic multilayer in which both the background index of refraction is spatially varied and a periodic resonant modulation is introduced. Samples of this kind have been of great interest for the semiconductor nanostructures community for a long time now [187, 189, 190]. As we shall see, most of the theory we require to explain the observed phenomena has been discussed in previous sections.

VI.3.1. Theory

The basic Hamiltonian for the setup is derived almost exactly like the one in the previous section with the difference of the introduction of an electronic coupling term. We assume an infinitely extended multilayer. In this sample, the nuclear resonant layers are thin enough for us to assume that there is only one atom per unit cell.

$$\mathcal{H} = \hbar\omega a_q^\dagger a_q + \hbar\omega a_{q+G}^\dagger a_{q+G} + \Omega(a_q^\dagger a_{q+G} + a_{q+G}^\dagger a_q) + g_q(a_q S_+ + a_q^\dagger S_-) + g_{q+G}(a_{q+G} S_+ + a_{q+G}^\dagger S_-) \tag{139}$$

where $a_q(a_q^\dagger)$ is the destruction (creation) operator for the first ('incoming') mode, $a_{q+G}(a_{q+G}^\dagger)$ for the second ('reflected') mode and Ω is a term describing the coupling of the two modes via the electronic scattering from the background index of refraction variation. As is well-known from standard optics and solid state physics, at the border of the first Brillouin zone, the bands will split forming a band gap with energetic width Ω. Finally the last two terms describe the coupling of the two modes with the bosonized nuclear exciton, whose creation and destruction operators are called S_+ and S_- respectively. The only difference indeed to the Hamiltonian for the nuclear optical lattice is the direct coupling term of the two modes. Previously, they had only coupled via their common coupling to the nuclear exciton (Fano-Agarwal coupling), but now they have a direct coupling term as well. It follows that there is bound to be some interference, between the coupling mechanisms. A photon can be reflected either via the electronic channel or the nuclear channel. Will the possible interference between these two different quantum paths show up in the spectroscopic signature? As it turns out, it will.

There are two ways to solve the above Hamiltonian. We could go along the lines of the last section, and simply diagonalize numerically. This is the most comfortable way; there are no zeros in the

(3×3) Hamiltonian, making a succinct presentation of the eigenvalue dispersion impossible, as the determinant is a full cubic equation. Alternatively we can go along the lines of Askitopoulos [190] and pre-diagonalize the part of the Hamiltonian that describes the interaction due to electronic scattering. After truncating the Hamiltonian in the one-excitation subspace, it can be represented in the matrix form

$$\begin{pmatrix} \Delta_q & \Omega & g_q \\ \Omega^* & \Delta_{q+G} & g_{q+G} \\ g_q^* & g_{q+G}^* & 0 \end{pmatrix}. \tag{140}$$

Supposing that $g_q = g_{q+G} = g$, we perform the pre-diagonalization of the top-left 2×2 matrix

$$\begin{pmatrix} \omega_+ & 0 & \sqrt{2}g \\ 0 & \omega_- & \sqrt{2}g \\ \sqrt{2}g^* & \sqrt{2}g^* & 0 \end{pmatrix} \tag{141}$$

where the upper two states are now symmetric and anti-symmetric superpositions of the the states where each mode is occupied and the other is not. The eigenvalues are

$$\omega_{+,-} = \frac{\omega_q - \omega_{q+G}}{2} \pm \sqrt{(\frac{\omega_q - \omega_{q+G}}{2})^2 + \Omega^2} \tag{142}$$

and the anti-crossing takes place where $\omega_q = \omega_q + G$ which is of course at the border of the first Brillouin zone.

We have to take into account that $\Omega >> g$, which means that the electronic band gap which is described by the pre-diagonalization is so large that it dwarfs the reach of the nuclear-x-ray interaction in terms of energy detuning. This means that we can effectively ignore one of the above modes; we simply pick whether we want to describe the system at the upper or lower edge of the band gap and only take the interaction with the relevant mode into account. The other mode will have a negligible effect on the Hamiltonian, which reduces to

$$H = \Delta_+ a_+^\dagger a_+ + \sqrt{2}(g a_+^\dagger + g^* a_+) \tag{143}$$

The whole derivation is really a more rigorous form of the observation that the dips close to the band gap of a periodic multilayer can be approximated as Lorentzian close to their center, as shown in Fig. 59

This is consistent with some earlier literature. Bendickson *et al*. derived a transfer matrix method-based way of calculating the density of modes in one-dimensional periodic nanostructures [191], and found that they display peaks where the reflectivity displays dips. On a more theoretical level, John *et al*. found that the properties of spontaneous emission of one [192] and

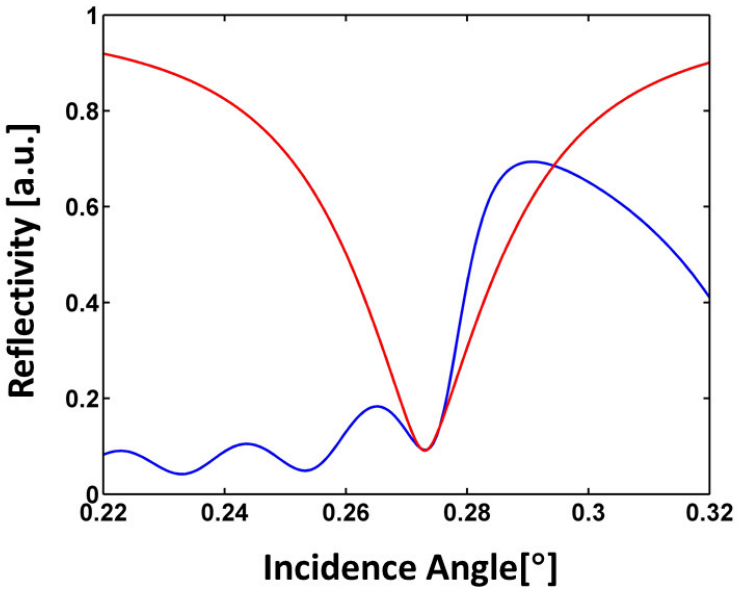

Figure 59: *Contrasting view of a cavity mode reflectivity (red) and the reflectivity of a distributed Bragg reflector close to the band gap (blue). In the region of the dips close to the band gap, the system can be described as a cavity to first approximation*

multiple atoms [193] are strongly altered close to the band gap when the resonant medium is inserted into a photonic crystal. They pinpointed as the reason the extremely high density of photonic states, which rises asymptotically to infinity at the band gap border. But in real, finite systems, the density of photonic states does not rise to infinity. Instead as Bendickson *etal*. have shown, it displays Lorentzian peaks at the points where the reflectivity displays Lorentzian dips. In other words, these dips mimic the effects of cavity modes, which is a different way to state what we have derived above. Askitopoulos *etal*. used this to implement strong coupling in such a system [190] We continue in the spirit of the derivation in Chapter IV.3.1-4. It can be easily seen, that the final result will be the same, since under the conditions we have named (proximity to a reflectivity dip) the reflectivity of the resonant DBR should display the same systematic behaviour as the reflectivity of a single cavity mode. This has led some researchers to name such a resonant DBR a 'unfolded microcavity' [190]. Other researchers predicted and observed 'micro-cavity-like polariton dispersion' in similar systems [194, 195]. To reinforce this point in our system, we show a simulation of a six period 10 nm C/1 nm ^{57}Fe-multilayer in Fig. 60. It clearly shows that at every reflectivity dip, an anti-crossing like behaviour occurs in the energy-resolved reflectivity. All of this is consistent with the well-known fact that at these dips periodic structures support standing

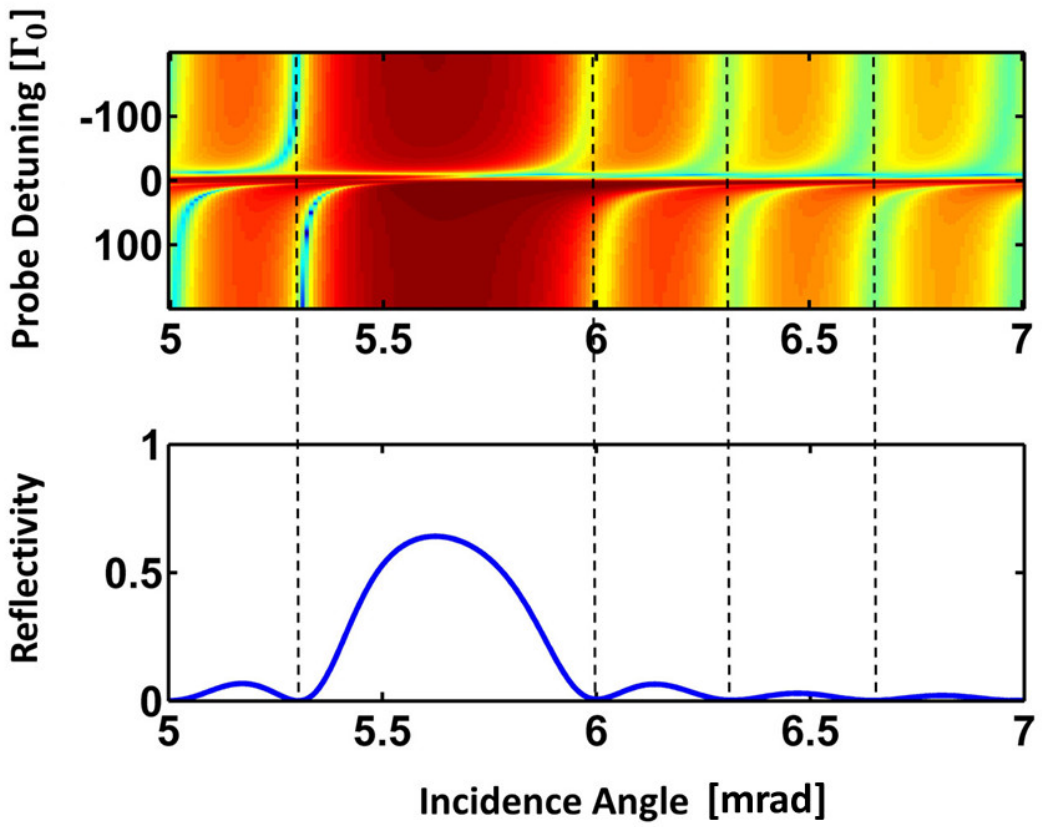

Figure 60: *Reflectivity of a* 10 *nm C/*1 *nm* ^{57}*Fe-multilayer with six periods. The lower panel shows the energy-integrated reflectivity. The upper panel displays the energy-resolved reflectivity around the nuclear resonance. The x-axis displays the angle of incidence, the y-axis the energy detuning. The reflectivity is encoded logarithmically in the color bar. Around* 5.5 *mrad, the anticrossing of the band gap is visible; this is essentially the same effect as described in the section on monochromatic optical lattices. More interestingly, at every position where the energy-integrated reflectivity displays a dip, the energy-resolved reflectivity reveals an anti-crossing behaviour of that dip. This indicates, as discussed in the text, that the dips function as single modes which interact with the nuclear ensembles in the resonant one-dimensional photonic crystal.*

waves [190, 196]

VI.3.2. Experiment

The experiment took place during the same beamtime as the work on the coupling of resonant layers in a dispersive cavity in Chapter V.3, which we refer the reader to for details of the setup. Of course, it suffered from much the same problems, and the data is subject to similar limitations as

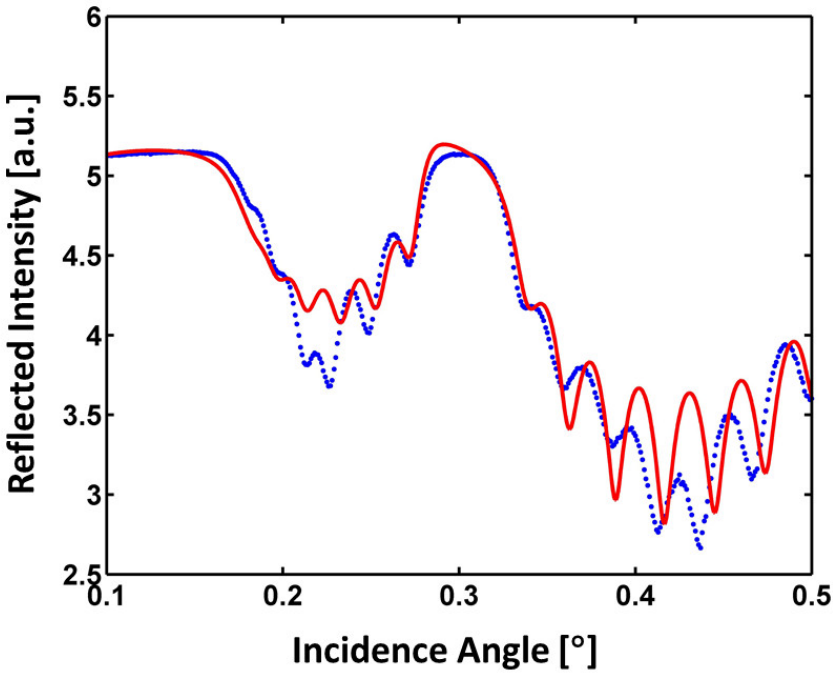

Figure 61: *Fit of the reflectivity curve of the nuclear resonant one-dimensional photonic crystal. The parameters extracted are given in table VI.1.*

in the previous experiment. One exception applies; we have introduced a slit before the KB-mirror shown in Fig. 28 which reduced the beam size and with it the divergence. Otherwise, little has changed. For the postprocessing of the data we refer the reader to Appendix B where we have covered the scheme in some detail.

VI.3.3. Results

As usual, we begin by taking a non-resonant reflectivity curve and using the fit program GenX [110] to extract the parameters of the sample. The reflectivity and its fit are shown in Fig. 61; the corresponding properties of one period are shown in Tab. VI.1.

Since the beam width was not changed from the dispersive-cavity-experiment, we expect that it is the same, about $17\mu m$. On the other hand, we have introduced slits in front of the KB mirror, which reduces the divergence of the beam; the fit's result for the divergence is 7.85×10^{-5} rad. The sample itself is a 20mm$\times$20mm$\times$0.5 mm silicon wafer with the nanostructure magnetron-sputtered on top. A sketch is shown in Fig. 62.

	Carbon	Stainless Steel	Carbon	Platinum
Thickness [nm]	3.7	0.45	3.85	1.8
Density [g/cm^3]	1.96	7.56	1.96	20.7
Roughness mean squared [nm]	0.88	0.6	0.88	0.7

Table VI.1: *Properties of the one-dimensional photonic crystal according to the GenX fit. Additional parameters important to the fit are given in the text.*

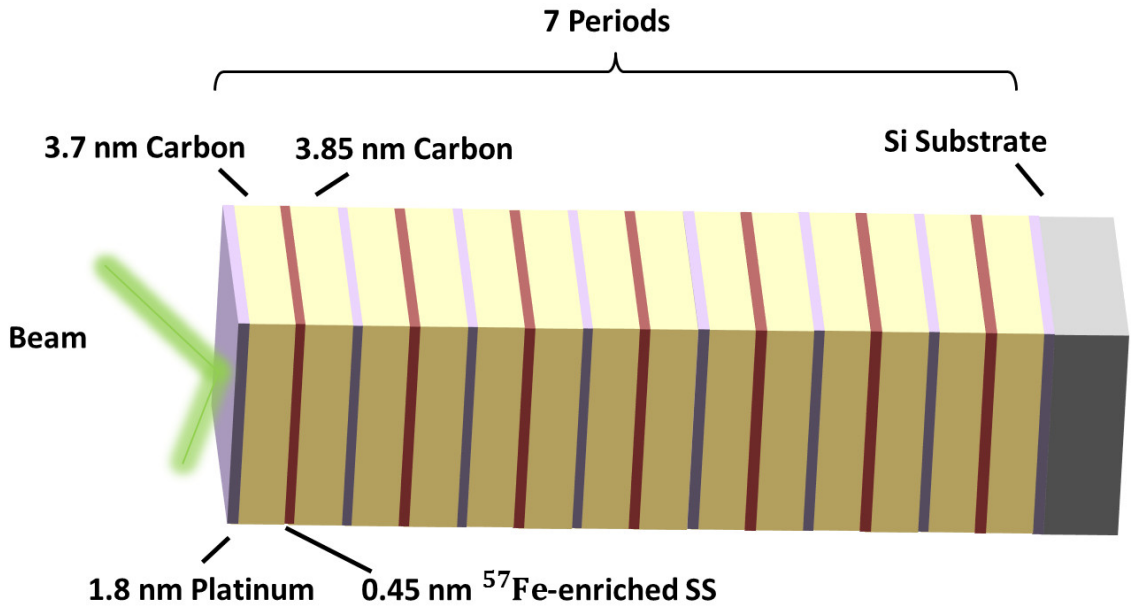

Figure 62: *Sketch of the nuclear resonant one-dimensional photonic crystal, sizes are not to scale.*

As usual, the parameters only represent averages of the actual, fluctuating widths of individual periods. From these parameters, we proceed as outlined in Chapter V.3., by fitting the post-processed spectra to the data and assigning the angles accordingly. Ordered spectra and simulations are depicted in Fig. 63. Not only are the general features of this rather complicated dispersion visible, but the quantitative agreement is excellent as well.

To support the claim we have made in the theoretical section of this chapter, in Fig. 64 we show a detail from the spectra in Fig. 63.

The range of angles corresponds to the first minimum near the edge of the band gap, i.e. the region we have claimed was qualitatively similar to a cavity. Our claim is clearly confirmed by Fig. 64 (a). The anti-crossing-like behaviour is visible, and shows the same Fano-like features as [57] and in Chapter V.II. Hence, strong coupling has not been reached, but we have achieved

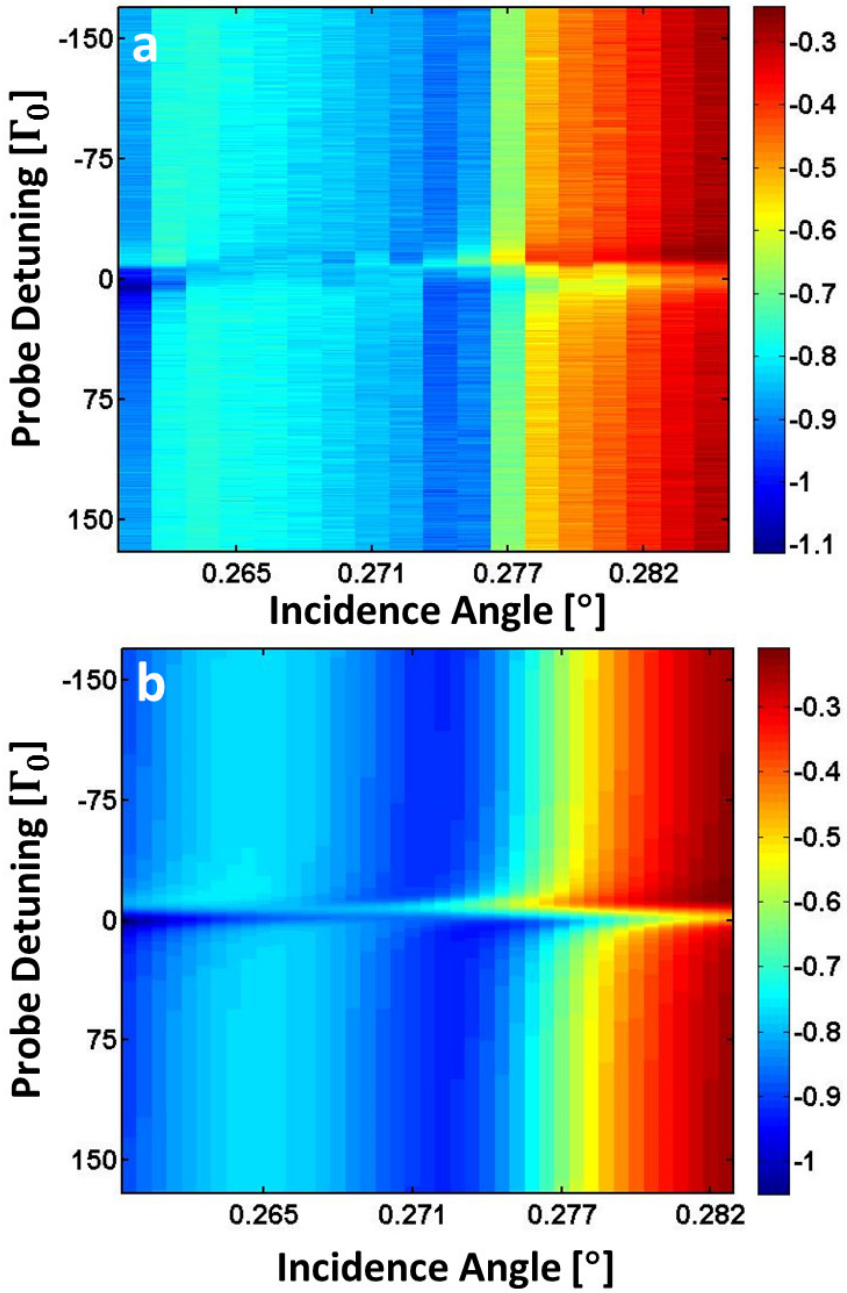

Figure 63: *Reflectivity measurements and simulations of the nuclear resonant one-dimensional photonic crystal. (a) The experimental data, post-processed and sorted by comparison with the simulation. (b) The simulation, which was performed by using the parameters extracted from the GenX fit. The y-axes display the detuning of the stainless steel absorber foil, the x-axes the angle of incidence. The reflected intensities are displayed logarithmically in the color map. Agreement is very well.*

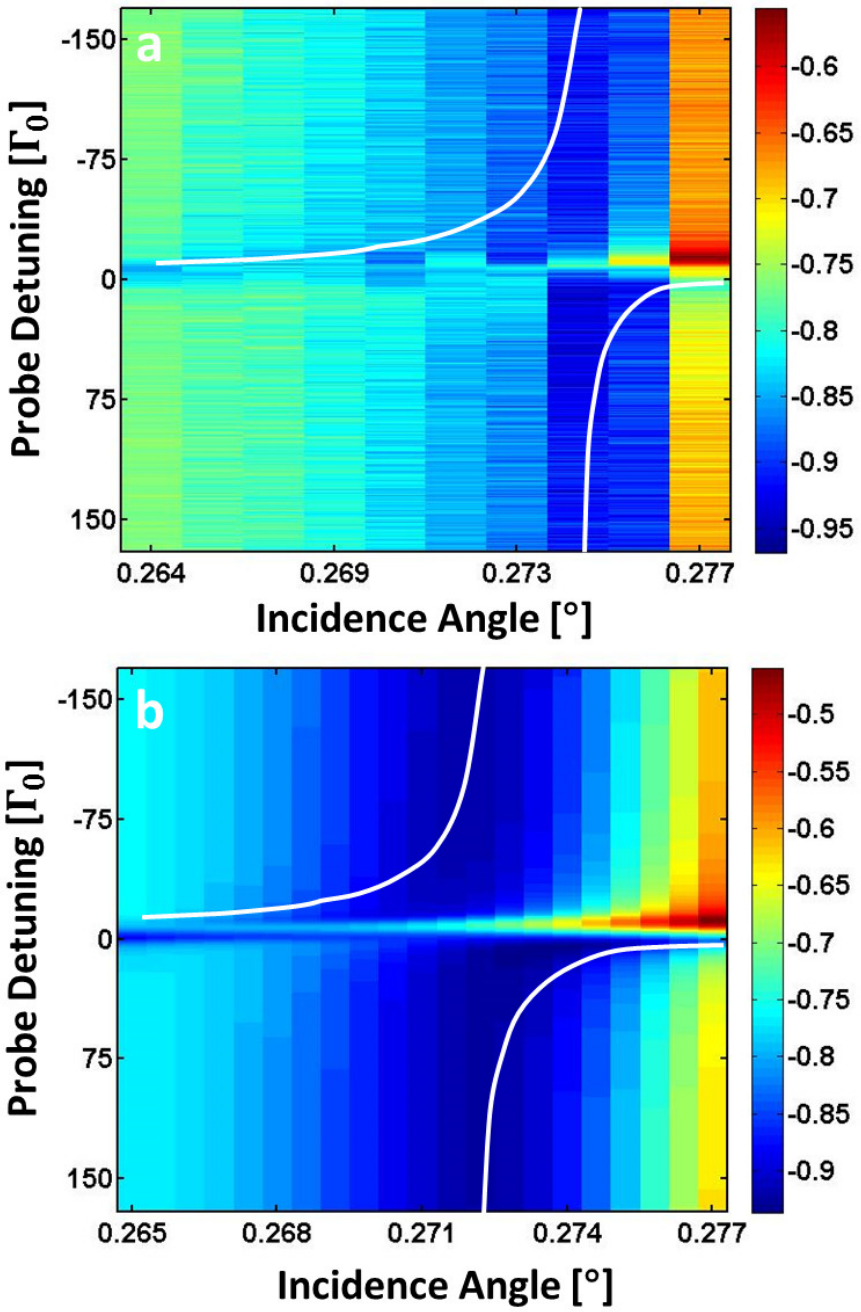

Figure 64: *Detail of the measurements and simulations in Fig. 64. The y-axes show the SS absorber foil detuning, the x-axes the angle of incidence. The reflected intensities are encoded logarithmically in the color map. The anticrossing of the dip is well resolved and visible. The spectra display Fano resonances, as in [57]. The white lines are guides to the eye to show the anticrossing behaviour due to the mode/nuclear ensemble coupling.*

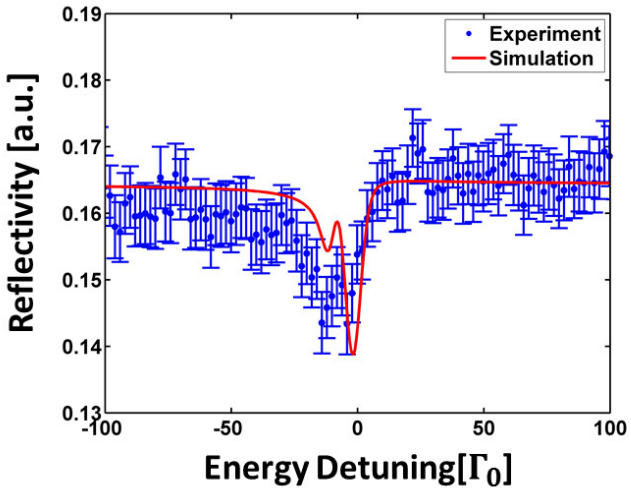

Figure 65: *Dispersive splitting between the branches of the dispersion relation in the region between two standing waves. The angle is* 0.267°. *The magnitude of the individual dips is not well retrieved, but the magnitude of the splitting is.*

our aim of demonstrating that close to the band gap of a nuclear resonant photonic crystal, cavity QED-like phenomena appear.

We also point out that, as discussed, there are multiple cavity-like dips which are indicative of standing waves. Consequently, we expect that between these dips there may be a dispersive splitting of the kind we have observed in previous section. In Fig. 64 both the simulation and the experiment show just such a splitting in the region between 0.266° and 0.268°. In the simulations, two narrow dips are visible at the same angle; in the data it is harder to discern them. We therefore show a line cut in Fig. 65.

VI.4. Ptychographic synchrotron Mössbauer spectroscopy

In several chapters in this thesis we have measured Mössbauer spectra with the help of synchrotron radiation. The two techniques we have employed here are the ESRF-based synchrotron Mössbauer source and time-gating detection of synchrotron radiation. Like all experimental schemes, these too have drawbacks and associated problems. The SMS for instance has shown instabilities in our experiments. It is also signally dependent on the quality of the $FeBO_3$-crystal. If the crystal presently used at the ESRF is damaged, dirty or lost, no others of comparable quality are available, and the quality of the source suffers accordingly. Furthermore, the more spectrally narrow the bandwidth of the source, the fewer photons get scattered, even adjusting for the bandwidth. This fickleness is particularly annoying in grazing incidence measurements, or experiments that require both a high intensity and good energy resolution. Furthermore, it is by no means clear whether SMS devices can be replicated at other sources, due to the aforementioned dependence on crystal quality.

Time-gated detection, on the other hand is a far more robust technique. It is widely used at NRS beamlines worldwide, and its specifications can be changed according to the needs of the experiment. For example the time gating window can be made shorter or longer depending on how photon-hungry the experiment is. Furthermore, it is permissible to use even when the isotope in question has a decay time much longer than the time window between electron bunches, like Tantalum [197]. The drawback is, again, that there is a balance to be found between resolution and measured intensity. Time-gated detection relies on photons being scattered in the absorber foil. The more photons scattered, the better the signal statistics. But only thick foils scatter strongly, and thick foils have the side effect of blurring the resolution, since multiple scattering occurs, which broadens the linewidth.

In order to deal with these two issues, we here propose a new technique, which has the potential to combine a high signal rate with excellent resolution. This is the spectroscopic extension of a microscopy technique called ptychography [198, 199, 200, 201] which has received a lot of attention in the past years, particularly in the fields of x-ray imaging. The added benefit of ptychography is not only the reconstruction of high-resolution images, but also the retrieval of the phase of the imaged sample.

The principle of ptychography, pictured in Fig. 66 is fairly simple. We have a semi-transparent sample, and a so-called probe, which is the beam the sample is illuminated with. The probe is smaller in extension then the sample, which is usually referred to as the object. Both can be represented by $N \times M$ matrices; N and M are ultimately the number of pixel rows and columns

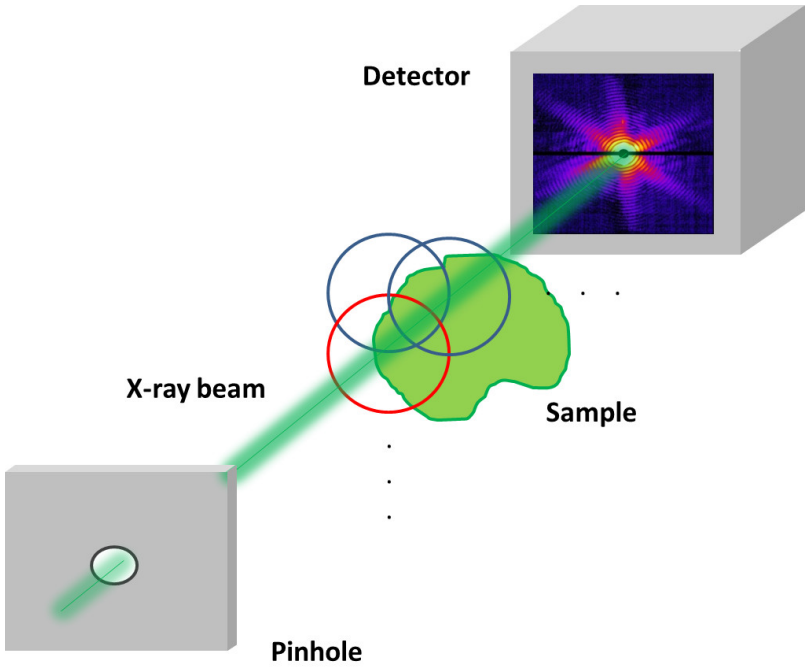

Figure 66: *The concept of ptychography. A beam (green line) is scanned in discrete steps across a sample. The footprints on the sample overlap for each step. The circles indicate the beam positions and their overlap. In the far-field, a 2D detector measured the far-field diffraction pattern, which consists of the magnitudes squared of the 2D Fourier transform of the sample (object) times the beam (probe).*

of the detecting camera. In the case of the object matrix, its magnitudes determine the amount of radiation transmitted through the sample; its phases determine the phase shift the radiation undergoes at being scattered from the sample. This is a valid treatment if the sample is optically thin enough, which is usually the case for x-rays.

The matrix of the probe determines magnitudes and phases of the incoming beam. Most ptychography schemes require an excellent knowledge of the probe; but there are some which are able to reconstruct both the probe and the object without prior knowledge of the two merely from the measured diffraction patterns [202]. However, we restrict ourselves to the case where the probe is known in the following.

In an actual experiment, the probe is scanned across the sample in discrete, but overlapping steps. Overlapping means that the beam in one step illuminates partially the part of the sample that was illuminated in the previous step. In the far field, the diffraction pattern of the sample is measured by a 2D-detector. This diffraction pattern corresponds to the magnitudes squared of the 2D-Fourier transform of the probe multiplied with the sample. Now each diffraction pattern

contains information on the structure of the sample at the position of illumination. But due to the overlap of the probe positions, several diffraction patterns share information on the same part of the sample. This makes the measured information highly redundant and aids in the retrieval of the phase and magnitude of the object. The phase retrieval algorithm's basic steps are the following

- (1) Start with a guess of what the object looks like. In the most general case, this should be a random matrix. We will call this guess O_g.
- (2) Illuminate O_g with the probe at position $\vec{r}_i$, $P(\vec{r}_i)$, and calculate the 2D-Fourier transform of it: Ψ = FFT($P(\vec{r})O_g$), where we call the term to be transformed ψ_g
- (3) Now, replace the magnitudes with the ones measured in the experiment:$\Psi_c \frac{\sqrt{I}}{abs(\Psi)} e^{(arg(\Psi))}$. In the language of phase retrieval algorithms, this is the extremely common Fourier constraint, also used in error reduction and Fienup algorithms [203].
- (4) Apply the inverse Fourier transform to the result of the above step: $\psi_{c,g}$ = IFFT(Ψ_c).
- (5) Apply the following transformation: $O_{g,c} = O_g + \frac{|P(\vec{r}_i)|}{|P_{max}(\vec{r}_i)|} \frac{|P^*(\vec{r}_i)|}{|P_{max}(\vec{r}_i)|^2+\alpha} \beta(\psi_{c,g} - \psi_g)$. Here α functions effectively as a Wiener filter. The updated guess of the object is a mixture of the old object, and a new version which takes into account corrections calculated in the last step. β determines how the contributions to the update are weighted.
- (6) repeat steps (2)-(5) for all diffraction patterns and probe positions measured.
- (7) repeat steps (2)-(5) for an arbitrary number of steps, or until the solution fulfills some convergence criterion.

Rodenburg recommends values for α and β of 0.0001 and 0.9 respectively, but we have gotten better results by assuming 0.1 for both. Since the phase retrieval converges fairly quickly, we have usually just picked an arbitrary number of steps, or repeated the experiment for several initial guesses and took the average.

In the case that we want to treat, we construct a analogue situation in time-energy space. In this case the 'object' is the reflectivity or transmittivity spectrum of a sample containing Mössbauer nuclei. The probe is the analyzer foil which contains a single-line ensemble of the same nuclei. The setup is similar to time-gating detection; the foil is placed into the beam downstream from the sample on a Doppler drive. Moving the foil shifts the energy of the resonance via the Doppler effect; this is the equivalent of moving the beam across the sample. We record the temporal decay pattern of probe and object for a set of velocities of the Doppler drive; the velocities should

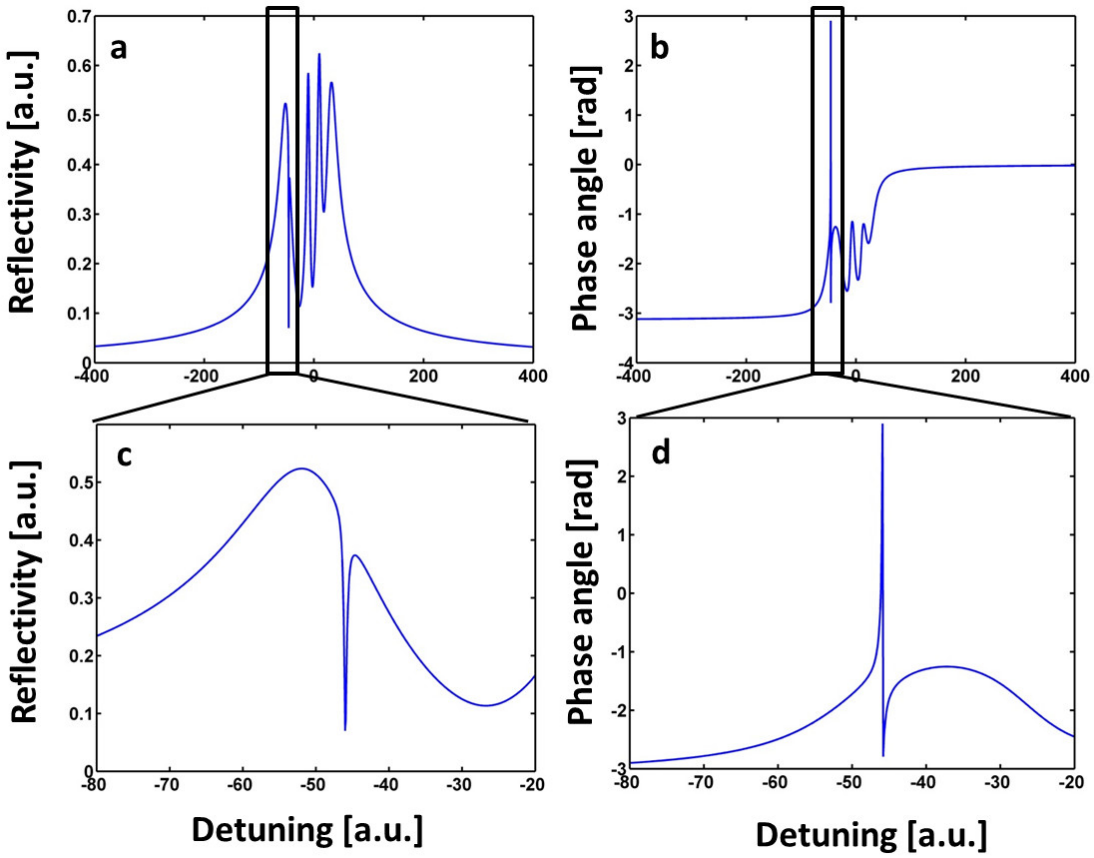

Figure 67: *Pattern used for the simulation of ptychographic data. In (a) we show a fictitious energy reflectivity spectrum, and in (b) the corresponding phase. In (c) and (d) we show a detail from (a) and (b) respectively. Note that the dip in the reflectivity has a linewidth of less then* $1\Gamma_0$.

be spaced such that the width of the absorption window of the foil overlaps for neighbouring velocities. The temporal decay patterns then contain plenty of redundant information which permits us to retrieve both the energy spectrum of the sample and its phase with the measured data, according to the above algorithm. Nothing needs to be changed, save for the replacement of $\vec{r}$ by ω.

To get a sense of the possibilities that ptychographic spectroscopy offers, we first show some results where we retrieve the energy spectrum and phase from a simulated pattern. The pattern is shown in Fig. 67, and consists of four superposed Lorentzians with different widths, with an EIT-like dip in one of them. The dip has a linewidth of less than $1\Gamma_0$.

To prepare the data, we assume a stainless-steel foil enriched with ^{57}Fe to 95%. We suppose that the foil is Doppler-shifted such that it ranges over $\pm 120\Gamma_0$. Its effective linewidth is about $10\Gamma_0$.

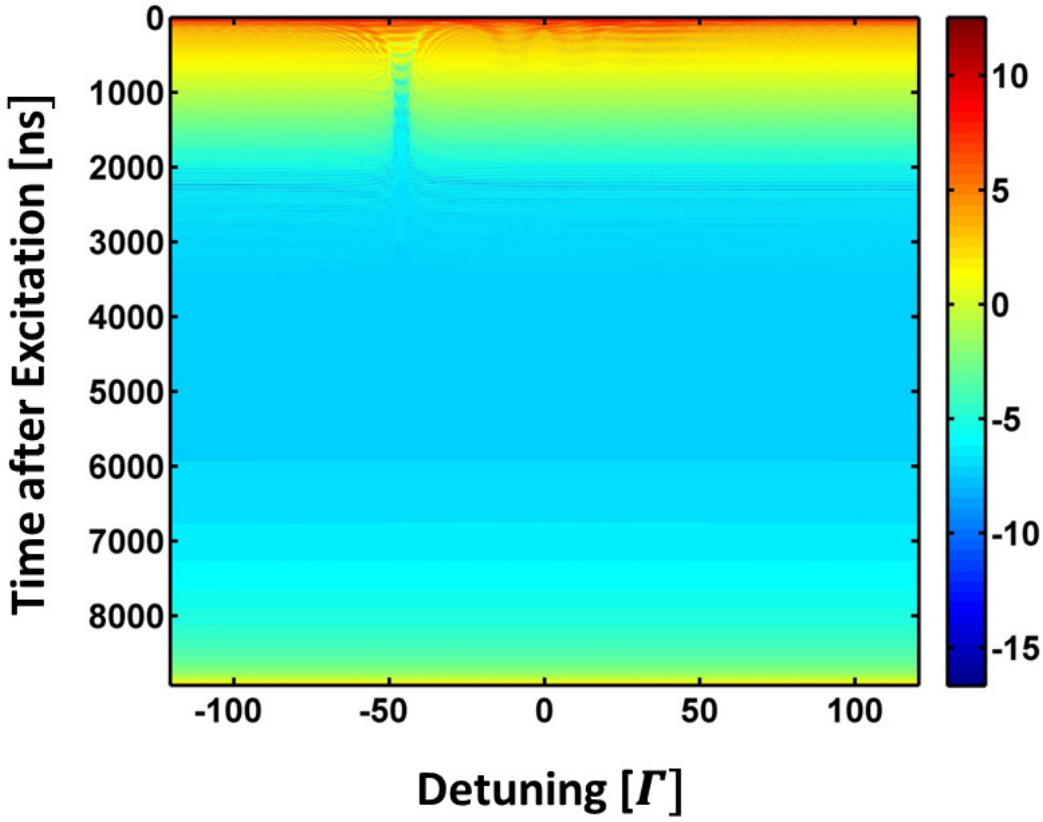

Figure 68: *Temporal decay patterns used for the simulation. The intensity is encoded logarithmically in the color map. The decay consists of the amplitudes squared of the Fourier transforms of the test pattern multiplied with the probe transform function at several positions. The slight rise at the end is due to the leakage effect of the discrete Fourier transform.*

We take 241 different spectra, each spaced $1\Gamma_0$ apart. We multiply each with the reflectivity shown in Fig. 67, Fourier transform it, and take the absolute value squared of the resulting temporal beat pattern. This is the set of diffraction patterns we will be working with. They are shown in Fig. 68.

Note that the length of the decay patterns are over 8000 ns. This is way longer than we could ever measure; We therefore set most of the pixels to zero, which can be repeated with real data by zero-padding. In real experiments we are limited to less time; for typical bunch structure modes at major facilities, the inter-bunch time lasts between 8ns and 800 ns. Since the Nyquist theorem states that the length of the time that the signal was measured determines the resolution of the energy spectrum achieved, we are particularly interested in whether ptychography will be able to retrieve the sub-linewidth structure, even when the time measured is theoretically not sufficient.

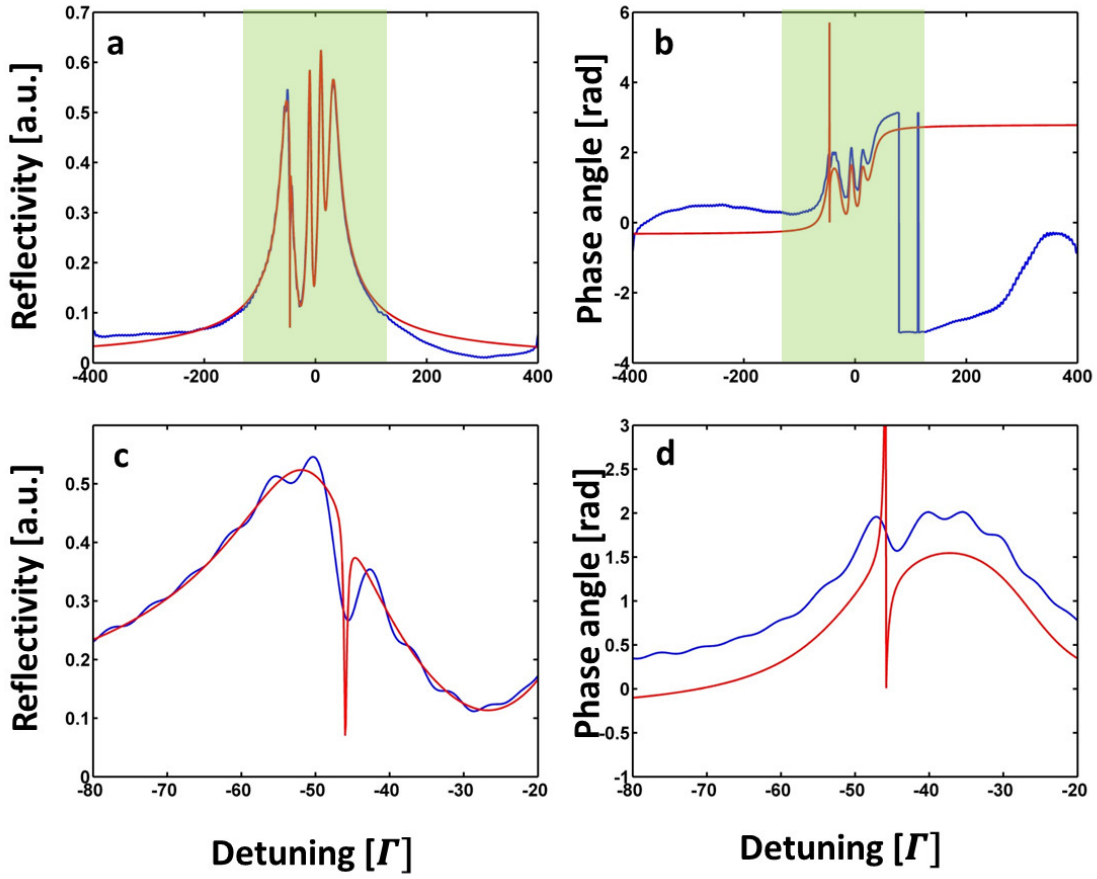

Figure 69: *Retrieved spectra from the simulated temporal decay patterns after running the ptychographic algorithm for* 10 *iterations. The original pattern is shown in red, the retrieved one in blue. (a) amplitude of the reflectivity, (b) phase of the reflectivity, (c) and (d) show details of (a) and (b) respectively. The green background indicates the part of the spectrum covered by the foil detuning. The retrieval is only good in this range, but nearly perfect for both phase and amplitude for broad linewidths; even the narrow-linewidth dip is roughly retrieved.*

We therefore set all pixels above the time of 174 ns to zero and run the ptychographic algorithm for 10 iterations. During the Fourier constraint step, the update includes updating the pixels with a value of zero. The results are depicted in Fig. 69.

The phase and amplitude retrieval works almost perfectly in the energy range which was probed by the probe; while the narrowband dip is not accurately reconstructed, evidence of its presence is found. The detail shows that only tiny deviations from the test patterns turn up. When we change the Fourier constraint slightly, and do not update the guess for pixels which are zero,

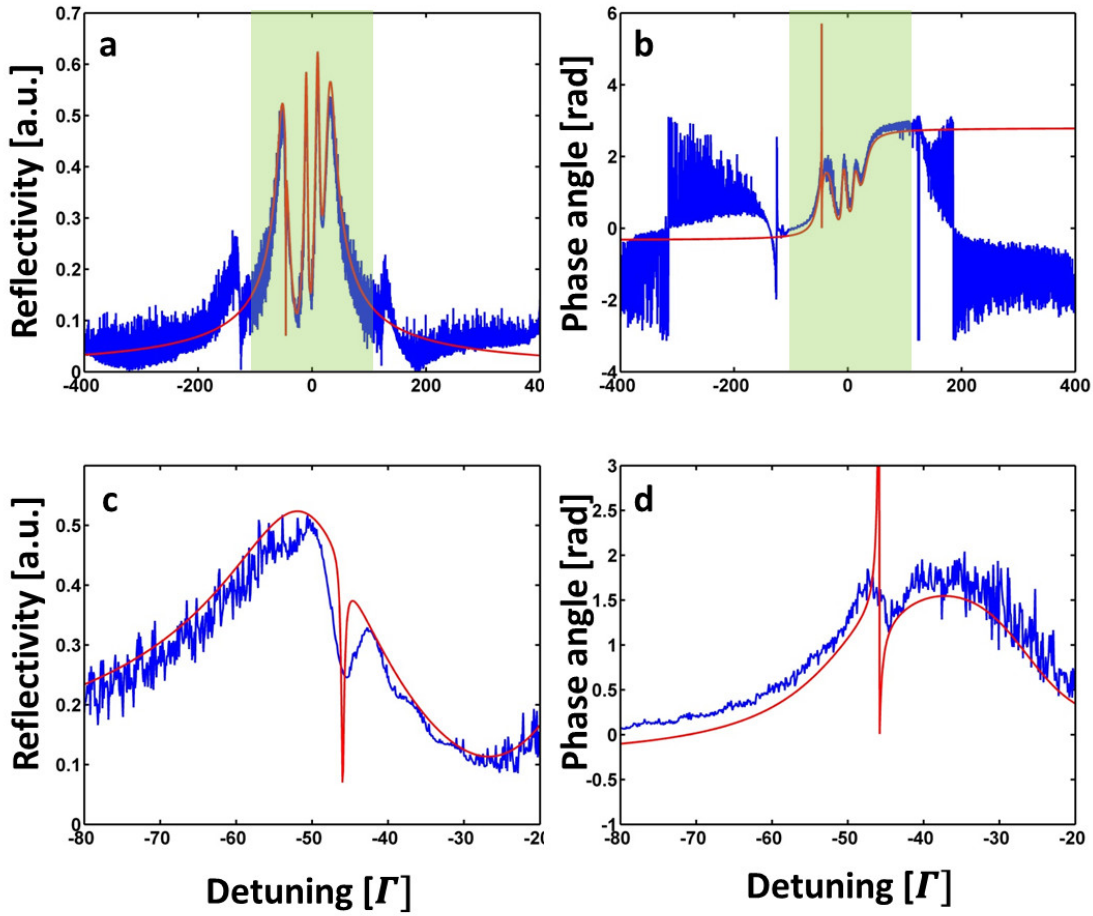

Figure 70: *Retrieved spectra from the simulated temporal decay patterns after running the ptychographic algortihm* 100 *times for* 10 *iterations and averaging the results. The original pattern is shown in red, the retrieved one in blue. (a) amplitude of the reflectivity, (b) phase of the reflectivity, (c) and (d) show details of (a) and (b) respectively. The green background indicates the part of the spectrum covered by the foil detuning. The retrieval is only good in this range, but nearly perfect for both phase and amplitude for broad linewidths; even the narrow-linewidth dip is roughly retrieved.*

the retrieval shows rather strong noise. To ameliorate this issue, we repeat the retrieval 100 times for 10 iterations, and average the results, which are shown in Fig. 70.

Despite the rather higher noise, the essential characteristics of the retrieval are still the same as for the former variation, although we cannot explain why the noisiness rises so drastically.
In realistic experimental conditions, we will often require a time-gating window for the first few nanoseconds after the incoming pulse. This is essentially equivalent to the beamstop which is often used in ptychography to block the primary beam, which might damage the detector. But

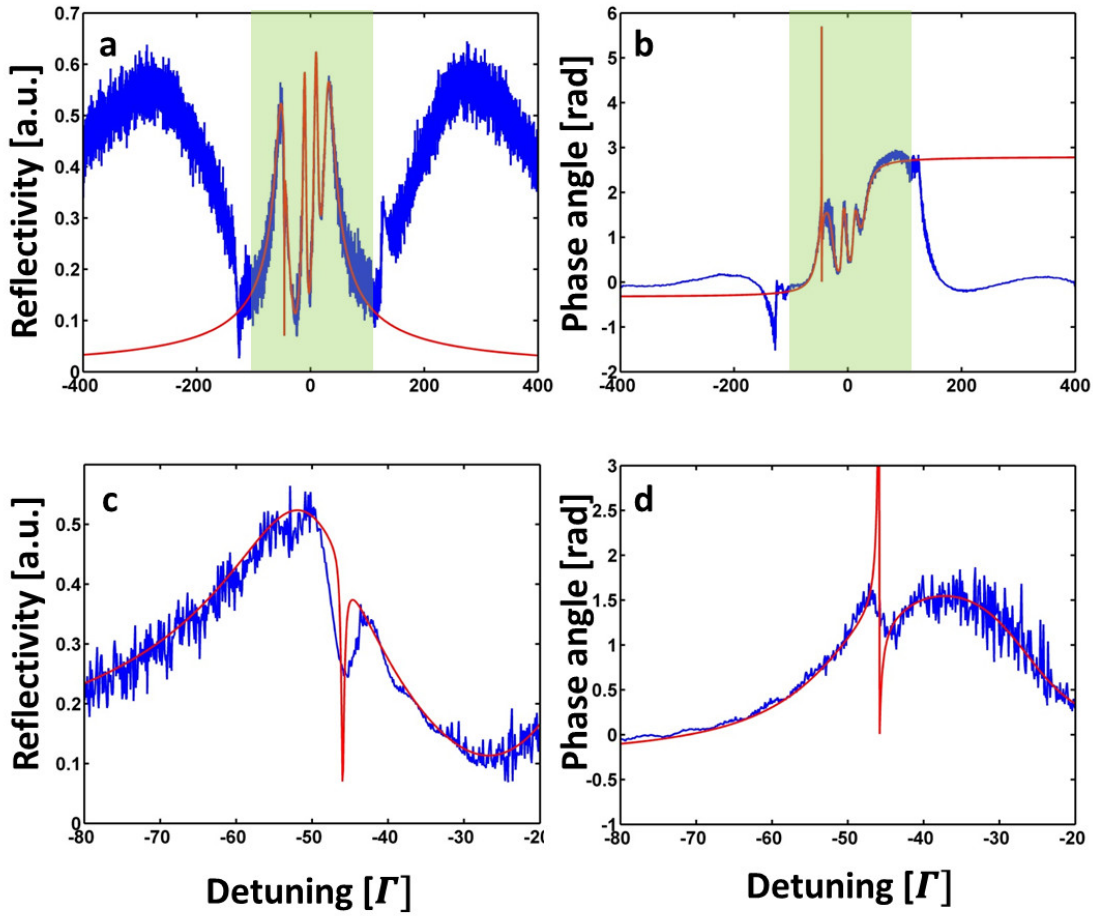

Figure 71: *(a) Retrieved amplitudes and (b) phases for a ptychographic algorithm implementation where only the range between 5 ns and 176 ns was updated by the Fourier constraint. The algorithm ran for 20 iterations for 100 times, and the results were averaged. Only in the area marked by the green square are the retrievals reliable; this is the range over which the foil was scanned. (c) and (d) show details of (a) and (b) respectively.*

of course, this might mean that some crucial information is missing from the temporal decay patterns, which might be detrimental to the quality of phase retrieval. To gauge the damage we inflict by the time-gating, we set the first six nanoseconds equal to zero in the diffraction patterns, and update the Fourier constraints only between 6 and 174 ns. Again, we repeat the phase retrieval 100 times and average the results, which can be seen in Fig. 71.

In the range covered by the detuning of the probe/analyzer foil, the retrieval is excellent if noisy. But the prediction outside of that range is now catastrophically bad. We conclude that the phase and amplitude retrieval is only reliable in ranges covered by the probe, which fits with experience

in optical experiments [198] Nevertheless, the final verdict can only be that ptychography is an extremely promising tool for performing Mössbauer spectroscopy at a synchrotron with added phase retrieval.

To further test the waters we here use a dataset from a different experiment, which fulfills all conditions required to perform a ptychographic analysis. The data is taken from an experiment which probed the appearance of slow-light x-ray pulses in cavities [55]; it is not in the scope of this thesis to explain the experiment, in detail, so we just briefly sketch the setup and data acquisition process.

The setup was as for any typical reflectivity experiment sketched many times throughout this thesis. The polarizer-analyzer setup mentioned in the Chapter III.6 was employed; this permitted us to work without a time-gating window. The time of arrival of a photon and the Mössbauer drive velocity at that time were recorded in analogue and digitalized with very high precision; this allowed us to bin the data at will and vary the overlap and number of our measured decay patterns. This is not trivial, since it has some impact on the counting statistics; a rough binning will result in good counting statistics at late times, potentially improving the resolution; on the other hand it will reduce the overlap of the probe function positions, which might reduce the retrieval quality. Of course the possibilities are ultimately limited by the fact that the spectrum changes; we do not want to mix up parts of the spectra with distinctly different values of the phase and amplitude in the same temporal decay pattern. At any rate, it turns out the results are remarkably stable across many variations of the bin size. We show the measured data in Fig. 72. The bin size is 2 ns and $2.5\Gamma_0$;

Finally, the retrieved data is shown in Fig. 73. Before performing the reconstruction, we have zero-padded the data by 400 bins ($\approx$ 800 ns), which means that the theoretically possible resolution is about 1 MHz - less than a linewidth. We used the Fourier constraint where we update the guesses even when the measured value of intensity is zero counts. Comparisons with data obtained from simulations of the cavity reflectivity are not completely satisfactory however. These are shown in Fig. 74. The simulations were made using the quantum optical model from [54]. Since the data was already analyzed in [55], we have employed the parameters obtained from the fit therein.

While the qualitative agreement is acceptable for both amplitude and phase, the quantitative agreement is far from perfect. The phase varies much more in the QO simulation; in the amplitude, the ptychographic retrieval has resulted in a lot of superfluous, noisy structure which is not present in the simulation. The relative heights of peaks and dips also do not agree very well. Keep in mind however that the QO simulation is also based on a fit of the same data; it might

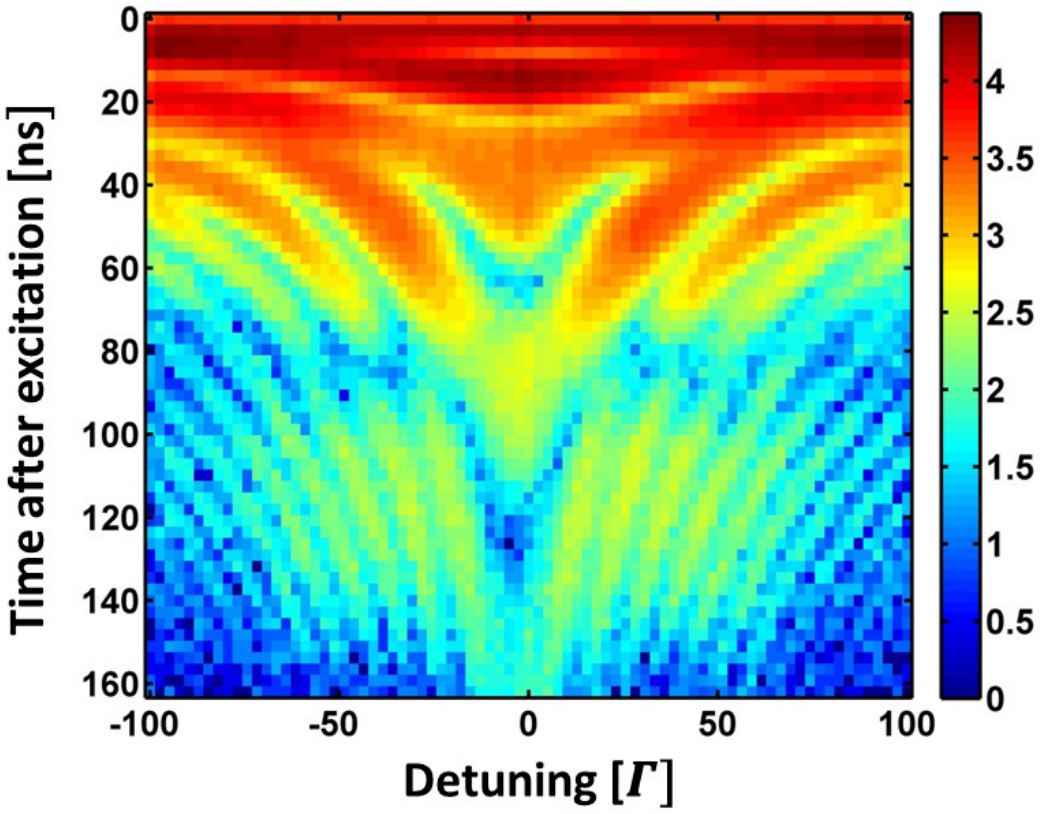

Figure 72: *Temporal decay patterns of a combined cavity/foil setup for different detunings of the foil. The intensity is encoded logarithmically in the color map. [55]*

be faulty in its own right. We conclude that more work is needed, particularly on well-known, simple forward scattering spectra which may help us gauge the reliability of the technique.

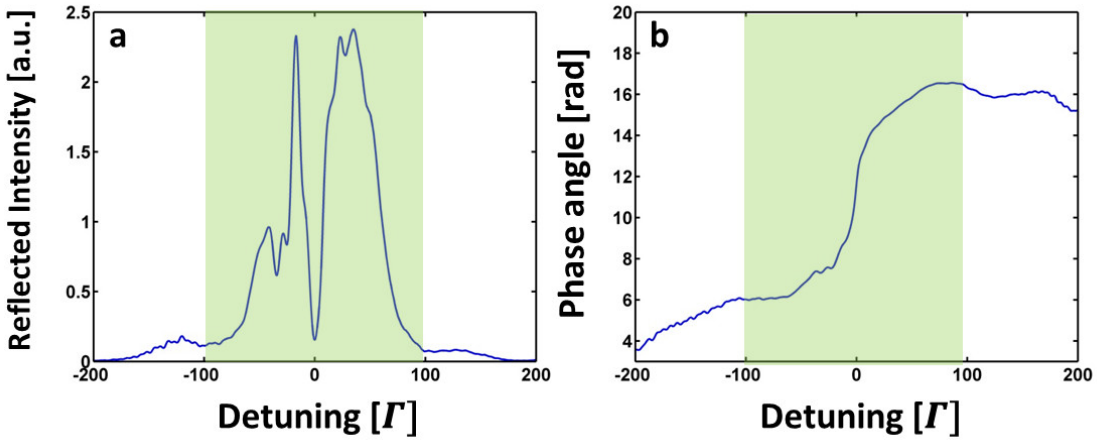

Figure 73: *In (a) we show the retrieved intensity from the data shown in Fig. 72, in (b) the corresponding phase. The green background indicates the range of detuning of the foil, i.e. the part of the spectrum we can rely on as per the simulations.*

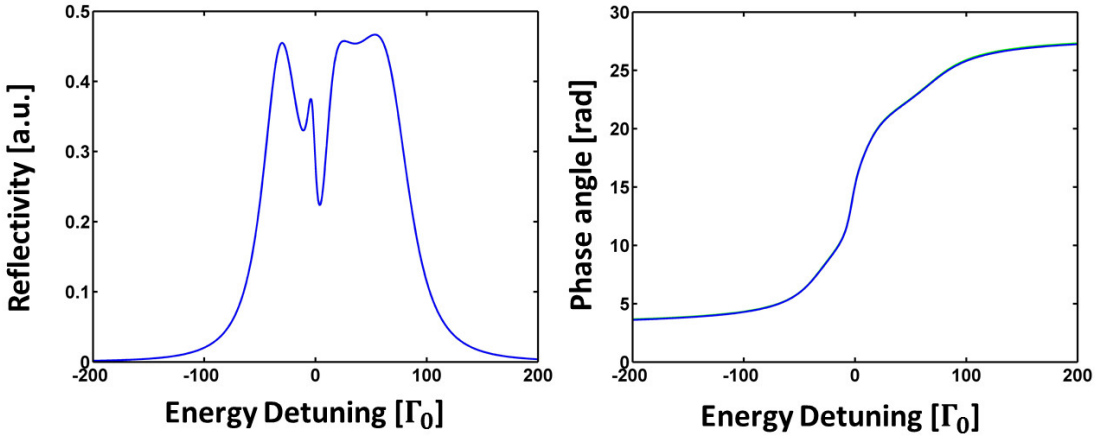

Figure 74: *Quantum optical simulation of the cavity reflectivity and phase response. To calculate the simulation, the data in Fig. 72 was fitted with a quantum optical model [54, 55]. Qualitative agreement with the ptychographically retrieved amplitudes and phases in Fig. 73 is reasonable, but quantitative agreement is poor.*

Chapter VII

Conclusion and Outlook

The aim of this thesis was to investigate whether it was possible to observe the strong coupling of x-rays and resonant ensembles of atoms or nuclei. We have achieved this in several ways. We have observed, in the energy domain, a splitting of the band gap of a nuclear optical lattice - a periodic resonant system of ^{57}Fe-nuclei. This is the fingerprint of the strong coupling of the collective of nuclei with the electromagnetic field that it is illuminated by. We have furthermore achieved the strong coupling of two ensembles of iron nuclei via the vacuum interaction in two shared cavity modes. In the latter experiment, we have observed the spectroscopic trademark of strong coupling: two dips in the frequency spectrum that result from the interaction of two resonant systems with the same energy. But strong coupling is of particular interest to physicists because of its temporal dynamics. Expressed in these terms, the two ensembles exchange their excitation several times before they ultimately decay irreversibly. We have observed the temporal beating, also known as Rabi-oscillations, that is the tell-tale sign of this process.

We succeeded in observing the frequency-domain splitting in a periodic system where both the resonant and the non-resonant index of refraction vary; a system that also yielded Fano resonances and dispersionless modes in the band gap, and therefore shows an extraordinarily rich phenomenology that ought to be examined more closely in future experiments. We have thus shown that the interaction of x-rays and light can be controlled to a high degree. In turn, we expect that the results of this work can be used in the future to control the properties of x-rays in ways not achieved before.

We also performed some tentative steps in new experimental directions. Hitherto, hard x-ray cavity quantum electrodynamics was limited to the ^{57}Fe isotope for its resonant systems. By observing the collective Lamb shift and the Fano resonances indicative of interference between

resonant and non-resonant scattering with a layer of Tantalum in a cavity, we have unambiguously demonstrated that electronic resonances can be suitable for quantum optics applications as well. Given the ubiquity of usable electronic resonances across all x-ray energies, this opens up a whole research programme in searching for new systems to achieve strong coupling with - and strong coupling does not seem out of reach, either by the more indirect methods of this work, or by straightforward optimization of cavities. Given that we have demonstrated the uses of periodic systems for x-ray quantum optics in this work, it does not seem inconceivable that genuine crystals with suitable resonances might be used to further the field's agenda. Potassium chromate, for instance, is a crystalline material that has a very strong and narrow K-edge white line. And the bandwidths of crystal reflections are far narrower than those of nanostructured periodic multilayers can ever hope to be.

Another way towards strong coupling might be the use of narrow-bandwidth DBR defect cavity modes, whose use for x-ray quantum optics we have demonstrated here. This system could also bring about the possibility of transmission measurements for x-ray cavity quantum electrodynamics. Measuring the correlations between the reflected and transmitted beam could help us get a closer look at the quantum nature of the x-ray-matter interactions.

For this type of sophisticated spectroscopy it is often convenient to know the phase of the detected radiation. We have applied ptychography, originally a microscopic imaging technique to Mössbauer spectroscopy and shown that it is extremely promising not just for retrieving the phase of the detected radiation, but also for finding the energy spectrum of the probe with far greater precision then theoretically permitted by the foil spectrum (which determines the resolution). This particular achievement could gain traction even beyond x-ray quantum optics since it is also applicable for the purposes regular Mössbauer spectroscopy at synchrotron radiation sources.

Chapter VIII

Appendix

VIII.1. Appendix A: SMS data postprocessing

In this section we describe the postprocessing of the data obtained from SMS experiments. The experimental issues are described in the relevant Chapter V.3; here we limit us strictly to the data correction. A typical spectrum is shown in Fig. 75.

We remove the sinusoidal background by fitting a sinusoid to the high- and low-energy parts of each spectrum. We expect that these should approximate a constant background according to our theory; By dividing the spectra by the fitted sinusoidal function, the sinusoidal background is removed and replaced by the expected flat one. The principle is explained in Fig. 76.

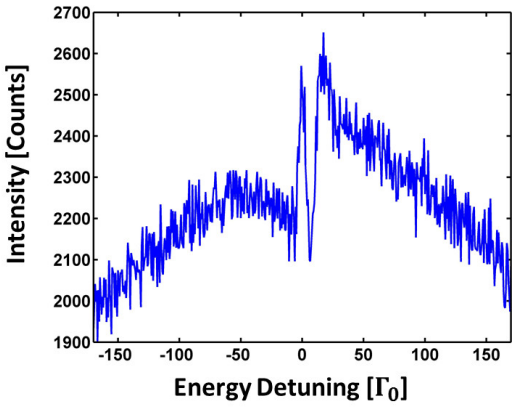

Figure 75: *Example of the raw data of a reflectivity spectrum. The sinusoidal background is clearly visible; as is the fact that both sides of the data show different spectral features. This is likely the result of some instability in the setup, as discussed in the main text.*

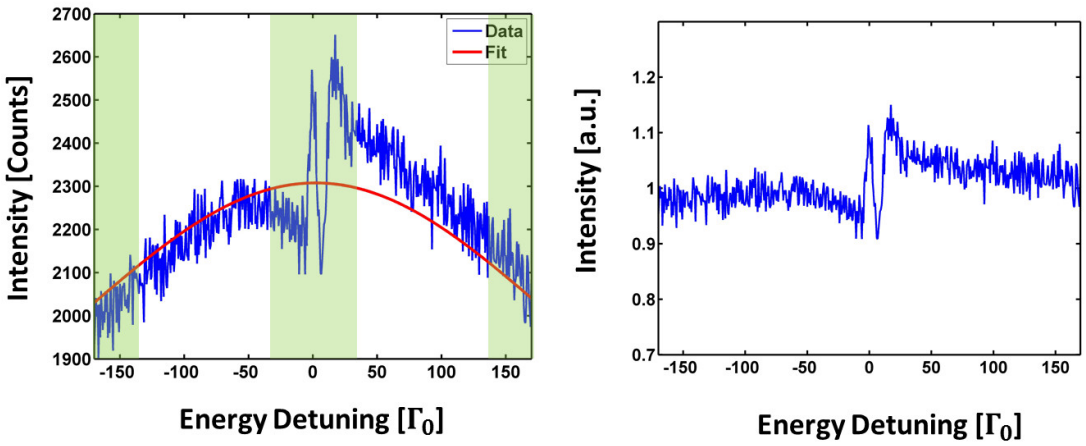

Figure 76: *Data postprocessing scheme. The background was fitted in the regions overlaid in green, so the actual data would not disrupt the fit of the purely unphysical sinusoidal background. The data was divided by the corresponding sine, and yielded the right image.*

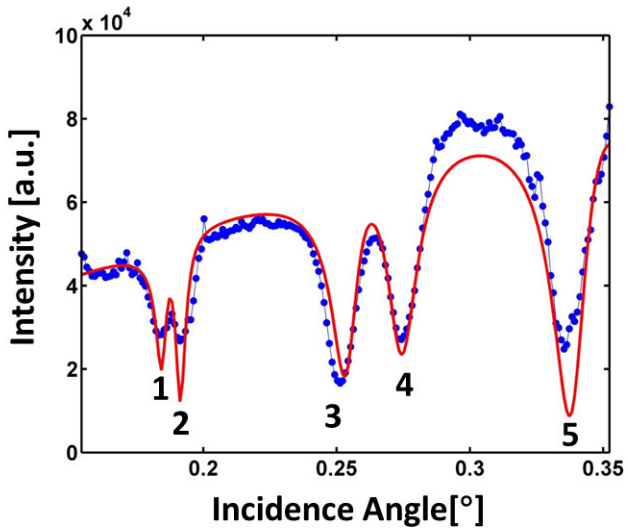

[h!]

Figure 77: *Measured reflected intensity curve (blue) at 11215 eV of a cavity with a resonant iridium layer embedded. The cavity dimensions are Pt 1.9 nm / C 24.3 nm / Ir 2.2 nm / C 24.4 nm / Pt 16.7 nm / Si Substrate, which was extracted from a fit (red). The fit satisfyingly reproduces the measured intensity. Small deviations stem from sample inhomogeneity. The reflectivity is however measured only over a short angular range which somewhat diminishes the reliability of the fit.*

VIII.2. Appendix B: The Iridium white line

In this appendix we will give a brief account of an experimental attempt to observe Fano resonances and the Lamb shift with an Iridium layer in a thin film cavity. Again, we will use the L_{III} edge, which in this case has the energy of 11215 eV and an spectral width of 5.25 eV. A particular difference to the L_{III} edge of Tantalum is the fact that the white line is somewhat smaller relative to the continuum absorption step from the background index of refraction. We therefore expect that the spoiling of the cavity above the white line, which we have already observed for the Tantalum cavities, will play an even stronger role here, particularly when compared with the magnitude of the spectral signatures of the Iridium-Cavity mode interaction. This is precisely what we observe, although, as we shall see, to a much stronger degree than our theoretical tools predict. We will also point out here that we have failed to observe a sufficient amount of fluorescent radiation to measure the collective Lamb shift of Iridium in a cavity.

For now, we proceed among the lines of the experiment on the Tantal line. In Fig. 77 we have plotted the reflectivity of the cavity in a $\theta - 2\theta$-scan along with a fit obtained by the program GenXref.

	Platinum	Carbon	Iridium	Carbon	Platinum
Thickness [nm]	3	24.2	2.3	24.2	17.9
Density [g/cm^3]	21.49	2.27	23.34	2.27	21.49
Roughness mean squared [nm]	0.43	0.35	1.8	0.0437	0.896

Table VIII.1: *Properties of the Iridium thin film cavity extracted from the Parratt algorithm fit.*

The properties of the cavity that were included into the fit were the thickness of individual layers, their roughness, the density of the materials, the width of the beam, its intensity and an offset of the angle θ from 2θ which can occur if the sample's alignment is not sufficiently precise. The fit is very satisfying; the resulting thin film properties are given in table VIII.1. The thicknesses are very close to those expected from the calibration of the sputtering rates. Any deviations can be explained by imprecisions in the amount of time the sample spent under the sputtering target - as mentioned, this was regulated manually - and by fluctuations in the chamber pressure and the temperature of the targets, which can change the sputtering rate. The densities are quite close to the literature values for the materials, which gives the fit additional credibility. Concerning the layer roughnesses, there is a huge outlier in the for the Iridium layer, which is an order of magnitude larger than the others. This, however, is not inconceivable. Iridium was sputtered with a small 1-inch target, while all other layers were sputtered with larger 2-inch diameter targets. Experience indicates that the former yields higher roughnesses due to smaller deposition rates, although we did not explore this in a systematic way. Generally, the roughnesses do not tend to influence the fit at low angles very much; even significant changes in the roughnesses do not deteriorate the fit quality meaningfully. We conclude that the fit is mostly reliable and that any changes stem from sample inhomogeneity. We also point out that the third mode, which is the one whose spectral response we will be examining, is fitted particularly well. A problem with the fit is that it is across a very small angular range; a larger would have increased quality, but at higher angles the effect of roughnesses etc. dominate over that of thicknesses and densities, so we may have confidence that the results are correct.

We now introduce the parameters obtained by the fit into our own implementation of the Parratt algorithm, and calculate the reflectivity. The result is shown in Fig. 78.

It displays the features already observed and discussed in the last section, such as an obvious normal mode splitting, a slight decline in the quality of the higher energy normal mode. As discussed this is the result of the electronic continuum.

In light of these promising results and simulations, it is all the more astonishing that the actual

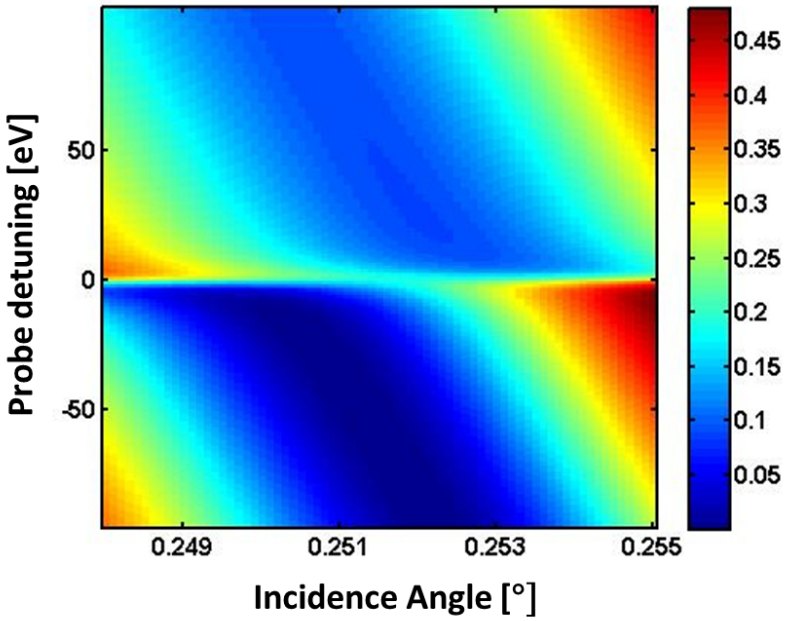

Figure 78: *Resonant reflectivity of an Iridium-containing cavity as calculated by the Parratt-formalism. The cavity dimensions are Pt 1.9 nm / C 24.3 nm / Ir 2.2 nm / C 24.4 nm / Pt 16.7 nm / Si Substrate. The x-axis shows the angle of incidence, the y-axis the detuning of the energy from the Ir-L_{III} white line at 11215 eV, and the reflected intensity is encoded in the color bar. While the transfer matrix formalism manages to give a more accurate reproduction of the experimental results, it is still not satisfying.*

measurements, shown in Fig. 79 do not conform to them. The higher energy normal mode is barely distinguishable from the background. In the Tantalum sample, and in the simulations for this one, the spectral width of the cavity is hardly affected by the Iridium layer enhanced absorption above resonance, only the dip is a little bit more shallow. But in this sample the cavity seems to have a spectral width that is beyond our chosen angular range to resolve, while the lower energy normal mode seems perfectly normal.
It is obvious that the experimental data shown in Fig. 79 can not seriously be simulated by the quantum optical model.

We only present an extremely rough approximation in Fig. 80.

This is to give the reader an impression of the vague order of magnitude of the parameters involved. The results are given in table VIII.2. The simulation is at odds with the data in ways so fundamental that we will eschew comparing them in a more detailed manner. The following brief discussion will suffice. It appears that κ is much too small for the higher energy normal mode,

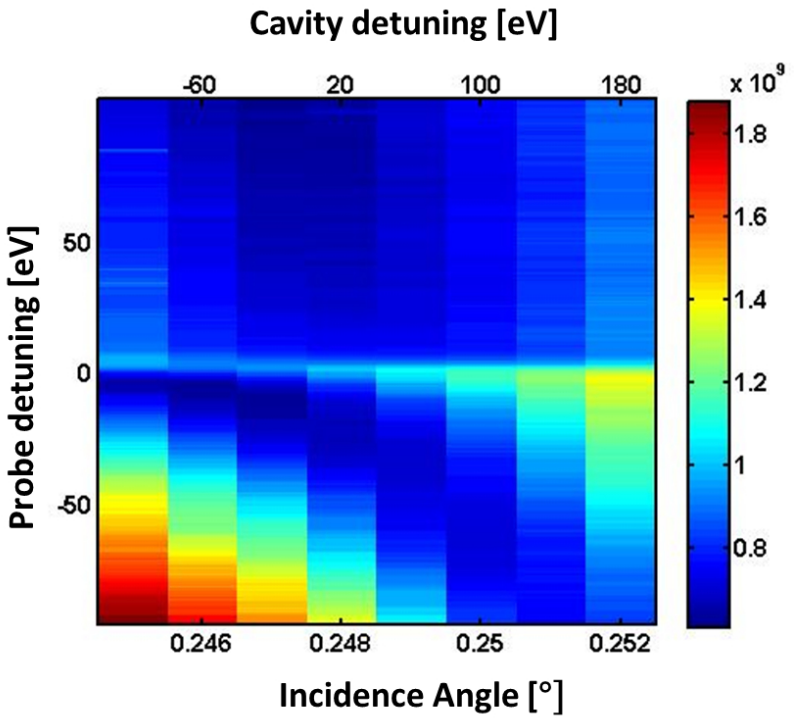

Figure 79: *Reflected intensity of a cavity containing Iridium. The dimensions of the cavity are Pt 1.9 nm / C 24.3 nm / Ir 2.2 nm / C 24.4 nm / Pt 16.7 nm / Si Substrate, as extracted from a fit to the reflected intensity at 0 eV detuning from the Ir-L_{III} white line at 11215 eV. The y axis shows the detuning, the x-axis shows the angle of incidence of the incoming radiation, and the intensity is encoded in the color bar in terms of reflected photons per 5 seconds. We point out that the high-energy normal mode is not observed very well. This is likely due to the step in the imaginary part of the background index of refraction of iridium, and the resulting enhanced absorption which spoils the cavity.*

but too big for the lower-energy normal mode. It also seems that the curvature of the normal mode dispersion is much stronger in the experimental data than in the calculated simulation. This would point to the fact that a higher collective coupling strength should be used. But it turns out that, upon doing just that, the reflectivity around the white line energy becomes far too high across all angles in the simulation compared to the rather feeble measured reflection. Any attempt to ameliorate one failing of the simulation will inexorably diminish agreement with the data at another point. We must conclude that this experiment has been a partial success at best. What could be the reasons for this, and how can we improve this experiment?

(a) It is possible that the failure can be blamed on beamline performance. The above series of reflectivities was repeated several times. The first few runs did not yield usable spectra, likely

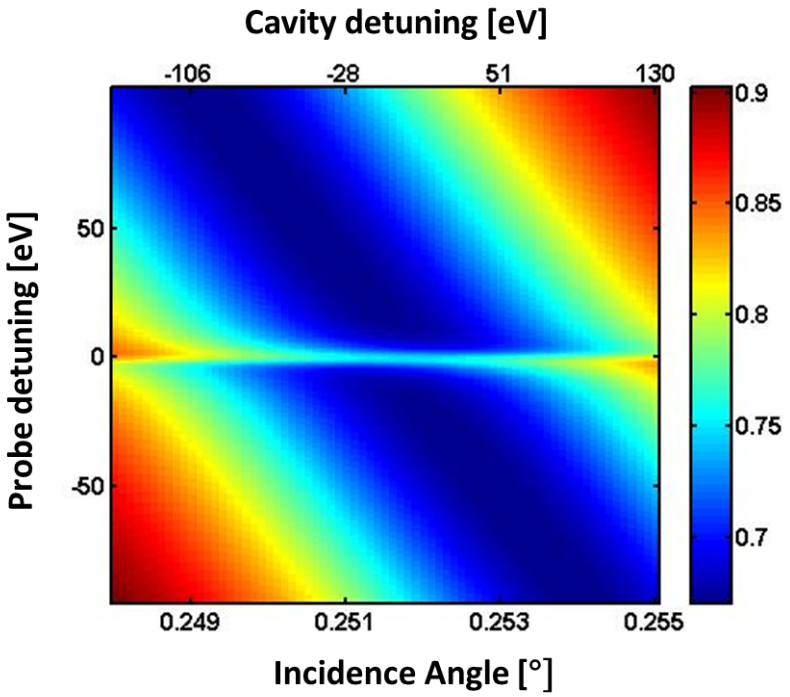

Figure 80: *Reflectivity of a cavity containing iridium as the resonant layer, as calculated by a quantum optical model of the system. The y-axis shows the detuning from the Ir L_{III} white line at 11215 eV, the upper x-axis shows the energetic detuning of the cavity from the incident x-ray energy, the lower x-axis shows the angle of the incident x-ray radiation. The reflectivity is encoded in the color map. The cavity's properties are g = 15, κ = 155, κ_r = 34, γ = 5.25. Even though the reflectivity seems to display a kind of normal mode splitting, the splitting is not resolved; the enhanced intensity at 0 eV detuning is due to interference between the normal modes, not due to a genuine splitting. The strong coupling limit is therefore not reached. While the simulation does not really succeed in reproducing the experimental results, it is close enough to conclude that we have not reached the strong coupling limit, but rather the intermediate coupling regime ($\gamma < g < \kappa$).*

because of beam stability issues. In between measurements, the beam was observed to jitter rapidly on an x-ray eye detector. At the time, it was blamed on vibrations caused by nearby construction work. When the measurements were repeated during the night, the above data was taken. It may be that although the situation improved, the problems were not resolved entirely. We did not check whether the beam was indeed still unstable after the measurement of the data, and it is not entirely clear why beam instability should result in spectra such as the ones we observed. Hence, this is really little more than informed speculation.

(b) In contrast, it is almost certain that the relatively low contrast between the white line resonance and the background electronic continuum absorption has contributed to the problems, though it is

	κ	κ_r	γ	$\sqrt{N}$g
Strength [eV]	155	34	5.25	15

Table VIII.2: *Parameters of the simulation of the quantum optical model.*

not clear to which extent. A possible alternative might be the use of IrO_2 as the resonant material, which has a white line of similar height as pure Ir, but a much lower background absorption. IrO_2 layers should be comparatively easy to fabricate by sputtering in a mixed Ar/O_2 atmosphereref, and this should certainly be the first step to improving the experiment.
(c) related to the preceding paragraph is the possibility that in thin films of Ir the physics of the white line might be different, or it might even be unobservable. It is not unlikely that Ir/C interface effects result in a breakdown of the Coulomb forces between excited electrons and holes that result in the excitonic white line resonances. This could explain our failure to gather enough statistics to observe the Lamb shift.Another point supporting this interpretation is that it explains the deviation between the measured data and the simulations obtained by the TMM. Finally, a cavity of different design that we examined did show almost no serious resonant effects. The Iridium layer in that particular cavity was designed to be a single monolayer, i.e. approximately 4-5 Å. In this case, such hypothetical interface effects would dominate the layer of course. This hypothesis can be checked by repeating the experiment with thicker resonant Ir layers and observing whether the effect persists.

Bibliography

[1] W. C. Röntgen. Über eine neue Art von Strahlen. *Annalen der Physik*, 300(1):1–11, 1898.

[2] W. L. Bragg W. H. Bragg. The reflection of x-rays by crystals. *Proceedings of the Royal Society of London. Series A, Containing Papers of a Mathematical and Physical Character*, 88(605):428–438, 1913.

[3] J. Als-Nielsen and D. McMorrow. *Elements of modern X-ray physics*. Wiley-VCH.

[4] R. V. Pound and G. A. Rebka. Gravitational red-shift in nuclear resonance. *Phys. Rev. Lett.*, 3:439–441, Nov 1959.

[5] A. Ruhlandt, M. Krenkel, M. Bartels, and T. Salditt. Three-dimensional phase retrieval in propagation-based phase-contrast imaging. *Phys. Rev. A*, 89:033847, Mar 2014.

[6] L. Dubrovinsky, N. Dubrovinskaia, E. Bykova, M. Bykov, V. Prakapenka, C. Prescher, K. Glazyrin, H.-P. Liermann, M. Hanfland, M. Ekholm, Q. Feng, L.V. Pourovskii, M. Katsnelson, J.M. Wills, and I.A. Abrikosov. The most incompressible metal Osmium at static pressures above 750 gigapascals. *Nature*, 525:226–229, Sep 2015.

[7] M. Le Tacon, A. Sacuto, A. Georges, G. Kotliar, Y. Gallais, D. Colson, and A. Forget. Two energy scales and two distinct quasiparticle dynamics in the superconducting state of underdoped cuprates. *Nature Physics*, 2:537–543, 2006.

[8] B.W.J. McNeil and N.R. Thompson. X-ray free-electron lasers. *Nature Photonics*, 4:814–821, 2010.

[9] Roy J. Glauber. Coherent and incoherent states of the radiation field. *Phys. Rev.*, 131:2766–2788, Sep 1963.

[10] Roy J. Glauber. The quantum theory of optical coherence. *Phys. Rev.*, 130:2529–2539, Jun 1963.

[11] J. H. Eberly, N. B. Narozhny, and J. J. Sanchez-Mondragon. Periodic spontaneous collapse and revival in a simple quantum model. *Phys. Rev. Lett.*, 44:1323–1326, May 1980.

[12] C. Monroe, D. M. Meekhof, B. E. King, and D. J. Wineland. A "Schrödinger Cat" superposition state of an atom. *Science*, 272(5265):1131–1136, 1996.

[13] M. Brune, F. Schmidt-Kaler, A. Maali, J. Dreyer, E. Hagley, J. M. Raimond, and S. Haroche. Quantum Rabi oscillation: A direct test of field quantization in a cavity. *Phys. Rev. Lett.*, 76:1800–1803, Mar 1996.

[14] J. M. Raimond, M. Brune, and S. Haroche. Manipulating quantum entanglement with atoms and photons in a cavity. *Rev. Mod. Phys.*, 73:565–582, Aug 2001.

[15] D. J. Wineland, J. J. Bollinger, W. M. Itano, F. L. Moore, and D. J. Heinzen. Spin squeezing and reduced quantum noise in spectroscopy. *Phys. Rev. A*, 46:R6797–R6800, Dec 1992.

[16] Masahiro Kitagawa and Masahito Ueda. Squeezed spin states. *Phys. Rev. A*, 47:5138–5143, Jun 1993.

[17] R. E. Slusher, L. W. Hollberg, B. Yurke, J. C. Mertz, and J. F. Valley. Observation of squeezed states generated by four-wave mixing in an optical cavity. *Phys. Rev. Lett.*, 55:2409–2412, Nov 1985.

[18] Alexandre Blais, Ren-Shou Huang, Andreas Wallraff, S. M. Girvin, and R. J. Schoelkopf. Cavity quantum electrodynamics for superconducting electrical circuits: An architecture for quantum computation. *Phys. Rev. A*, 69:062320, Jun 2004.

[19] M. G. Raizen, R. J. Thompson, R. J. Brecha, H. J. Kimble, and H. J. Carmichael. Normal-mode splitting and linewidth averaging for two-state atoms in an optical cavity. *Phys. Rev. Lett.*, 63:240–243, Jul 1989.

[20] C. Weisbuch, M. Nishioka, A. Ishikawa, and Y. Arakawa. Observation of the coupled exciton-photon mode splitting in a semiconductor quantum microcavity. *Phys. Rev. Lett.*, 69:3314–3317, Dec 1992.

[21] A. Wallraff, D.I. Schuster, A. Blais, L. Frunzio, R.-S. Huang, J. Majer, S. Kumar, S.M. Girvin, and R.J. Schoelkopf. Strong coupling of a single photon to a superconducting qubit using circuit quantum electrodynamics. *Nature*, 431:162–167, 2004.

[22] K. Baumann, C. Guerlin, F. Brennecke, and T. Esslinger. Dicke quantum phase transition with a superfluid gas in an optical cavity. *Nature*, 464:1301–1306, 2010.

[23] Yu. Shvyd'ko. *X-ray Optics: High-Energy-Resolution Applications*. Optical Sciences. Springer-Verlag Berlin Heidelberg, 2004.

[24] Yu.V. Shvyd'ko, S. Stoupin, A. Cunsolo, A.H. Said, and X. Huang. High-reflectivity high-resolution x-ray crystal optics with diamonds. *Nature Physics*, 6:196–199, 2010.

[25] A. Snigirev, V. Kohn, I. Snigireva, A. Souvorov, and B. Lengeler. Focusing high-energy x rays by compound refractive lenses. *Appl. Opt.*, 37(4):653–662, Feb 1998.

[26] B. Lengeler, C. G. Schroer, M. Richwin, J. Tümmler, M. Drakopoulos, A. Snigirev, and I. Snigireva. A microscope for hard x rays based on parabolic compound refractive lenses. *Applied Physics Letters*, 74(26):3924–3926, 1999.

[27] F. Döring, A.L. Robisch, C. Eberl, M. Osterhoff, A. Ruhlandt, T. Liese, F. Schlenkrich, S. Hoffmann, M. Bartels, T. Salditt, and H.U. Krebs. Sub-5 nm hard x-ray point focusing by a combined Kirkpatrick-Baez mirror and multilayer zone plate. *Opt. Express*, 21(16):19311–19323, Aug 2013.

[28] P. Eisenberger and S. L. McCall. X-ray parametric conversion. *Phys. Rev. Lett.*, 26:684–688, Mar 1971.

[29] P. M. Eisenberger and S. L. McCall. Mixing of x-ray and optical photons. *Phys. Rev. A*, 3:1145–1151, Mar 1971.

[30] Bernhard Adams, Patricia Fernandez, Wah-Keat Lee, Gerhard Materlik, Dennis M. Mills, and Dmitri V. Novikov. Parametric down conversion of X-ray photons. *Journal of Synchrotron Radiation*, 7(2):81–88, Mar 2000.

[31] B. Adams, Y. Nishino, D.V. Novikov, G. Materlik, and D.M. Mills. Parametric down conversion of x-rays, recent experiments. *Nuclear Instruments and Methods in Physics Research Section A: Accelerators, Spectrometers, Detectors and Associated Equipment*, 467Ű468, Part 2:1019 – 1020, 2001. Proceedings of the 7th Int. Conf. on Synchrotron Radiation Instru entation.

[32] F. J. Lynch, R. E. Holland, and M. Hamermesh. Time dependence of resonantly filtered gamma rays from fe^{57}. *Phys. Rev.*, 120:513–520, Oct 1960.

[33] Samuel M. Harris. Quantum-mechanical model of Mössbauer line narrowing. *Phys. Rev.*, 163:280–285, Nov 1967.

[34] Samuel M. Harris. Quantum mechanical calculation of Mössbauer transmission. *Phys. Rev.*, 124:1178–1185, Nov 1961.

[35] M. N. Hack and M. Hamermesh. Effect of radiofrequency resonance on the natural line form. *Il Nuovo Cimento (1955-1965)*, 19(3):546–557, 1961.

[36] S. H. Autler and C. H. Townes. Stark effect in rapidly varying fields. *Phys. Rev.*, 100:703–722, Oct 1955.

[37] I. Tittonen, M. Lippmaa, E. Ikonen, J. Lindén, and T. Katila. Observation of Mössbauer resonance line splitting caused by Rabi oscillations. *Phys. Rev. Lett.*, 69:2815–2818, Nov 1992.

[38] S. Shwartz, M. Fuchs, J. B. Hastings, Y. Inubushi, T. Ishikawa, T. Katayama, D. A. Reis, T. Sato, K. Tono, M. Yabashi, S. Yudovich, and S. E. Harris. X-ray second harmonic generation. *Phys. Rev. Lett.*, 112:163901, Apr 2014.

[39] T.E. Glover, D.M. Fritz, M. Cammarata, T.K. Allison, Sinisa Coh, J.M. Feldkamp, H. Lemke, D. Zhu, Y. Feng, R.N. Coffee, M. Fuchs, S. Ghimire, J. Chen, S. Shwartz, D.A. Reis, S.E. Haarris, and J.B. Hastings. X-ray and optical wave mixing. *Nature*, 488:603–608, 2012.

[40] Yoneda H., Y. Inubushi, K. Nagamine, Y. Michine, H. Ohashi, K. Yumoto, H. Yamauchi, H. Mimura, H. Kitamura, T. Katayama, T. Ishikawa, and M. Yabashi. Atomic inner-shell laser at 1.5-ångström wavelength pumped by an x-ray free-electron laser. *Nature*, 524:446–449, 2015.

[41] N. Rohringer, R. Duncan, R.A. London, M. Purvis, F. Albert, J. Dunn, J.D. Bozek, C. Bostedt, A. Graf, R. Hill, Hau-Riege S.P., and J.J. Rocca. Atomic inner-shell x-ray laser at 1.46 nanometres pumped by an x-ray free-electron laser. *Nature*, 481:488–491, 2012.

[42] M. Fuchs, M. Trigo, J. Chen, S. Ghimire, S. Shwartz, M. Kizina, M. Jiang, T. Henighan, C. Bray, G. Ndabashimiye, P.H. Bucksbaum, Y. Feng, S. Herrmann, G.A. Carini, J. Pines, P. Hart, C. Kenney, S. Guillet, S. Boutet, G. Williams, M. Messerschmidt, M.M. Seibert, S. Moeller, J.B. Hastings, and D.A. Reis. Anomalous nonlinear x-ray compton scattering. *Nature Physics*, 11:964–970, 2015.

[43] F. Vagizov, V. Antonov, Y.V. Radeonychev, R.N. Shakhmuratov, and O. Kocharovskaya. Coherent control of the waveforms of recoilless γ-ray photons. *Nature*, 508:80–83, 2014.

[44] R. N. Shakhmuratov, F. G. Vagizov, V. A. Antonov, Y. V. Radeonychev, Marlan O. Scully, and Olga Kocharovskaya. Transformation of a single-photon field into bunches of pulses. *Phys. Rev. A*, 92:023836, Aug 2015.

[45] Y. V. Radeonychev, V. A. Antonov, F. G. Vagizov, R. N. Shakhmuratov, and Olga Kocharovskaya. Conversion of recoilless γ radiation into a periodic sequence of short intense pulses in a set of several sequentially placed resonant absorbers. *Phys. Rev. A*, 92:043808, Oct 2015.

[46] E. Shwartz and S. Shwartz. Difference-frequency generation of optical radiation from two-color x-ray pulses. *Opt. Express*, 23(6):7471–7480, Mar 2015.

[47] S. Shwartz and S. E. Harris. Polarization entangled photons at x-ray energies. *Phys. Rev. Lett.*, 106:080501, Feb 2011.

[48] Wen-Te Liao, Adriana Pálffy, and Christoph H. Keitel. Coherent storage and phase modulation of single hard-x-ray photons using nuclear excitons. *Phys. Rev. Lett.*, 109:197403, Nov 2012.

[49] Wen-Te Liao and Adriana Pálffy. Proposed entanglement of x-ray nuclear polaritons as a potential method for probing matter at the subatomic scale. *Phys. Rev. Lett.*, 112:057401, Feb 2014.

[50] Wen-Te Liao, Christoph H. Keitel, and Adriana Pálffy. All-electromagnetic control of broadband quantum excitations using gradient photon echoes. *Phys. Rev. Lett.*, 113:123602, Sep 2014.

[51] Jonas Gunst, Christoph H. Keitel, and Adriana Pálffy. Logical operations with single x-ray photons via dynamically-controlled nuclear resonances. *Sci. Rep.*, 6:25136, 2016.

[52] R. Röhlsberger, Schlage K., B. Sahoo, S. Couet, and R. Rüffer. Collective Lamb shift in single photon superradiance. *Science*, 328:1248, 2010.

[53] R. Röhlsberger, H.C. Wille, K. Schlage, and B. Sahoo. Electromagnetically induced transparency with resonant nuclei in a cavity. *Nature*, 482:199–203, 2011.

[54] Kilian P. Heeg and Jörg Evers. Quantum optics with Mössbauer nuclei in a cavity. *Phys. Rev. A*, 88:043828, Oct 2013.

[55] Kilian P. Heeg, Johann Haber, Daniel Schumacher, Lars Bocklage, Hans-Christian Wille, Kai S. Schulze, Robert Loetzsch, Ingo Uschmann, Gerhard G. Paulus, Rudolf Rüffer, Ralf Röhlsberger, and Jörg Evers. Tunable subluminal propagation of narrow-band x-ray pulses. *Phys. Rev. Lett.*, 114:203601, May 2015.

[56] Kilian P. Heeg, Hans-Christian Wille, Kai Schlage, Tatyana Guryeva, Daniel Schumacher, Ingo Uschmann, Kai S. Schulze, Berit Marx, Tino Kämpfer, Gerhard G. Paulus, Ralf Röhlsberger, and Jörg Evers. Vacuum-assisted generation and control of atomic coherences at x-ray energies. *Phys. Rev. Lett.*, 111:073601, Aug 2013.

[57] K. P. Heeg, C. Ott, D. Schumacher, H.-C. Wille, R. Röhlsberger, T. Pfeifer, and J. Evers. Interferometric phase detection at x-ray energies via Fano resonance control. *Phys. Rev. Lett.*, 114:207401, May 2015.

[58] Kilian P. Heeg and Jörg Evers. Collective effects between multiple nuclear ensembles in an x-ray cavity-QED setup. *Phys. Rev. A*, 91:063803, Jun 2015.

[59] A. Palffy and X. Kong. Personal communication.

[60] Xianjing Kong. *Collective effects of nuclei in single-photon superradiance*. PhD thesis, Ruprecht-Karls-Universität Heidelberg, 2016.

[61] Shiwu Gao. Lindblad approach to quantum dynamics of open systems. *Phys. Rev. B*, 57:4509–4517, Feb 1998.

[62] Melvin Lax. Multiple scattering of waves. *Rev. Mod. Phys.*, 23:287–310, Oct 1951.

[63] R. Röhlsberger. *Nuclear Condensed Matter Physics with Synchrotron Radiation. Basic Principles, Methodology and Applications.* Number 208 in Springer Tracts in Modern Physics. Springer-Verlag Berlin Heidelberg, 2004.

[64] The center for x-ray optics. http://www.cxro.lbl.gov.

[65] Rudolf L. Mössbauer. Kernresonanzfluoreszenz von Gammastrahlung in Ir-191. *Zeitschrift für Physik*, 151(2):124–143, 1958.

[66] Rudolf L. Mössbauer. Kernresonanzabsorption von Gammastrahlung in Ir191. *Naturwissenschaften*, 45(22):538–539, 1958.

[67] Willis E. Lamb. Capture of neutrons by atoms in a crystal. *Phys. Rev.*, 55:190–197, Jan 1939.

[68] R. H. Dicke. The effect of collisions upon the Doppler width of spectral lines. *Phys. Rev.*, 89:472–473, Jan 1953.

[69] Lyman G. Parratt. X-ray resonance absorption lines in the Argon K spectrum. *Phys. Rev.*, 56:295–297, Aug 1939.

[70] Charles Kittel. *Quantum theory of solids*. Wiley-VCH, 2nd edition, 1987.

[71] J. P. Hannon and G. T. Trammell. Mössbauer diffraction. II. dynamical theory of Mössbauer optics. *Phys. Rev.*, 186:306–325, Oct 1969.

[72] J. P. Hannon and G. T. Trammell. Mössbauer diffraction. I. quantum theory of gamma-ray and x-ray optics. *Phys. Rev.*, 169:315–329, May 1968.

[73] J.P. Hannon and G.T. Trammell. Coherent γ-ray optics. *Hyperfine Interactions*, 123(1):127–274, 1999.

[74] G. V. Smirnov. Nuclear resonant scattering of synchrotron radiation. *Hyperfine Interactions*, 97(1):551–588, 1996.

[75] Yu Kagan, A M Afanas'ev, and V G Kohn. On excitation of isomeric nuclear states in a crystal by synchrotron radiation. *Journal of Physics C: Solid State Physics*, 12(3):615, 1979.

[76] G.V. Smirnov. General properties of nuclear resonant scattering. *Hyperfine Interactions*, 123(1):31–77, 1999.

[77] Xiangjin Kong, Wen-Te Liao, and Adriana Pálffy. Field control of single x-ray photons in nuclear forward scattering. *New Journal of Physics*, 16(1):013049, 2014.

[78] W.T. Liao and S. Ahrens. Gravitational and relativistic deflection of x-ray superradiance. *Nature Photonics*, 9, 2015.

[79] M. Brown, R. E. Peierls, and E. A. Stern. White lines in x-ray absorption. *Phys. Rev. B*, 15:738–744, Jan 1977.

[80] G. D. Mahan. Collective excitations in x-ray spectra of metals. *Phys. Rev. B*, 11:4814–4824, Jun 1975.

[81] G. D. Mahan. Excitons in metals: Infinite hole mass. *Phys. Rev.*, 163:612–617, Nov 1967.

[82] S. Hau-Riege. *High-Intensity X-rays - Interaction with Matter*. Wiley-VCH, 2011.

[83] J. J. Rehr and R. C. Albers. Theoretical approaches to x-ray absorption fine structure. *Rev. Mod. Phys.*, 72:621–654, Jul 2000.

[84] B. Roulet, J. Gavoret, and P. Nozières. Singularities in the x-ray absorption and emission of metals. i. first-order parquet calculation. *Phys. Rev.*, 178:1072–1083, Feb 1969.

[85] David C. Langreth. Singularities in the x-ray absorption and emission of metals. *Phys. Rev.*, 182:973–974, Jun 1969.

[86] P. Nozières and C. T. de Dominicis. Singularities in the x-ray absorption and emission of metals. III. one-body theory exact solution. *Phys. Rev.*, 178:1097–1107, Feb 1969.

[87] J. Frenkel. On the transformation of light into heat in solids. I. *Phys. Rev.*, 37:17–44, Jan 1931.

[88] Takashi Yamamoto. Assignment of pre-edge peaks in k-edge x-ray absorption spectra of 3d transition metal compounds: electric dipole or quadrupole? *X-Ray Spectrometry*, 37(6):572–584, 2008.

[89] E. Gerdau, R. Rüffer, H. Winkler, W. Tolksdorf, C. P. Klages, and J. P. Hannon. Nuclear Bragg diffraction of synchrotron radiation in yttrium iron garnet. *Phys. Rev. Lett.*, 54:835–838, Feb 1985.

[90] E. Gerdau, R. Rüffer, R. Hollatz, and J. P. Hannon. Quantum beats from nuclei excited by synchrotron radiation. *Phys. Rev. Lett.*, 57:1141–1144, Sep 1986.

[91] U. van Bürck, R. L. Mössbauer, E. Gerdau, R. Rüffer, R. Hollatz, G. V. Smirnov, and J. P. Hannon. Nuclear Bragg scattering of synchrotron radiation with strong speedup of coherent decay, measured on antiferromagnetic $^{57}febo_3$. *Phys. Rev. Lett.*, 59:355–358, Jul 1987.

[92] E. E. Alp, T. M. Mooney, T. Toellner, W. Sturhahn, E. Witthoff, R. Röhlsberger, E. Gerdau, H. Homma, and M. Kentjana. Time resolved nuclear resonant scattering from ^{119}Sn nuclei using synchrotron radiation. *Phys. Rev. Lett.*, 70:3351–3354, May 1993.

[93] W. Sturhahn and E. Gerdau. Evaluation of time-differential measurements of nuclear-resonance scattering of x rays. *Phys. Rev. B*, 49:9285–9294, Apr 1994.

[94] W. Sturhahn. Conuss and phoenix: Evaluation of nuclear resonant scattering data. *Hyperfine Interactions*, 125(1):149–172, 2000.

[95] R. Callens, R. Coussement, C. L'abbé, S. Nasu, K. Vyvey, T. Yamada, Y. Yoda, and J. Odeurs. Stroboscopic detection of nuclear forward-scattered synchrotron radiation. *Phys. Rev. B*, 65:180404, Apr 2002.

[96] R. Callens, R. Coussement, T. Kawakami, J. Ladrière, S. Nasu, T. Ono, I. Serdons, K. Vyvey, T. Yamada, Y. Yoda, and J. Odeurs. Principles of stroboscopic detection of nuclear forward-scattered synchrotron radiation. *Phys. Rev. B*, 67:104423, Mar 2003.

[97] R. Coussement, S. Cottenier, and C. L'abbé. Time-integrated nuclear resonant forward scattering of synchrotron radiation. *Phys. Rev. B*, 54:16003–16009, Dec 1996.

[98] D.P. Siddons, J.B. Hastings, U. Bergmann, F. Sette, and M. Krisch. Mössbauer spectroscopy using synchrotron radiation: overcoming detector limitations. *Nuclear Instruments and Methods in Physics Research Section B: Beam Interactions with Materials and Atoms*, 103(3):371 – 375, 1995.

[99] E.E. Alp, W. Sturhahn, and T.S. Toellner. Polarizer–analyzer optics. *Hyperfine Interactions*, 125(1):45–68, 2000.

[100] D.P. Siddons, U. Bergmann, and J.B. Hastings. Polarization effects in resonant nuclear scattering. *Hyperfine Interactions*, 123(1):681–719, 1999.

[101] B. Marx, K. S. Schulze, I. Uschmann, T. Kämpfer, R. Lötzsch, O. Wehrhan, W. Wagner, C. Detlefs, T. Roth, J. Härtwig, E. Förster, T. Stöhlker, and G. G. Paulus. High-precision x-ray polarimetry. *Phys. Rev. Lett.*, 110:254801, Jun 2013.

[102] B. Marx, I. Uschmann, S. Höfer, R. Lötzsch, O. Wehrhan, E. Förster, M. Kaluza, T. Stöhlker, H. Gies, C. Detlefs, T. Roth, J. Härtwig, and G.G. Paulus. Determination of high-purity polarization state of x-rays. *Optics Communications*, 284(4):915 – 918, 2011.

[103] Vasily Potapkin, Aleksandr I. Chumakov, Gennadii V. Smirnov, Jean-Philippe Celse, Rudolf Rüffer, Catherine McCammon, and Leonid Dubrovinsky. The ^{57}Fe Synchrotron Mössbauer Source at the ESRF. *Journal of Synchrotron Radiation*, 19(4):559–569, Jul 2012.

[104] A. I. Chumakov, M. V. Zelepukhin, G. V. Smirnov, U. van Bürck, R. Rüffer, R. Hollatz, H. D. Rüter, and E. Gerdau. Time spectra of a nearly-single-line pure nuclear reflection excited by synchrotron radiation. *Phys. Rev. B*, 41:9545–9547, May 1990.

[105] G. V. Smirnov, A. I. Chumakov, V. B. Potapkin, R. Rüffer, and S. L. Popov. Multispace quantum interference in a ^{57}fe synchrotron Mössbauer source. *Phys. Rev. A*, 84:053851, Nov 2011.

[106] G. V. Smirnov, U. van Bürck, A. I. Chumakov, A. Q. R. Baron, and R. Rüffer. Synchrotron Mössbauer source. *Phys. Rev. B*, 55:5811–5815, Mar 1997.

[107] A. Elshabini and F.D. Barlow. The thin film technology handbook. 1998.

[108] J. P. Hannon, N. V. Hung, G. T. Trammell, E. Gerdau, M. Mueller, R. Rüffer, and H. Winkler. Grazing-incidence antireflection films. i. basic theory. *Phys. Rev. B*, 32:5068–5080, Oct 1985.

[109] R. Röhlsberger. Theory of x-ray grazing incidence reflection in the presence of nuclear resonance excitation. *Hyperfine Interactions*, 123(1):301–325, 1999.

[110] Matts Björck and Gabriella Andersson. *GenX*: an extensible X-ray reflectivity refinement program utilizing differential evolution. *Journal of Applied Crystallography*, 40(6):1174–1178, Dec 2007.

[111] R. Röhlsberger, H. Thomas, K. Schlage, E. Burkel, O. Leupold, and R. Rüffer. Imaging the magnetic spin structure of exchange-coupled thin films. *Phys. Rev. Lett.*, 89:237201, Nov 2002.

[112] Hidekazu Mimura, Satoshi Matsuyama, Hirokatsu Yumoto, Hideyuki Hara, Kazuya Yamamura, Yasuhisa Sano, Masafumi Shibahara, Katsuyoshi Endo, Yuzo Mori, Yoshinori Nishino, Kenji Tamasaku, Makina Yabashi, Tetsuya Ishikawa, and Kazuto Yamauchi. Hard x-ray diffraction-limited nanofocusing with Kirkpatrick-Baez mirrors. *Japanese Journal of Applied Physics*, 44(4L):L539, 2005.

[113] B. Lengeler, C. G. Schroer, M. Richwin, J. Tümmler, M. Drakopoulos, A. Snigirev, and I. Snigireva. A microscope for hard x rays based on parabolic compound refractive lenses. *Applied Physics Letters*, 74(26):3924–3926, 1999.

[114] Eberhard Spiller and Armin Segmüller. Propagation of x rays in waveguides. *Applied Physics Letters*, 24(2):60–61, 1974.

[115] Wang J., M.J. Bedzyk, T.L. Penner, and M. Caffrey. Structural studies of membranes and surface layers up to 1,000 Å thick using x-ray standing waves. *Nature*, 354:377–380, 1991.

[116] J. Wang, M.J. Bedzyk, and M. Caffrey. Resonance-enhanced x-rays in thin films: A structure probe for membranes and surface layers. *Science*, 258, 1992.

[117] F. Pfeiffer, C. David, M. Burghammer, C. Riekel, and T. Salditt. Two-dimensional x-ray waveguides and point sources. *Science*, 297(5579):230–234, 2002.

[118] W. Jark, A. Cedola, S. Di Fonzo, M. Fiordelisi, S. Lagomarsino, N. V. Kovalenko, and V. A. Chernov. High gain beam compression in new-generation thin-film x-ray waveguides. *Applied Physics Letters*, 78(9):1192–1194, 2001.

[119] Y. P. Feng, S. K. Sinha, H. W. Deckman, J. B. Hastings, and D. P. Siddons. X-ray flux enhancement in thin-film waveguides using resonant beam couplers. *Phys. Rev. Lett.*, 71:537–540, Jul 1993.

[120] F. Pfeiffer, T. Salditt, P. Høghøj, I. Anderson, and N. Schell. X-ray waveguides with multiple guiding layers. *Phys. Rev. B*, 62:16939–16943, Dec 2000.

[121] T. Salditt, S. P. Krüger, C. Fuhse, and C. Bähtz. High-transmission planar x-ray waveguides. *Phys. Rev. Lett.*, 100:184801, May 2008.

[122] R. Röhlsberger, K. Schlage, T. Klein, and O. Leupold. Accelerating the spontaneous emission of x rays from atoms in a cavity. *Phys. Rev. Lett.*, 95:097601, Aug 2005.

[123] F. Schenk. *Optimization of resonances for multilayer x-ray resonators*. PhD thesis, Georg-August-Universität Göttingen, 2011.

[124] S.P. Krüger. *Optimization of waveguide optics for lensless x-ray imaging*. PhD thesis, Georg-August-Universität Göttingen, 2011.

[125] P. Karimov and E.Z. Kurmaev. Application of genetic algorithms for the optimization of x-ray waveguides. *Physics Letters A*, 320(2Ű3):234 – 237, 2003.

[126] L. G. Parratt. Surface studies of solids by total reflection of x-rays. *Phys. Rev.*, 95:359–369, Jul 1954.

[127] I. H. Deutsch, R. J. C. Spreeuw, S. L. Rolston, and W. D. Phillips. Photonic band gaps in optical lattices. *Phys. Rev. A*, 52:1394–1410, Aug 1995.

[128] M. Artoni, G. La Rocca, and F. Bassani. Resonantly absorbing one-dimensional photonic crystals. *Phys. Rev. E*, 72:046604, Oct 2005.

[129] J.P. Hannon and G.T. Trammell. Coherent γ-ray optics. *Hyperfine Interactions*, 123-124(1-4):127–274, 1999.

[130] A. Gibaud, G. Vignaud, and S. K. Sinha. The correction of geometrical factors in the analysis of X-ray reflectivity. *Acta Crystallographica Section A*, 49(4):642–648, Jul 1993.

[131] V. Weisskopf and E. Wigner. Berechnung der natürlichen Linienbreite auf Grund der Diracschen Lichttheorie. *Zeitschrift für Physik*, 63(1):54–73, 1930.

[132] E. T. Jaynes and F. W. Cummings. Comparison of quantum and semiclassical radiation theories with application to the beam maser. *Proceedings of the IEEE*, 51(1):89–109, Jan 1963.

[133] Enrico Fermi. Quantum theory of radiation. *Rev. Mod. Phys.*, 4:87–132, Jan 1932.

[134] I. I. Rabi, S. Millman, P. Kusch, and J. R. Zacharias. The molecular beam resonance method for measuring nuclear magnetic moments. The magnetic moments of $_3Li^6$, $_3Li^7$ and $_9F^{19}$. *Phys. Rev.*, 55:526–535, Mar 1939.

[135] L. Allen and J.H. Eberly. *Two-level atoms and optical Resonance*. Dover, 1987.

[136] F. W. Cummings. Stimulated emission of radiation in a single mode. *Phys. Rev.*, 140:A1051–A1056, Nov 1965.

[137] M. Scully and S. Zubairy. *Quantum Optics*. Cambridge University Press, 1997.

[138] G.S. Agarwal. *Quantum Optics*. Cambridge University Press, 2013.

[139] E. M. Purcell. Spontaneous emission probabilities at radio frequencies. *Physical Review*, 69:681+, 1946.

[140] Perry R. Rice and Robert J. Brecha. *Cavity Induced Transparency*. Springer US, Boston, MA, 1996.

[141] E. Peter, P. Senellart, D. Martrou, A. Lemaître, J. Hours, J. M. Gérard, and J. Bloch. Exciton-photon strong-coupling regime for a single quantum dot embedded in a microcavity. *Phys. Rev. Lett.*, 95:067401, Aug 2005.

[142] R. H. Dicke. Coherence in spontaneous radiation processes. *Phys. Rev.*, 93:99–110, Jan 1954.

[143] M. Gross and S. Haroche. Superradiance: An essay on the theory of collective spontaneous emission. *Physics Reports*, 93(5):301 – 396, 1982.

[144] Marlan O. Scully, Edward S. Fry, C. H. Raymond Ooi, and Krzysztof Wódkiewicz. Directed spontaneous emission from an extended ensemble of n atoms: Timing is everything. *Phys. Rev. Lett.*, 96:010501, Jan 2006.

[145] Anatoly A. Svidzinsky and Marlan O. Scully. On the evolution of n-atom state prepared by absorption of a single photon. *Optics Communications*, 283(5):753 – 757, 2010. Quo vadis Quantum Optics?

[146] Marlan O. Scully. Collective Lamb shift in single photon Dicke superradiance. *Phys. Rev. Lett.*, 102:143601, Apr 2009.

[147] Tom Bienaimé, Nicola Piovella, and Robin Kaiser. Controlled Dicke subradiance from a large cloud of two-level systems. *Phys. Rev. Lett.*, 108:123602, Mar 2012.

[148] J. J. Hopfield. Theory of the contribution of excitons to the complex dielectric constant of crystals. *Phys. Rev.*, 112:1555–1567, Dec 1958.

[149] Y.O. Dudin, L. Li, F. Bariani, and A. Kuzmich. Observation of coherent many-body Rabi oscillations. *Nature Phys.*, 8:790–794, 2012.

[150] S. M. Dutra and P. L. Knight. Spontaneous emission in a planar Fabry-Pérot microcavity. *Phys. Rev. A*, 53:3587–3605, May 1996.

[151] Ho Trung Dung and Kikuo Ujihara. Three-dimensional nonperturbative analysis of spontaneous emission in a Fabry-Perot microcavity. *Phys. Rev. A*, 60:4067–4082, Nov 1999.

[152] Suc-Kyoung Hong, Seog Woo Nam, and Hyung Jin Yang. Cooperative spontaneous emission of nano-emitters with inter-emitter coupling in a leaky microcavity. *Journal of Optics*, 17(10):105401, 2015.

[153] Ottavia Jedrkiewicz and Rodney Loudon. Theory of transient spontaneous emission by an atom in a planar microcavity. *Phys. Rev. A*, 60:4951–4964, Dec 1999.

[154] G. Agarwal. *Quantum statistical theories of spontaneous emission and their relation to other approaches*. Springer Tracts in Modern Physics, Vol. 70, 1974.

[155] F. De Martini, M. Marrocco, and D. Murra. Transverse quantum correlations in the active microscopic cavity. *Phys. Rev. Lett.*, 65:1853–1856, Oct 1990.

[156] Kikuo Ujihara. Spontaneous emission and the concept of effective area in a very short optical cavity with plane-parallel dielectric mirrors. *Japanese Journal of Applied Physics*, 30(5B):L901, 1991.

[157] Xufeng Zhang, Chang-Ling Zou, Liang Jiang, and Hong X. Tang. Strongly coupled magnons and cavity microwave photons. *Phys. Rev. Lett.*, 113:156401, Oct 2014.

[158] H.J. Carmichael. *Statistical Methods in Quantum Optics II*. Springer, 2008.

[159] S. Filipp, M. Göppl, J. M. Fink, M. Baur, R. Bianchetti, L. Steffen, and A. Wallraff. Multimode mediated qubit-qubit coupling and dark-state symmetries in circuit quantum electrodynamics. *Phys. Rev. A*, 83:063827, Jun 2011.

[160] Youngwoon Choi, Sungsam Kang, Sooin Lim, Wookrae Kim, Jung-Ryul Kim, Jai-Hyung Lee, and Kyungwon An. Quasieigenstate coalescence in an atom-cavity quantum composite. *Phys. Rev. Lett.*, 104:153601, Apr 2010.

[161] S. Bajt, S. B. Clark, S. R. Sutton, M. L. Rivers, and J. V. Smith. Synchrotron x-ray microprobe determination of chromate content using x-ray absorption near-edge structure. *Analytical Chemistry*, 65(13):1800–1804, 1993.

[162] Yueyun Hu, Wenxing Liu, Yong Sun, Xi Shi, Jun Jiang, Yaping Yang, Shiyao Zhu, Jörg Evers, and Hong Chen. Electromagnetically-induced-transparency–like phenomenon with resonant meta-atoms in a cavity. *Phys. Rev. A*, 92:053824, Nov 2015.

[163] Yusuf Turek, Yong Li, and C. P. Sun. Electromagnetically-induced-transparency–like phenomenon with two atomic ensembles in a cavity. *Phys. Rev. A*, 88:053827, Nov 2013.

[164] Ed Hinds. Personal communication.

[165] B. Sahoo, K. Schlage, J. Major, U. von Hörsten, W. Keune, H. Wende, and R. Röhlsberger. Preparation and characterization of ultrathin stainless steel films. *AIP Conf. Proc.*, 1347, 2011.

[166] C. Strohm. Personal communication.

[167] Yong-Chun Liu, Xingsheng Luan, Hao-Kun Li, Qihuang Gong, Chee Wei Wong, and Yun-Feng Xiao. Coherent polariton dynamics in coupled highly dissipative cavities. *Phys. Rev. Lett.*, 112:213602, May 2014.

[168] Eberhard Spiller and Leon Golub. Fabrication and testing of large area multilayer coated x-ray optics. *Appl. Opt.*, 28(14):2969–2974, Jul 1989.

[169] Rolf-Peter Haelbich, Armin Segmüller, and Eberhard Spiller. Smooth multilayer films suitable for x-ray mirrors. *Applied Physics Letters*, 34(3):184–186, 1979.

[170] D. H. Bilderback. Reflectance of x-ray mirrors from 3.8 to 50 kev (3.3 to 0.25Å). *Proc. SPIE*, 0315:90–102, 1982.

[171] C. Weisbuch, M. Nishioka, A. Ishikawa, and Y. Arakawa. Observation of the coupled exciton-photon mode splitting in a semiconductor quantum microcavity. *Phys. Rev. Lett.*, 69:3314–3317, Dec 1992.

[172] M. Grabherr, R. Jager, M. Miller, C. Thalmaier, J. Herlein, R. Michalzik, and K. J. Ebeling. Bottom-emitting vcsel's for high-cw optical output power. *IEEE Photonics Technology Letters*, 10(8):1061–1063, Aug 1998.

[173] Shanhui Fan, Joshua N. Winn, Adrian Devenyi, J. C. Chen, Robert D. Meade, and J. D. Joannopoulos. Guided and defect modes in periodic dielectric waveguides. *J. Opt. Soc. Am. B*, 12(7):1267–1272, Jul 1995.

[174] Lev I. Deych, Alexey Yamilov, and A. A. Lisyansky. Local polariton modes and resonant tunneling of electromagnetic waves through periodic Bragg multiple quantum well structures. *Phys. Rev. B*, 64:075321, Jul 2001.

[175] Y. D. Chong, David E. Pritchard, and Marin Soljačić. Quantum theory of a resonant photonic crystal. *Phys. Rev. B*, 75:235124, Jun 2007.

[176] T. Holstein and H. Primakoff. Field dependence of the intrinsic domain magnetization of a ferromagnet. *Phys. Rev.*, 58:1098–1113, Dec 1940.

[177] J. Kasprzak, Richard, S. M. Kundermann, H. Baas, P. Jeambrun, J. Keeling, F. Marchetti, M. Szymanska, R. Andre, J. Staehli, V. Savona, P. Littlewood, R. Deveaud, and L. Dang. Bose-Einstein condensation of exciton polaritons. *Nature*, 443:409–414, 2006.

[178] Stefan Rist, Patrizia Vignolo, and Giovanna Morigi. Photonic spectrum of bichromatic optical lattices. *Phys. Rev. A*, 79:053822, May 2009.

[179] Matthias Weidemüller, Andreas Hemmerich, Axel Görlitz, Tilman Esslinger, and Theodor W. Hänsch. Bragg diffraction in an atomic lattice bound by light. *Phys. Rev. Lett.*, 75:4583–4586, Dec 1995.

[180] Alexander Schilke, C. Zimmermann, Philippe W. Courteille, and William Guerin. Optical parametric oscillation with distributed feedback in cold atoms. *Nature Photonics*, 6:101–104, 2012.

[181] S. Jorda, U. Rössler, and D. Broido. Fine structure of excitons and polariton dispersion in quantum wells. *Phys. Rev. B*, 48:1669–1677, Jul 1993.

[182] M. Hübner, J. Kuhl, T. Stroucken, A. Knorr, S. W. Koch, R. Hey, and K. Ploog. Collective effects of excitons in multiple-quantum-well Bragg and anti-Bragg structures. *Phys. Rev. Lett.*, 76:4199–4202, May 1996.

[183] E.L. Ivchenko, A.I. Nesvizhskii, and S. Jorda. Resonant Bragg reflection from quantum-well structures. *Superlattices and Microstructures*, 16(1):17 – 20, 1994.

[184] M. Hübner, J. P. Prineas, C. Ell, P. Brick, E. S. Lee, G. Khitrova, H. M. Gibbs, and S. W. Koch. Optical lattices achieved by excitons in periodic quantum well structures. *Phys. Rev. Lett.*, 83:2841–2844, Oct 1999.

[185] J. P. Prineas, C. Ell, E. S. Lee, G. Khitrova, H. M. Gibbs, and S. W. Koch. Exciton-polariton eigenmodes in light-coupled $In_{0.04}Ga_{0.96}As/GaAs$ semiconductor multiple-quantum-well periodic structures. *Phys. Rev. B*, 61:13863–13872, May 2000.

[186] Tomoe Ikawa and Kikuo Cho. Fate of the superradiant mode in a resonant Bragg reflector. *Phys. Rev. B*, 66:085338, Aug 2002.

[187] M. V. Erementchouk, L. I. Deych, and A. A. Lisyansky. Optical properties of one-dimensional photonic crystals based on multiple-quantum-well structures. *Phys. Rev. B*, 71:235335, Jun 2005.

[188] D. Goldberg, L. Deych, A. Lisyansky, Z. Shi, V. Menon, V. Tokranov, M. Yakimov, and S. Oktyabrsky. Exciton-lattice polartions in multiple-quantum-well-based photonic crystals. *Nature Photonics*, 3:662–666, 2009.

[189] E. L. Ivchenko, M. M. Voronov, M. V. Erementchouk, L. I. Deych, and A. A. Lisyansky. Multiple-quantum-well-based photonic crystals with simple and compound elementary supercells. *Phys. Rev. B*, 70:195106, Nov 2004.

[190] A. Askitopoulos, L. Mouchliadis, I. Iorsh, G. Christmann, J. J. Baumberg, M. A. Kaliteevski, Z. Hatzopoulos, and P. G. Savvidis. Bragg polaritons: Strong coupling and amplification in an unfolded microcavity. *Phys. Rev. Lett.*, 106:076401, Feb 2011.

[191] Jon M. Bendickson, Jonathan P. Dowling, and Michael Scalora. Analytic expressions for the electromagnetic mode density in finite, one-dimensional, photonic band-gap structures. *Phys. Rev. E*, 53:4107–4121, Apr 1996.

[192] Sajeev John and Tran Quang. Spontaneous emission near the edge of a photonic band gap. *Phys. Rev. A*, 50:1764–1769, Aug 1994.

[193] Sajeev John and Tran Quang. Localization of superradiance near a photonic band gap. *Phys. Rev. Lett.*, 74:3419–3422, Apr 1995.

[194] Fabio Biancalana, Leonidas Mouchliadis, Celestino Creatore, Simon Osborne, and Wolfgang Langbein. Microcavity polaritonlike dispersion doublet in resonant Bragg gratings. *Phys. Rev. B*, 80:121306, Sep 2009.

[195] K. Sebald, SK. S. Rahman, M. Cornelius, T. Kaya, J. Gutowski, T. Klein, A. Gust, D. Hommel, and S. Klembt. Bragg polaritons in a ZnSe-based unfolded microcavity at elevated temperatures. *Applied Physics Letters*, 108(12), 2016.

[196] K. Okamoto, T. Noma, A. Komoto, W. Kubo, M. Takahashi, A. Iida, and H. Miyata. X-ray waveguide mode in resonance with a periodic structure. *Phys. Rev. Lett.*, 109:233907, Dec 2012.

[197] I. Serdons, R. Callens, R. Coussement, S. Gheysen, J. Ladrière, S. Morimoto, S. Nasu, J. Odeurs, Y. Yoda, and G. Wortmann. Stroboscopic detection of the ^{181}Ta-mössbauer resonance with synchrotron radiation. *Nuclear Instruments and Methods in Physics Research Section B: Beam Interactions with Materials and Atoms*, 251(1):297 – 303, 2006.

[198] J. M. Rodenburg, A. C. Hurst, A. G. Cullis, B. R. Dobson, F. Pfeiffer, O. Bunk, C. David, K. Jefimovs, and I. Johnson. Hard-x-ray lensless imaging of extended objects. *Phys. Rev. Lett.*, 98:034801, Jan 2007.

[199] Henry N. Chapman. Phase-retrieval x-ray microscopy by Wigner-distribution deconvolution. *Ultramicroscopy*, 66(3):153 – 172, 1996.

[200] J. M. Rodenburg and H. M. L. Faulkner. A phase retrieval algorithm for shifting illumination. *Applied Physics Letters*, 85(20):4795–4797, 2004.

[201] Andrew M. Maiden and John M. Rodenburg. An improved ptychographical phase retrieval algorithm for diffractive imaging. *Ultramicroscopy*, 109(10):1256 – 1262, 2009.

[202] Pierre Thibault, Martin Dierolf, Oliver Bunk, Andreas Menzel, and Franz Pfeiffer. Probe retrieval in ptychographic coherent diffractive imaging. *Ultramicroscopy*, 109(4):338 – 343, 2009.

[203] J. R. Fienup. Phase retrieval algorithms: a comparison. *Appl. Opt.*, 21(15):2758–2769, Aug 1982.

Danksagung

In erster Linie möchte ich mich ganz herzlich bei Herrn Prof. Dr. Ralf Röhlsberger dafür bedanken, dass er mir ermöglicht hat, diese Doktorarbeit in seiner Gruppe anzufertigen. Ich fand von Anfang an ideale Bedingungen vor, vor allem aber genau die richtige Mischung aus Betreuung, Anregung, und Lenkung einerseits, und andererseits der Ermutigung selbst eigenen Ideen nachzugehen, sowie der dazu nötigen Freiheit. Auch hat er sich nicht daran gestört, wenn ich mich auf der Suche nach dem richtigen Weg von Nebensächlichkeiten habe ablenken lassen, oder auch ein paar Sackgassen mitgenommen habe. Diese Doktorarbeit hätte vielleicht schneller fertig werden können; es hätte mir allerdings bedeutend weniger Spass gemacht.
Weiterhin danke ich auch allen Mitgliedern der Gruppe für ihre Hilfe und Unterstützung, zuvorderst aber Kai Schlage, der sich drei Jahre lang von mir unterbrechen liess um Fragen schwankender Qualität und Dringlichkeit zu beantworten, ohne mich ein einziges mal zurechtzuweisen. Gleiches gilt für Cornelius Strohm, dessen Geduld aber auf Grund der Entfernung seines Büros weniger intensiv strapaziert wurde. Auch Daniel Schumacher, Lars Bocklage, Svenja Willing, Jakob Gollwitzer, Christian Adolff, Andrey Siemens, Tatiana Gurieva und Denise Erb möchte ich vielmals danken. Sie alle haben bei zahlreichen Strahlzeiten geholfen, und ohne sie wäre diese Dissertation nicht zu Stande gekommen. Nicht zuletzt haben sie dafür gesorgt, dass die Strahlzeiten, und die sonstige Arbeitszeit wesentlich unterhaltsamer und kurzweiliger verlief als dies sonst üblich ist.
Auch ausserhalb des DESY möchte ich einigen Leuten danken. Jörg Evers und Kilian Heeg vom Max-Planck-Institut für Kernphysik sind nicht nur ausgiebig in dieser Arbeit zitiert, sondern haben auch mit grosser Sorgfalt und Geduld meine Novizenfragen theoretischer Natur beantwortet, und viele anregende Diskussionen angenommen und aufgeworfen. Insbesondere Kilian möchte ich nochmals herzlich für das Korrekturlesen der Arbeit danken.
Des weiteren danke ich Ingo Uschmann, Kai-Sven Schulze, Berit Marx, Robert Loetzsch und Hendrik Bernwardt von der Friedrich-Schiller-Universität Jena für ihre wesentliche Mithilfe während der Strahlzeiten. Ferner möchte ich den Belegschaften der Strahlführungslinien P01 und ID18, für die ich hier stellvertretend Hans-Christian Wille und Rudolf Rüffer nenne für ihre Unterstützung danken.

Zu guter Letzt möchte ich mich bei meinen Eltern bedanken. Ohne ihre bedingungslose Unterstützung in jeder Hinsicht hätte ich in den letzten zehn Jahren nichts geschafft.

Eidesstattliche Erklärung

Hiermit erkläre ich an Eides statt, dass ich die vorliegende Dissertationsschrift selbst verfasst und keine anderen als die angegebenen Quellen und Hilfsmittel benutzt habe.

I hereby declare, on oath, that I have written the present dissertation by my own and have not used other than the acknowledged resources and aids.

Hamburg, den